Coupling Textural, Magnetic, and Modeling Techniques to Understand Precambrian Paleoenvironments

Thesis by

Sarah Pearl Slotznick

In Partial Fulfillment of the Requirements for
the degree of
Doctor of Philosophy

CALIFORNIA INSTITUTE OF TECHNOLOGY
Pasadena, California

2016
(Defended May 19, 2016)

ACKNOWLEDGEMENTS

First and foremost, I would like to thank my advisors Woody Fischer and Joe Kirschvink for their intellectual guidance through my graduate school career. Woody helped me develop these projects through formative discussions, was always available for a quick chat when large or small questions popped up, and always made certain I remembered the forest, not simply the trees. Joe encouraged me to explore my interests wherever they took me, gave me free rein of his laboratory, and helped develop other important academic skills, in addition to research, by encouraging my teaching and mentoring of undergraduate researchers, visitors, and Ge124b students.

I would also like to acknowledge the many collaborators and co-authors who aided me during the projects detailed in this dissertation. Don Winston, Jerry Zieg, and John Grotzinger facilitated my exploration of the Belt Supergroup, and shared their detailed knowledge of the region in the field from years of work in Montana, without which this work would not have been possible. Sam Webb allowed me to be one of the first users on his new beamline and promptly answered my numerous questions whether they be frantic texts for troubleshooting at midnight or analysis concerns weeks later. Mike Jackson and Bruce Moskowitz at the Institute for Rock Magnetism taught me how to handle the MPMS and VSM as well as aiding me substantially in data interpretation. John Eiler taught me that all rocks are metamorphic.

This dissertation required four field seasons in Montana, and my field assistants filled incredibly important roles. Tim Lyons and UCR students helped me initially explore the geology of Glacier National Park from an academic viewpoint. The 2013 Agouron Field Course participants, especially JC Creveling and Ted Present, tolerated long drives and monotonous metamorphosed rocks to help me complete a 275 mile sampling transect across western Montana as well as providing intellectual conversations that aided my critical thinking about the Belt Supergroup. Austin Chadwick and Steven Skinner provided tremendous aid hauling rocks while climbing mountains, often the same mountain over and over again, while remaining cheerful and ready to discuss new field observations. I'd like to thank Tess Puig, Kathy Lima, Julie Lee, Alice Oh, Jennifer Leonardini, Janice Grancich, Lisa Christiansen, Heather Steele, Mark Garcia, Chi Ma, Yunbin Guan, Dian Buchness, Liz Boyd, and Marcia Hudson for their administrative and technical support helping these field seasons and research projects happen as well as guiding me through my graduate school years.

Alex Sessions, my academic advisor, helped guide me through the challenges of required classes. I had several mentors in my first few years here at Caltech who helped steer my trajectory as a graduate student, including Lauren Edgar, June Wicks, Daniel Stolper, Anne Dekas, Maggie Osborne, and Katie Snell. Lab group members Kristin Bergmann, Jena Johnson, Lewis Ward, Jim Hemp, Kyle Bradley, Usha Lingappa, Lizzy Trower, Joe "Vinny" Biasi, and Jennifer Buz continuously showed me new exciting research in the broad field of Geobiology, helped provide isotopic support for my work, kept me company at the synchrotron and through the analysis process, and constantly troubleshot issues with the ultra-high resolution scanning SQuID magnetic microscope to keep it running.

My first-year pit crew—Stephen Cox, Morgan Raven, Elizabeth Trembath-Reichert, David Case, Jeff Prancevic, Jena Johnson—kept me company during the challenging first year and in the equally challenging years that followed. Kirsten Siebach, my officemate, dealt with my less-than-neat organization methods, was always willing to help me make decisions, even insignificant ones, and commiserated with me through the past 2 months while working on our theses. Alison Piasecki, Giuliana Viglione, Frank Sousa, Jason Price, Sean Mullin, and many others in the division provided much-needed office visits and traveled with me to explore the regional geology of the southwestern United States.

My friends outside of the GPS Division—first-year cohort Aero-ME-BioChem, EXPLiCIT, Bookclub, Material Science, GHC, 157th—have made my time here at Caltech much more enjoyable by providing much needed breaks from research. My roommates—Jackie Villadsen, Sunita Darbe, and Chengyun Hau—and my boyfriend Steven Skinner played a vital role in keeping me optimistic and happy throughout my time in graduate school by always being available during tough times, no matter the time of day. Lastly, I'd like to thank my family for their continuous support of my geologic career; from encouraging my scientific interests at a young age, giving me an appreciation for travel and exploration, supporting me through my 25-year student career, and even proof-reading this thesis, they have always been there for me.

ABSTRACT

The oxygenation of our planet is perhaps the greatest transition in its history, dramatically affecting geochemical cycles and the evolution of life. Major first-order questions still remain about late Archean and Proterozoic environments, even as newly developed geochemical techniques provide additional constraints and create subtle conundrums. I apply a new approach to classic localities to understand Precambrian redox character and paleoenvironmental conditions by combining textural observations from optical and electron microscopy, isotopic measurements, and (synchrotron-based) x-ray spectroscopy with scanning magnetic microscopy and bulk rock magnetic experiments. Models paired with data from the literature provide additional context for these measurement results.

The first portion of this dissertation focuses on understanding the predominant microbial metabolism recorded in the 2.72 Ga Tumbiana Formation stromatolites. I proposed that these stromatolites formed in shallow, anoxic waters and record a global signature of unique autotrophy distinct from younger systems dominated by oxygenic photosynthesis. The next portion of this dissertation uses the redox sensitivity of iron as a tool to investigate paleoredox conditions of the 1.45 Ga lower Belt Supergroup during a potentially transitional time-period in surface environments. Observations of primary mineralogy in early diagenetic pyrite and detrital iron oxides suggest an oxygenated water-column overlying anoxic, sulfidic pore-fluids very similar to the modern. The final portion of this dissertation assesses the effects of prevalent secondary overprints on the use of iron as a paleoredox proxy. Theoretical data-driven models combined with trends from the Belt Supergroup highlight the mobility of iron during progressive burial metamorphism as well as in diagenetic transformations and reactions with infiltrating fluids. Applying coupled techniques, specifically including textural methods, is vital for untangling

secondary alterations from primary records of environmental conditions during the Precambrian.

PUBLISHED CONTENT AND CONTRIBUTIONS

Slotznick, S. P., and Fischer, W. W., 2016, Examining Archean methanotrophy: Earth and Planetary Science Letters, v. 441, p. 52-59. doi: 10.1016/j.epsl.2016.02.013

> S.P.S. participated in development of the project, made petrographic observations, prepared samples, interpreted results, constructed the model, and wrote much of the manuscript.

Slotznick, S. P., Zieg, J., Webb, S. M., Kirschvink, J. L., and Fischer, W. W., 2015, Iron Mineralogy and Redox Chemistry of the Mesoproterozoic Newland Formation in the Helena Embayment, Belt Supergroup, Montana: Northwest Geology, v. 44, p. 55-72.

> S.P.S. participated in conception of the project, collected samples from Montana, measured samples using coupled techniques, analyzed data, interpreted results, and wrote much of the manuscript.

Slotznick, S. P., Winston, D., Webb, S. M., Kirschvink, J. L., and Fischer, W. W., 2016, Iron mineralogy and redox conditions during deposition of the Mid-Proterozoic Appekunny Formation, Belt Supergroup, Glacier National Park: Geological Society of America Special Papers, v. 522, doi: 10.1130/2016.2522(09).

> S.P.S. participated in conception of the project, collected samples from Montana, made field observations, measured stratigraphic sections, measured samples using coupled techniques, analyzed data, interpreted results, and wrote much of the manuscript.

TABLE OF CONTENTS

LIST OF TABLES

LIST OF FIGURES

Chapter 1

Introduction

1.1 Background

The rise of atmospheric oxygen and subsequent oxygenation of oceans and lakes was a dramatic environmental shift that changed our planet and the life inhabiting it. A major rise in oxygen occurred ~2.35 billion years ago (Ga) in an event called the Great Oxidation Event (GOE) (Bekker et al., 2004; Farquhar et al., 2000). Although some scientists believed the GOE was spurred by the biological innovation of oxygenic photosynthesis (e.g. Johnson et al., 2013; Kopp et al., 2005; Williamson et al., 2011), oxygen would have been toxic to many organisms and required radical changes of evolutionary pathways for early life (Fischer et al., 2016; Sleep and Bird, 2008).

Before the GOE, atmospheric oxygen was constrained to low levels by mass-independent fractionation of sulfur isotopes (<0.001% present atmospheric levels) (Farquhar et al., 2000; Pavlov and Kasting, 2002) and by detrital redox-sensitive mineral grains (<0.015 % present atmospheric levels) (Johnson et al., 2014). During this anoxic time period, transition metals were prevalent in the oceans and heavily utilized by microbes for nutrients, energy, and chemical building blocks (Eck and Dayhoff, 1966; Schoepp-Cothenet et al., 2012; Williams and Frausto Da Silva, 2003; Zerkle et al., 2005). However, transitions in redox state of the Earth's atmosphere and oceans after the GOE changed the proportions of metals used in early organisms (Williams and Frausto Da Silva, 2003; Zerkle et al., 2005). The changing redox conditions also affected the evolution of complex eukaryote cells. Oxygen is required in making certain biological compounds (e.g. sterols) contained in all eukaryotes (e.g. Brocks et al., 2003; Fischer, 2016; Raymond and Blankenship, 2004) and almost all eukaryotes today contain mitochondria. Although acquired late in the development of eukaryotic cells (Pittis and Gabaldón, 2016), mitochondria perform the oxidative-phosphorylation reactions that allow the aerobic metabolisms observed in most modern eukaryotes today (Embley and Martin, 2006). Better understanding of aqueous environmental conditions during the Archean and Proterozoic, especially oxygen and sulfur levels, will allow better understanding of the constraints and pacing of evolution.

Several different techniques have been applied in recent years to understand the paleoenvironment during these critical periods for development of life on Earth. Much of the focus has been on redox conditions; therefore, many new methods have been developed focusing on transition metals as a window into redox processes on the ancient Earth. Observations of iron mineralogy in sedimentary rocks have been utilized for over 50 years to understand changes in redox during the time period surrounding the GOE (e.g. Cloud, 1968; Holland, 1984), and a new geochemical proxy called iron speciation builds upon the fundamental redox sensitivity of iron to more quantitatively provide redox determinations of water column chemistry from ancient rocks (Poulton and Canfield, 2005, 2011). Iron speciation studies have revealed a hitherto unobserved complexity in paleoenvironmental conditions with redox character varying from oxic to ferruginous (anoxic) to euxinic (H_2S-rich, anoxic) over short time periods, between geographic locations, and within single basins (Fig. 1.1A) (e.g. Canfield et al., 2013; Gilleaudeau and Kah, 2015; Sperling et al., 2015). If correct, this would fundamentally change our canonical understanding of Precambrian time (Fig. 1.1B) and force re-evaluation of environmental constraints on the evolution of life. In this dissertation, I use distinct multi-part techniques in a new approach for understanding Precambrian paleoenvironments at key evolutionary stages.

1.2 Dissertation Summary

The oldest fossil evidence for life on Earth occurs in disputed microfossils from the 3.45 Ga Apex Chert and the 3.43 Ga Strelley Pool Formation (Brasier et al., 2015; Schopf, 1993; Wacey et al., 2012) as well as in the stromatolites of the Strelley Pool Formation (Allwood et al., 2006; Hofmann et al., 1999; Lowe, 1980) (Fig. 1.1C). However, these stromatolites are possibly abiogenic based on their regular laminae and surface normal accretion (Grotzinger and Knoll, 1999;

Lowe, 1994). The oldest non-disputed biologically-mediated stromatolites are those from the 2.72 Ga Tumbiana Formation, Fortescue Group, Western Australia which show trapped-and-bound detrital grains, organic carbon globules, and laminae that vary systematically in thickness (Awramik and Buchheim, 2009; Coffey et al., 2013; Flannery and Walter, 2012; Lepot et al., 2009; Wacey et al., 2010) (Fig. 1.1C). In Chapter 2 of this dissertation, I discuss work targeting these stromatolites to understand the microbial metabolic processes they record and the surrounding environmental conditions before the GOE.

The Tumbiana Formation contains a unique organic carbon isotope signature that is very depleted in ^{13}C compared to younger samples; it is the type section of a global isotopic signature called the Fortescue Excursion (Eigenbrode and Freeman, 2006; Fischer et al., 2009; Hayes et al., 1983; Hayes et al., 1999; Schidlowski et al., 1983; Schoell and Wellmer, 1981). Early work suggested the excursion could be due biological cycling of methane in an "Age of Global Methanotrophy" before the rise of oxygen (Hayes, 1994; Schoell and Wellmer, 1981). Later developments suggested the methanotrophy could be anaerobic in nature (Hinrichs, 2002); however, molecular biomarkers were found in the Fortescue Group that suggested the presence of cyanobacteria and oxygenic photosynthesis, although later they were proposed to be from secondary migrating fluids or surface contamination (Brocks et al., 2003; Brocks et al., 1999; French et al., 2015; Rasmussen et al., 2008). Therefore, further studies have variably chosen aerobic or anaerobic photosynthetic metabolic processes paired with methanotrophy to explain the carbonate isotopic signal (Coffey et al., 2013; Eigenbrode and Freeman, 2006; Stüeken et al., 2015; Thomazo et al., 2009; Yoshiya et al., 2012). I combined textural petrographic observations, magnetic microscopy, microscale isotopic sampling, and modeling of the Archean carbonate system with literature values of Phanerozoic methanotrophy to highlight that these samples, although slightly affected by surface weathering, preserve a real signal that is not suggestive of methanotrophy, neither aerobic nor anaerobic in nature. Instead I propose that an alternative metabolism, the reductive acetyl Coenzyme A (CoA) pathway, could be responsible for the inorganic and organic carbon isotope signatures captured in the Tumbiana stromatolites. The reductive acetyl CoA pathway is a primitive carbon fixation metabolism that can also generate energy or be paired with other catabolic pathways, and it is currently used by a number of anaerobic microbes including acetogens, methanogens, and sulfate reducers (Fuchs, 2011; Martin, 2012; Nitschke and Russell, 2012). The reductive acetyl CoA pathway is restricted to anaerobic metabolisms due to oxygen-sensitive enzymes and incredibly reducing potentials, suggesting that the shallow-water stromatolites were deposited in an anoxic environment. The Tumbiana Formation stromatolites represent a completely distinct biological system in an anoxic Archean world with foreign microbial processes dominating the ecosystem.

About 500 million years after the GOE, fossil evidence for eukaryotes begins to appear in the rock record (Fig. 1.1C) (Knoll et al., 2006). The delayed appearance of eukaryotic fossils after the rise of oxygen and slow evolution from single celled eukaryotes to multicellularity to animals have been the subjects of intense debate beyond the scope of this work; however, environmental factors such as redox conditions and oxygen levels have often been suggested to determine the timing of these evolutionary events (e.g. Anbar and Knoll, 2002; Kah and Bartley, 2011). Eukaryotes mark their appearance in the rock record through large complex microfossils (e.g. Bergmann et al., 2013; Javaux et al., 2004; Lamb et al., 2009; Xiao et al., 1997; Yan and Liu, 1993) and the first body macrofossils. *Grypania spiralis* macrofossils are found in the 1.85 Ga iron formations of Canada and the United States (Han and Runnegar, 1992; Knoll et al., 2006) as well as in the Mesoproterozoic Gaoyuzhuang Formation in China and the 1.45 Ga Greyson Formation of the Belt Supergroup in Montana (Walcott, 1899; Walter et al., 1976; Walter et al., 1990). The lower Belt Supergroup contains other diverse macro- and microfossils, a few of which have been interpreted to be eukaryotes (Adam et al., 2014; Fedonkin and Yochelson, 2002; Horodyski, 1993; Horodyski et al., 1989; Retallack et al., 2013). In Chapters 3, 4, and 5, I investigate the formations in which these putative eukaryotes were found to understand the redox conditions and paleoenvironment of shallow waters as well as in deeper parts of the mid-Proterozoic Belt Basin.

The Belt Supergroup is a classic, well-studied mid-Proterozoic stratigraphic sequence due to its incredible preservation, expanded thickness, and large areal extent with outcrops exposed in Montana, Idaho, Washington, Alberta, and British Columbia. Many previous studies have focused on understanding the redox character and depositional environment of the lower Belt strata within the Belt Supergroup; initial work using iron mineralogy, sedimentological features, and sulfur and carbon isotopes and abundances suggested euxinic deep waters with oxic waters in persistent stratification (Gellatly and Lyons, 2005; Huebschman, 1973; Luepke and Lyons, 2001; Lyons et al., 2000). A recent study using iron speciation instead interpreted that ferruginous conditions dominated during lower Belt deposition, and that ferruginous conditions were an important redox state throughout much of the Proterozoic (Planavsky et al., 2011; Poulton and Canfield, 2011). A further study on the lower Belt Supergroup using nitrogen isotopes has expanded this view by suggesting shallow waters were oxic in a stratified basin (Stüeken, 2013). I chose to investigate the redox nature of the Belt Basin by similarly utilizing iron mineralogy and chemistry, but in a new approach combining textural observations from field geology, optical microscopy, magnetic microscopy, and (synchrotron) microprobe x-ray spectroscopy with bulk rock magnetic measurements. I sampled the lower Belt Group across a range of well-characterized metamorphic conditions from sub-biotite to garnet zone (Duke and Lewis, 2010) in order to understand not only the primary mineralogy for redox interpretations, but also how iron mineralogy changes after deposition in diagenetic and metamorphic reactions and how these overprints could be untangled. My analyses found that extensive recrystallization and diagenetic/metamorphic transformations had occurred, even in the best-preserved parts of the Belt Basin. However, primary mineralogy was preserved in recrystallized early diagenetic pyrite and sulfate as well as detrital iron oxides such as magnetite and hematite. I suggest that the Belt Basin was primarily oxic with suboxic, anoxic, and/or sulfidic pore waters similar to modern environments. This work helps connect eukaryote development to conditions in which they are known to thrive.

One concern when utilizing iron mineralogy for paleoredox interpretations is that subsequent diagenetic and metamorphic alterations of iron minerals could occur and blur environmental information. In Chapters 5 and 6, I investigate these questions by studying transformations of the iron mineralogy within the same sedimentary rock formations across a range of metamorphic conditions from <300°C (sub-biotite zone) to >575°C (kyanite or sillimanite zone). Using data from the literature on Paleozoic siliciclastic and carbonate sequences in Maine and Vermont, it is clear that increasing metamorphic grade can affect paleoredox proxies by moving iron from carbonates, oxides, and sulfides to silicate minerals. In lower grade rocks, pyrrhotite formation and diagenetic iron carbonate formation are important transformations that severely affect proxies and, without detailed geological observations, require unsupported assumptions of metamorphic reactions to untangle. Interestingly, these theoretical modeled results match trends observed in the lower Belt rocks of Montana and Idaho across the sub-biotite and biotite zone. A definitive pyrrhotite-siderite isograd was mapped in the sub-biotite zone with additional appearances of iron silicates and oxides as metamorphic grade increased. Even in the best-preserved strata, Fe-rich carbonates, nano-phase pyrrhotite, and base-metal sulfides were observed, highlighting the mobility of iron in secondary diagenetic transformations. Utilization of textural methods to observe cross-cutting relationships and relative timing of mineralization is vital when studying Earth History using the sedimentary rock record. All Precambrian sedimentary rocks have been metamorphosed, so studies investigating environmental conditions and their ties to evolutionary biology must take this under consideration. Coupling textural, magnetic, and modeling techniques has allowed me to peel away secondary overprints to provide a window into Precambrian paleoenvironments.

1.3 Figures

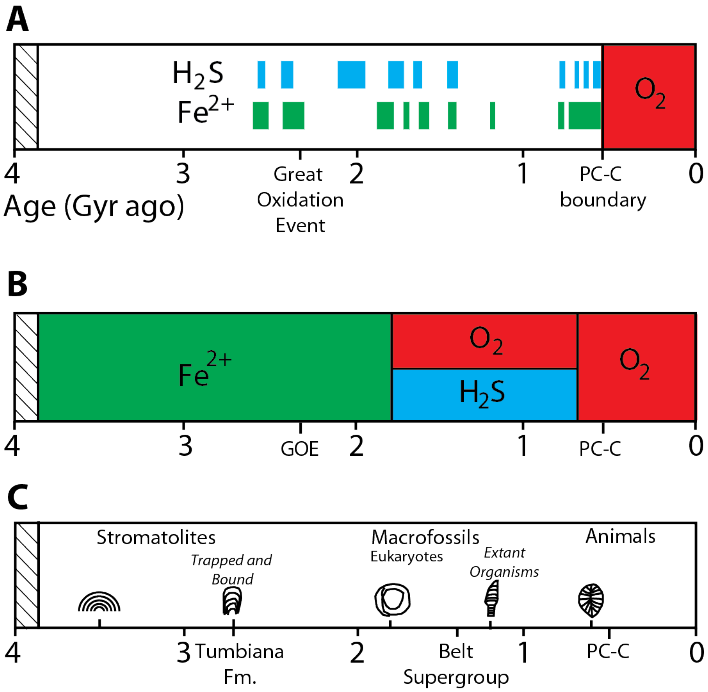

Figure 1.1: A) Recent views of redox from geochemical proxies, specifically iron speciation, using an outdated compilation (Planavsky et al., 2011) where Fe^{2+} stands for ferruginous conditions, H_2S for euxinic, and O_2 for oxic. B) Canonical views of Precambrian redox conditions (Canfield, 1998; Cloud, 1968). C) Evolution of life summary based on the fossil record (references in text; Knoll et al., 2006). Abbreviations: PC-C—Precambrian-Cambrian boundary, GOE—Great Oxidation Event, Fm.—Formation. Region with dashed lines marks the end of the sedimentary rock record on Earth. Parts A and B modified from Planavsky et al. (2011).

1.4 References

Adam, Z., Mogk, D., Skidmore, M., and Butterfield, N., Microfossils from the Greyson Formation, Lower Belt Supergroup: Support for early Mesoproterozoic biozonation, *in* Proceedings Geological Society of America Abstracts with Programs2014, Volume 46, p. 71.

Allwood, A. C., Walter, M. R., Kamber, B. S., Marshall, C. P., and Burch, I. W., 2006, Stromatolite reef from the Early Archaean era of Australia: Nature, v. 441, no. 7094, p. 714-718.

Anbar, A. D., and Knoll, A., 2002, Proterozoic ocean chemistry and evolution: a bioinorganic bridge?: science, v. 297, no. 5584, p. 1137-1142.

Awramik, S. M., and Buchheim, H. P., 2009, A giant, Late Archean lake system: The Meentheena Member (Tumbiana Formation; Fortescue Group), Western Australia: Precambrian Research, v. 174, no. 3, p. 215-240.

Bekker, A., Holland, H., Wang, P.-L., Rumble, D., Stein, H., Hannah, J., Coetzee, L., and Beukes, N., 2004, Dating the rise of atmospheric oxygen: Nature, v. 427, no. 6970, p. 117-120.

Bergmann, K. D., Grotzinger, J. P., and Fischer, W. W., 2013, Biological influences on seafloor carbonate precipitation: Palaios, v. 28, no. 2, p. 99-115.

Brasier, M. D., Antcliffe, J., Saunders, M., and Wacey, D., 2015, Changing the picture of Earth's earliest fossils (3.5–1.9 Ga) with new approaches and new discoveries: Proceedings of the National Academy of Sciences, v. 112, no. 16, p. 4859-4864.

Brocks, J. J., Buick, R., Summons, R. E., and Logan, G. A., 2003, A reconstruction of Archean biological diversity based on molecular fossils from the 2.78 to 2.45 billion-year-old Mount Bruce Supergroup, Hamersley Basin, Western Australia: Geochimica et Cosmochimica Acta, v. 67, no. 22, p. 4321-4335.

Brocks, J. J., Logan, G. A., Buick, R., and Summons, R. E., 1999, Archean molecular fossils and the early rise of eukaryotes: Science, v. 285, no. 5430, p. 1033-1036.

Canfield, D., 1998, A new model for Proterozoic ocean chemistry: Nature, v. 396, no. 6710, p. 450-453.

Canfield, D. E., Ngombi-Pemba, L., Hammarlund, E. U., Bengtson, S., Chaussidon, M., Gauthier-Lafaye, F., Meunier, A., Riboulleau, A., Rollion-Bard, C., and Rouxel, O., 2013, Oxygen dynamics in the aftermath of the Great

Oxidation of Earth’s atmosphere: Proceedings of the National Academy of Sciences, v. 110, no. 42, p. 16736-16741.

Cloud, P. E., 1968, Atmospheric and Hydrospheric Evolution on the Primitive Earth: Science, v. 160, no. 3829, p. 729-736.

Coffey, J., Flannery, D., Walter, M., and George, S., 2013, Sedimentology, stratigraphy and geochemistry of a stromatolite biofacies in the 2.72 Ga Tumbiana Formation, Fortescue Group, Western Australia: Precambrian Research, v. 236, p. 282-296.

Duke, E. F., and Lewis, R. S., 2010, Near infrared spectra of white mica in the Belt Supergroup and implications for metamorphism: American Mineralogist, v. 95, no. 7, p. 908-920.

Eck, R., and Dayhoff, M. O., 1966, Evolution of the structure of ferredoxin based on living relics of primitive amino acid sequences: Science, v. 152, p. 363-366.

Eigenbrode, J. L., and Freeman, K. H., 2006, Late Archean rise of aerobic microbial ecosystems: Proceedings of the National Academy of Sciences, v. 103, no. 43, p. 15759-15764.

Embley, T. M., and Martin, W., 2006, Eukaryotic evolution, changes and challenges: Nature, v. 440, no. 7084, p. 623-630.

Farquhar, J., Bao, H., and Thiemens, M., 2000, Atmospheric influence of Earth's earliest sulfur cycle: Science, v. 289, no. 5480, p. 756-758.

Fedonkin, M. A., and Yochelson, E. L., 2002, Middle Proterozoic (1.5 Ga) Horodyskia moniliformis Yochelson and Fedonkin, the oldest known tissue-grade colonial eucaryote: Smithsonian Contributions to Paleobiology, v. 94, p. 29.

Fischer, W., Schroeder, S., Lacassie, J., Beukes, N., Goldberg, T., Strauss, H., Horstmann, U., Schrag, D., and Knoll, A., 2009, Isotopic constraints on the Late Archean carbon cycle from the Transvaal Supergroup along the western margin of the Kaapvaal Craton, South Africa: Precambrian Research, v. 169, no. 1, p. 15-27.

Fischer, W. W., 2016, Breathing room for early animals: Proceedings of the National Academy of Sciences, v. 113, no. 7, p. 1686-1688.

Fischer, W. W., Hemp, J., and Valentine, J. S., 2016, How did life survive Earth's great oxygenation?: Current Opinion in Chemical Biology, v. 31, p. 166-178.

Flannery, D., and Walter, M., 2012, Archean tufted microbial mats and the Great Oxidation Event: new insights into an ancient problem: Australian Journal of Earth Sciences, v. 59, no. 1, p. 1-11.

French, K. L., Hallmann, C., Hope, J. M., Schoon, P. L., Zumberge, J. A., Hoshino, Y., Peters, C. A., George, S. C., Love, G. D., and Brocks, J. J., 2015, Reappraisal of hydrocarbon biomarkers in Archean rocks: Proceedings of the National Academy of Sciences, v. 112, no. 19, p. 5915-5920.

Fuchs, G., 2011, Alternative pathways of carbon dioxide fixation: insights into the early evolution of life?: Annual review of microbiology, v. 65, p. 631-658.

Gellatly, A. M., and Lyons, T. W., 2005, Trace sulfate in mid-Proterozoic carbonates and the sulfur isotope record of biospheric evolution: Geochimica et Cosmochimica Acta, v. 69, no. 15, p. 3813-3829.

Gilleaudeau, G. J., and Kah, L. C., 2015, Heterogeneous redox conditions and a shallow chemocline in the Mesoproterozoic ocean: evidence from carbon–sulfur–iron relationships: Precambrian Research, v. 257, p. 94-108.

Grotzinger, J. P., and Knoll, A. H., 1999, Stromatolites in Precambrian carbonates: evolutionary mileposts or environmental dipsticks?: Annual review of earth and planetary sciences, v. 27, no. 1, p. 313-358.

Han, T.-M., and Runnegar, B., 1992, Megascopic eukaryotic algae from the 2.1-billion-year-old Negaunee Iron-Formation, Michigan: Science, v. 257, no. 5067, p. 232-235.

Hayes, J., 1994, Global methanotrophy at the Archean-Proterozoic transition: Early life on Earth, v. 84, p. 220-236.

Hayes, J., Wedeking, K., and Kaplan, I., 1983, Precambrian organic geochemistry- Preservation of the record: Earth's earliest biosphere: Its origin and evolution(A 84-43051 21-51). Princeton, NJ, Princeton University Press, 1983, p. 93-134.

Hayes, J. M., Strauss, H., and Kaufman, A. J., 1999, The abundance of 13C in marine organic matter and isotopic fractionation in the global biogeochemical cycle of carbon during the past 800 Ma: Chemical Geology, v. 161, no. 1, p. 103-125.

Hinrichs, K. U., 2002, Microbial fixation of methane carbon at 2.7 Ga: Was an anaerobic mechanism possible?: Geochemistry, geophysics, geosystems, v. 3, no. 7, p. 1-10.

Hofmann, H., Grey, K., Hickman, A., and Thorpe, R., 1999, Origin of 3.45 Ga coniform stromatolites in Warrawoona group, Western Australia: Geological Society of America Bulletin, v. 111, no. 8, p. 1256-1262.

Holland, H. D., 1984, The chemical evolution of the atmosphere and oceans, Princeton University Press.

Horodyski, R. J., 1993, Paleontology of Proterozoic shales and mudstones: examples from the Belt Supergroup, Chuar Group and Pahrump Group, western USA: Precambrian Research, v. 61, no. 3, p. 241-278.

Horodyski, R. J., Winston, D., and Whipple, J. W., 1989, Paleontology of the middle Proterozoic belt supergroup, *in* Winston, D., Horodyski, R. J., and Whipple, J. W., eds., Middle Proterozoic Belt Supergroup, Western Montana: Great Falls, Montana to Spokane, Washington: 28th International Geological Congress, Field Trip Guidebook T334, p. 7-26.

Huebschman, R. P., 1973, Correlation of fine carbonaceous bands across a Precambrian stagnant basin: Journal of Sedimentary Research, v. 43, no. 3, p. 688-699.

Javaux, E. J., Knoll, A. H., and Walter, M. R., 2004, TEM evidence for eukaryotic diversity in mid ‐ Proterozoic oceans: Geobiology, v. 2, no. 3, p. 121-132.

Johnson, J. E., Gerpheide, A., Lamb, M. P., and Fischer, W. W., 2014, O2 constraints from Paleoproterozoic detrital pyrite and uraninite: Geological Society of America Bulletin, v. 126, no. 5-6, p. 813-830.

Johnson, J. E., Webb, S. M., Thomas, K., Ono, S., Kirschvink, J. L., and Fischer, W. W., 2013, Manganese-oxidizing photosynthesis before the rise of cyanobacteria: Proceedings of the National Academy of Sciences, v. 110, no. 28, p. 11238-11243.

Kah, L. C., and Bartley, J. K., 2011, Protracted oxygenation of the Proterozoic biosphere: International Geology Review, v. 53, no. 11-12, p. 1424-1442.

Knoll, A. H., Javaux, E. J., Hewitt, D., and Cohen, P., 2006, Eukaryotic organisms in Proterozoic oceans: Philosophical Transactions of the Royal Society B: Biological Sciences, v. 361, no. 1470, p. 1023-1038.

Kopp, R. E., Kirschvink, J. L., Hilburn, I. A., and Nash, C. Z., 2005, The Paleoproterozoic snowball Earth: a climate disaster triggered by the evolution of oxygenic photosynthesis: Proceedings of the National Academy of Sciences of the United States of America, v. 102, no. 32, p. 11131-11136.

Lamb, D., Awramik, S., Chapman, D., and Zhu, S., 2009, Evidence for eukaryotic diversification in the~ 1800 million-year-old Changzhougou Formation, North China: Precambrian Research, v. 173, no. 1, p. 93-104.

Lepot, K., Benzerara, K., Rividi, N., Cotte, M., Brown, G. E., and Philippot, P., 2009, Organic matter heterogeneities in 2.72 Ga stromatolites: alteration versus preservation by sulfur incorporation: Geochimica et Cosmochimica Acta, v. 73, no. 21, p. 6579-6599.

Lowe, D. R., 1980, Stromatolites 3,400-myr old from the archean of Western Australia: Nature, v. 284, no. 5755, p. 441-443.

-, 1994, Abiological origin of described stromatolites older than 3.2 Ga: Geology, v. 22, no. 5, p. 387-390.

Luepke, J. J., and Lyons, T. W., 2001, Pre-Rodinian (Mesoproterozoic) supercontinental rifting along the western margin of Laurentia: geochemical evidence from the Belt-Purcell Supergroup: Precambrian Research, v. 111, no. 1, p. 79-90.

Lyons, T. W., Luepke, J. J., Schreiber, M. E., and Zieg, G. A., 2000, Sulfur geochemical constraints on Mesoproterozoic restricted marine deposition: lower Belt Supergroup, northwestern United States: Geochimica et Cosmochimica Acta, v. 64, no. 3, p. 427-437.

Martin, W. F., 2012, Hydrogen, metals, bifurcating electrons, and proton gradients: the early evolution of biological energy conservation: FEBS letters, v. 586, no. 5, p. 485-493.

Nitschke, W., and Russell, M. J., 2012, Redox bifurcations: mechanisms and importance to life now, and at its origin: Bioessays, v. 34, no. 2, p. 106-109.

Pavlov, A., and Kasting, J., 2002, Mass-independent fractionation of sulfur isotopes in Archean sediments: strong evidence for an anoxic Archean atmosphere: Astrobiology, v. 2, no. 1, p. 27-41.

Pittis, A. A., and Gabaldón, T., 2016, Late acquisition of mitochondria by a host with chimaeric prokaryotic ancestry: Nature, v. 531, no. 7592, p. 101-104.

Planavsky, N. J., McGoldrick, P., Scott, C. T., Li, C., Reinhard, C. T., Kelly, A. E., Chu, X., Bekker, A., Love, G. D., and Lyons, T. W., 2011, Widespread iron-rich conditions in the mid-Proterozoic ocean: Nature, v. 477, no. 7365, p. 448-451.

Poulton, S. W., and Canfield, D. E., 2005, Development of a sequential extraction procedure for iron: implications for iron partitioning in continentally derived particulates: Chemical Geology, v. 214, no. 3, p. 209-221.

-, 2011, Ferruginous conditions: a dominant feature of the ocean through Earth's history: Elements, v. 7, no. 2, p. 107-112.

Rasmussen, B., Fletcher, I. R., Brocks, J. J., and Kilburn, M. R., 2008, Reassessing the first appearance of eukaryotes and cyanobacteria: Nature, v. 455, no. 7216, p. 1101-1104.

Raymond, J., and Blankenship, R. E., 2004, Biosynthetic pathways, gene replacement and the antiquity of life: Geobiology, v. 2, no. 4, p. 199-203.

Retallack, G. J., Dunn, K. L., and Saxby, J., 2013, Problematic Mesoproterozoic fossil Horodyskia from Glacier National Park, Montana, USA: Precambrian Research, v. 226, p. 125-142.

Schidlowski, M., Hayes, J., and Kaplan, I., 1983, Isotopic inferences of ancient biochemistries- Carbon, sulfur, hydrogen, and nitrogen: Earth's earliest biosphere: Its origin and evolution(A 84-43051 21-51). Princeton, NJ, Princeton University Press, 1983, p. 149-186.

Schoell, M., and Wellmer, F.-W., 1981, Anomalous 13C depletion in early Precambrian graphites from Superior Province, Canada.

Schoepp-Cothenet, B., van Lis, R., Philippot, P., Magalon, A., Russell, M. J., and Nitschke, W., 2012, The ineluctable requirement for the trans-iron elements molybdenum and/or tungsten in the origin of life: Scientific reports, v. 2.

Schopf, J. W., 1993, Microfossils of the Early Archean Apex chert: new evidence of the antiquity of life: Science, v. 260, no. 5108, p. 640-646.

Sleep, N. H., and Bird, D. K., 2008, Evolutionary ecology during the rise of dioxygen in the Earth's atmosphere: Philosophical Transactions of the Royal Society of London B: Biological Sciences, v. 363, no. 1504, p. 2651-2664.

Sperling, E. A., Wolock, C. J., Morgan, A. S., Gill, B. C., Kunzmann, M., Halverson, G. P., Macdonald, F. A., Knoll, A. H., and Johnston, D. T., 2015, Statistical analysis of iron geochemical data suggests limited late Proterozoic oxygenation: Nature, v. 523, no. 7561, p. 451-454.

Stüeken, E., Buick, R., and Schauer, A., 2015, Nitrogen isotope evidence for alkaline lakes on late Archean continents: Earth and Planetary Science Letters, v. 411, p. 1-10.

Stüeken, E. E., 2013, A test of the nitrogen-limitation hypothesis for retarded eukaryote radiation: nitrogen isotopes across a Mesoproterozoic basinal profile: Geochimica et Cosmochimica Acta, v. 120, p. 121-139.

Thomazo, C., Ader, M., Farquhar, J., and Philippot, P., 2009, Methanotrophs regulated atmospheric sulfur isotope anomalies during the Mesoarchean

(Tumbiana Formation, Western Australia): Earth and Planetary Science Letters, v. 279, no. 1, p. 65-75.

Wacey, D., Gleeson, D., and Kilburn, M., 2010, Microbialite taphonomy and biogenicity: new insights from NanoSIMS: Geobiology, v. 8, no. 5, p. 403-416.

Wacey, D., Menon, S., Green, L., Gerstmann, D., Kong, C., Mcloughlin, N., Saunders, M., and Brasier, M., 2012, Taphonomy of very ancient microfossils from the~ 3400Ma Strelley Pool Formation and~ 1900Ma Gunflint Formation: New insights using a focused ion beam: Precambrian Research, v. 220, p. 234-250.

Walcott, C. D., 1899, Pre-Cambrian fossiliferous formations: Geological Society of America Bulletin, v. 10, no. 1, p. 199-244.

Walter, M., Oehler, J. H., and Oehler, D. Z., 1976, Megascopic algae 1300 million years old from the Belt Supergroup, Montana: a reinterpretation of Walcott's Helminthoidichnites: Journal of Paleontology, v. 50, p. 872-881.

Walter, M., Rulin, D., and Horodyski, R. J., 1990, Coiled carbonaceous megafossils from the Middle Proterozoic of Jixian (Tianjin) and Montana: American Journal of Science, v. 290, p. 133-148.

Williams, R. P. J., and Frausto Da Silva, J. J. R., 2003, Evolution was chemically constrained: Journal of Theoretical Biology, v. 220, no. 3, p. 323-343.

Williamson, A., Conlan, B., Hillier, W., and Wydrzynski, T., 2011, The evolution of Photosystem II: insights into the past and future: Photosynthesis research, v. 107, no. 1, p. 71-86.

Xiao, S., Knoll, A. H., Kaufman, A. J., Yin, L., and Zhang, Y., 1997, Neoproterozoic fossils in Mesoproterozoic rocks? Chemostratigraphic resolution of a biostratigraphic conundrum from the North China Platform: Precambrian Research, v. 84, no. 3, p. 197-220.

Yan, Y.-z., and Liu, Z.-l., 1993, Significance of eukaryotic organisms in the microfossil flora of Changcheng system: Acta Micropalaeontol. Sin, v. 10, p. 167-180.

Yoshiya, K., Nishizawa, M., Sawaki, Y., Ueno, Y., Komiya, T., Yamada, K., Yoshida, N., Hirata, T., Wada, H., and Maruyama, S., 2012, In situ iron isotope analyses of pyrite and organic carbon isotope ratios in the Fortescue Group: Metabolic variations of a Late Archean ecosystem: Precambrian Research, v. 212, p. 169-193.

Zerkle, A. L., House, C. H., and Brantley, S. L., 2005, Biogeochemical signatures through time as inferred from whole microbial genomes: American Journal of Science, v. 305, no. 6-8, p. 467-502.

Chapter 2

Examining Archean Methanotrophy

Originally published in:

Slotznick, S. P., and Fischer, W. W., 2016, Examining Archean methanotrophy: Earth and Planetary Science Letters, v. 441, p. 52-59. doi: 10.1016/j.epsl.2016.02.013

2.1 Abstract

The carbon isotope ratios preserved in sedimentary rocks can be used to fingerprint ancient metabolisms. Organic carbon in Late Archean samples stands out from that of other intervals with unusually low $\delta^{13}C$ values (~ -45 to -60‰). It was hypothesized that these light compositions record ecosystem-wide methane cycling and methanotrophy, either of the aerobic or anaerobic variety. To test this idea, we studied the petrography and carbon and oxygen isotope systematics of well-known and spectacular occurrences of shallow water stromatolites from the 2.72 Ga Tumbiana Formation of Western Australia. We examined the carbonate cements and kerogen produced within the stromatolites, because methanotrophy is expected to leave an isotopic fingerprint in these carbon reservoirs. Mathematical modeling of Archean carbonate chemistry further reveals that methanotrophy should still have a discernible signature preserved in the isotopic record, somewhat diminished from those observed in Phanerozoic sedimentary basins due to higher dissolved inorganic carbon concentrations. These stromatolites contain kerogen with $\delta^{13}C_{org}$ values of ~ -50‰. By microsampling different regions and textures within the stromatolites, we determined that the isotopic compositions of the authigenic calcite cements show a low degree of variation and are nearly identical to values estimated for seawater at this time; the lack of low and variable $\delta^{13}C_{carb}$ values implies that methanotrophy does not explain the low $\delta^{13}C_{org}$ seen in the coeval kerogen. These observations do not support a methanotrophy hypothesis, but instead hint that the Late Archean may constitute an interval wherein autotrophs employed markedly different biochemical processes of energy conservation and carbon fixation.

2.2 Introduction

It is widely recognized that organic matter contained in sedimentary successions of Late Archean age (circa 2.5 to 2.9 Ga) has unusually ^{13}C-depleted isotopic compositions ($\delta^{13}C_{org}$ ~ -45 to -60‰ PDB) compared to younger intervals (Phanerozoic $\delta^{13}C_{org}$ ~ -22 to -32‰ PDB) (Eigenbrode and Freeman, 2006;

Fischer et al., 2009; Schoell and Wellmer, 1981; Thomazo et al., 2009). From its discovery in ultra-mature Late Archean kerogens from the Superior Province and the Tumbiana Formation of the Fortescue Group, Western Australia, it was hypothesized that this isotopic signal reflects the enhanced paleoenvironmental cycling of methane (Hayes, 1994; Schoell and Wellmer, 1981).

Oxidation and assimilation of methane by methanotrophic organisms yields exceptionally ^{13}C-depleted biomass. Recognizing this, Hayes (1994) introduced the concept of a Late Archean "Age of Global Methanotrophy", to explain the δ^{13}C values seen in Archean organic matter. This was originally envisioned as aerobic methanotrophy (Hayes, 1994), but later based on two discoveries—microbial consortia capable of anaerobic oxidation of methane (AOM) in modern anoxic environments (Boetius et al., 2000) and the widespread mass independent fractionation of sulfur isotopes in Archean basins (Farquhar et al., 2000)—Hinrichs (2002) updated the idea to include AOM, expanding on a point made similarly by Schoell and Wellmer (1981) on the basis of modern sedimentary pore fluid biogeochemical profiles. By comparing accumulation rates of methane oxidation from modern methane seeps, anoxic coastal sediment, and the Tumbiana Formation, Hinrichs (2002) showed that AOM processes could reasonably explain the Archean isotopic signal, possibly even under the condition of lower seawater sulfate concentrations. Subsequent studies developed biogeochemical variations on this theme again involving oxygenic photosynthesis or anoxygenic photosynthetic pathways, but these hypotheses all draw on abundant ecosystem methanotrophy in large part to explain the ^{13}C-depleted kerogen, with the disappearance of this isotopic signal in younger Precambrian strata due to either a decline in atmospheric methane or changes in the relative abundance of electron acceptors for methanotrophy (Coffey et al., 2013; Eigenbrode and Freeman, 2006; Stüeken et al., 2015; Thomazo et al., 2009; Yoshiya et al., 2012).

Despite its attractiveness, there are several outstanding issues with the global methanotrophy hypothesis that could benefit from further testing. 1) While substantially more ^{13}C-depleted than expected by carboxylation from the Calvin cycle, the isotopic composition of Late Archean organic matter is not unique for methanotrophs and is consistent with other biochemical pathways (Blaser et al., 2013; Fischer et al., 2009; Gelwicks et al., 1989). 2) Sulfate levels may have been sufficiently low as to greatly limit the extent of sulfate reduction-driven AOM in Late Archean marine basins (Crowe et al., 2014), though methane oxidation might have been instead accomplished anaerobically via ferric iron phases (Beal et al., 2009) or high-valent nitrogen-bearing compounds (Haroon et al., 2013). Finally, 3) existing data from Archean carbonates with exceptionally low $\delta^{13}C_{org}$ values do not host isotopic and textural features one might expect of carbonates produced in environments of prevalent methanotrophy.

Fortunately, environments in which methanotrophy is a principal part of the carbon mass flux leave isotopic signatures not just in the organic phases present, but also in the carbonate phases produced; this forms the logic for an approach to test the global methanotrophy hypothesis. Both aerobic methanotrophy and AOM increase dissolved inorganic carbon (DIC) in the environment and strongly alter the carbon isotope ratios by adding isotopically light DIC. Furthermore, AOM also generates a strong flux of alkalinity and thus promotes the precipitation of carbonates as described by the following net reaction: $CH_4 + SO_4^{-2} + Ca^{+2} \rightarrow CaCO_3 + H_2S + H_2O$ (Michaelis et al., 2002). Authigenic carbonates formed by methanotrophic processes have been widely observed in modern marine sediments (e.g. Luff and Wallmann, 2003; Marlow et al., 2014) and can be readily preserved in the geological record where they have been recognized on the basis of isotopic and textural features in Phanerozoic strata, and perhaps as old as 635 Ma (Bristow and Grotzinger, 2013; Peckmann and Thiel, 2004). AOM creates both carbonate and organic matter with remarkably low $\delta^{13}C$ values (Bristow and Grotzinger, 2013)(Table S2.1). We compiled a comprehensive C isotope dataset from AOM sites preserved in Phanerozoic basins (Table S2.1); the data illustrate that $\delta^{13}C_{carb}$ values can be down to -59‰ and $\delta^{13}C_{org}$ values can be as low as -133‰, with typical $\delta^{13}C$ values both substantially more variable and much lower overall than Archean values.

To test the methanotrophy hypothesis, we closely examined the petrographic textures and isotopic compositions of kerogen and authigenic carbonate cements in stromatolites collected from the Late Archean Tumbiana Formation—an archive that has become an effective stratotype for ^{13}C-depleted Archean organic matter (Eigenbrode and Freeman, 2006; Hayes, 1994; Thomazo et al., 2009). These rocks are well suited for this analysis because they contain both kerogen and authigenic calcite cements preserved in stromatolitic laminations. We measured the carbonate cements that precipitated in the stromatolites at a finer texture-specific scale than has been done previously to look for any evidence of AOM, and combined traditional C and O isotope ratio measurements on the carbonate cements with clumped isotope analyses to evaluate the impacts of post-depositional processes on these materials. Finally we interpret the data in the context of a model of Archean carbonate chemistry, and discuss other potential metabolisms that might better explain the observations, such as the possibility that the ^{13}C-depleted Archean kerogens reflect an entirely different mode of biochemical carboxylation.

2.3 Geological background and methods

The Tumbiana Formation was deposited at 2721 ± 4 Ma during an interval of rifting and subsidence, and onlaps the Pilbara craton (Blake et al., 2004). It ranges in thickness from a few meters up to 320 m, and is lithologically diverse, consisting of conglomerates, shale, mudstones, siltstones, sandstones, breccias, basalts, tuff, and limestone (Thorne and Trendall, 2001). It is notably laterally variable containing many different facies that have been proposed to represent either lacustrine (Awramik and Buchheim, 2009; Buick, 1992; Coffey et al., 2013) or shallow marine settings (Sakurai et al., 2005; Thorne and Trendall, 2001); notably however, these facies all reflect shallow water paleoenvironments. This contrasts with typical methanotrophic environments both today and in Phanerozoic basins (typically slope/deep marine or within sedimentary pore fluids, (Campbell et al., 2002; Campbell, 2006; Marlow et al., 2014; Michaelis et al., 2002) making the highly ^{13}C-depleted kerogens in the Tumbiana Formation intriguing and unique.

Samples were collected from outcrops of the Meentheena Member of the Tumbiana Formation at the Redmont/Knossos Area, Western Australia (22°02'44" S, 118°59'34" E) (Fig. 2.1). The Meentheena Member constitutes the uppermost sequence of the Tumbiana Formation, and is composed of a 30 to 50 m thick unit of interbedded carbonate (mainly limestone) and immature siliciclastic and volcaniclastic lithologies. The unit also contains spectacular occurrences of a diversity of well-preserved stromatolites (Awramik and Buchheim, 2009; Coffey et al., 2013; Flannery and Walter, 2012)—the lithologies targeted in this study. In the sampling locality, the exposure of the Meentheena Member outcrop is 11 m thick (Fig. S2.1). Here the Meentheena Member contains trough cross-stratified and wave-rippled sandstones and grainstones from coarse to very fine-grained, the latter of which become interbedded with stromatolites up section. Associated with mudcracks, these stromatolites developed in an intertidal environment that deepens to dominantly subtidal facies upsection (Sakurai et al., 2005).

Outcrop samples were cut into slabs and polished to reveal textures and provide fresh surfaces for analysis. Petrographic thin sections were made from book-matched surfaces of the slabs sampled for isotopic analysis, and imaged using light and electron microscopy. Scanning electron microscopy (SEM) and X-ray dispersive spectroscopy (EDS) were performed using a combined ZEISS 1550VP Field Emission SEM and Oxford INCA Energy 300 X-ray dispersive spectrometer at Caltech.

Powders for carbonate $\delta^{13}C$ and $\delta^{18}O$ isotopic analysis were collected using a micro-rotary drill with a 2 mm bit. Diverse textures (stromatolite with abundant grains, stromatolite with abundant cement, intercolumn sediment, across areas of differential recrystallization) were sampled in order to create a detailed cm-scale isotope ratio map of textures within these ancient microbial structures, and uncover the effects of diagenesis. Samples for organic $\delta^{13}C$ measurements were made on 5 to 10 g bulk stromatolite samples targeting organic-rich laminae, and, excluding intercolumn sedimentary fill, cut and then powdered using a mortar and pestle.

Inorganic $\delta^{13}C$ and $\delta^{18}O$ isotopic measurements were performed at the University of Michigan Stable Isotope Laboratory. Carbonate sample powders were placed in stainless steel combustion boats and baked under vacuum at 200°C to remove volatiles and water. Samples were then places in borosilicate reaction vessels and reacted at 77°C with 4 drops of anhydrous phosphoric acid for 8 minutes in a Finnigan MAT Kiel IV preparation device coupled directly to the inlet of a Finnigan MAT 253 isotope ratio mass spectrometer. For 19 of the 50 samples, replicate splits were measured to assess accuracy and precision. Two NBS standards (NBS 18 and NBS 19) were run with the samples. Oxygen isotope ratio data were corrected for acid fractionation and source mixing by calibration to a best-fit regression line defined by standards. Analytical uncertainty is better than 0.1‰ for both carbon and oxygen isotopes. Data are reported in delta notation relative to VPDB standard.

For clumped isotope analysis at Caltech, sample powders were dried at 50°C. Five to ten milligrams of sample powder were dissolved in 90°C phosphoric acid for twenty minutes. The CO_2 was purified by gas chromatography in the method developed by Passey et al. (2010), and different isotopologues of carbon dioxide (cardinal masses 44 through 49) were measured on a modified Finnigan MAT253 gas-source mass spectrometer. Sample unknowns were analyzed for eight acquisitions in seven cycles, with each cycle bracketed by measurements of reference gas. Raw values for Δ^{47} were calculated relative to the reference gas, and then converted to the absolute reference frame by Ghosh et al. (2006) for low-temperature samples (<55°C) and the absolute reference frame by Eiler et al. (2009) for higher temperature samples using the transfer function as in Dennis et al. (2011). From clumped isotope temperatures and oxygen isotope ratio data, we estimated the $\delta^{18}O$ of the water from which the carbonates precipitated using the relationship from Kim and O'Neil (1997).

For organic carbon analyses, sample powders were placed in tin combustion boats and decarbonated with hydrochloric acid. $\delta^{13}C_{org}$ values were measured at UC Davis using a PDZ Europa ANCA-GSL elemental analyzer coupled to a PDZ Europa 20-20 continuous flow isotope ratio mass spectrometer. The samples were combusted at 1020°C with chromium oxide and silvered cobaltous/cobaltic oxide catalysts. Following combustion, the helium carrier and analytes flowed through a water trap. Sample unknowns were calibrated against NIST standard reference materials and analytical uncertainty was better than 0.10‰. Data are reported in delta notation relative to VPDB.

2.4 Results

The Tumbiana stromatolites analyzed here are columnar laminated structures ranging in height from 4 cm to 18 cm. They are erect, non-branching with wide-intercolumn fill areas occurring in small clumps or within bioherms consistent with previous descriptions by Coffey et al. (2013) and Awramik and Buchheim (2009). Biological influence in the formation of these structures is suggested by laminae that systematically vary in thickness over the stromatolite apices, a criterion for biogenicity (Buick et al., 1981) (Fig. 2.2A). Additionally, at their edges, these laminae bend beyond the angle of repose and imply trapping and binding by some cohesive agent, such as microbial filaments (Frantz et al., 2015), with subsequent cementation. The laminae are composed of micritic calcite cements, varying in thickness from < 200 μm to 2 mm, alternating with thinner dark siliceous layers, with small amounts of residual kerogen. While some of the carbonate appears to have been recrystallized, this recrystallization varies in coarseness between layers (Figs. 2.2B, S2.2). Microscopy reveals a component of detrital material within the carbonate laminae, often in detrital layers filled with aluminosilicates, apatite, chlorite, and quartz (Figs. 2.2D, S2.2). The fill material deposited between stromatolites varies in composition between hand samples, but is predominantly siliciclastic sediment and carbonate cement with more rare detrital carbonate grains (Figs. 2.2CD, S2.2). It is important to note that petrographic textures of calcite cements and kerogen in laminations both support the interpretation that these phases had authigenic and coeval origins in the stromatolites (Grotzinger and Knoll, 1999; Lepot et al., 2008). Additionally, the detailed textures of the Tumbiana stromatolites are distinct from Phanerozoic AOM seep carbonates, which are dominated by homogeneous and clotted microcrystalline carbonates, and rarer stromatolitic fabrics with complex and variable carbonate accretion orientations, botryoidal cements, irregular filled cavities, and *in situ* brecciation (Peckmann and Thiel, 2004). In modern methanic carbonates precipitated in anoxic bottom waters, large extensive structures of slabs, pavements, and upward growing chimneys and mounds are observed, but their internal structure is thrombolytic/clotted and distinct from the textures seen in Tumbiana stromatolites (Michaelis et al., 2002; Peckmann et al., 2001b).

$\delta^{13}C_{carb}$ and $\delta^{18}O$ measurements of the micritic cements reveal a narrow range of values, from -0.93‰ to 1.18‰ (PDB) and -19.00‰ to -14.20‰ (PDB), respectively (Table S2.2). The data are distributed tightly with a mean and standard deviation of $\delta^{13}C_{carb}$ 0.57 ± 0.38‰ (1σ) and $\delta^{18}O_{carb}$ -18.40 ± 0.89‰ (Fig. 2.3A). Clumped isotope measurements reveal the impacts of both burial diagenetic and near surface weathering processes. Temperature estimates near the centroid of the $\delta^{13}C_{carb}$ distribution are 114 ± 9°C. We interpret this as a diagenetic temperature, which is supported by the very low $\delta^{18}O$ values observed. The $\delta^{18}O$ composition of the water in equilibrium with the carbonates at these temperatures is ~ -3‰ VSMOW, consistent with recrystallization in the presence of ice-free marine and to a lesser degree relatively heavy meteoric pore fluids. In areas of the samples where near surface weathering has taken place (marked clearly by the oxidation of ferrous iron in pyrite and carbonate and resulting in the precipitation of secondary oxides, Fig. S2.3), the isotopic data show a trend with clumped temperature, causing $\delta^{18}O$ to increase and $\delta^{13}C_{carb}$ to drop (albeit very slightly ~1‰). From this we interpret that infiltration and exchange with heavier meteoric waters raised the $\delta^{18}O$ values, as average precipitation in Western Australia has $\delta^{18}O$ values from -4.07‰ to -6.44‰ VSMOW (Liu et al., 2010) and a mean annual temperature *ca*. 30°C. Meteoric waters infiltrating the surface rock or near subsurface would be close to ambient air temperature and thus both lower the temperature and increase the $\delta^{18}O$ values of the carbonate.

Our measured $\delta^{13}C_{carb}$ values conform with other carbonate isotopic measurements on the Tumbiana Formation throughout the basin in a variety of carbonate facies (e.g. Awramik and Buchheim, 2009; Coffey et al., 2013; Eigenbrode and Freeman, 2006; Thomazo et al., 2009; Yoshiya et al., 2012), and from Late Archean carbonate platforms more broadly (Fischer et al., 2009). When the $\delta^{13}C$ data are mapped back onto the sampled stromatolitic surfaces, little variation and no texture-specific pattern is visible among the values aside from the alteration trend discussed above due to surface weathering (Fig. 2.3). Notably, no differences were observed between stromatolitic cements and detrital, intercolumn-filling carbonate. This lack of variation is highly distinct from expectations of carbonates precipitated in methanic environments, which show distinct isotopic signatures for different textures as well as wider variation (5-10‰) within textures at similar length scales (e.g. Campbell et al., 2002; Peckmann et al., 2001b). The results show $\delta^{13}C_{carb}$ values with an isotopic composition very similar to that estimated for dissolved inorganic carbon in Late Archean seawater, not the variable and ^{13}C-depleted values observed in modern and ancient AOM environments (Table S2.1). While it remains possible that an unwavering mixture of isotopically distinct DIC pools could result in the same near seawater value, this scenario is unlikely based on the low degree of variation between fabrics, paleoenvironments (facies), and global comparisons.

$\delta^{13}C_{org}$ measurements show that the kerogen in the stromatolitic laminae is notably ^{13}C-depleted with values from -49.91‰ to -53.2‰ (PDB), matching well with other organic measurements made on Tumbiana Formation carbonate outcrops in the Redmont area (Coffey et al., 2013; Eigenbrode and Freeman, 2006; Stüeken et al., 2015; Yoshiya et al., 2012). It is important to note that at a bulk-scale sedimentary organic matter can integrate biological sources with distinct isotopic compositions (Freeman et al., 1990); bulk values need to be considered as possible mixtures accordingly. *In situ* ion microprobe measurements of kerogen from the Tumbiana Formation uncovered two populations of $\delta^{13}C_{org}$ values around -52.3‰ and -34.4‰; the former was interpreted as a signature of methanotrophy while the latter a signal of photoautotrophy (Williford et al., 2016). That our measured bulk $\delta^{13}C_{org}$ values reflect one of these populations suggests that these unusual ^{13}C-depleted values accurately describe the composition of a microbial community which makes up the majority of the kerogen in the sedimentary rock, and are not spurious values resulting from a mixture of biomass from different populations with isotopic compositions substantially different than bulk observations. Importantly, these community values are substantially lower than those expected from carboxylation using Rubisco and the Calvin cycle (e.g. Guy et al., 1993), but not commonly as low as those observed in known methanotrophic biomass.

2.5 Results in the context of Archean carbonate chemistry

Although the $\delta^{13}C_{carb}$ values suggest that methanotrophy was not a dominant metabolic process occurring in the Tumbiana stromatolites, it is important to consider this data in the context of the differing seawater carbonate chemistry that characterized the early Earth (Fischer et al., 2009; Grotzinger and Kasting, 1993; Hotinski et al., 2004). To alleviate the faint young sun paradox, it is thought that the early atmosphere contained a higher concentration of greenhouse gases, specifically CO_2 (Owen et al., 1979; Sagan and Mullen, 1972). The amount of CO_2 that existed in the Late Archean atmosphere is not well-constrained and model dependent; most efforts to quantify this found a lower limit of partial pressure of CO_2 at 0.03 atm with an upper limit at 5 atm (Grotzinger and Kasting, 1993). Seawater in equilibrium with the early atmosphere would have had higher amounts of dissolved inorganic carbonate species (DIC), and would tend to mute the metabolic signal of AOM in authigenic carbonates, all else kept equal (e.g. Bristow and Grotzinger, 2013).

To test this, we constructed a simple mathematical model that describes the carbonate chemistry and carbon isotope systematics of possible AOM environments for any concentration of atmospheric CO_2 building on similar logic to previous approaches (Bristow and Grotzinger, 2013; Fischer et al., 2009). To solve the carbonate system we used a range of pCO_2 and pH values and the Matlab solver developed by Zeebe and Wolf-Gladrow (2001). pH of Late Archean seawater is not known with certainty, but can be constrained to within limits. From basin analysis of carbonate platforms and carbon cycle theory, it appears that the fluid Earth throughout Precambrian time produced carbonates to alleviate fluxes of carbon and alkalinity in a fashion similar to today (Grotzinger and James, 2000; Higgins et al., 2009). Leveraging this carbonate mineral saturation and higher pCO_2, it is likely that the pH of seawater was lower (Grotzinger and Kasting, 1993); a more recent model calculates for a pCO_2 of 10^5 μatm, a pH of 6.9 (Halevy et al., 2010). For the Meentheena Member of the Tumbiana Formation, the basin history is not understood sufficiently well to solve the carbonate chemistry with a high degree of confidence—it could be marine (e.g. Sakurai et al., 2005) or lacustrine (e.g. Awramik and Buchheim, 2009) in origin. However from lithological constraints, one can reasonably assume that $CaCO_3$ saturation states in this body of water were greater than unity, but were probably less than ~10 (Bergmann et al., 2013; Higgins et al., 2009). Because carbonate production was not tied to sources of alkalinity at the mouths of rivers that fed the Fortescue basin, it is also reasonable to assume calcium concentrations were in excess of carbonate ion concentrations (e.g. Higgins et al., 2009). This provides coarse constraints on the more likely solution space for DIC content of the basin waters, and a description of the order-of-magnitude uncertainty in the reconstruction (Figs. 2.4, S2.4).

To calculate the expected isotopic composition of authigenic carbonate, we used a closed box model that depends on a simple isotope mass balance between two pools: seawater DIC ($\delta^{13}C$ = 0‰) and ^{13}C-depleted DIC metabolically derived from the oxidation of methane ($\delta^{13}C$ = -60‰). This simple mixing relationship is observed in authigenic structures above the sediment in the modern anoxic environment of the Black Sea (Michaelis et al., 2002; Peckmann et al., 2001b), as well as increasingly with depth in sediment pore-fluid AOM environments (Bristow and Grotzinger, 2013). Bracketing the ranges of $\delta^{13}C$ from modern AOM environments and assuming a similar relative metabolic fluxes of methane oxidation to organic matter production in Archean environments (Bristow and Grotzinger, 2013), calculations show that an Archean AOM environments should have $\delta^{13}C$ values between -2‰ and -30‰ (Fig. 2.4*)*. This calculation assumes a degree of coupling between methane oxidation and DIC and organic carbon production. Although lower global productivity may have characterized the Archean biosphere, the assumption of similar metabolic fluxes only considers rates of AOM needed to produce enough biomass to leave the depleted $\delta^{13}C_{org}$ signature (Hinrichs, 2002); due to poor energetics, anaerobic methanotrophy has characteristically low growth yields and must oxidize substantial amounts of methane to obtain sufficient energy from this process for growth (~99:1; Thauer et al., 2008). Altogether, we observe that the typically ^{13}C-depleted AOM carbonate values should have been only somewhat muted by higher DIC (Fig. 2.4). Supporting the results of this calculation, we note that low and variable $\delta^{13}C$ values have been observed in authigenic carbonates in Archean strata. These are captured by early diagenetic siderite preserved in iron formation and ferruginous shales, and have been widely interpreted as the products of anaerobic microbial metabolism, likely dissimilatory iron reduction (Fischer et al., 2009; Johnson et al., 2013).

Thus despite their highly ^{13}C-depleted kerogens, Tumbiana stromatolites do not record $\delta^{13}C_{carb}$ values expected for AOM carbonates precipitated under conditions of Archean carbonate chemistry. This result suggests that AOM was not especially prevalent in this paleoenvironment, and that the microbial mats present during the development of these sedimentary structures were not comprised of large proportion of methanotrophs. While it remains possible that either or both aerobic and anaerobic methanotrophy were present as important metabolisms on the early Earth, it appears that neither was responsible for the striking isotopic signature seen in Tumbiana kerogens.

2.6 Alternative Carbon Fixation Pathways

If methanotrophy was not responsible for the notably low $\delta^{13}C_{org}$ values in the Tumbiana Formation, what are the alternatives? Under the somewhat delicate assumption that carbon isotope fractionations of biosynthetic pathways have not significantly changed since their inception, one reasonable and attractive possibility is the reductive acetyl Coenzyme A (CoA) pathway (sometimes called the Wood-Ljungdahl pathway), which a number of anaerobic microbes (including acetogens, methanogens, and sulfate reducers) use to synthesize acetyl-CoA from carbon dioxide (Fischer et al., 2009). This is the only known carbon fixation pathway that does carboxylation and at the same time generates ATP (Fuchs 2011), using a clever biochemical energy conservation scheme termed electron bifurcation (Martin, 2012; Nitschke and Russell, 2012; Thauer et al., 2008). Autotrophic acetogens using the reductive acetyl-CoA pathway produce acetate with large fractionations (ε = -38‰ to -68‰) from substrate DIC, with a large kinetic isotope effect likely associated with the key enzyme of that pathway: carbon-monoxide dehydrogenase (Blaser et al., 2013; Gelwicks et al., 1989). The produced acetate can further fuel heterotrophic metabolisms and propagate this light isotopic signal in the ecosystem. Thus we hypothesize that the low $\delta^{13}C$ values of Tumbiana Formation kerogens—and perhaps those observed in Archean strata elsewhere (e.g. Fischer et al., 2009)—reflect the greater predominance of reductive acetyl-CoA pathway as an entry point for CO_2 into the biosphere. Interestingly, from theory it has been argued that the reductive acetyl-CoA pathway represents the most primitive form of carbon fixation known (Fuchs, 2011; Martin, 2012; Nitschke and Russell, 2012); our observations provide some geological support for this idea.

Finally, the average standard redox potentials for reactions in the reductive acetyl-CoA pathway are more reducing than all other known carboxylation pathways, and the key enzymes involved make extensive use of cofactors that are highly O_2-sensitive (Fuchs, 2011). Consequently, this pathway was never evolutionarily adapted for aerobic metabolisms. If it is correct that the unique isotopic signature seen in Tumbiana Formation organic matter reflects carboxylation via this pathway, it suggests that O_2 levels in these shallow current-swept and well-lit paleoenvironments were sufficiently low to support significant populations of these anaerobic microorganisms.

2.7 Acknowledgements

Support for this work was provided by the Agouron Institute (grant number AI-GC17.09.3), NSF Division of Earth Sciences award EAR-1349858, the NSF Graduate Research Fellowship program (S.P.S.), NASA Earth and Space Fellowship (S.P.S.), and the David and Lucile Packard Foundation (W.W.F.). Thanks to John Grotzinger, Renata Cummins, Daniel Stolper, and Kristin Bergmann for helpful comments and aid with clumped isotope measurements. We also thank John Higgins, Itay Halevy, David Fike, and two anonymous reviewers for helpful feedback that substantially improved the quality of the study.

2.8 Figures

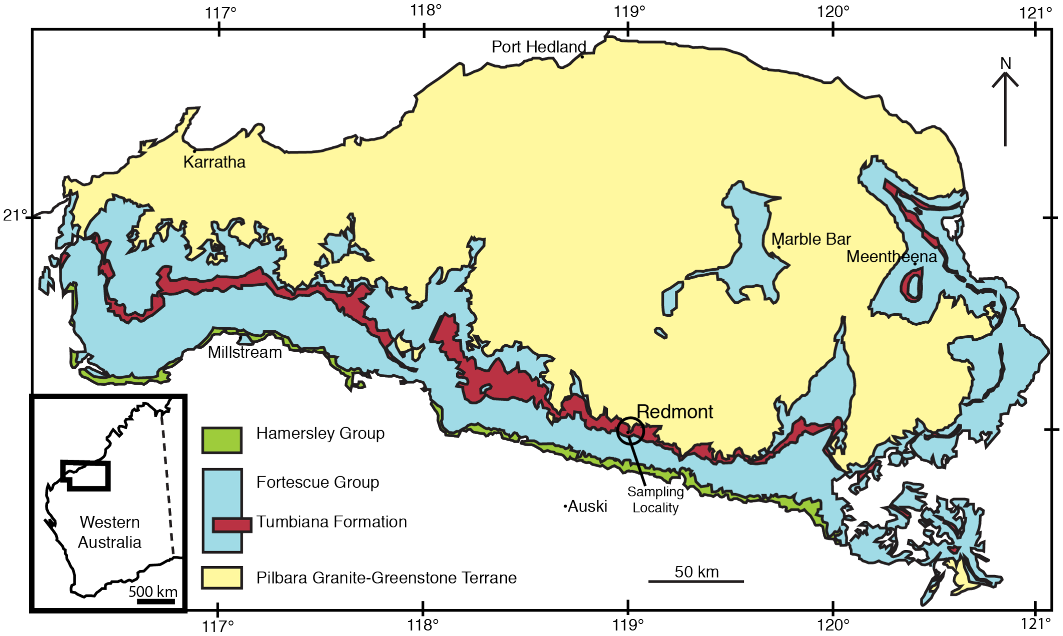

Figure 2.1: General geological map of Tumbiana Formation exposures modified from Sakurai et al. (2005). The Redmont sampling locality is marked.

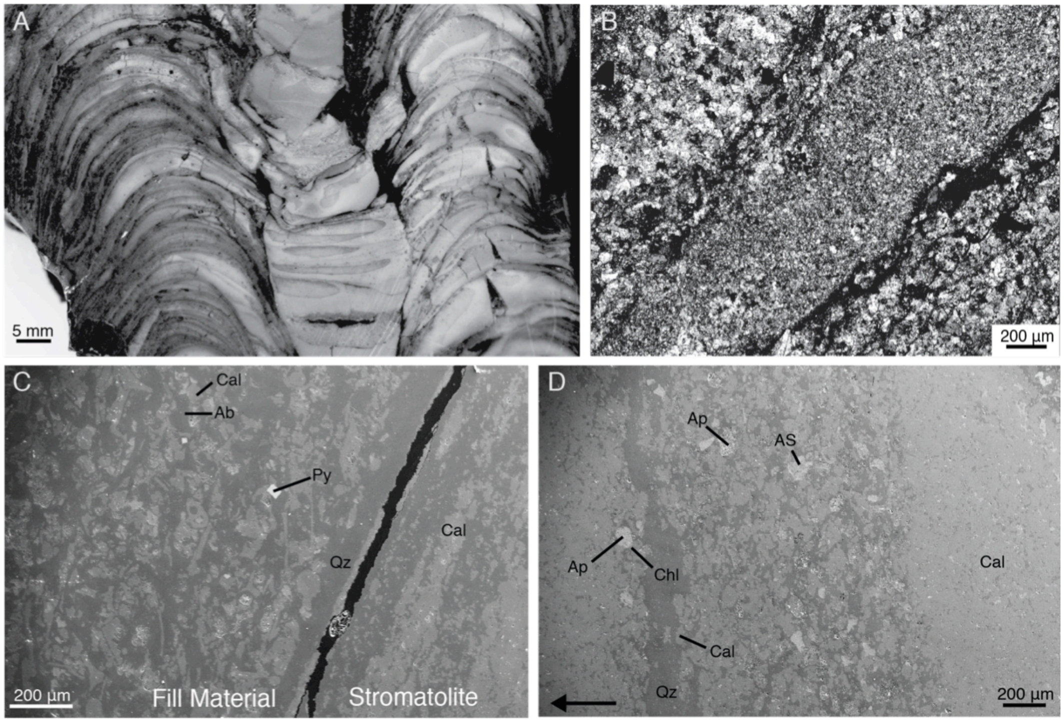

Figure 2.2: (A) Image of TB2f stromatolite. Note the laminae thicken and thin across stromatolite apices. (B) Photomicrograph in transmitted cross-polarized light shows differential coarseness of recrystallization between laminae in TA1b. (C) Scanning electron image of the contact between stromatolite versus fill material in TA1b. (D) Scanning electron image of a layer of detrital sediment within intercolumn fill material in TB2b. Abbreviations for minerals identified using X-ray dispersive spectroscopy: Ab = Albite, Ap = Apatite, AS = Fe, Mg aluminosilicate, Cal = Calcite, Chl = Chlorite, Py = Pyrite, Qz = Quartz. Arrow shows up direction if image is rotated.

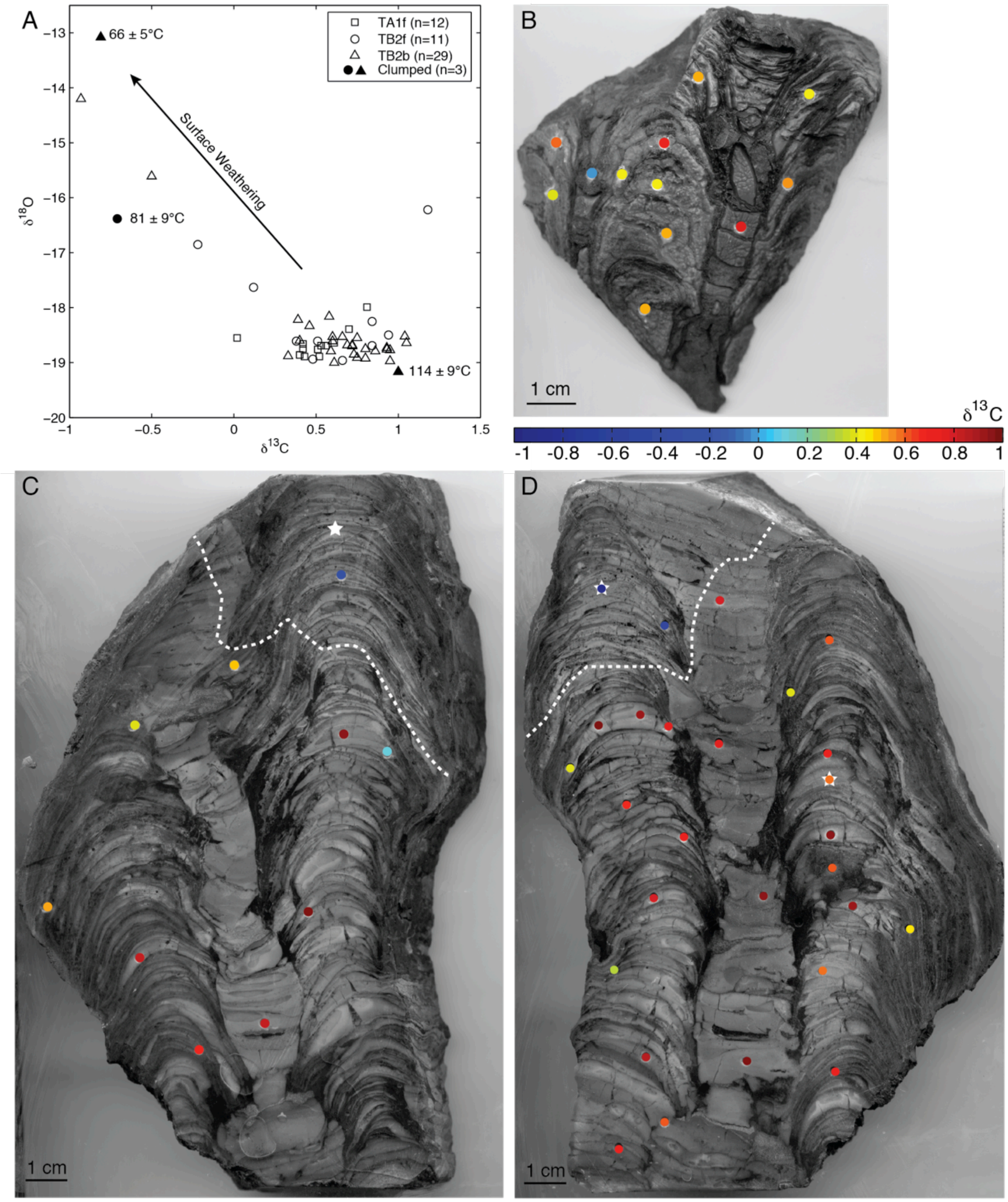

Figure 2.3: Carbon, oxygen, and clumped isotope data from Tumbiana stromatolites. (A) Crossplot of carbon and oxygen isotope ratios from micromilled carbonate textures. Clumped isotope temperature estimates are shown in filled symbols, and record a trend with C and O isotopes in regions of near-surface weathering. Locations of analytical spots and mapped $\delta^{13}C_{carb}$ values for (B) TA1f, (C) TB2f, and (D) TB2b. Colorbar of isotopic values shown in (B) is the same for all samples. White stars indicate locations of clumped isotope spots sampled ~ 5 mm below the surface. Dashed white lines show area affected by meteoric water infiltration, delimited by presence of secondary iron oxides (Fig. S2.3).

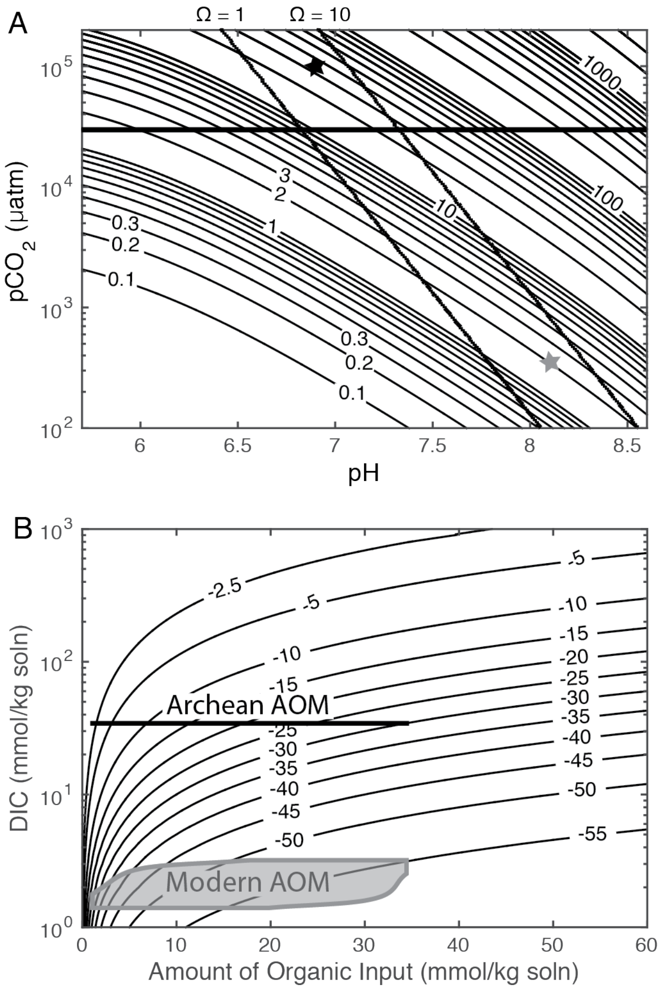

Figure 2.4: Estimates of the C isotopic composition of hypothetical AOM carbonate under conditions of Archean seawater carbonate chemistry. (A) Calculation of DIC in mmol/kg as a function of atmospheric CO_2 and seawater pH. Horizontal black line marks a lower limit of pCO_2 from Grotzinger and Kasting (1993). For reference, diagonal black curves mark calculated saturation states ($\Omega = 1$ and $\Omega = 10$) given modern [Ca^{2+}]. Grey star shows modern seawater, and black star is a reasonable Archean seawater estimate using constraints from Halevy et al. (2010). (B) AOM carbonate signature with modern AOM region based off DIC and $\delta^{13}C_{carb}$ values and hypothetical Archean AOM carbonate estimate based off DIC estimates from (A).

2.9 Supplemental Tables

Table S2.1: Examples of carbon isotopic signatures from Phanerozoic AOM sites

Age	Location	δ^{13}Corg (‰ PDB)	δ^{13}Ccarb (‰ PDB)	Reference*
Modern	Eel River Basin	-15 to -106	-3 to -40	1-3
Modern	Hydrate Ridge	-102 to -128	-24 to -58	4-6
Modern	Black Sea	-27 to -112	-25 to -41	7-9
Modern	Gulf of Mexico	-48 to -99	-18 to -55	10-12
Modern	Aleutian Margin	-124 to -130	–42 to –51	13
Modern	Nankai Trough, Japan	---	-36 to -56	14
Modern	Voring Plateau, Norwegian Sea	-43 to -133	-31 to -59	15-18
Miocene	Marmorito, Italy	-83 to -116	–17 to -50	19-21
Miocene	Pietralunga, Italy	-42 to -109	-22 to -40	22, 23
Oligocene	Lincoln Creek Fm., Washington	-90 to -120	-10 to -51	7, 24
Eocene to Miocene	Scotland District, Barbados	---	-20 to -50	25, 26
Cretaceous	Tepee Buttes, Colorado	---	-40 to -45	27-29
Cretaceous	Canadian Arctic	---	-35 to -50	30
Cretaceous	Hokkaido, Japan	-104 to -129	-41 to -45	31, 32
Cretaceous	Raukumara Peninsula, New Zealand	-37 to -99	7 to -29	33
Cretaceous to Jurassic	California	-31 to -122	-19 to -44	34, 35
Jurassic	Alexander Island, Antarctica	---	-34 to -45	36
Jurassic	Beauvoism, France	-68 to -76	-12 to -27	20
Carboniferous	Harz Mountains, Germany	---	-8 to -32	37
Carboniferous	Ganibobis, Namibia	---	7 to -52	38
Devonian	Holland Mound, Morocco	---	-11 to -22	39, 40

---

* References: 1. Hinrichs et al. (2000), 2. Orphan et al. (2002), 3. Orphan et al. (2004), 4. Elvert et al. (1999), 5. Elvert et al. (2001), 6. Greinert et al. (2001), 7. Thiel et al. (2001), 8. Peckmann et al. (2001b), 9. Michaelis et al. (2002), 10. Zhang et al. (2002), 11. Zhang et al. (2003), 12. Roberts and Aharon (1994), 13. Greinert et al. (2002), 14. Sakai et al. (1992), 15. Mazzini et al. (2005), 16. Mazzini et al. (2006), 17. Ivanov et al. (2010), 18. Chevalier et al. (2014), 19. Thiel et al. (1999), 20. Peckmann et al. (1999b), 21. Cavagna et al. (1999), 22. Terzi (1993), 23. Peckmann et al. (2004), 24. Peckmann et al. (2002), 25. Torrini et al. (1990), 26. Gill et al. (2005), 27. Kauffman et al. (1996), 28. Shapiro and Fricke (2002), 29. Shapiro (2004), 30. Beauchamp and Savard (1992), 31. Hikida et al. (2003), 32. Ogihara (2008), 33. Kiel et al. (2013), 34. Campbell et al. (2002), 35. Birgel et al. (2006), 36. Kelly et al. (1995), 37. Peckmann et al. (2001a), 38. Himmler et al. (2008), 39. Peckmann et al. (1999a), 40. Peckmann et al. (2005)

Table S2.2: Isotopic Data from the Tumbiana Formation

Specimen name	Sample	$\delta^{13}C_{carb}$ (PDB)	$\delta^{13}O_{carb}$ (PDB)	Weathered	$\delta^{13}O_{water}$ (SMOW)	Temperature ± 1σ	$\delta^{13}C_{org}$ (PDB)
TA1f, 1	TA1f	0.81	-17.99	0	--	--	--
TA1f, 2	TA1f	0.56	-18.69	0	--	--	--
TA1f, 3	TA1f	0.51	-18.76	0	--	--	--
TA1f, 4	TA1f	0.70	-18.39	0	--	--	--
TA1f, 5	TA1f	0.42	-18.75	0	--	--	--
TA1f, 6	TA1f	0.53	-18.69	0	--	--	--
TA1f, 7	TA1f	0.52	-18.89	0	--	--	--
TA1f, 8	TA1f	0.02	-18.55	0	--	--	--
TA1f, 9	TA1f	0.61	-18.64	0	--	--	--
TA1f, 10	TA1f	0.42	-18.66	0	--	--	--
TA1f, 11	TA1f	0.40	-18.86	0	--	--	--
TA1f, 12	TA1f	0.43	-18.89	0	--	--	--
TB2b, 2	TB2b	0.95	-18.97	0	--	--	--
TB2b, 3	TB2b	1.04	-18.52	0	--	--	--
TB2b, 4	TB2b	0.75	-18.91	0	--	--	--
TB2b, 5	TB2b	0.93	-18.76	0	--	--	--
TB2b, 6	TB2b	1.05	-18.64	0	--	--	--
TB2b, 7	TB2b	0.39	-18.22	0	--	--	--
TB2b, 8	TB2b	0.66	-18.53	0	--	--	--
TB2b, 9	TB2b	-0.93	-14.20	1	--	--	--
TB2b, 10	TB2b	-0.50	-15.61	1	--	--	--
TB2b, 11	TB2b	0.40	-18.60	0	--	--	--
TB2b, 12	TB2b	0.60	-18.61	0	--	--	--
TB2b, 13	TB2b	0.69	-18.68	0	--	--	--
TB2b, 14	TB2b	0.59	-18.79	0	--	--	--
TB2b, 15b	TB2b	0.95	-18.77	0	--	--	--
TB2b, 16	TB2b	0.60	-18.53	0	--	--	--
TB2b, 17	TB2b	0.46	-18.33	0	--	--	--
TB2b, 18	TB2b	0.93	-18.73	0	--	--	--
TB2b, 19	TB2b	0.58	-18.16	0	--	--	--
TB2b, 20	TB2b	0.73	-18.85	0	--	--	--
TB2b, 21	TB2b	0.33	-18.88	0	--	--	--
TB2b, 22	TB2b	0.86	-18.79	0	--	--	--
TB2b, 23	TB2b	0.61	-19.00	0	--	--	--
TB2b, 24	TB2b	0.80	-18.92	0	--	--	--
TB2b, 25	TB2b	0.80	-18.75	0	--	--	--
TB2b, 26	TB2b	0.72	-18.68	0	--	--	--
TB2b, 27	TB2b	0.72	-18.70	0	--	--	--
TB2b, 28	TB2b	0.75	-18.55	0	--	--	--
TB2f, 1	TB2f	0.94	-18.50	0	--	--	--
TB2f, 2	TB2f	-0.22	-16.85	1	--	--	--
TB2f, 3	TB2f	1.18	-16.22	0	--	--	--
TB2f, 4	TB2f	0.84	-18.25	0	--	--	--
TB2f, 5	TB2f	0.84	-18.69	0	--	--	--
TB2f, 6	TB2f	0.66	-18.96	0	--	--	--
TB2f, 7	TB2f	0.51	-18.61	0	--	--	--
TB2f, 8	TB2f	0.48	-18.94	0	--	--	--
TB2f, 9	TB2f	0.12	-17.63	0	--	--	--
TB2f, 10	TB2f	0.38	-18.61	0	--	--	--
Clump1	TB2b	1.00	-19.17	0	-3.10	114 ± 9	--
Clump2	TB2b	-0.81	-13.08	1	-5.07	56 ± 5	--
Clump3	TB2f	-0.71	-16.38	1	-4.60	81 ± 9	--
Org_TA1	TA1 (f&b)	--	--	--	--	--	-53.2
Org_TB2, 1	TB2 (f&b)	--	--	--	--	--	-49.91
Org_TB2, 2	TB2 (f&b)	--	--	--	--	--	-52.07

2.10 Supplemental Figures

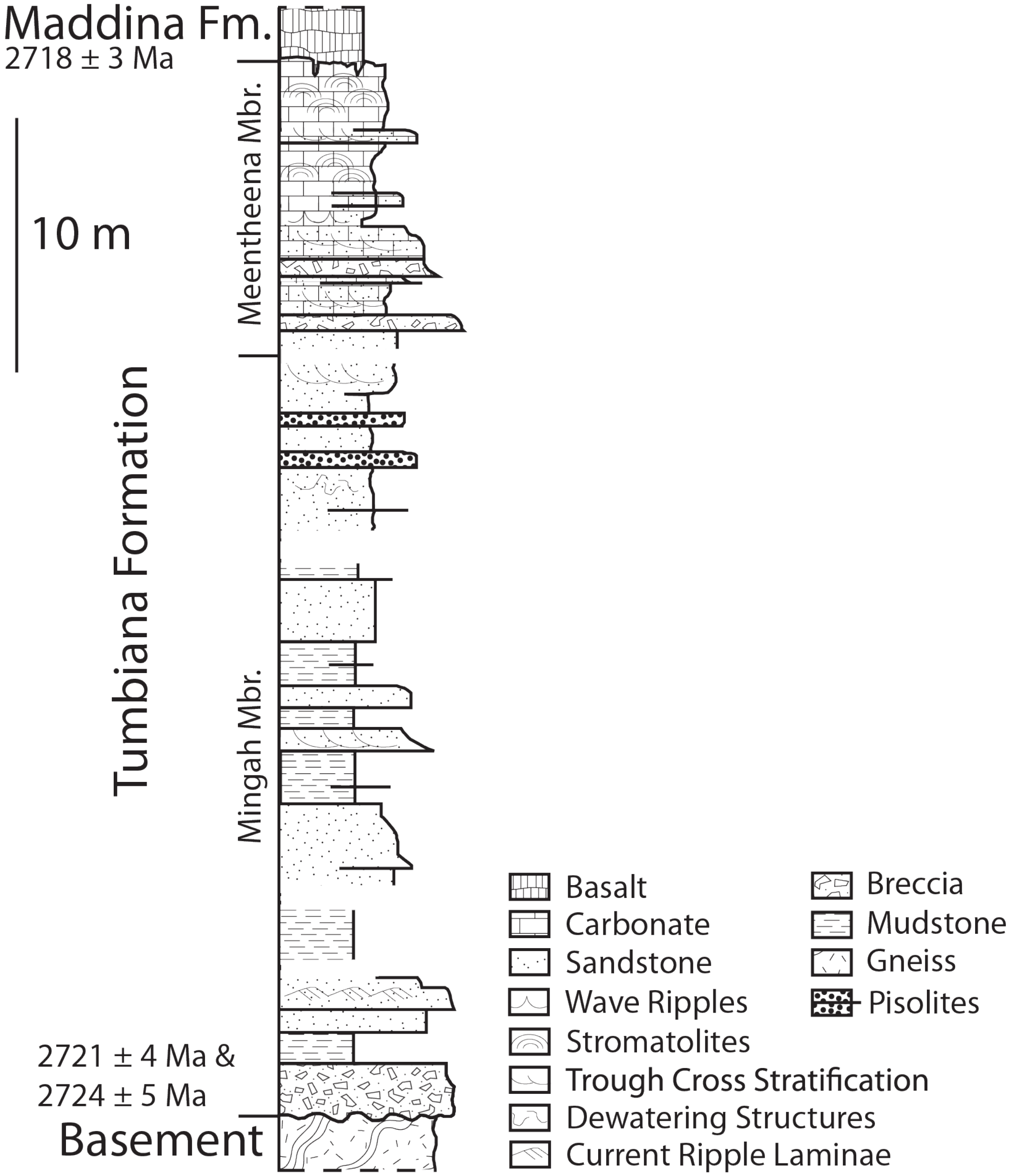

Figure S2.1: Stratigraphic column of the study locality, modified from Sakurai et al. (2005) with age constraints from Blake et al. (2004).

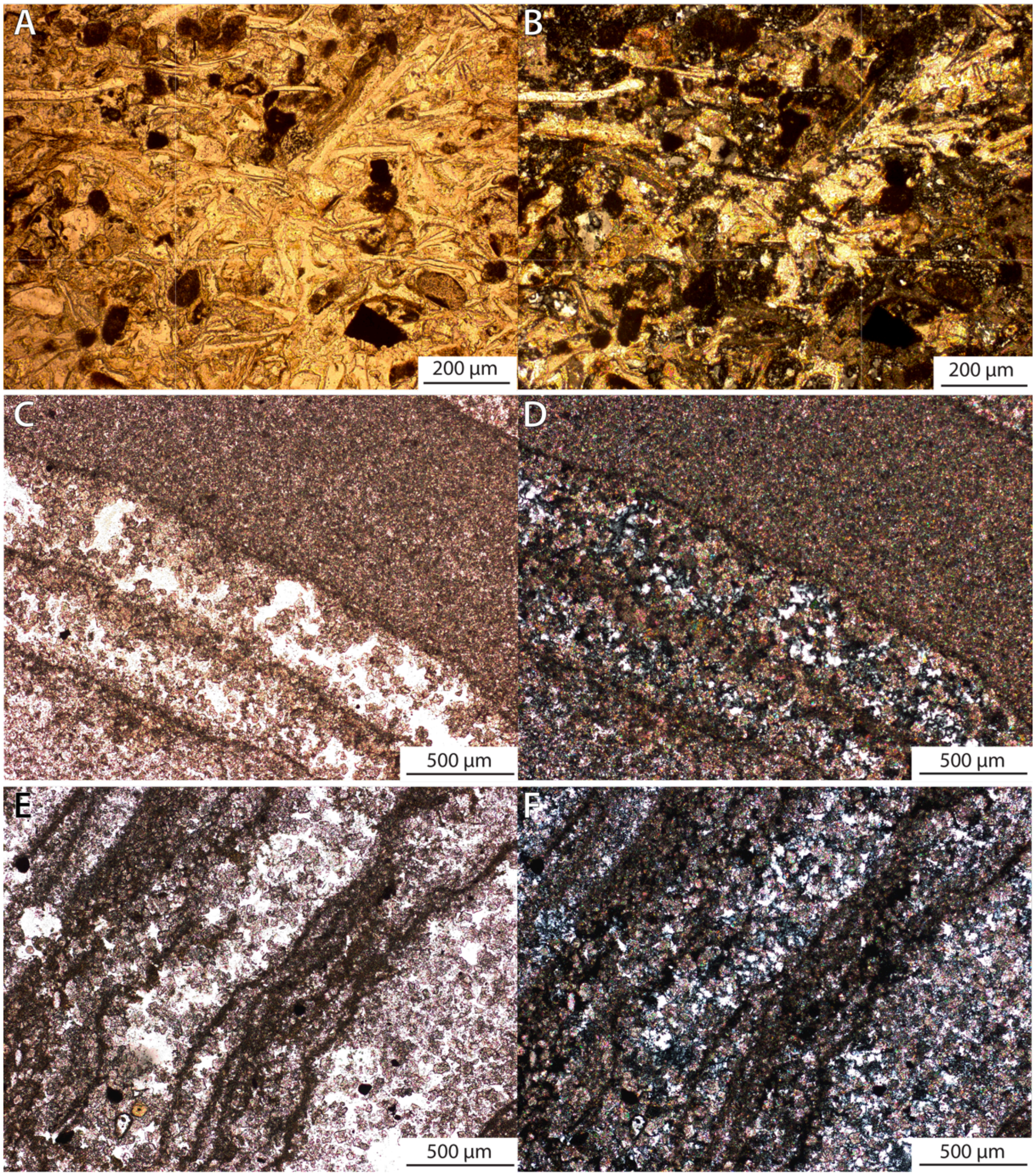

Figure S2.2: Plane-polarized (A) and cross-polarized (B) transmitted light microscope images of fill material in TA1b highlighting rare detrital carbonate grains with siliciclastic detrital minerals and carbonate cement. Plane-polarized (C) and cross-polarized (D) transmitted light microscope images of stromatolitic layers in TB2b highlighting proportion of carbonate versus siliciclastic minerals in variably recrystallized laminae. Plane-polarized (E) and cross-polarized (F) transmitted light microscope images of stromatolitic laminae in TB2b with "trapped-and-bound" detrital minerals beyond the angle of repose.

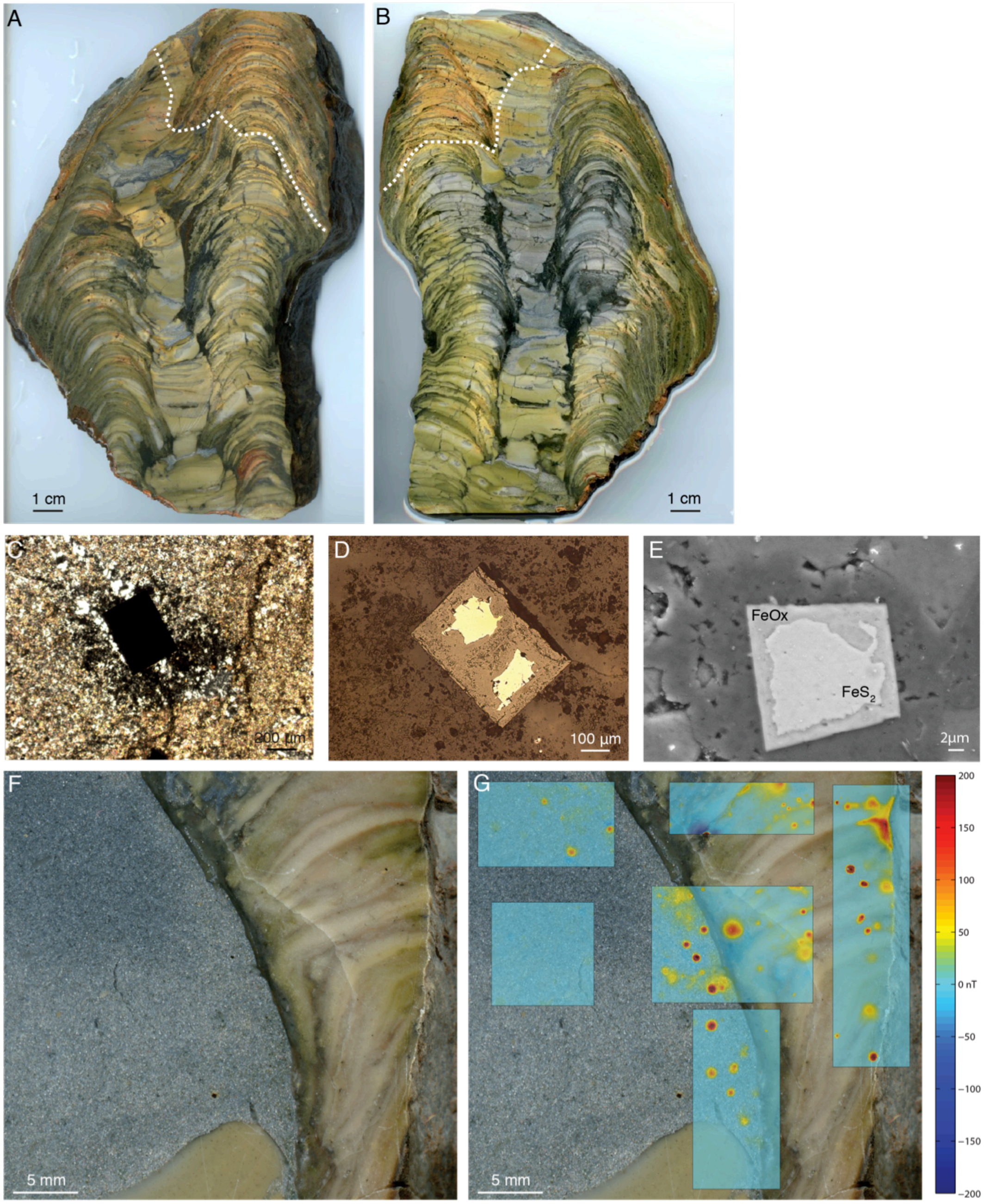

Figure S2.3: Color photograph showing secondary iron oxides forming from near surface oxidation of ferrous iron in pyrite and carbonate for (A) TB2f (B) TB2b. C) Transmitted cross-polarized light microscope image of a euhedral opaque mineral on TB2b thin section. D) Reflected light photomicrograph of same crystal highlighting brighter iron sulfide core with iron oxide rim, interpreted as oxidation during near-surface weathering. E) Scanning electron microscope image highlighting another euhedral pyrite (FeS_2) core with iron oxide (FeOx) rim on

TA1b, confirmed by X-ray dispersive spectroscopy. Ultra-high resolution scanning SQuID microscopy (UHRSSM) of small regions on TA2f was performed at the Caltech Paleomagnetics Laboratory after giving the sample a strong magnetization perpendicular to slab surface showing magnetic dipoles in warm colors (G) with a resolution of 40 or 80 μm. These dipoles represent magnetic minerals and match the locations of the dark euhedral phases (F). We interpret these as oxidized pyrite similar to those seen in petrographic work and interpret the magnetic signal to be derived from secondary iron oxides.

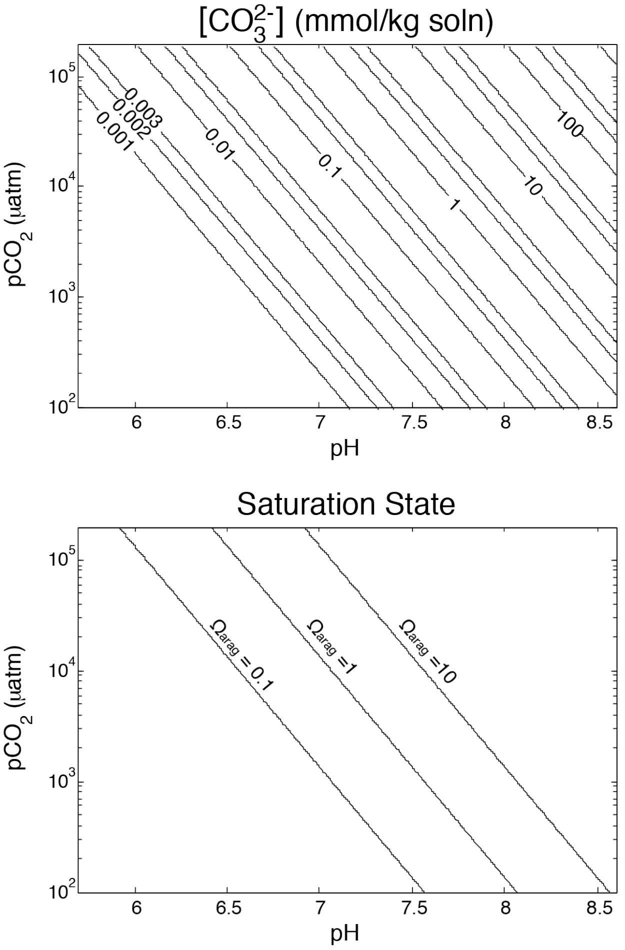

Figure S2.4: Calculations showing constraints on the carbonate chemistry of Tumbiana basin waters over a range of $CaCO_3$ saturation states. Upper panel: calculation of $[CO_3^{2-}]$ in mmol/kg as a function of atmospheric CO_2 and seawater pH. Lower panel: assuming modern $[Ca^{2+}]$ (10.28 mmol/kg solution, Zeebe and Wolf-Gladrow (2001)) and standard temperature, pressure, and salinity, saturation state for aragonite precipitation was calculated. Due to the linearity of this calculation, changes in the $[Ca^{2+}]$ will scale simply with the saturation state, *i.e.* Ω =10 at modern $[Ca^{2+}]$ is equivalent to Ω =1 at 10 times modern $[Ca^{2+}]$.

2.11 References

Awramik, S. M., and Buchheim, H. P., 2009, A giant, Late Archean lake system: The Meentheena Member (Tumbiana Formation; Fortescue Group), Western Australia: Precambrian Research, v. 174, no. 3, p. 215-240.

Beal, E. J., House, C. H., and Orphan, V. J., 2009, Manganese- and iron-dependent marine methane oxidation: Science, v. 325, no. 5937, p. 184-187.

Beauchamp, B., and Savard, M., 1992, Cretaceous chemosynthetic carbonate mounds in the Canadian Arctic: Palaios, p. 434-450.

Bergmann, K. D., Grotzinger, J. P., and Fischer, W. W., 2013, Biological influences on seafloor carbonate precipitation: Palaios, v. 28, no. 2, p. 99-115.

Birgel, D., Thiel, V., Hinrichs, K.-U., Elvert, M., Campbell, K. A., Reitner, J., Farmer, J. D., and Peckmann, J., 2006, Lipid biomarker patterns of methane-seep microbialites from the Mesozoic convergent margin of California: Organic Geochemistry, v. 37, no. 10, p. 1289-1302.

Blake, T., Buick, R., Brown, S., and Barley, M., 2004, Geochronology of a Late Archaean flood basalt province in the Pilbara Craton, Australia: constraints on basin evolution, volcanic and sedimentary accumulation, and continental drift rates: Precambrian Research, v. 133, no. 3, p. 143-173.

Blaser, M. B., Dreisbach, L. K., and Conrad, R., 2013, Carbon isotope fractionation of 11 acetogenic strains grown on H2 and CO2: Applied and environmental microbiology, v. 79, no. 6, p. 1787-1794.

Boetius, A., Ravenschlag, K., Schubert, C. J., Rickert, D., Widdel, F., Gieseke, A., Amann, R., Jørgensen, B. B., Witte, U., and Pfannkuche, O., 2000, A marine microbial consortium apparently mediating anaerobic oxidation of methane: Nature, v. 407, no. 6804, p. 623-626.

Bristow, T. F., and Grotzinger, J. P., 2013, Sulfate availability and the geological record of cold-seep deposits: Geology, v. 41, no. 7, p. 811-814.

Buick, R., 1992, The antiquity of oxygenic photosynthesis: evidence from stromatolites in sulphate-deficient Archaean lakes: Science, v. 255, no. 5040, p. 74-77.

Buick, R., Dunlop, J., and Groves, D., 1981, Stromatolite recognition in ancient rocks: an appraisal of irregularly laminated structures in an Early Archaean chert-barite unit from North Pole, Western Australia: Alcheringa, v. 5, no. 3, p. 161-181.

Campbell, K., Farmer, J., and Des Marais, D., 2002, Ancient hydrocarbon seeps from the Mesozoic convergent margin of California: carbonate geochemistry, fluids and palaeoenvironments: Geofluids, v. 2, no. 2, p. 63-94.

Campbell, K. A., 2006, Hydrocarbon seep and hydrothermal vent paleoenvironments and paleontology: past developments and future research directions: Palaeogeography, Palaeoclimatology, Palaeoecology, v. 232, no. 2, p. 362-407.

Cavagna, S., Clari, P., and Martire, L., 1999, The role of bacteria in the formation of cold seep carbonates: geological evidence from Monferrato (Tertiary, NW Italy): Sedimentary Geology, v. 126, no. 1, p. 253-270.

Chevalier, N., Bouloubassi, I., Stadnitskaia, A., Taphanel, M.-H., and Damsté, J. S. S., 2014, Lipid biomarkers for anaerobic oxidation of methane and sulphate reduction in cold seep sediments of Nyegga pockmarks (Norwegian margin): discrepancies in contents and carbon isotope signatures: Geo-Marine Letters, v. 34, no. 2-3, p. 269-280.

Coffey, J., Flannery, D., Walter, M., and George, S., 2013, Sedimentology, stratigraphy and geochemistry of a stromatolite biofacies in the 2.72 Ga Tumbiana Formation, Fortescue Group, Western Australia: Precambrian Research, v. 236, p. 282-296.

Crowe, S. A., Paris, G., Katsev, S., Jones, C., Kim, S.-T., Zerkle, A. L., Nomosatryo, S., Fowle, D. A., Adkins, J. F., and Sessions, A. L., 2014, Sulfate was a trace constituent of Archean seawater: Science, v. 346, no. 6210, p. 735-739.

Dennis, K. J., Affek, H. P., Passey, B. H., Schrag, D. P., and Eiler, J. M., 2011, Defining an absolute reference frame for 'clumped isotope' studies of CO2: Geochimica et Cosmochimica Acta, v. 75, no. 22, p. 7117-7131.

Eigenbrode, J. L., and Freeman, K. H., 2006, Late Archean rise of aerobic microbial ecosystems: Proceedings of the National Academy of Sciences, v. 103, no. 43, p. 15759-15764.

Eiler, J. M., Bonifacie, M., and Daëron, M., 2009, 'Clumped isotope'thermometry for high-temperature problems: Geochimica et Cosmochimica Acta, v. 73, no. 13, p. A322.

Elvert, M., Greinert, J., Suess, E., and Whiticar, M. J., 2001, Carbon isotopes of biomarkers derived from methane-oxidizing microbes at Hydrate Ridge, Cascadia convergent margin: Geophysical Monograph-American Geophysical Union, v. 124, p. 115-130.

Elvert, M., Suess, E., and Whiticar, M. J., 1999, Anaerobic methane oxidation associated with marine gas hydrates: superlight C-isotopes from saturated and unsaturated C20 and C25 irregular isoprenoids: Naturwissenschaften, v. 86, no. 6, p. 295-300.

Farquhar, J., Bao, H., and Thiemens, M., 2000, Atmospheric influence of Earth's earliest sulfur cycle: Science, v. 289, no. 5480, p. 756-758.

Fischer, W., Schroeder, S., Lacassie, J., Beukes, N., Goldberg, T., Strauss, H., Horstmann, U., Schrag, D., and Knoll, A., 2009, Isotopic constraints on the Late Archean carbon cycle from the Transvaal Supergroup along the western margin of the Kaapvaal Craton, South Africa: Precambrian Research, v. 169, no. 1, p. 15-27.

Flannery, D., and Walter, M., 2012, Archean tufted microbial mats and the Great Oxidation Event: new insights into an ancient problem: Australian Journal of Earth Sciences, v. 59, no. 1, p. 1-11.

Frantz, C., Petryshyn, V., and Corsetti, F., 2015, Grain trapping by filamentous cyanobacterial and algal mats: Implications for stromatolite microfabrics through time: Geobiology, v. 13, no. 5, p. 409-423.

Freeman, K. H., Hayes, J., Trendel, J.-M., and Albrecht, P., 1990, Evidence from carbon isotope measurements for diverse origins of sedimentary hydrocarbons: Nature, v. 343, no. 6255, p. 254-256.

Fuchs, G., 2011, Alternative pathways of carbon dioxide fixation: insights into the early evolution of life?: Annual review of microbiology, v. 65, p. 631-658.

Gelwicks, J. T., Risatti, J. B., and Hayes, J., 1989, Carbon isotope effects associated with autotrophic acetogenesis: Organic Geochemistry, v. 14, no. 4, p. 441-446.

Ghosh, P., Adkins, J., Affek, H., Balta, B., Guo, W., Schauble, E. A., Schrag, D., and Eiler, J. M., 2006, 13 C–18 O bonds in carbonate minerals: A new kind of paleothermometer: Geochimica et Cosmochimica Acta, v. 70, no. 6, p. 1439-1456.

Gill, F. L., Harding, I. C., Little, C. T., and Todd, J. A., 2005, Palaeogene and Neogene cold seep communities in Barbados, Trinidad and Venezuela: An overview: Palaeogeography, Palaeoclimatology, Palaeoecology, v. 227, no. 1, p. 191-209.

Greinert, J., Bohrmann, G., and Elvert, M., 2002, Stromatolitic fabric of authigenic carbonate crusts: result of anaerobic methane oxidation at cold seeps in 4,850 m water depth: International Journal of Earth Sciences, v. 91, no. 4, p. 698-711.

Greinert, J., Bohrmann, G., and Suess, E., 2001, Gas hydrate-associated carbonates and methane-venting at Hydrate Ridge: classification, distribution and origin of authigenic lithologies: Geophysical Monograph-American Geophysical Union, v. 124, p. 99-114.

Grotzinger, J. P., and James, N. P., 2000, Carbonate sedimentation and diagenesis in the evolving Precambrian world, Tusla, Oklahoma, SEPM Special Publication, v. 67.

Grotzinger, J. P., and Kasting, J. F., 1993, New constraints on Precambrian ocean composition: The Journal of Geology, p. 235-243.

Grotzinger, J. P., and Knoll, A. H., 1999, Stromatolites in Precambrian carbonates: evolutionary mileposts or environmental dipsticks?: Annual review of earth and planetary sciences, v. 27, no. 1, p. 313-358.

Guy, R. D., Fogel, M. L., and Berry, J. A., 1993, Photosynthetic fractionation of the stable isotopes of oxygen and carbon: Plant Physiology, v. 101, no. 1, p. 37-47.

Halevy, I., Johnston, D. T., and Schrag, D. P., 2010, Explaining the structure of the Archean mass-independent sulfur isotope record: Science, v. 329, no. 5988, p. 204-207.

Haroon, M. F., Hu, S., Shi, Y., Imelfort, M., Keller, J., Hugenholtz, P., Yuan, Z., and Tyson, G. W., 2013, Anaerobic oxidation of methane coupled to nitrate reduction in a novel archaeal lineage: Nature, v. 500, no. 7464, p. 567-570.

Hayes, J., 1994, Global methanotrophy at the Archean-Proterozoic transition: Early life on Earth, v. 84, p. 220-236.

Higgins, J., Fischer, W., and Schrag, D., 2009, Oxygenation of the ocean and sediments: consequences for the seafloor carbonate factory: Earth and Planetary Science Letters, v. 284, no. 1, p. 25-33.

Hikida, Y., Suzuki, S., Togo, Y., and IJIRI, A., 2003, An exceptionally well-preserved fossil seep community from the Cretaceous Yezo Group in the Nakagawa area, Hokkaido, northern Japan: Paleontological Research, v. 7, no. 4, p. 329-342.

Himmler, T., Freiwald, A., Stollhofen, H., and Peckmann, J., 2008, Late Carboniferous hydrocarbon-seep carbonates from the glaciomarine Dwyka Group, southern Namibia: Palaeogeography, Palaeoclimatology, Palaeoecology, v. 257, no. 1, p. 185-197.

Hinrichs, K.-U., Summons, R. E., Orphan, V., Sylva, S. P., and Hayes, J. M., 2000, Molecular and isotopic analysis of anaerobic methane-oxidizing communities in marine sediments: Organic Geochemistry, v. 31, no. 12, p. 1685-1701.

Hinrichs, K. U., 2002, Microbial fixation of methane carbon at 2.7 Ga: Was an anaerobic mechanism possible?: Geochemistry, geophysics, geosystems, v. 3, no. 7, p. 1-10.

Hotinski, R., Kump, L., and Arthur, M., 2004, The effectiveness of the Paleoproterozoic biological pump: A δ13C gradient from platform carbonates of the Pethei Group (Great Slave Lake Supergroup, NWT): Geological Society of America Bulletin, v. 116, no. 5-6, p. 539-554.

Ivanov, M., Mazzini, A., Blinova, V., Kozlova, E., Laberg, J.-S., Matveeva, T., Taviani, M., and Kaskov, N., 2010, Seep mounds on the southern Vøring Plateau (offshore Norway): Marine and Petroleum Geology, v. 27, no. 6, p. 1235-1261.

Johnson, C. M., Ludois, J. M., Beard, B. L., Beukes, N. J., and Heimann, A., 2013, Iron formation carbonates: Paleoceanographic proxy or recorder of microbial diagenesis?: Geology, v. 41, no. 11, p. 1147-1150.

Kauffman, E. G., Arthur, M. A., Howe, B., and Scholle, P. A., 1996, Widespread venting of methane-rich fluids in Late Cretaceous (Campanian) submarine springs (Tepee Buttes), Western Interior seaway, USA: Geology, v. 24, no. 9, p. 799-802.

Kelly, S. R., Ditchfield, P. W., Doubleday, P. A., and Marshall, J. D., 1995, An Upper Jurassic methane-seep limestone from the fossil Bluff Group forearc basin of Alexander Island, Antarctica: Journal of Sedimentary Research, v. 65, no. 2.

Kiel, S., Birgel, D., Campbell, K. A., Crampton, J. S., Schiøler, P., and Peckmann, J., 2013, Cretaceous methane-seep deposits from New Zealand and their fauna: Palaeogeography, Palaeoclimatology, Palaeoecology, v. 390, p. 17-34.

Kim, S.-T., and O'Neil, J. R., 1997, Equilibrium and nonequilibrium oxygen isotope effects in synthetic carbonates: Geochimica et Cosmochimica Acta, v. 61, no. 16, p. 3461-3475.

Lepot, K., Benzerara, K., Brown, G. E., and Philippot, P., 2008, Microbially influenced formation of 2,724-million-year-old stromatolites: Nature Geoscience, v. 1, no. 2, p. 118-121.

Liu, J., Fu, G., Song, X., Charles, S. P., Zhang, Y., Han, D., and Wang, S., 2010, Stable isotopic compositions in Australian precipitation: Journal of Geophysical Research: Atmospheres (1984–2012), v. 115, no. D23.

Luff, R., and Wallmann, K., 2003, Fluid flow, methane fluxes, carbonate precipitation and biogeochemical turnover in gas hydrate-bearing sediments at Hydrate Ridge, Cascadia Margin: numerical modeling and mass balances: Geochimica et Cosmochimica Acta, v. 67, no. 18, p. 3403-3421.

Marlow, J. J., Steele, J. A., Ziebis, W., Thurber, A. R., Levin, L. A., and Orphan, V. J., 2014, Carbonate-hosted methanotrophy represents an unrecognized methane sink in the deep sea: Nature communications, v. 5.

Martin, W. F., 2012, Hydrogen, metals, bifurcating electrons, and proton gradients: the early evolution of biological energy conservation: FEBS letters, v. 586, no. 5, p. 485-493.

Mazzini, A., Aloisi, G., Akhmanov, G., Parnell, J., Cronin, B., and Murphy, P., 2005, Integrated petrographic and geochemical record of hydrocarbon seepage on the Vøring Plateau: Journal of the Geological Society, v. 162, no. 5, p. 815-827.

Mazzini, A., Svensen, H., Hovland, M., and Planke, S., 2006, Comparison and implications from strikingly different authigenic carbonates in a Nyegga complex pockmark, G11, Norwegian Sea: Marine Geology, v. 231, no. 1, p. 89-102.

Michaelis, W., Seifert, R., Nauhaus, K., Treude, T., Thiel, V., Blumenberg, M., Knittel, K., Gieseke, A., Peterknecht, K., and Pape, T., 2002, Microbial reefs in the Black Sea fueled by anaerobic oxidation of methane: Science, v. 297, no. 5583, p. 1013-1015.

Nitschke, W., and Russell, M. J., 2012, Redox bifurcations: mechanisms and importance to life now, and at its origin: Bioessays, v. 34, no. 2, p. 106-109.

Ogihara, S., 2008, Acyclic hydrocarbons and ketones in cold-seep carbonates from central Hokkaido, northern Japan: Geochemical Journal, v. 42, no. 5, p. 421-427.

Orphan, V., Ussler, W., Naehr, T., House, C., Hinrichs, K.-U., and Paull, C., 2004, Geological, geochemical, and microbiological heterogeneity of the seafloor around methane vents in the Eel River Basin, offshore California: Chemical Geology, v. 205, no. 3, p. 265-289.

Orphan, V. J., House, C. H., Hinrichs, K.-U., McKeegan, K. D., and DeLong, E. F., 2002, Multiple archaeal groups mediate methane oxidation in anoxic cold seep sediments: Proceedings of the National Academy of Sciences, v. 99, no. 11, p. 7663-7668.

Owen, T., Cess, R., and Ramanathan, V., 1979, Early Earth: an enhanced carbon dioxide greenhouse to compensate for reduced solar luminosity: Nature, v. 277, p. 640-642.

Passey, B. H., Levin, N. E., Cerling, T. E., Brown, F. H., and Eiler, J. M., 2010, High-temperature environments of human evolution in East Africa based on bond ordering in paleosol carbonates: Proceedings of the National Academy of Sciences, v. 107, no. 25, p. 11245-11249.

Peckmann, D.-G. J., Walliser, O. H., Riegel, W., and Reitner, J., 1999a, Signatures of hydrocarbon venting in a Middle Devonian carbonate mound (Hollard Mound) at the Hamar Laghdad (Antiatlas, Morocco): Facies, v. 40, no. 1, p. 281-296.

Peckmann, J., Gischler, E., Oschmann, W., and Reitner, J., 2001a, An Early Carboniferous seep community and hydrocarbon-derived carbonates from the Harz Mountains, Germany: Geology, v. 29, no. 3, p. 271-274.

Peckmann, J., Goedert, J., Thiel, V., Michaelis, W., and Reitner, J., 2002, A comprehensive approach to the study of methane ‐ seep deposits from the Lincoln Creek Formation, western Washington State, USA: Sedimentology, v. 49, no. 4, p. 855-873.

Peckmann, J., Little, C., Gill, F., and Reitner, J., 2005, Worm tube fossils from the Hollard Mound hydrocarbon-seep deposit, Middle Devonian, Morocco: Palaeozoic seep-related vestimentiferans?: Palaeogeography, Palaeoclimatology, Palaeoecology, v. 227, no. 1, p. 242-257.

Peckmann, J., Reimer, A., Luth, U., Luth, C., Hansen, B., Heinicke, C., Hoefs, J., and Reitner, J., 2001b, Methane-derived carbonates and authigenic pyrite from the northwestern Black Sea: Marine Geology, v. 177, no. 1, p. 129-150.

Peckmann, J., and Thiel, V., 2004, Carbon cycling at ancient methane–seeps: Chemical Geology, v. 205, no. 3, p. 443-467.

Peckmann, J., Thiel, V., Michaelis, W., Clari, P., Gaillard, C., Martire, L., and Reitner, J., 1999b, Cold seep deposits of Beauvoisin (Oxfordian; southeastern France) and Marmorito (Miocene; northern Italy): microbially induced authigenic carbonates: International Journal of Earth Sciences, v. 88, no. 1, p. 60-75.

Peckmann, J., Thiel, V., Reitner, J., Taviani, M., Aharon, P., and Michaelis, W., 2004, A microbial mat of a large sulfur bacterium preserved in a Miocene methane-seep limestone: Geomicrobiology Journal, v. 21, no. 4, p. 247-255.

Roberts, H. H., and Aharon, P., 1994, Hydrocarbon-derived carbonate buildups of the northern Gulf of Mexico continental slope: a review of submersible investigations: Geo-Marine Letters, v. 14, no. 2-3, p. 135-148.

Sagan, C., and Mullen, G., 1972, Earth and Mars: evolution of atmospheres and surface temperatures: Science, v. 177, no. 4043, p. 52-56.

Sakai, H., Gamo, T., Ogawa, Y., and Boulegue, J., 1992, Stable isotopic ratios and origins of the carbonates associated with cold seepage at the eastern Nankai Trough: Earth and Planetary Science Letters, v. 109, no. 3, p. 391-404.

Sakurai, R., Ito, M., Ueno, Y., Kitajima, K., and Maruyama, S., 2005, Facies architecture and sequence-stratigraphic features of the Tumbiana Formation in the Pilbara Craton, northwestern Australia: Implications for depositional environments of oxygenic stromatolites during the Late Archean: Precambrian Research, v. 138, no. 3, p. 255-273.

Schoell, M., and Wellmer, F.-W., 1981, Anomalous 13C depletion in early Precambrian graphites from Superior Province, Canada.

Shapiro, R., and Fricke, H., 2002, Tepee Buttes: Fossilized methane-seep ecosystems: Field Guides, v. 3, p. 94-101.

Shapiro, R. s., 2004, Recognition of fossil prokaryotes in Cretaceous methane seep carbonates: relevance to astrobiology: Astrobiology, v. 4, no. 4, p. 438-449.

Stüeken, E., Buick, R., and Schauer, A., 2015, Nitrogen isotope evidence for alkaline lakes on late Archean continents: Earth and Planetary Science Letters, v. 411, p. 1-10.

Terzi, C., 1993, The ‘‘Calcari a Lucina’’(Lucina Limestones) of the Tuscan–Romagna Apennines as indicators of Miocene cold seep activity (Northern Apennines, Italy): Giornale di Geologia, v. 55, no. 2, p. 71-81.

Thauer, R. K., Kaster, A.-K., Seedorf, H., Buckel, W., and Hedderich, R., 2008, Methanogenic archaea: ecologically relevant differences in energy conservation: Nature Reviews Microbiology, v. 6, no. 8, p. 579-591.

Thiel, V., Peckmann, J., Richnow, H. H., Luth, U., Reitner, J., and Michaelis, W., 2001, Molecular signals for anaerobic methane oxidation in Black Sea seep carbonates and a microbial mat: Marine Chemistry, v. 73, no. 2, p. 97-112.

Thiel, V., Peckmann, J., Seifert, R., Wehrung, P., Reitner, J., and Michaelis, W., 1999, Highly isotopically depleted isoprenoids: molecular markers for ancient methane venting: Geochimica et Cosmochimica Acta, v. 63, no. 23, p. 3959-3966.

Thomazo, C., Ader, M., Farquhar, J., and Philippot, P., 2009, Methanotrophs regulated atmospheric sulfur isotope anomalies during the Mesoarchean (Tumbiana Formation, Western Australia): Earth and Planetary Science Letters, v. 279, no. 1, p. 65-75.

Thorne, A., and Trendall, A. F., 2001, Geology of the Fortescue Group, Pilbara Craton, Western Australia, Geological Survey of Western Australia, Department of Minerals and Energy.

Torrini, R., Speed, R., and Claypool, G., Origin and geologic implications of diagenetic limestone in fault zones of Barbados, *in* Proceedings Transactions of the 12th Caribbean Geological Conference1990, p. 366-375.

Williford, K., Ushikubo, T., Lepot, K., Kitajima, K., Hallmann, C., Spicuzza, M., Kozdon, R., Eigenbrode, J., Summons, R., and Valley, J., 2016, Carbon and sulfur isotopic signatures of ancient life and environment at the microbial scale: Neoarchean shales and carbonates: Geobiology, v. 14, no. 2, p. 105-128.

Yoshiya, K., Nishizawa, M., Sawaki, Y., Ueno, Y., Komiya, T., Yamada, K., Yoshida, N., Hirata, T., Wada, H., and Maruyama, S., 2012, In situ iron isotope analyses of pyrite and organic carbon isotope ratios in the Fortescue Group: Metabolic variations of a Late Archean ecosystem: Precambrian Research, v. 212, p. 169-193.

Zeebe, R. E., and Wolf-Gladrow, D. A., 2001, CO2 in seawater: equilibrium, kinetics, isotopes, Gulf Professional Publishing.

Zhang, C. L., Li, Y., Wall, J. D., Larsen, L., Sassen, R., Huang, Y., Wang, Y., Peacock, A., White, D. C., and Horita, J., 2002, Lipid and carbon isotopic evidence of methane-oxidizing and sulfate-reducing bacteria in association with gas hydrates from the Gulf of Mexico: Geology, v. 30, no. 3, p. 239-242.

Zhang, C. L., Pancost, R. D., Sassen, R., Qian, Y., and Macko, S. A., 2003, Archaeal lipid biomarkers and isotopic evidence of anaerobic methane oxidation associated with gas hydrates in the Gulf of Mexico: Organic Geochemistry, v. 34, no. 6, p. 827-836.

Chapter 3

Iron Mineralogy and Redox Chemistry of the Mesoproterozoic Newland Formation in the Helena Embayment, Belt Supergroup, MT

Originally published in:
Slotznick, S. P., Zieg, J., Webb, S. M., Kirschvink, J. L., and Fischer, W. W., 2015, Iron Mineralogy and Redox Chemistry of the Mesoproterozoic Newland Formation in the Helena Embayment, Belt Supergroup, Montana: Northwest Geology, v. 44, p. 55-72.

3.1 Introduction

The Mesoproterozoic era falls in the period between 1.85 to 0.85 Ga called “the boring billion”, sandwiched between the rise of multi-cellularity and animals in the Neoproterozoic and the Great Oxygenation Event and rise of oxygen in the Paleoproterozoic (Holland, 2006). However, important evolutionary developments occurred over the period with the rise of eukaryotes and macroscopic organisms (Knoll et al., 2006). The Belt Supergroup contains some of the early micro- and macrofossils that have been attributed to eukaryotes (Horodyski et al., 1989). One particularly well-studied example is found in the Greyson Shale of the Helena Embayment region in southwestern Montana (Fig. 3.1A). First identified by Charles Doolittle Walcott (1899) and later renamed (Walter et al., 1976), *Grypania spiralis* is a curved or coiled ribbon, 0.2 to 1.7 mm wide, and 6 to 14 mm in coiled diameter, and has been interpreted as eukaryotic algae as well consortia of several microscopic organisms (Horodyski et al., 1989; Knoll et al., 2006; Walter et al., 1976). Due to our understanding of eukaryotic phylogeny, the fact that most modern eukaryotes are aerobic, and the requirement of oxygen in making certain biological compounds (sterols) contained in eukaryotes, eukaryotes have been tied to oxygenic conditions (e.g. Brocks et al., 2003; Embley and Martin, 2006; Raymond and Blankenship, 2004). Therefore, there is a need to understand more about the environmental conditions in which early macroscopic organisms lived to understand the pacing of eukaryotic evolution and how it might have been aided, frustrated, or unaffected by changing environmental conditions during the Proterozoic.

However, understanding the redox state of ancient oceans has been a longstanding problem since a good oxygen barometer has not yet been developed. In general, geologists and geochemists have looked at iron, sulfur, and other redox sensitive elements as records of oxygen levels, but these approaches often give discordant answers. Some studies have suggested a fully oxygenated mid-Proterozoic ocean (Cloud, 1968; Holland, 1984, 2006), while others have suggested a stratified system with anoxic and/or euxinic deep oceans (Canfield, 1998; Poulton and Canfield, 2011). Aerobic/oxic environments are defined as having >80 μM O_2, anoxic/ferruginous have <5 μM O_2, and euxinic environments are anoxic with H_2S also present (Raiswell & Canfield 1998). Even within the subset of studies focused on samples of the Belt Supergroup, there have been conflicting hypotheses about redox conditions. Due to their preservation and low metamorphic grade (Duke and Lewis, 2010), the strata contained in the Helena Embayment, specifically the shale-dominated Newland Formation, have been the main target for understanding the ancient redox character and geochemistry of the Belt Basin. Sulfate concentrations and sulfur isotopes (Gellatly and Lyons, 2005; Luepke and Lyons, 2001; Lyons et al., 2000) as well as presence of basin-wide sedimentary laminations in the shales of the Newland and Prichard Formations similar to those found in the Black Sea (Lyons et al., 2000) were initially argued as evidence of a chemically stratified euxinic basin during deposition of the lower Belt Supergroup. Bottom water suboxic to euxinic conditions were also suggested by the high (several wt.%) organic content observed in shales (Lyons et al., 2000), and the syndepositional to early diagenetic abundant pyrite and sulfide-hosted base metal deposits of Cu, Co, and Ag (Graham et al., 2012; White et al., 2014). Others suggested the euxinic conditions forming early diagenetic pyrite were restricted to pore waters (Schieber, 1989c). In sharp contrast, iron speciation results indicate anoxic and ferruginous conditions for basinal waters of the lower Belt Supergroup (Planavsky et al., 2011). Iron speciation is a recently-developed bulk geochemical technique that uses sequential extraction to estimate proportions of different reactive iron minerals within a given rock sample (Poulton and Canfield, 2005), which are then mapped to redox conditions based on empirical calibrations from modern sediment samples. Additionally, recent nitrogen isotope measurements of samples from the Chamberlain, Greyson, and Newland Formations suggest oxygenated portions of the water column (Stüeken, 2013).

In this study, we focus on samples of the Newland Formation from the Black Butte Deposit in the Helena Embayment since previous workers investigating mid-Proterozoic redox conditions used drill core specimens from this deposit to avoid complications of recent surface oxidation (Gellatly and Lyons, 2005; Luepke and Lyons, 2001; Lyons et al., 2000; Planavsky et al., 2011). To help reconcile the different redox interpretations and test the iron speciation results, we investigated the iron mineralogy of the Newland Formation using a range of petrographic, spectroscopic, and rock magnetic techniques that help shed light on both the paleoenvironmental processes of iron deposition in the sediments as well as post-depositional modifications to those phases. Bulk rock magnetism experiments provide sensitive techniques to identify ferromagnetic minerals, including magnetic iron sulfide phases. Magnetic iron sulfides such as pyrrhotite have not previously been identified in materials collected from the Newland Formation, but have been widely observed throughout correlative units elsewhere in the lower Belt Supergroup (e.g. Luepke, 1999; Luepke and Lyons, 2001; Slotznick et al., 2016). Much of the pyrrhotite in the rock record is interpreted to be due to the metamorphic alteration of pyrite or precipitation from high temperature fluids (Craig and Vokes, 1993; Hall, 1986); and pyrrhotite observed in Belt strata reflects both of these post-depositional processes (Luepke, 1999). Pyrite can transform to pyrrhotite beginning at 200°C (Hall, 1986) if a suitable reducing environment or organic matter is present, although some experiments suggest even lower temperature transitions are possible (Moreau et al., 2005; Raub et al., 2012). Thus the presence of pyrrhotite can provide a tool for understanding metamorphic temperatures and metasomatic conditions of the Newland Formation at the Black Butte Deposit, aiding us in recognizing if bulk geochemical proxies have been compromised by post-depositional alteration. Additionally, synchrotron-based X-ray spectroscopy provided a complimentary tool to discover and image a wide range of non-magnetic iron minerals such as chalcopyrite and pyrite while confirming the presence or absence of pyrrhotite. By applying these paired magnetic and spectroscopic techniques to the Belt Supergroup, we should be able to improve upon previous bulk geochemical studies in deducing how iron was being deposited and transformed in the environment to reconstruct ancient redox conditions.

3.2 Geologic Setting

The Helena Embayment is an E-W trending limb of the larger Belt Basin, with strata broadly correlative to three of the four stratigraphic groups recognized elsewhere in the basin: lower Belt Group, Ravalli Group, Middle Belt Carbonate Group (Fig. 3.1A; Graham et al., 2012; Winston and Link, 1993). Fine-grained siliciclastics and carbonates dominate the lower Belt in the northern part of the Helena Embayment near the Black Butte Deposit (Fig. 3.1B). The Neihart Quartzite is a basal quartz arenite sandstone with planar and trough cross-bedding, parallel lamination, and lenses of pebbles lying unconformably on early Proterozoic gneiss basement (Schieber, 1989b; Walcott, 1899). Overlying the Neihart quartzite, the Chamberlain Formation is a wavy laminated to bedded black shale, siltstone and sandstone with lenses of molar tooth hash near the top (Zieg, 1986). The Chamberlain Formation grades into the Newland Formation. The Newland Formation varies considerably in thickness across the Embayment from 610 m to over 3000 m, but is approximately 1,100 m in the region of the Black Butte Cu-Co-Ag deposit near the northern margin of the Helena Embayment (Nelson, 1963; Walcott, 1899; Zieg, 1986). The Newland Formation is subdivided into two informal members: a lower parallel-laminated shale interbedded with debris flows, turbidites, and carbonates and an upper shale with more abundant carbonate beds (Zieg, 1986). Conformably overlying the Newland Formation is the Greyson Formation of wavy laminated siltstone and dark shale, which as been assigned by some to the lower Belt Group (Graham et al., 2012; Ross and Villeneuve, 2003; Winston and Link, 1993) and by others to the Ravalli Group (Harrison, 1972; Mudge et al., 1968). The red siltstone and claystone Spokane Formation overlies the Greyson Formation as part of the Ravalli Group. The Empire Formation (Ravalli Group) and the Helena Formation (Middle Belt Carbonate) also outcrop in the Helena Embayment, but these two units are not exposed in the Black Butte region. Instead, the Spokane is uncomfortably overlain by the Cambrian Flathead Sandstone (Fig. 3.1B; Deiss, 1935).

3.2.1 Black Butte Deposit

The strata-bound Black Butte Cu-Co-Ag Deposit occurs in the Newland Formation associated with spectacular synsedimentary pyrite-rich horizons that extend over a 25 km by 8 km area, although the main ore mineralization is localized to a fault-bounded block 8 km by 4 km (Fig. 3.1C). Three mineralized zones occur in the lower member, which are separated stratigraphically by approximately 600 m and divided by the Volcano Valley Fault (VVF). They have been named the Johnny Lee Upper Sulfide Zone (USZ), the Lowry Middle Sulfide Zone (MSZ) and the Johnny Lee Lower Sulfide Zone (LSZ) (Figs. 3.1B, 2; Zieg et al., 2013). The MSZ is still being studied and explored, and no samples were collected from it: this study focuses on the relatively well-characterized Johnny Lee deposits. Petrographic analyses have shown that the mineralization within the USZ and LSZ zones is distinct texturally and mineralogically although both contain abundant early and late diagenetic pyrite and early diagenetic barite (Graham et al., 2012). Much of the early diagenetic pyrite is framboidal or occurs in small fine-grained aggregates including small circular tubes proposed to reflect pyritized microbial filaments (McGoldrick and Zieg, 2004) and chimneys (Present et al., in review). The early diagenetic pyrite is interpreted to form from fault controlled iron-rich fluids moving through the sedimentary pile and venting at or just below the sediment surface at low temperatures (Graham et al., 2012; White et al., 2014), or from diagenetic transformations of detrital iron oxides under conditions of microbial sulfate reduction in shallow pore fluids (Schieber, 1989c). Based on framboidal textures, a general lack of base metal enrichments, and S isotopes, several authors have extended these arguments to suggest water-column precipitation of pyrite from euxinic bottom waters (Lyons et al., 2000; White et al., 2014). A secondary diagenetic phase, especially prevalent in the USZ, formed overgrowth rims and coarse cements of pyrite. Sulfur isotope data implies the sulfur for these secondary pyrites was sourced from seawater (Zieg and Leitch, 1999). Some galena and sphalerite phases occurring in the USZ are tied to diagenetic fluids, but these minerals are not prevalent especially when compared to surrounding non-mineralized strata; Pb and Zn are not yet recognized in economic concentrations (Graham et al., 2012; White et al., 2014).

Although many Co-Ni-As-Cu rich sulfides formed relatively early during diagenesis in the USZ, a third mineralization event prior to lithification in both zones created most of the chalcopyrite as well as some chalcocite, bornite, tennenite, cobaltite, and chlorite (LSZ only) while remobilized base metals in the USZ formed siegenite (White et al., 2014). The LSZ contains a higher percentage of chalcopyrite than the USZ, although more mineralization results in a higher tonnage for the USZ. Thermodynamic calculations suggest these hydrothermal fluids were between 125°C and 225°C (White et al., 2014). In late post-lithification events, dolomite and ankerite (USZ only) precipitated within the mineralized zones (Graham et al., 2012).

3.3 Methods

In this study, samples from near both the USZ and LSZ were collected and analyzed to understand the richness in iron mineralization processes in the Newland Formation in this part of the Belt basin (Fig. 3.2.) Twenty-five quarter-core block samples were collected in July 2013 from 4 different cores housed in the Tintina Resources, Inc. core shed, White Sulphur Springs, MT. Samples were cut using a non-magnetic brass blade into 3 cm by 2 cm billets, and made into polished thin or thick sections for further analyses. Table 3.1 summarizes the sample data for the 11 samples from 10 quarter-cores that were analyzed in detail.

Non-destructive rock magnetic experiments were performed on thick sections or billets returned from thin sections for all 11 samples using a 2G Enterprises SQuID magnetometer following the RAPID protocols, and analyzed using the RAPID Matlab (The Mathworks, Inc.) scripts (Kirschvink et al., 2008). The RAPID protocol used here includes measurements of alternating field (AF) demagnetization of the natural remanent magnetization (NRM), anhysteretic remanent magnetization (ARM) acquisition and demagnetization, isothermal remanent magnetization (IRM) acquisition and demagnetization, backfield IRM acquisition, and rotational remanent magnetization (RRM) acquisition and demagnetization. Combined, these measurements quantify fundamental properties that can be used to distinguish different ferromagnetic minerals present in the samples (e.g. Peters and Dekkers, 2003). The destructive rock magnetic technique of KappaBridge thermal susceptibility was measured on neighboring specimens for one sample using an AGICO MFK1-FA KappaBridge and resulting data were analyzed in Matlab. Ultra-high resolution scanning SQuID Microscopy (UHRSSM) was performed on 5 of the sections with 100 μm pixels after giving them an IRM to locate and image ferromagnetic grains at the microscale.

Additional chemical imaging techniques were employed to study the non-magnetic iron- and sulfur-bearing mineral phases. Transmitted and reflected light microscopy was used to observe petrographic textures and preliminarily identify mineralogy. High-energy synchrotron-based microprobe X-ray ray fluorescence (XRF) at 13500 or 20200 eV was used to map elemental abundances with 35 μm pixels across regions in 10 representative sections at beamline 10-2 at the Stanford Synchrotron Radiation Lightsource. Additionally, synchrotron-based X-ray near-edge absorption spectroscopy (XANES/XAS) at sulfur energies (2400-2500 eV) was paired with redox imaging at the S K-edge using a new lower energy X-ray microprobe (beamline 14-3) to collect both full spectra and multiple energy maps with 4 μm resolution and determine the mineral chemistry (oxidation state, orbital electronics, type and number of neighbors) while retaining textural information. Differences in the shape of these K-edge absorption spectra allow us to easily distinguish between a wide range of materials (Fleet, 2005; Mosselmans et al., 1995). Paired with end-member XANES spectra, the absorptions at multiple excitation energies in diagnostic regions of the XANES spectrum were collected and fit to create large maps of the mineralogy in samples. Principle component analysis of this multiple energy data was used to target and check for additional minerals. Chalcopyrite and pyrrhotite have similarities in their S K-edge spectra and thus the elemental maps made by high-energy XRF at 10-2 were used to evaluate the abundance of Cu. Synchrotron XANES and XRF analyses were performed at the Stanford Synchrotron Radiation Lightsource. Additional petrographic observations and mineral identifications were made using a ZEISS 1550VP FESEM, scanning electron microscope in the Caltech GPS Division Analytical Facility. This instrument is paired with an Oxford X-Max SDD X-ray Energy Dispersive Spectrometer (EDS) system and was used to determine X-ray spectra of elemental abundance at sub-micron sized spots on 3 thin sections to confirm the presence of chalcopyrite and galena implied from synchrotron data.

3.4 Results

Rock magnetic techniques both confirmed previous observations (Graham et al., 2012; White et al., 2014) and highlighted the presence of iron mineralization not previously described in the Newland Formation shales at the Black Butte Deposit.

3.4.1 Rotational Remanent Magnetization (RRM)

The presence of RRM can be used to identify magnetic iron-sulfide phases like pyrrhotite, although the sensitivity limits are not well understood (Snowball, 1997; Thomson, 1990). RRM is acquired during the application of an alternating field of 90 mT (950 Hz) perpendicular to the spin axis of a sample while it is rotating at a given speed. Studies have shown that B_{RRM} (normalized field strength of acquired RRM) varies with speed and direction of rotation so the sample is rotated clockwise and counterclockwise from 0 to 20 revolutions per second, rps (e.g. Suzuki et al., 2006). Two samples, T029-56 and T095-140.36, indicated strong evidence for magnetic iron sulfides, $B_{RRM} > \pm 20\ \mu T$ at 5 rps (Potter and Stephenson, 1986; Suzuki et al., 2006), while the rest of the samples showed no signs of RRM with $B_{RRM} \approx 0$ (Fig. 3.3A). Importantly, UHRSSM imaging revealed the ferromagnetic grains in these two samples to be located in epoxy-filled holes (Figs. 3.4CD) created either for standard emplacement of a pyrite grain for textural S isotope analyses (Present et al., in review) or to fill porous textures when making thin sections, demonstrating that these grains are contaminants (metal alloys can produce strong RRM, Snowball, 1997). Thus, there is no evidence of magnetic iron sulfides in the Newland Formation, including the mineralized zones associated with the Black Butte Deposit.

3.4.2 Coercivity of Remanence Acquisition

The coercivity of remanence acquisition ($H_{cr'}$), defined as the magnetic field required to permanently flip half of the magnetic moments in a mineral, is a useful property to differentiate ferromagnetic minerals (Peters and Dekkers, 2003). Overall a measurement of how easily a mineral becomes magnetized, it is determined by taking the derivative of the acquisition of IRM curve and deconvolving the spectra into distinct peaks of different field strengths, which are the different coercivities of the mineral assemblage (Heslop et al., 2002; Robertson and France, 1994). Goethite is easily identified with coercivities over 1000 mT, and the range of 140-800 mT is unique for hematite. However, extensive data collection has shown that the coercivity ranges for hematite, magnetite, titanomagnetite, greigite, and pyrrhotite overlap between 16-140 mT—though the averages of hematite (270 mT), pyrrhotite (53 mT), greigite (75 mT) are higher than those for magnetite and titanomagnetite (30 mT). Thus mineral identifications solely using $H_{cr'}$ for identification have some margin of error and benefit from additional analyses (Table 3.2).

Notably, three groups of ferromagnetic mineralogy can be separated based on H_{cr}' and stratigraphic/lithologic information (Fig. 3.3B). All of the samples collected far outside the strongly mineralized sulfide zones (T095-38, T095-53, T112-334, T112-384) primarily contain finely disseminated pyrite and show very similar mid-coercivity peaks interpreted to be magnetite. Sample T095-38 also shows a striking high-coercivity goethite peak; this sample contains fractures mineralized with oxides seen in hand sample and described in the core log for this stratigraphic height. Sample T029-61.21 has early diagenetic pyrite textures with minimal secondary recrystallization and contains the same magnetite mid-coercivity peak as the four samples described above. The other three samples exhibiting early diagenetic textures (T029-56, T029-140.36, T095-389), including the two samples with known ferromagnetic contamination, have slightly higher coercivity spectra. While T095-389 did not show RRM, it does have an epoxied hole with a standard, which could be contaminated by a ferromagnetic mineral/alloy similar to samples T029-140.36 and T095-389. Therefore we interpret the characteristic slightly higher H_{cr}' peak of these three samples to be due to contamination and not representative of early textures. Lastly, three samples display multiple generations of sulfide-bearing minerals including late displacive and replacive textures (T095-156, T101-389, T101-390). These samples show a range of mid- to low-coercivity spectra suggesting larger grain size and/or multi-domain magnetite (Peters and Dekkers, 2003).

3.4.3 Lowrie-Fuller Test

To further examine the grain size and magnetic domain state, we employed a rock magnetic technique called the Lowrie-Fuller test—a measure of ferromagnetic grain size based on the relative stability of IRM versus ARM to applied demagnetizing AF (Lowrie and Fuller, 1971; Xu and Dunlop, 1995). In single domain grains, ARM is more stable and less easily demagnetized than IRM, while in larger multidomain grains, IRM is more stable and less easily demagnetized using AF than ARM. Although the exact physics are poorly understood, if the ARM is consistently stronger than the IRM then single domain or pseudo single domain (<10 μm) particles probably represent the majority of the magnetized minerals in a sample. While most of the samples appear to contain single-domain or pseudo-single domain particles, T095-156 (which had low coercivity spectra) does contain multi-domain grains (Fig. 3.3C). T095-38 also is shown to contain multi-domain grains, but this sample contains goethite, which would bias the Lowrie-Fuller test toward multi-domain results. From this data, multi-domain magnetite is more common in samples with replacive textures suggesting it could have formed from recrystallization or authigenic precipitation—this can be tested if it shows a chemical remanent magnetization.

3.4.4 Fuller Test of NRM

Magnetite appears to be the primary ferromagnetic component in the majority of the Newland Formation shale samples. As a result, we can apply a useful rock magnetic experiment called the Fuller Test of NRM to determine if the magnetization carried by the magnetite is detrital or chemical in origin. This test uses the ratio of the NRM:IRM compared to empirical calibrations and synthetic ARM:IRM relationships of a given sample (Fuller et al., 1988; Fuller et al., 2002). Empirical calibrations on rocks with magnetite as the primary ferromagnetic mineral suggest that the weak NRM:IRM ratios of 1:1000 occur in sedimentary rocks with detrital remanent magnetization formed during primary deposition and ratios of 1:10 represents chemical remanent magnetization when magnetite has grown *in situ* or authigenically in a sample (Fuller et al., 2002). The ARM:IRM curve is used for comparison to demonstrate which changes in the shape of the curve are characteristic of the sample. Most samples of the Newland Formation show an NRM:IRM ratio of 1:1000, which is consistent with weak detrital remanent magnetization (Fig. 3.3D). T112-334 shows indication of chemical remanent magnetization, in which magnetite is an authigenic phase that either grew during early diagenesis or during a later diagenetic mineralization. UHRSSM maps showed the locations of disperse dipoles of ferromagnetic grains throughout samples in fine-grained material, located close to and far from secondary cross-cutting textures, consistent with a detrital origin (Figs. 3.4AB). However, due to the sub-micron size of these grains, the ferromagnetic minerals in the regions with dipoles could not be visualized via petrography.

3.4.5 KappaBridge Thermal Susceptibility

To further study the magnetite, a neighboring sample from T101-389 was used for destructive thermal susceptibility experiments using a KappaBridge. Powdered rock was slowly heated from -190°C to 700°C and then cooled to 40°C while the susceptibility from a weak induced field was measured at 20 second intervals. Susceptibility measures the ability of a sample to be magnetized in the presence of an applied field. Thus it is a magnetic measurement that integrates the entire assemblage of minerals in a sample, although ferromagnetic minerals usually dominate the signal. Changes in susceptibility during heating and cooling are produced by mineralogical transformations within the sample. A drop in susceptibility at 580°C indicates the presence of magnetite as it becomes paramagnetic at its Curie temperature (Fig. 3.5A). The low-temperature Verwey transition typical for magnetite at -150°C as it transforms from weakly magnetic monoclinic magnetic structure and to ferromagnetic cubic structure was not observed in this sample; either it was suppressed due to low abundance with other phases dominating the signal, or the magnetite contains a small weight percent titanium (Kozłowski et al., 1996; Moskowitz et al., 1998). A slight drop in susceptibility at 80°C is suggestive of goethite decomposing and reacting with sulfur to form pyrite or decomposition of titanomagnetite (Charilaou et al., 2011; Minyuk et al., 2013). Although the typical pyrite/chalcopyrite decomposition peak to magnetite is not seen (Li and Zhang, 2005; Minyuk et al., 2013), some new magnetite and a substantial amount of pyrrhotite were formed after heating to 700°C in an argon atmosphere based on the fact that the cooling curves increase in susceptibility during cooling with distinct peaks at 580°C and at 320°C the respective Curie temperatures for those minerals (Fig. 3.5B). The creation of these minerals suggests there were non-magnetic iron sulfides in these samples that transformed into magnetic minerals during the heating process.

3.4.6 X-ray Spectroscopy

Iron sulfide phases were visually identified in all of the samples using light microscopy. We used X-ray spectroscopy, specifically XANES and XRF, to evaluate the exact chemical composition and crystal structure of these phases (Table 3.2). Ferrous disulfide was identified as the major sulfide-bearing phase in all the samples (Fig. 3.6). The ferrous disulfide minerals marcasite and pyrite have similar S K-edge spectra using XANES and can only be readily distinguished by the Fe L-edge (Mosselmans et al., 1995) or X-ray diffraction, which were not measured here. However, petrography shows that the disulfides phases present in these samples are pyrite. Chalcopyrite was observed as a major component of T101-389 (Figs. 3.4E, 3.6). Sulfate salts were also identified in many of the samples including laths of barite that show differential compaction of sedimentary laminae (Figs. 3.4F, 3.6). However, in the samples with disseminated pyrite, small domains of sulfate (10-20 μm in size) were found both alone and associated with pyrite, suggesting some of the sulfate minerals could be iron sulfates instead of barite (Figs. 3.4GH, 3.6). EDS and high-energy XRF maps were used to confirm the presence of chalcopyrite (as opposed to pyrrhotite); however, the XRF maps also highlight interesting patterns in base metal mineralization. Some replacive pyrite grains contain greater amounts of As, Pb, Zn, or Cu (Figs. 3.7DEG), while other regions hosted chalcophile metals as dominant cations in sulfide phases like Cu in chalcopyrite (Figs. 3.7A-F,H). Microprobe X-ray spectroscopy paired mapping capabilities, coupled with traditional petrographic and bulk chemical techniques, provide an exciting new tool for mineral analysis opening new avenues for inquiry into trace metal abundances, redox states and gradients, and mineral phase identification.

3.5 Discussion and Conclusions

Bulk rock magnetic techniques employed in this study confirm the absence of pyrrhotite in shales of the Newland Formation near the Black Butte Deposit, in contrast to its ubiquitous presence in correlative units at higher metamorphic grades to the northwest (Slotznick et al., 2016). This result confirms that these rocks have not been heated to very high temperatures, and while hydrothermal fluids did cause overprinting and recrystallization of sulfide phases, no pyrrhotite was formed with this mineralization. This is important for bulk geochemical studies such as iron speciation (Planavsky et al., 2011) because pyrrhotite may be misplaced in sequential chemical extraction with the magnetite fraction and/or result in incorrect iron calculations due to its unique chemistry during the pyrite extraction—both could make a basin appear more ferruginous than it was by incorrectly identifying the iron mineralogy (Asael et al., 2013; Schumann et al., 2012)). Samples collected far outside the massive sulfide mineralization zones contain early diagenetic disseminated pyrite grains (Schieber, 1989a); copper, zinc, and lead sulfides are rare in these areas but their presence still signals some mineralization extends beyond the regions of economic interest. Sulfide phases tied to these hydrothermal fluids should be taken into account when using Belt strata to interpret the ancient redox conditions and processes operating in the Belt Basin, because these phases show iron was mobile and likely advected from elsewhere in the sediment pile. The hydrothermal fluids could have also sourced iron for some of the magnetite present in the samples and/or been responsible for recrystallization processes.

The identification of magnetite in Newland Formation shales provides important insights into the redox character and mode of iron delivery in this part of the Belt Basin. Rock magnetic experiments indicate that magnetite is primarily detrital in origin, with limited evidence for authigenic magnetite in some samples. Though pyrite is commonly the most abundant iron-bearing mineral present in these diagenetically stabilized lithologies, detrital magnetite represents an important sedimentary vector for iron delivery to this basin that is not a direct measure of redox conditions in seawater. Furthermore, detrital iron oxides might bias iron speciation data toward compositions that appear more anoxic and ferruginous (Planavsky et al., 2011); during deposition Belt Basin waters could have either been more oxic or more euxinic depending on the relative abundances of these oxides and other iron-bearing minerals. Petrography and X-ray imaging reveal that pyrite is ever-present as small framboids and disseminated grains exhibiting textures that are consistent with the formation of much of this pyrite in the water column or in sediments during early diagenesis (Graham et al., 2012; Schieber, 1989a; Wilkin et al., 1996). We speculate that detrital iron oxides were an important source of reactive iron for early pyrite formation (e.g. Canfield and Berner, 1987; Reynolds et al., 2000; Schieber, 1989c). Many samples (not just limited to economically meaningful sulfide mineralization zones) show additional sulfide phases in late diagenetic textures that mark iron sourced by hydrothermal fluids. If iron sources did not limit early pyrite formation more broadly, perhaps this was limited by the abundance of H_2S in the bottom water, bacterial sulfate reduction/sulfur oxidation rates, and/or sedimentation rates. More work is needed to better understand the interplay between these factors (Present et al., in review), but what is clear at present is that we do not see clear evidence for the ferruginous water column conditions during the depositional of Newland Formation shales put forward on the basis of iron speciation data (Planavsky et al., 2011).

Based on our observations, we hypothesize that bottom waters in Helena Embayment during the deposition of the Newland Formation were suboxic or possibly euxinic (Gellatly and Lyons, 2005; Lyons et al., 2000), and that detrital fluxes played an important role in delivery of iron into the Helena Embayment, much of which was transformed into pyrite during sulfate reduction associated with early diagenesis of these organic-rich sediments (Lyons et al., 2000; Strauss and Schieber, 1990). This is a similar mode of iron deposition and pyrite production today in modern euxinic basins and anoxic pore waters in marine sediments (e.g. Berner, 1984), and implies a degree of continuity of redox conditions and processes operating in large sedimentary basins over the past one and a half billion years.

3.6 Acknowledgements

We thank John Grotzinger, Ted Present, Andy Knoll, Ken Williford, and the members of the 2013 Agouron Field Course for assistance with sample collection. Support for this work was provided by the Agouron Institute, Tobacco

Root Geological Society Scholarship, Belt Association Student Research Grant, the David and Lucile Packard Foundation (W.W.F.), NSF Graduate Research Fellowship program (S.P.S.), and NASA Earth and Space Fellowship (S.P.S.). Portions of this research were carried out at the Stanford Synchrotron Radiation Lightsource, a Directorate of SLAC National Accelerator Laboratory and an Office of Science User Facility operated for the U.S. Department of Energy Office of Science by Stanford University.

3.7 Tables

Table 3.1: Detailed Sample Data

Sample Name	Drill Core	GPS of Drill Core Collar	Sulfide Zones	Depth of Billet (m)	Stratigraphy	Description
T029-56	SC11-029	N 46° 46' 54.8" W 110° 54' 46.33"	USZ, LSZ	56.475-56.50	Upper Newland right above USZ	Early unfilled circular tube network of iron sulfides 1-4mm in diameter with .5mm thick walls in larger massive sulfide zone
T029-61.21	SC11-029	N 46° 46' 54.8" W 110° 54' 46.33"	USZ, LSZ	61.205-61.235	Upper Newland right above USZ	Early diagenetic barite laths with differential compaction of laminated dolomitic shale with intergrown sub-parallel iron sulfide blebs rimmed with altered barite
T095-38	SC11-095	N 46° 46' 44.76" W 110° 55' 32.7"	USZ	38.70-38.76	Upper Newland far above USZ	Grey laminated silty dolomitic shale with abundant dolomite veins and iron oxide along fracture surfaces
T095-53	SC11-095	N 46° 46' 44.76" W 110° 55' 32.7"	USZ	53.50-53.56	Upper Newland far above USZ	Black laminated dolomitic shale with disseminated iron sulfides
T095-140.36	SC11-095	N 46° 46' 44.76" W 110° 55' 32.7"	USZ	140.375-140.405	Upper Newland	Early diagenetic iron sulfide nodules with differential compaction, laminae, and wavy laminae in larger massive sulfide zone, minor altered barite
T095-156	SC11-095	N 46° 46' 44.76" W 110° 55' 32.7"	USZ	156.815-156.845	Upper Newland	Large iron sulfide bleb within cross-cutting late iron sulfide band in micro-faulted grey laminated dolomitic shale
T095-389	SC11-095	N 46° 46' 44.76" W 110° 55' 32.7"	USZ	389.22-389.255	Upper Newland right above USZ	Grey laminated dolomitic shale with small debris flows and early iron sulfide broken tubes, complete to disaggregated framboids, and fine-grained laminations
T101-389	SC12-101	N 46° 46' 53.15" W 110° 54' 21.17"	LSZ	389.935-389.96	Lower Newland in LSZ	Multiple generations of cross-cutting sulfides (up to 3mm blebs) in heavily recrystallized dolomite and shale within larger massive sulfide zone
T101-390	SC12-101	N 46° 46' 53.15" W 110° 54' 21.17"	LSZ	390.085-390.11	Lower Newland in LSZ	Multiple generations of cross-cutting sulfides in heavily recrystallized dolomite and shale within larger massive sulfide zone
T112-334	SC12-112	N 46° 46' 51.53" W 110° 53' 58.67"	LSZ	334.62-334.64	Lower Newland in Volcano Valley Fault Shear Zone	Black laminated shale with disseminated iron sulfides
T112-384	SC12-112	N 46° 46' 51.53" W 110° 53' 58.67"	LSZ	384.43-334.49	Lower Newland right below LSZ	Sheared black and grey silty shale with intergrown iron sulfide blebs (<1mm) and disseminated iron sulfides

Table 3.2: Mineralogical Identifications from Samples of Newland Formation from Black Butte Deposit

Sample name	Bulk Techniques				S XANES and EDS							High-Energy XRF*			
	Mag	**Goe**	**Pyr**	**Cont**	**Py**	**Pyr**	**FerS**	**CuPy**	**Cov**	**Gal**	**SO4**	**AsPb**	**Cu**	**Zn**	**Ni**
T029-56				X	X†			X†	X†	X†		X	X	t	
T029-61.21	X				X						X	t	X	X	
T095-38	X	X										X	X	X	t
T095-53	X				X						X	X	X	X	t
T095-140.36				X								X			
T095-156	X				X							t			
T095-389				X	X†			X†	X†	X	X	X			
T101-389	X				X		X	X				X	X	X	
T101-390	X											X	X	t	
T112-334	X				X						X	X	X	X	t
T112-384	X											t	t		t

Abbreviations: XANES = X-ray Absoption Near Edge Spectroscopy, EDS = X-ray Energy Dispersive Spectroscopy, XRF = X-ray Fluorescence, Mag = Magnetite, Goe = Goethite, Pyr = Pyrrhotite, Cont = Contamination, Py = Pyrite, FerS =Ferric Disulfide, CuPy = Chalcopyrite, Cov = Covellite, Gal = Galena, SO4 = Sulfate often Barite, AsPb = Arsenic and/or Lead

*For XRF, t=trace, X = important mineral constituent

† Data from Present et al., in review based on reflected light petrography

3.8 Figures

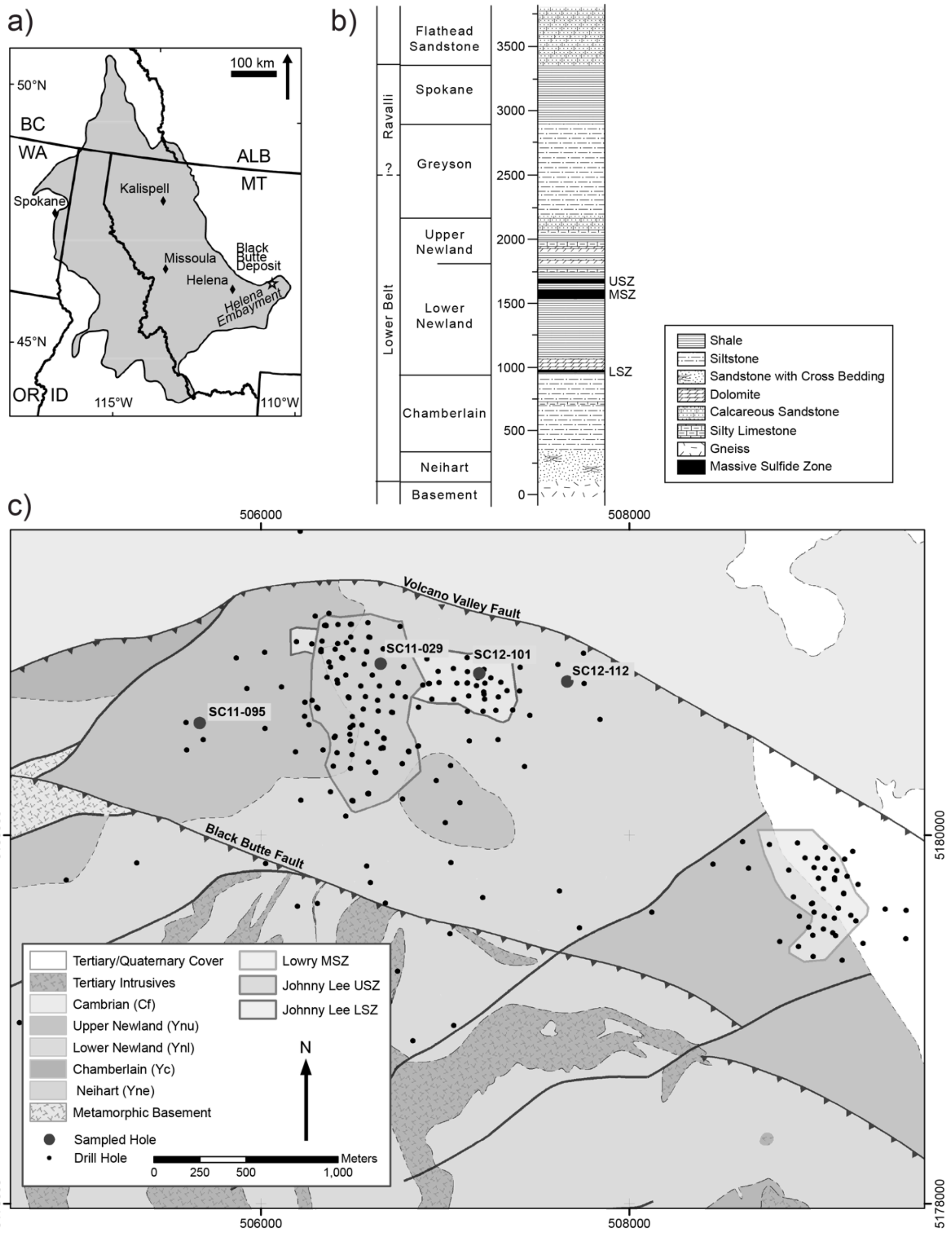

Figure 3.1: a) Map showing the extent of Belt Supergroup outcrops and the location of the Black Butte Deposit within the Helena Embayment. b) General stratigraphic column of Belt Supergroup strata in the Black Butte Deposit region of the Helena Embayment with height in meters. Note: USZ = Upper Sulfide Zone, MSZ = Middle Sulfide Zone, LSZ = Lower Sulfide Zone. c) Geologic Map of the Black Butte Deposit region with locations of all drill cores drilled by Tintina Resources Inc. and Cominco American Inc. and labels for the drill cores that were sampled in this study.

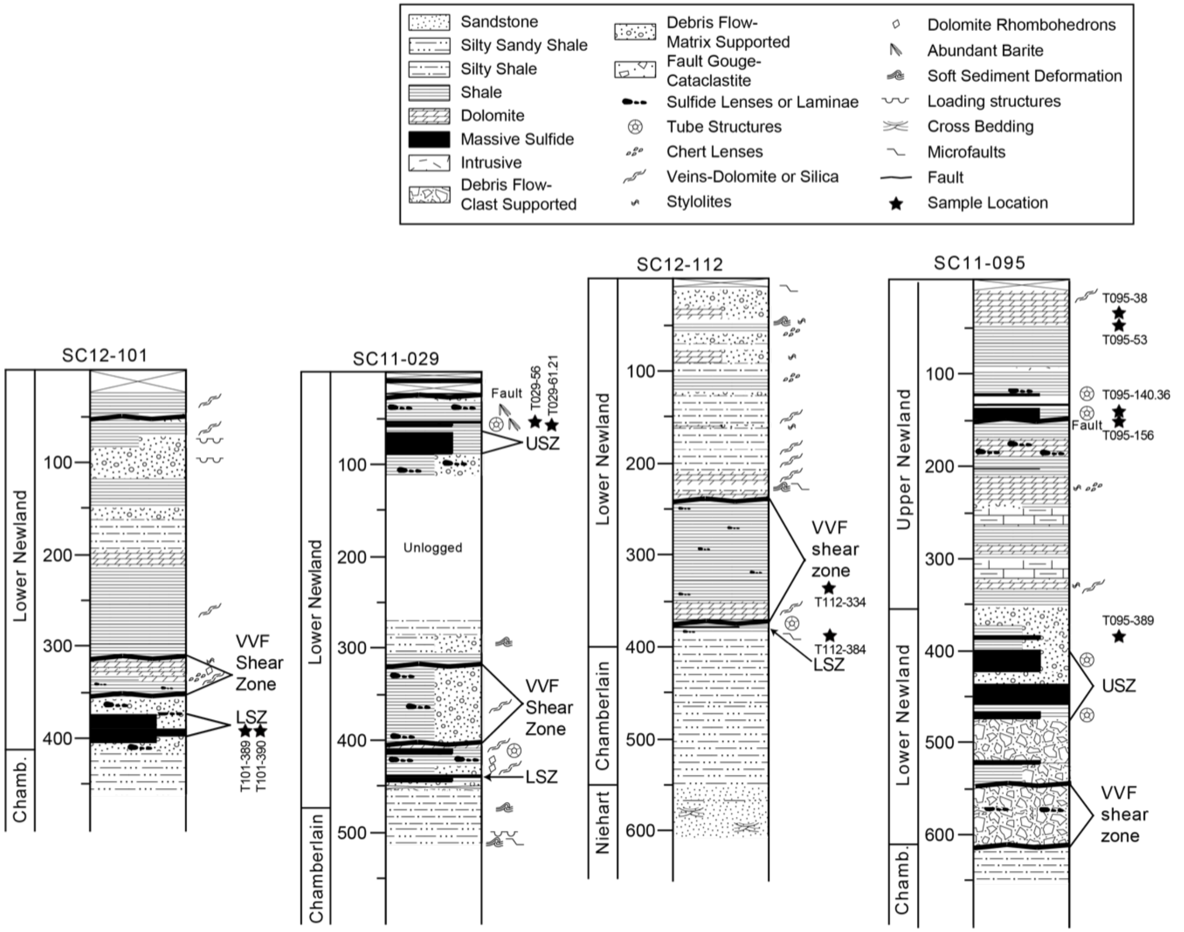

Figure 3.2: Lithostratigraphic columns of the drill cores from the Black Butte Deposit area examined in this study. Labeled black stars mark the stratigraphic positions of samples analyzed. Cores are not aligned by stratigraphic datum, and core depth is in meters.

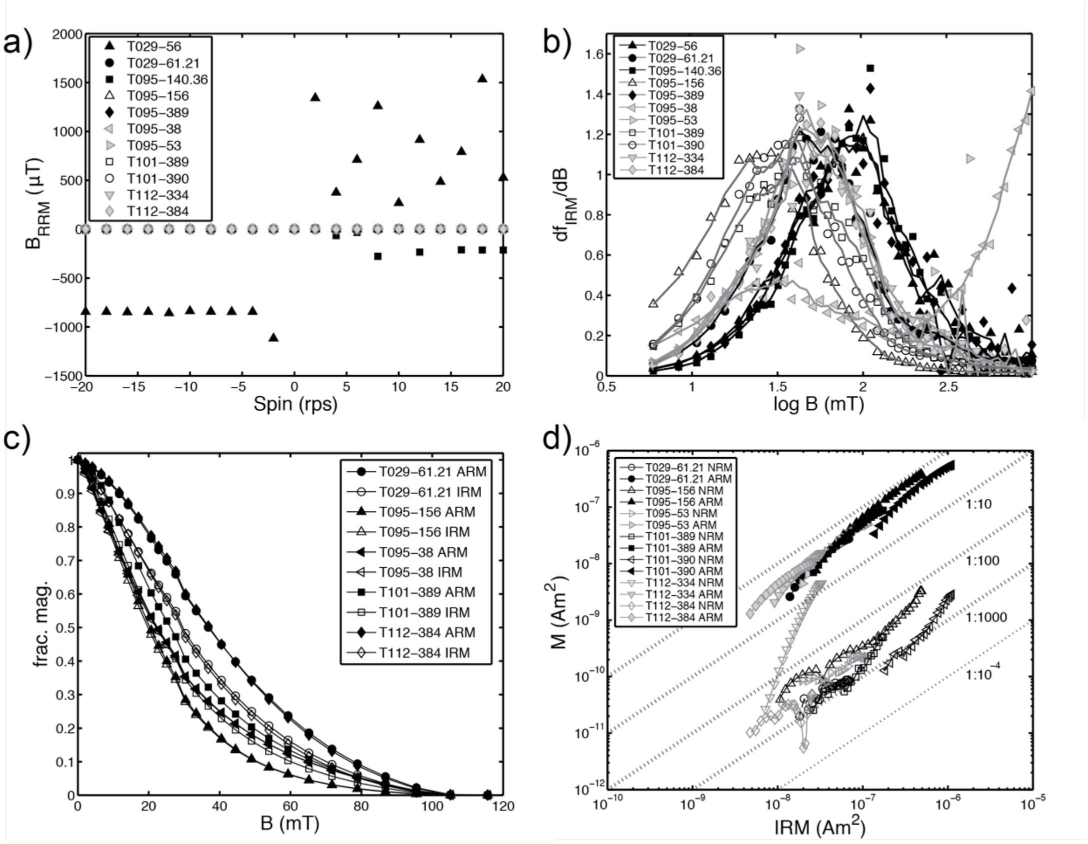

Figure 3.3: Rock magnetic data from shale samples of the Newland Formation. a) Rotational remanent magnetization (RRM) data to assess the presence or absence of magnetic iron sulfide phases. Negative spin speed indicated counter-clockwise rotation around the spin axis when the perpendicular alternating field is applied. All 11 samples are plotted, but only 2 of the samples are clearly visible since most of the samples have $B_{RRM} \approx 0$ at all spin speeds. b) Data showing the derivative of the isothermal remanent magnetization (IRM) of all samples to determine the coercivity of remanence (H_{cr}') and from this information the ferromagnetic mineralogy. The applied field (B, x-axis) at the peaks of the spectra is the H_{cr}'. c) Results of representative samples from the Lowrie-Fuller test to inform domain state and grain size based on the relative strength of the IRM vs. the ARM curves as measured by the fraction of total magnetization (frac. mag., Y-axis) when a specific demagnetizing field is applied (B, x-axis). d) Results from the Fuller test to provide insight into the origins (detrital, chemical, thermal) of magnetization based on the ratio of the NRM (y-axis) to IRM (x-axis). The ratio of ARM:IRM is also plotted using the same axes.

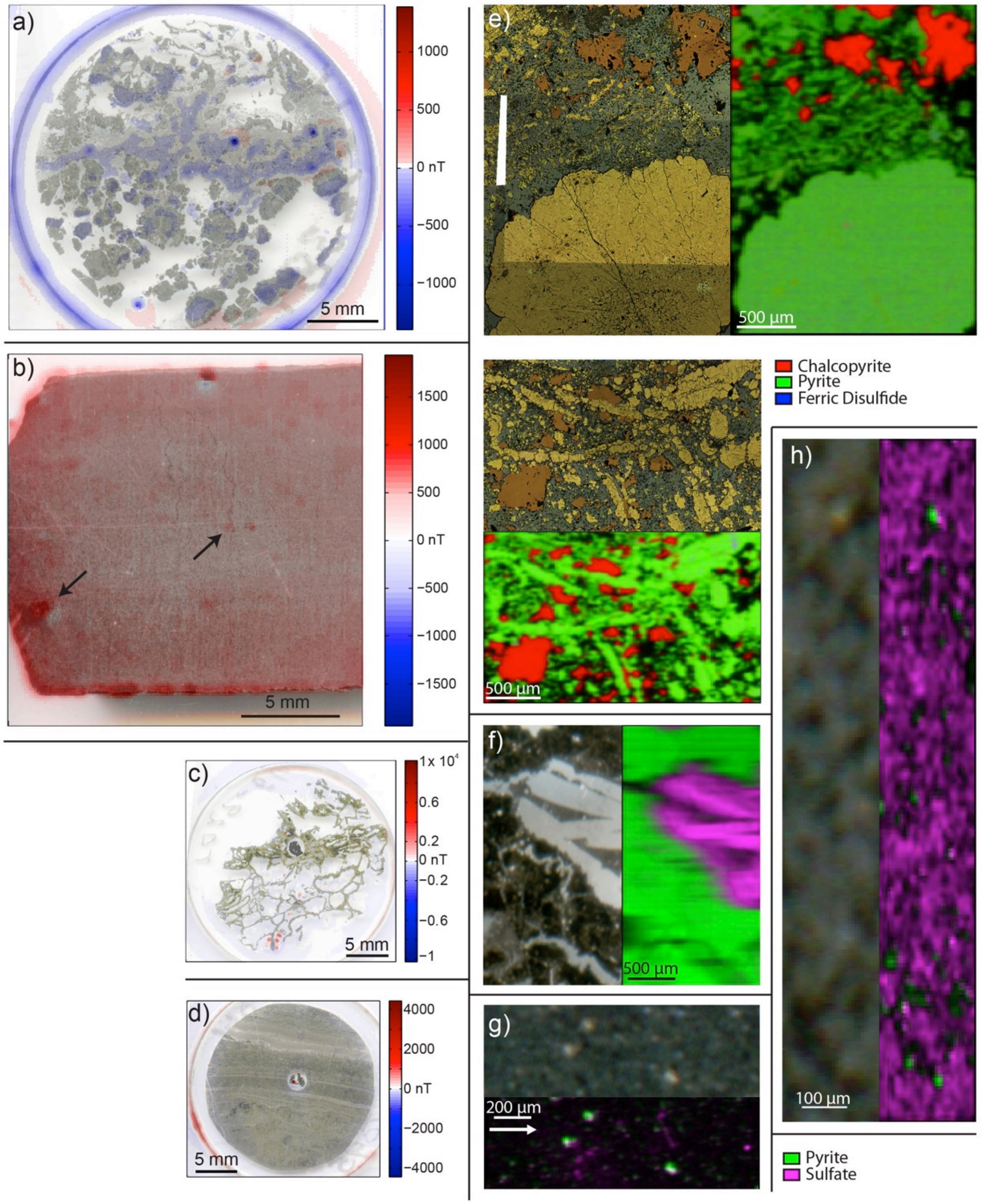

Figure 3.4: Parts a-d show UHRSSM magnetic microscopy images of ferromagnetic minerals. Hot and cool colors reflect magnetic vectors out of and into the page, respectively. a) Map of T101-389 showing scattered dipoles focused in fine-grained regions. b) Scattered dipoles including some that trend with post-depositional crosscutting features, such as pointed out by arrows, in T112-334. c) Image of T029-56 showing dipoles in epoxied holes around iron sulfide tube network that reflect contaminant phases introduced via standard preparation. d) Map of T095-140.36 showing single strong dipole in epoxied drill

hole with pyrite standard that reflect contaminant phases introduced during preparation. Parts e-h show paired reflected light microscopy or photograph on the left-top and multiple-energy maps fit to minerals using end-member S XANES spectra on the right-bottom. Samples are oriented with correct up direction; an arrow marks the up direction for part c e) Two mapped regions of T101-389 contain multiple generations of sulfide phases including chalcopyrite, pyrite, and a unique ferric disulfide. f) Map of T026-61.21 with barite laths surrounded by early diagenetic pyrite in layers. g) Disseminated pyrite grains with associated sulfate and distinct sulfate domains in T095-53. h) Disseminated pyrite with low abundance sulfur in matrix in T112-334. Scale bar provided for each image or image pair.

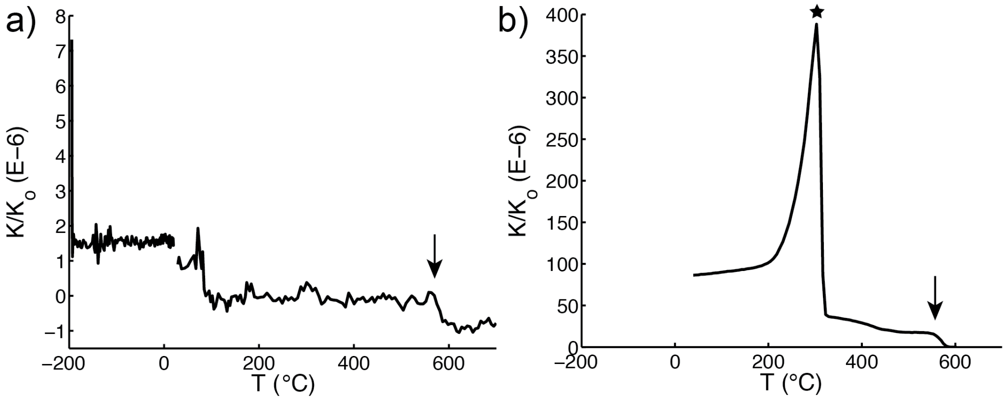

Figure 3.5: KappaBridge results for a representative shale sample, T101-389. a) Magnetic susceptibility during heating from -190°C to 700°C. b) Magnetic susceptibility during cooling from 700°C to 23°C. Note the different y-axis scale as there is increased susceptibility during this cooling phase. Data are normalized to the blank, an empty specimen holder measurement. Arrows mark the Curie temperature of magnetite (580°C) while the star marks the Curie temperature of pyrrhotite (320°C)

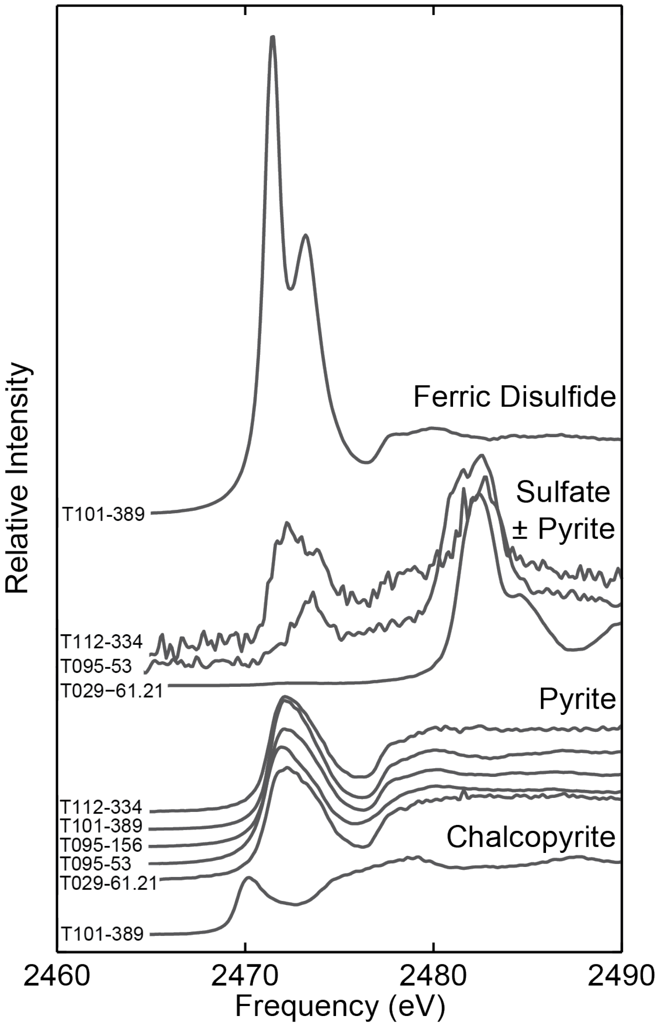

Figure 3.6: Synchrotron S K-edge XANES spectra for phases identified in all samples. An unnamed unique mineral, a ferric disulfide not previously found in natural samples, is identified based off its K-edge spectra, which shows Fe^{+3} bonding with di-sulfide valence sulfur.

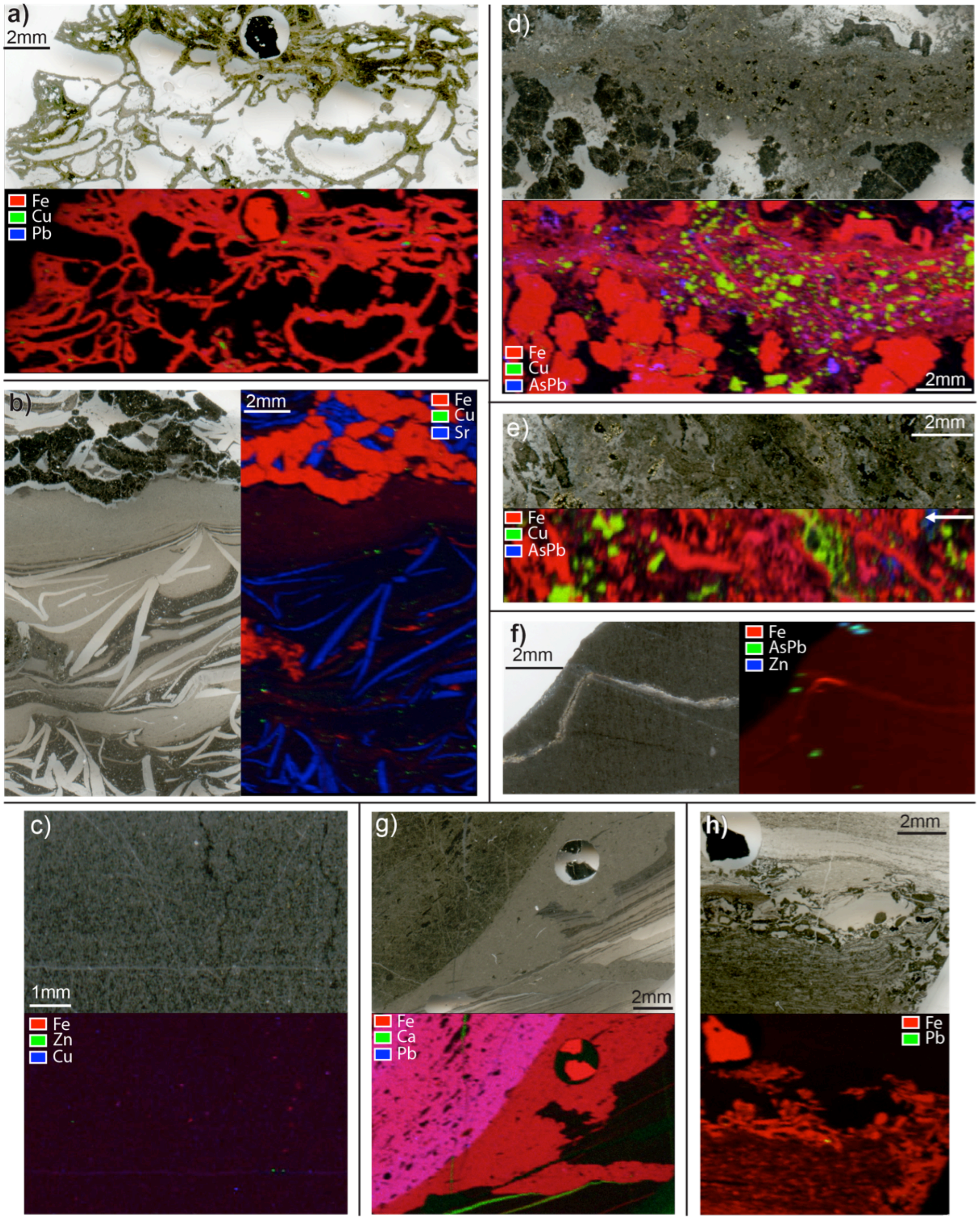

Figure 3.7: High-Energy XRF maps of metal abundances (right-bottom) shown alongside a light scan of a given sample in thick or thin section (left-top). Samples are oriented with correct up direction; an arrow marks the up direction for part e. a) Unfilled tubular network of iron sulfide cements with small inclusions of Pb- and Cu-bearing minerals in T029-56. b) Early diagenetic and recrystallized barite containing trace Sr with sub-parallel pyrite blebs and small Cu-bearing minerals in T029-61.21. c) Disseminated pyrite with distinct Zn and Cu minerals that show mineralization associated both along lamination and crosscutting features in T112-334. d) Multiple generations of sulfides including

pyrite and chalcopyrite with As- and Pb-rich grains, zones of finely disseminated grains, and zones within euhedral grains in T101-389 e) Closer look at multiple generations of iron sulfides and chalcopyrite with As- and Pb-rich grains and zones in larger grains in T101-390. f) Dolomite vein containing iron oxide with As-, Pb-, and Zn-rich minerals associated with smaller non-dolomitized fractures and/or laminations in T095-38. g) Vertical dolomitic veins cut Pb-rich pyrite bleb within a crosscutting pyrite aggregate in a laminated dolomitic shale in T095-156. h) Intraformational detrital iron sulfides parallel to, and deforming shale laminates with small amounts of galena in T095-389.

3.9 References

Asael, D., Tissot, F. L., Reinhard, C. T., Rouxel, O., Dauphas, N., Lyons, T. W., Ponzevera, E., Liorzou, C., and Chéron, S., 2013, Coupled molybdenum, iron and uranium stable isotopes as oceanic paleoredox proxies during the Paleoproterozoic Shunga Event: Chemical Geology, v. 362, p. 193-210.

Berner, R. A., 1984, Sedimentary pyrite formation: an update: Geochimica et Cosmochimica Acta, v. 48, no. 4, p. 605-615.

Brocks, J. J., Buick, R., Summons, R. E., and Logan, G. A., 2003, A reconstruction of Archean biological diversity based on molecular fossils from the 2.78 to 2.45 billion-year-old Mount Bruce Supergroup, Hamersley Basin, Western Australia: Geochimica et Cosmochimica Acta, v. 67, no. 22, p. 4321-4335.

Canfield, D., 1998, A new model for Proterozoic ocean chemistry: Nature, v. 396, no. 6710, p. 450-453.

Canfield, D. E., and Berner, R. A., 1987, Dissolution and pyritization of magnetite in anoxie marine sediments: Geochimica et Cosmochimica Acta, v. 51, no. 3, p. 645-659.

Charilaou, M., Löffler, J., and Gehring, A., 2011, Fe–Ti-O exchange at high temperature and thermal hysteresis: Geophysical Journal International, v. 185, no. 2, p. 647-652.

Cloud, P. E., 1968, Atmospheric and Hydrospheric Evolution on the Primitive Earth: Science, v. 160, no. 3829, p. 729-736.

Craig, J. R., and Vokes, F. M., 1993, The metamorphism of pyrite and pyritic ores: an overview: Mineralogical Magazine, v. 57, no. 1, p. 3-18.

Deiss, C., 1935, Cambrian-Algonkian unconformity in western Montana: Geological Society of America Bulletin, v. 46, no. 1, p. 95-124.

Duke, E. F., and Lewis, R. S., 2010, Near infrared spectra of white mica in the Belt Supergroup and implications for metamorphism: American Mineralogist, v. 95, no. 7, p. 908-920.

Embley, T. M., and Martin, W., 2006, Eukaryotic evolution, changes and challenges: Nature, v. 440, no. 7084, p. 623-630.

Fleet, M. E., 2005, XANES spectroscopy of sulfur in earth materials: The Canadian Mineralogist, v. 43, no. 6, p. 1811-1838.

Fuller, M., Kidane, T., and Ali, J., 2002, AF demagnetization characteristics of NRM, compared with anhysteretic and saturation isothermal remanence: an aid in the interpretation of NRM: Physics and Chemistry of the Earth, v. 27, no. 25-31, p. 1169-1177.

Gellatly, A. M., and Lyons, T. W., 2005, Trace sulfate in mid-Proterozoic carbonates and the sulfur isotope record of biospheric evolution: Geochimica et Cosmochimica Acta, v. 69, no. 15, p. 3813-3829.

Graham, G., Hitzman, M. W., and Zieg, J., 2012, Geologic Setting, Sedimentary Architecture, and Paragenesis of the Mesoproterozoic Sediment-Hosted Sheep Creek Cu-Co-Ag Deposit, Helena Embayment, Montana: Economic Geology, v. 107, no. 6, p. 1115-1141.

Hall, A. J., 1986, Pyrite-pyrrhotine redox reactions in nature: Mineralogical Magazine, v. 50, p. 223-229.

Harrison, J. E., 1972, Precambrian Belt basin of northwestern United States: Its geometry, sedimentation, and copper occurrences: Geological Society of America Bulletin, v. 83, no. 5, p. 1215-1240.

Heslop, D., Dekkers, M., Kruiver, P., and Van Oorschot, I., 2002, Analysis of isothermal remanent magnetization acquisition curves using the expectation-maximization algorithm: Geophysical Journal International, v. 148, no. 1, p. 58-64.

Holland, H. D., 1984, The chemical evolution of the atmosphere and oceans, Princeton University Press.

-, 2006, The oxygenation of the atmosphere and oceans: Philosophical Transactions of the Royal Society B: Biological Sciences, v. 361, no. 1470, p. 903-915.

Horodyski, R. J., Winston, D., and Whipple, J. W., 1989, Paleontology of the middle Proterozoic belt supergroup, *in* Winston, D., Horodyski, R. J., and Whipple, J. W., eds., Middle Proterozoic Belt Supergroup, Western Montana: Great Falls, Montana to Spokane, Washington: 28th International Geological Congress, Field Trip Guidebook T334, p. 7-26.

Kirschvink, J. L., Kopp, R. E., Raub, T. D., Baumgartner, C. T., and Holt, J. W., 2008, Rapid, precise, and high-sensitivity acquisition of paleomagnetic and rock-magnetic data: Development of a low-noise automatic sample changing system for superconducting rock magnetometers: Geochemistry Geophysics Geosystems, v. 9, no. 5.

Knoll, A. H., Javaux, E. J., Hewitt, D., and Cohen, P., 2006, Eukaryotic organisms in Proterozoic oceans: Philosophical Transactions of the Royal Society B: Biological Sciences, v. 361, no. 1470, p. 1023-1038.

Kozłowski, A., Kakol, Z., Kim, D., Zalecki, R., and Honig, J., 1996, Heat capacity of Fe 3-α M α O 4 (M= Zn, Ti, 0⩽ α⩽ 0.04): Physical Review B, v. 54, no. 17, p. 12093.

Li, H. Y., and Zhang, S. H., 2005, Detection of Mineralogical Changes in Pyrite Using Measurements of Temperature-Dependence Susceptibilities: Chinese Journal of Geophysics, v. 48, no. 6, p. 1454-1461.

Lowrie, W., and Fuller, M., 1971, Alternating field demagnetization characteristics of multidomain thermoremanent magnetization in magnetite: Journal of Geophysical Research, v. 76, no. 26, p. 6339-&.

Luepke, J. J., 1999, Goechemical trends in shales of the Belt Supergroup, Northwestern US: a marine model for the evolution of the Mesoproterozoic weatern Laurentian Margin [M.S. thesis: University Missouri-Columbia, 133 p.

Luepke, J. J., and Lyons, T. W., 2001, Pre-Rodinian (Mesoproterozoic) supercontinental rifting along the western margin of Laurentia: geochemical evidence from the Belt-Purcell Supergroup: Precambrian Research, v. 111, no. 1, p. 79-90.

Lyons, T. W., Luepke, J. J., Schreiber, M. E., and Zieg, G. A., 2000, Sulfur geochemical constraints on Mesoproterozoic restricted marine deposition: lower Belt Supergroup, northwestern United States: Geochimica et Cosmochimica Acta, v. 64, no. 3, p. 427-437.

McGoldrick, P., and Zieg, J., Massive microbes from the Mesoproterozoic of Montana, *in* Proceedings 17th Australia Geological Geological Convention Hobart, Australia, 2004, Volume 73, p. 100.

Minyuk, P., Tyukova, E., Subbotnikova, T., Kazansky, A. Y., and Fedotov, A., 2013, Thermal magnetic susceptibility data on natural iron sulfides of northeastern Russia: Russian Geology and Geophysics, v. 54, no. 4, p. 464-474.

Moreau, M., Ader, M., and Enkin, R., 2005, The magnetization of clay-rich rocks in sedimentary basins: low-temperature experimental formation of magnetic carriers in natural samples: Earth and Planetary Science Letters, v. 230, no. 1, p. 193-210.

Moskowitz, B. M., Jackson, M., and Kissel, C., 1998, Low-temperature magnetic behavior of titanomagnetites: Earth and Planetary Science Letters, v. 157, no. 3, p. 141-149.

Mosselmans, J., Pattrick, R., Van der Laan, G., Charnock, J., Vaughan, D., Henderson, C., and Garner, C., 1995, X-ray absorption near-edge spectra of transition metal disulfides FeS2 (pyrite and marcasite), CoS2, NiS2 and CuS2, and their isomorphs FeAsS and CoAsS: Physics and Chemistry of Minerals, v. 22, no. 5, p. 311-317.

Mudge, M. R., Erickson, R. L., Kleinkopf, M. D., and Zartman, R. E., 1968, Reconnaissance geology, geophysics, and geochemistry of the southeastern part of the Lewis and Clark Range, Montana.

Nelson, W. H., 1963, Geology of the Duck Creek Pass quadrangle, Montana, U.S. Geological Survey Bulletin, Volume 1121-J, p. 56.

Peters, C., and Dekkers, M., 2003, Selected room temperature magnetic parameters as a function of mineralogy, concentration and grain size: Physics and Chemistry of the Earth, Parts A/B/C, v. 28, no. 16, p. 659-667.

Planavsky, N. J., McGoldrick, P., Scott, C. T., Li, C., Reinhard, C. T., Kelly, A. E., Chu, X., Bekker, A., Love, G. D., and Lyons, T. W., 2011, Widespread iron-rich conditions in the mid-Proterozoic ocean: Nature, v. 477, no. 7365, p. 448-451.

Potter, D., and Stephenson, A., 1986, The detection of fine particles of magnetite using anhysteretic and rotational remanent magnetizations: Geophysical Journal International, v. 87, no. 2, p. 569-582.

Poulton, S. W., and Canfield, D. E., 2005, Development of a sequential extraction procedure for iron: implications for iron partitioning in continentally derived particulates: Chemical Geology, v. 214, no. 3, p. 209-221.

-, 2011, Ferruginous conditions: a dominant feature of the ocean through Earth's history: Elements, v. 7, no. 2, p. 107-112.

Present, T. M., Bergmann, K. D., Meyers, C. E., Slotznick, S. P., Creveling, J. R., Zieg, G. A., Fischer, W. W., Knoll, A. H., and Grotzinger, J. P., in review, Pyrite-walled tube structures in a Mesoproterozoic SEDEX massive sulfide deposit: Geological Society of America Bulletin.

Raub, T., Johnson, S. C., and Raub, T. D., 2012, Rock magnetic detection of the pyrite-to-pyrrhotite reduction: applications to hydrocarbon maturity, mineral resources, and biogeochemistry, American Geophysical Union, Fall Meeting: San Francisco, CA, p. GP34A-08.

Raymond, J., and Blankenship, R. E., 2004, Biosynthetic pathways, gene replacement and the antiquity of life: Geobiology, v. 2, no. 4, p. 199-203.

Reynolds, R. L., Rosenbaum, J. G., Sweetkind, D. S., Lanphere, M. A., Roberts, A. P., and Verosub, K. L., 2000, Recognition of primary and diagenetic magnetizations to determine the magnetic polarity record and timing of deposition of the moat-fill rocks of the Oligocene Creede Caldera, Colorado: Geological Society of America Special Papers, v. 346, p. 77-93.

Robertson, D., and France, D., 1994, Discrimination of remanence-carrying minerals in mixtures, using isothermal remanent magnetisation acquisition curves: Physics of the Earth and Planetary Interiors, v. 82, no. 3, p. 223-234.

Ross, G. M., and Villeneuve, M., 2003, Provenance of the Mesoproterozoic (1.45 Ga) Belt basin (western North America): Another piece in the pre-Rodinia paleogeographic puzzle: Geological Society of America Bulletin, v. 115, no. 10, p. 1191-1217.

Schieber, J., 1989a, Facies and origin of shales from the mid-Proterozoic Newland Formation, Belt Basin, Montana, USA: Sedimentology, v. 36, no. 2, p. 203-219.

Schieber, J., 1989b, The origin of the Neihart Quartzite, a basal deposit of the Mid-Proterozoic Belt Supergroup, Montana, USA: Geological Magazine, v. 126, no. 03, p. 271-281.

Schieber, J., 1989c, Pyrite mineralization in microbial mats from the mid-Proterozoic Newland Formation, Belt Supergroup, Montana, USA: Sedimentary geology, v. 64, no. 1, p. 79-90.

Schumann, R., Stewart, W., Miller, S., Kawashima, N., Li, J., and Smart, R., 2012, Acid–base accounting assessment of mine wastes using the chromium reducible sulfur method: Science of the Total Environment, v. 424, p. 289-296.

Slotznick, S. P., Winston, D., Webb, S. M., Kirschvink, J. L., and Fischer, W. W., 2016, Iron mineralogy and redox conditions during deposition of the Mid-Proterozoic Appekunny Formation, Belt Supergroup, Glacier National Park: Geological Society of America Special Papers, v. 522.

Snowball, I. F., 1997, The detection of single-domain greigite (Fe3S4) using rotational remanent magnetization (RRM) and the effective gyro field (Bg):

mineral magnetic and palaeomagnetic applications: Geophysical Journal International, v. 130, no. 3, p. 704-716.

Strauss, H., and Schieber, J., 1990, A sulfur isotope study of pyrite genesis: the Mid-Proterozoic Newland Formation, Belt Supergroup, Montana: Geochimica et Cosmochimica Acta, v. 54, no. 1, p. 197-204.

Stüeken, E. E., 2013, A test of the nitrogen-limitation hypothesis for retarded eukaryote radiation: nitrogen isotopes across a Mesoproterozoic basinal profile: Geochimica et Cosmochimica Acta, v. 120, p. 121-139.

Suzuki, Y., Kopp, R. E., Kogure, T., Suga, A., Takai, K., Tsuchida, S., Ozaki, N., Endo, K., Hashimoto, J., and Kato, Y., 2006, Sclerite formation in the hydrothermal-vent "scaly-foot" gastropod—possible control of iron sulfide biomineralization by the animal: Earth and Planetary Science Letters, v. 242, no. 1, p. 39-50.

Thomson, G. F., 1990, The anomalous demagnetization of pyrrhotite: Geophysical Journal International, v. 103, no. 2, p. 425-430.

Walcott, C. D., 1899, Pre-Cambrian fossiliferous formations: Geological Society of America Bulletin, v. 10, no. 1, p. 199-244.

Walter, M., Oehler, J. H., and Oehler, D. Z., 1976, Megascopic algae 1300 million years old from the Belt Supergroup, Montana: a reinterpretation of Walcott's Helminthoidichnites: Journal of Paleontology, p. 872-881.

White, J., Gammons, C. H., and Zieg, G., 2014, Paragenesis of cobalt and nickel in the Black Butte shale-hosted copper deposit, Belt Basin, Montana, USA: Mineralium Deposita, v. 49, no. 3, p. 335-351.

Wilkin, R., Barnes, H., and Brantley, S., 1996, The size distribution of framboidal pyrite in modern sediments: an indicator of redox conditions: Geochimica et Cosmochimica Acta, v. 60, no. 20, p. 3897-3912.

Winston, D., and Link, P., 1993, Middle Proterozoic rocks of Montana, Idaho and eastern Washington: the Belt Supergroup: Precambrian: Conterminous US: The Geology of North America, v. 2, p. 487-517.

Xu, S., and Dunlop, D. J., 1995, Toward a better understanding of the Lowrie-Fuller test: Journal of Geophysical Research: Solid Earth (1978–2012), v. 100, no. B11, p. 22533-22542.

Zieg, G., and Leitch, C., The geology of the Sheep Creek copper deposit, Meagher County, Montana, *in* Proceedings Belt Symposium III Abstracts, 1993: Montana Bureau of Mines and Geology1999, Volume 381.

Zieg, G., Scartozzi, V., Chutas, N., Albers, D., Gostomski, K., and Jones, J., 2013, Black Butte copper deposits, lower Belt Supergroup, Montana: Northwest Geology, v. 42, p. 131-147.

Zieg, G. A., 1986, Stratigraphy and sedimentology of the Middle Proterozoic Newland Limestone: Montana Bureau of Mines and Geology Special Publication, v. 94, p. 125-141.

Chapter 4

Iron Mineralogy and Redox Conditions During Deposition of the Mid-Proterozoic Appekunny Formation, Belt Supergroup, Glacier National Park

Originally published in:

Slotznick, S. P., Winston, D., Webb, S. M., Kirschvink, J. L., and Fischer, W. W., 2016, Iron mineralogy and redox conditions during deposition of the Mid-Proterozoic Appekunny Formation, Belt Supergroup, Glacier National Park: Geological Society of America Special Papers, v. 522, doi: 10.1130/2016.2522(09).

4.1 Abstract

The redox state of the mid-Proterozoic oceans, lakes, and atmospheres is still debated, but it is vital for understanding the emergence and rise of macroscopic organisms and eukaryotes. The Appekunny Formation, Belt Supergroup, Montana contains some of these early macrofossils dated between 1.47 Ga and 1.40 Ga and provides a well-preserved record of paleoenvironmental conditions. We analyzed the iron chemistry and mineralogy in samples from Glacier National Park, Montana by pairing the bulk rock magnetic techniques with textural techniques including light microscopy, scanning electron microscopy, and synchrotron-based X-ray absorption spectroscopy. Field observations of the Appekunny Formation combined with mineralogical information allowed revised correlations of stratigraphic members across the park. However, late diagenetic and/or metasomatic fluids affected primary iron phases as evidenced by prevalent postdepositional phases including base-metal sulfides. On the west side of the park, pyrrhotite and chlorite rims formed during burial metamorphism in at least two recrystallization events. These complex postdepositional transformations could affect bulk proxies for paleoredox. By pairing bulk and textural techniques, we show primary records of redox chemistry were preserved in early diagenetic and often recrystallized framboidal pyrite, submicron magnetite grains interpreted to be detrital in origin, and red-bed laminae interpreted to record primary detrital oxides. Based on these observations, we hypothesize that the shallow waters of the mid-Proterozoic Belt Basin were similar to those in modern marine and lacustrine waters: fully oxygenated, with detrital reactive iron fluxes that mineralized pyrite during organic diagenesis in suboxic, anoxic, and sulfidic conditions in sedimentary pore waters.

4.2 Introduction

Currently exposed across parts of Montana, Idaho, Washington, Alberta, and British Columbia, the Belt Supergroup is one of the best-preserved and extensive mid-Proterozoic sedimentary terranes (Fig. 4.1A). This thick sedimentary succession was deposited between 1470 Ma and 1401 Ma (Anderson and Davis, 1995; Evans et al., 2000; Sears et al., 1998), and provides an important paleontological perspective on the evolution of eukaryotes and multicellularity (Knoll et al., 2006). The Belt Supergroup is well-known for its stromatolites, but it also contains a diversity of other micro- and macrofossils (Horodyski et al., 1989). In the mudstones of its lower portion, two macrofossils have been studied in great detail. First identified by Charles Doolittle Walcott (1899) in the Greyson Shale and later renamed (Walter et al., 1976), *Grypania spiralis* is a curved or coiled ribbon, 0.2 to 1.7 mm wide, and 6 to 14mm in coiled diameter, and has been nonuniquely interpreted as eukaryotic algae as well as a consortia of several microscopic organisms (Horodyski et al., 1989; Knoll et al., 2006; Walter et al., 1976). Within the stratigraphically correlated Appekunny Formation, *Horodyskia moniliformi*s has the general appearance of a string of beads with diameters of 2.1-9.2 mm and lengths up to 15 cm, and has been interpreted to represent a wide range of different organisms including algae (Grey and Williams, 1990; Horodyski, 1993), prokaryotic colony (Knoll et al., 2006), tissue-grade colonial eukaryote (Fedonkin and Yochelson, 2002), sponge (Hofmann, 2001), foraminifer (Dong et al., 2008), and lichen (Retallack et al., 2013). No matter their affinity, understanding more about the environmental conditions where these early macroscopic organisms lived will tell us more about the pacing of evolution and how it might have been aided, frustrated, or unaffected by changing environmental conditions.

Major first order questions exist concerning the redox status of the oceans, lakes, and atmosphere during mid-Proterozoic time. Based broadly on a gap in the preserved record of banded iron formation, red beds, marine manganese deposits, and the conspicuous presence of carbonate platforms, it has been suggested that the mid-Proterozoic subaqueous basins were oxygenated at (nearly) all depths (Cloud, 1968; Holland, 1984, 2006; Slack et al., 2007). Based on theory and sulfur isotope records, others have suggested that if atmospheric oxygen values were lower than today with similar levels of marine primary production, then the deep oceans would have been anoxic and sulfidic (i.e. euxinic), with the consequence that the lack of banded iron formations was due to an increase in water column sulfide leading to iron sulfide precipitation (Canfield, 1998). Recently, bulk geochemical techniques have queried the composition and redox state of mid-Proterozoic basins using the sequential extraction technique known as iron speciation as well as trace metal work (e.g. Gilleaudeau and Kah, 2015; Kendall et al., 2009; Planavsky et al., 2011; Shen et al., 2003; Sperling et al., 2014). Iron speciation data suggest anoxic, euxinic, and oxic waters varying between different basins, different water depths, and temporally with dominant anoxic and sulfur poor (i.e. ferruginous) conditions despite the lack of iron formation deposition (Poulton and Canfield, 2011; Sperling et al., 2015). This new notion of a ferruginous Proterozoic world based on iron speciation is distinctly different from the aforementioned canonical views of mid-Proterozoic paleoenvironments.

Several geochemical studies have focused specifically on the paleoredox state and geochemistry of the Belt Basin during deposition of the Belt Supergroup. Arguments for a stratified euxinic basin during deposition of the lower Belt Supergroup were made on the basis of sulfate levels and sulfur isotopes (Gellatly and Lyons, 2005; Luepke and Lyons, 2001; Lyons et al., 2000) as well as presence of basinwide sedimentary laminations similar to those found in the Black Sea (Huebschman, 1973; Lyons et al., 2000). Bottom water suboxic to euxinic conditions were also inferred from the high (several weight percent) organic content observed in shales regionally (Lyons et al., 2000) and the conspicuous syndepositional to early diagenetic sulfide and base metal deposits of Pb, Cu and Zn (Graham et al., 2012; Hamilton et al., 1982; Huebschman, 1973; Slotznick et al., 2015). However, iron speciation results on the same samples suggested instead anoxic and ferruginous conditions for the water column during deposition of the lower Belt Supergroup (Planavsky et al., 2011). Additionally, recent nitrogen isotope studies suggested oxygenated surface waters (Stüeken, 2013). Importantly, most of these studies focused on samples from the Helena Embayment, which is distinct from, but stratigraphically correlated to, the units in Glacier National Park and the rest of the Belt Basin.

The Belt Supergroup exposures in Glacier National Park provide a well-studied region of low metamorphic grade in which to investigate iron mineralogy, and provide a different window into the redox status of the larger Belt Basin than previously-studied samples from the Helena Embayment (Lyons et al., 2000; Planavsky et al., 2011; Stüeken, 2013). Based on sedimentological indicators, the strata in the park were predominantly deposited within storm wave base, even including intervals of subaerial exposure, from a much more proximal part of the basin (Winston and Link, 1993). For many of these shallower environments, the local water column should reflect a higher degree of influence by oxygen in the atmosphere, with the null expectation that local anoxic and/or H_2S-rich conditions would be tied to sedimentary pore fluids. However, the sedimentary units at Glacier National Park are well-known for their brilliant green and red coloration, due to the variable and differential presence of reduced and oxidized iron-bearing minerals (Winston, 1986c). These differences have been hypothesized to reflect changing redox conditions even in these shallow waters (Stanley and Davies-Vollum, 2000) while others suggest they are diagenetic but broadly reflect syndepositional environments (Winston, 1986b; Winston, 2016). We focused our study of iron mineralogy, deposition, and preservation on the primarily green and gray-colored Appekunny Formation as well as the stratigraphic units above and below it using a unique and powerful combination of techniques to assess iron mineralization including rock magnetics, light and electron microscopy, and synchrotron X-ray spectroscopy. Characterization of the iron mineralization of the Appekunny, Prichard, and Grinnell Formations provides support for new stratigraphic correlations of the Appekunny Formation across Glacier National Park and suggests that the shallow waters of the Belt Basin were similar to today with an oxic water column overlying suboxic to anoxic to H_2S-rich pore waters.

4.3 Geologic Setting

The Belt Supergroup is composed of mixed siliciclastic and carbonate rocks in units that thicken from Glacier National Park to the west, reaching a maximum of 15-20 km (Winston and Link, 1993). Several tectonostratigraphic models for the origin and development of the Belt Basin have been proposed including a large lake in an intercontinental rift (Winston, 1986b), a marine setting along the rifted margin of North America (Price, 1964), a lake or restricted marine setting from a remnant ocean basin (Hoffman, 1988), or a restricted marine/isolated lake setting due to supercontinental rifting (Luepke and Lyons, 2001; Lyons et al., 2000). Part of this debate is due to the preservation of shallow water and potentially fluvial sediments on the eastern edge of the basin, whereas a western margin was rifted away during the breakup of Rodinia (Stewart, 1972). Sediment provenance studies suggest a predominantly western source for the lower two-thirds of the Belt, with a predominately Laurentian source observed in Glacier National Park and the Helena Embayment (González-Álvarez et al., 2006; Ross and Villeneuve, 2003).

The Belt Supergroup has been divided into 4 main stratigraphic groups: the lower Belt, the Ravalli Group, the Piegan Group, and the Missoula Group (Whipple et al., 1984; Winston, 1986a; Winston, 2007) (Fig. 4.1B). The lower Belt is primarily dark colored mudstones and siltstones with iron sulfides, interpreted as deep basinal turbidites (Cressman, 1989). The Ravalli Group contains red and green mudstones and siltstones and light-colored sandstones deposited in shallower environments; some units and members display evidence of episodic subaerial exposure/playa environments (Winston, 2016; Winston and Link, 1993). The Piegan Group is composed of cyclic and/or graded dolomite, mudstone, and sandstone beds with common stromatolites, ooids, and molar tooth structures; it is interpreted to preserve the subtidal midshelf (Pratt, 2001) or underfilled lake deposits with less detrital input (Winston, 2007). The Missoula Group contains red to green mudstones, and pink quartz sandstones with thin intervals of carbonate and dark gray mudstones interpreted to be alluvial, playa, and shallow subaqueous sequences (Winston and Link, 1993). Despite this well-recognized coarse stratigraphic architecture, more detailed stratigraphic correlations between different parts of the Belt Basin have been challenging in part due to facies changes and local stratigraphic nomenclature. Notably, some have grouped the Appekunny Formation, composed of green and gray mudstones and siltstones, in the Ravalli Group with the overlying Grinnell Formation, composed of red and green mudstones and sandstones (e.g. Whipple et al., 1997; Whipple et al., 1984; Fig. 4.1B). Others, due to its dramatic thinning and absence toward the west, have considered this unit to pass westward into the Prichard Formation making it part of the lower Belt (Winston and Link, 1993) and/or it has been correlated with the Greyson Formation of the Helena Embayment (Harrison, 1972; Winston, 1986a) which is similarly nebulously assigned, sometimes with the lower Belt (Graham et al., 2012; Ross and Villeneuve, 2003; Winston and Link, 1993) and other times with the Ravalli Group (Harrison, 1972; Mudge et al., 1968). Observations of the stratigraphy and iron-mineralogy and geochemistry may help shed light onto these possible correlation schemes by providing additional data on the key transition from the east side of Glacier National Park to its western side.

The Belt Supergroup is variably well-preserved across its present extent with known metamorphic gradients. In general, the degree of metamorphism increases to the west, with the best-preserved, lowest temperature exposures in Glacier National Park and the Helena Embayment (Duke and Lewis, 2010). Within Glacier National Park, several studies have quantified the amount of metamorphism and postdepositional alteration of these rocks. Maxwell and Hower (1967) examined the structural changes of white mica (illite) from $1M_d$ or 1M polymorphs in low-grade samples to 2M polymorphs in more deeply buried samples with the transition complete by the biotite isograd (Frey, 1987). Samples from the Appekunny Formation, Grinnell Formation, and Missoula Group in Glacier National Park were between 41% and 62% 2M polytype, suggesting sub-biotite zone metamorphism. Eslinger and Savin (1973) found a similar range from 21 to 61% 2M polytype in samples from the Appekunny Formation, Grinnell Formation, and Helena Formation primarily from the east side of the park, which also increased with burial depth as interpreted from stratigraphic level. Oxygen isotope geothermometry of quartz and white micas indicated metamorphic temperatures between 225°C and 310°C, suggesting sub-biotite zone to near-biotite zone (Eslinger and Savin, 1973). A new high throughput technique using near-infrared spectroscopy to observe shifts in the Al-OH absorption band in white micas, which were correlated basinwide using other metamorphic studies (including those cited already), observed the Belt rocks of Glacier National Park to be some of the best preserved in the sub-biotite zone (Duke and Lewis, 2010).

Although the strata in Glacier National Park have not been as strongly heated and metamorphosed as those to the west in the Belt Basin, several observations of the mineralogy and petrography of the rocks within Glacier National Park have documented the effects of mineralization due to later diagenetic and/or metasomatic fluids. These observations include euhedral authigenic monazites in the Appekunny Formation and Grinnell Formation with dates ranging from 300 Ma to 1400 Ma, interpreted to reflect the protracted flow of basinal brines through these units (González-Álvarez et al., 2006). Peaks in age spectra at 1400 Ma, 1000-900 Ma, 600 Ma, and 300 Ma suggest an episodic nature to the metasomatism, which could be linked to continental-scale tectonic processes (González-Álvarez and Kerrich, 2010). Rare-earth element abundances throughout the stratigraphic units in Glacier National Park highlight a mixture of near-primary compositions with two distinct alteration patterns that are more pronounced in sandstones, perhaps due to their greater permeability; the enrichment and depletion patterns suggest at least some of the alteration fluids were oxidizing and alkaline (González-Álvarez and Kerrich, 2010).

Previous studies have not directly examined the impact of these metasomatic fluids on the iron mineralogy in samples from Glacier National Park. However, some paleomagnetic measurements of the Grinnell Formation in

Glacier National Park were noted to have overprints from phases of intermediate coercivity between 50 and 100 mT or Curie temperature between 210°C and 610°C, which were distinct from a component that demagnetized at over 665°C (Vitorello and Van der Voo, 1977). The wide coercivity and temperature range given for the overprint component could be indicative of secondary hematite, maghemite, titanomagnetite, magnetite, pyrrhotite, or greigite, whereas the high temperature component is uniquely hematite (Dunlop and Özdemir, 1997; Peters and Dekkers, 2003). The high temperature component weakly passed a fold test, has a vector direction similar to other localities from the same time period, and thus was interpreted as primary (Vitorello and Van der Voo, 1977). Other samples of the Grinnell Formation in the northwestern portion of the park were not affected by these overprints and matched other samples across the Belt Basin, which also pass the field test for antiparallel reversals (Elston et al., 2002).

4.4 Sample Descriptions and Field Relationships

Samples were collected in Glacier National Park focusing on stratigraphic sections of the Appekunny Formation and extending into the overlying Grinnell Formation and the underlying Prichard Formation. To minimize effects on iron mineralogy possibly due to temporal and paleoenvironmental variation and/or heterogeneous distribution of altering fluid flow, samples were collected carefully from locations covering the entire Appekunny Formation on outcrops occurring on both the west and east limbs of the Akamina syncline, a broad SE-NW trending structure running through Glacier National Park (Fig. 4.1A; Dahlstrom, 1970; Whipple et al., 1992).

The Appekunny Formation (Ross, 1959; Willis, 1902) has been divided into five informal members (Whipple et al., 1984) based on stratigraphic measurements on Apekuni Mountain in the Many Glacier region (Fig. 4.2B; Whipple et al., 1997). We revisited this type locality and one of us (Slotznick) remeasured the stratigraphic section to describe these members in greater detail (Fig. 4.2A). Based on the Apekuni Mountain section, the descriptions of these members by J.W. Whipple, and previous field excursions by one of us (Winston) with J.W. Whipple, we identified and sampled outcrops of all five members on the east side of the park exposed along the Going-to-the-Sun Road. These sampled outcrops show very similar lithofacies and stratigraphy to the Many Glacier section, although we did not measure a detailed stratigraphic section along the Going-to-the-Sun Road. Observations and interpretations of sedimentary structures in these members vary slightly from previous authors and are described next for completeness.

Member 1 of the Appekunny Formation and the underlying Altyn Formation show a conformable gradational interbedded contact (over 10 m) of siltstone and argillite beds with carbonate layers. Based on Whipple et al. (1997), the base of member 1 was defined as a 1-m-thick greenish white quartz sandstone bed, above which sandstone continued to be interbedded with green siltstone and argillite for several meters. Member 1 consists of mostly planar, sometimes gently undulating laminated maroon siltstone with millimeter-thick laminae interstratified with equally thick layers of red claystone. Ripple cross-stratification is present at the millimeter to decimeter wavelength scale (Fig. 4.3A) with uncommon broad centimeter-tall hummocky cross-stratification. A thick quartz arenite sandstone bed in the middle of member 1 has been used as a key marker bed across the park (Whipple et al., 1984), and it is 24 m thick in the Apekuni Mountain section. Rare rip-up mud chips are found; overall, the member is interpreted as reflecting subaqueous sediment transport and deposition. Although mainly maroon to red in color, some grayish green intervals are observed; while sometimes discontinuous pinching out as lenses, others are distinct stratigraphic units that span large distances along strike. Samples of each colored lithotype were sampled and analyzed with the maroon sample taken from lower in the succession than the green sample. Member 1 is 173 m thick at Apekuni Mountain. *Horodyskia moniliformi*s was first found in the Appekunny Formation at Apekuni Mountain (Horodyski, 1982), and most fossils occur below the thick quartz sandstone marker bed in the middle of member 1 (Fedonkin and

Yochelson, 2002; Retallack et al., 2013). Additional fossil examples have been collected in member 1 along the Going-to-the-Sun Road and at Rising Wolf Mountain in the Two Medicine region (Fedonkin and Yochelson, 2002; Retallack et al., 2013). One *Horodyskia* specimen was collected at Otokomi Mountain north of the Going-to-the-Sun Road, but no stratigraphic information is available for it (Horodyski, 1982).

Member 2 and member 1 have a gradational interbedded contact with the top of member 1 set at the uppermost maroon beds (Whipple et al., 1992). Although very similar to member 1 in lithology, member 2 notably has an increased proportion of green siltstone to mudstone creating thicker beds up to a meter thick; these beds of well-sorted silt laminae often exhibit plumose fracturing. Planar to gently undulating to wavy lamination was observed on the centimeter to meter-scale with ripple cross stratification and broad decimeter-scale hummock cross-stratification. Along the Going-to-the-Sun Road, multiple meter-thick beds display soft-sediment deformation structures including loading and the ball-and-pillow structures noted in the middle of member 2 (Fig. 4.3B). A few quartz sandstone beds are observed throughout the section, but they are thinner than those in member 1. Overall, member 2 is 145 m thick at Apekuni Mountain.

Member 3 contains several 2-5-m-thick pinkish brown quartz arenite sandstone beds and lenses/load structures; the lowest of these beds marks its base (Whipple et al., 1992). These arenite intervals contain common large millimeter-sized pyrite grains and goethite psuedomorphs after pyrite. Interbedded within the arenite sandstone and between these sandstone beds, there is grayish green siltstone with small amounts of claystone in thinly planar to wavy laminae. Most strikingly, this member contains common large hummocky cross stratification up to a decimeter in height and up to meter-scale in wavelength, and in some locations, steep walled decimeter-scale gutters cut into the underlying beds (Figs. 4.3CD). Additionally, member 3 differs from member 2 with increased claystone, the presence of common fining upward cycles, and an orange-red weathering appearance of some intervals. Ripples and mud cracks are found throughout the member, the latter especially common near quartz arenite sandstone layers. No implied mechanism of formation is interpreted for the mud cracks; they could be either subaqueous or subaerial. Scattered rusty weathering iron oxide phases were observed in road-cut outcrop exposures, whereas fresh-cut samples revealed iron sulfides suggesting the oxides are dominantly a recent near-surface weathering product. At Apekuni Mountain, member 3 is 72 m thick.

Member 4 is composed of green to dark greenish gray to dark to medium gray interbedded siltstone and claystone in millimeter to centimeter-thick lenticular and pinch and swell layers. These are more silty than the microcouplets noted throughout the Prichard Formation (Winston and Link, 1993). Finely laminated, member 4 is fissile, weathering in thin plates, and it is poorly exposed. The base of the member is defined by the first occurrence of this thinly laminated siltstone (Whipple et al., 1992). Notable characteristics include the abundance of red iron oxides on parting surfaces, presumably from the exposure and surface weathering of iron sulfides. Scour pits and convolute bedding from soft sediment deformation are also common and a defining characteristic (Fig. 4.3E). Hummocky-cross stratification is still present in this member, but it is less common and smaller in scale than member 3. Similarly, pinkish-brown quartz arenite sandstone beds are still found in this unit. Mudcracks and mudchip breccias are also found throughout this member, often associated with quartz sandstone but occasionally in green siltstone and claystone instead.

Member 5 is composed of fining-upward couplets (3 mm to 10 cm) and microlaminae (<3 mm) of planar laminated green siltstone and claystone. Abundant mud cracks and mud chip breccias (much more common than in member 4) highlight alternating subaerial desiccation and flooding of a shoreline muddy flat (Fig. 4.3F). The fine lamination of this unit results in weathering of the unit in thin plates, especially on Apekuni Mountain where recent freeze-thaw cycles have made this unit be poorly exposed. Member 5 and member 4 have a complex gradational contact with a few intervals of member 5-type beds found over a 75 m interval. The base of the contact is unclear from previous work, so it is defined here as transition from a majority of member 4-type intervals of pinch-and-swell centimeter to millimeter thick laminations with scour pits, convolute bedding, and hummocky cross-stratification to even thinner beds with a predominance of microlaminae with mud cracks and mud chips characterizing member 5. This makes member 4 185 m thick at Apekuni Mountain with a thin member 5 measuring 48 m in thickness.

Appekunny member 5 grades conformably up into the overlying Grinnell Formation. The base of the Grinnell Formation is defined by the lowest occurrence of red to purplish red mud-cracked claystone and siltstone beds (Whipple et al., 1984), although interbedded green and red beds continue for several tens of meters above this contact. Although the proportion varies, the Grinnell Formation contains more white quartz arenite sandstone lenticular beds throughout than the Appekunny Formation, and it preserves a wide range of shallow-water sedimentary structures from ripple marks and cross stratification to mud cracks and mud chip/mud ball breccias.

Exposures of Appekunny member 5 continue on the west side of Glacier National Park (e.g. Fig. 4.2D). Here, it was interpreted to overlie the Prichard Formation with a thick transition zone containing wavy laminated and lenticular layers of calcareous claystone and siltstone as well as beds and lenses of quartz arenite, stromatolitic limestone (Whipple et al., 1997). Rare mud cracks are noted in a few intervals. The precise contact between the Appekunny Formation and Prichard Formation was not exposed within the park from previous stratigraphic descriptions, and it was postulated Appekunny member 3 and 4 could even have extended to the west side of the park (Whipple et al., 1997; Whipple et al., 1992). However, in the neighboring Whitefish and Flathead Range, the contact was suggested to be gradational, although there were questions about the identification of the Appekunny Formation in this locality (Harrison et al., 1998; Whipple et al., 1984).

A previously unpublished stratigraphic section was measured by coauthor Winston on the east side of Mount Brown and it is shown here in Figure 4.2C. This locality is 3 km from a published section measured by J.W. Whipple at Beaver Medicine Falls, Edwards Mountain (Fig. 4.2D; Whipple et al., 1997), and it was measured in an effort to improve stratigraphic correlations within the park. Based on the new descriptions and definitions of the members of the Appekunny Formation from the type-section and revisiting the east side of Mount Brown, we present here new stratigraphic interpretations for these units.

At the base of the section, there is an 89 m thick package of medium gray siltstone to dark gray claystone microlaminae, subcentimeter-scale pinch-and-swell couplets, and even couplets (Fig. 4.3G). Soft sediment deformation including convolute bedding is found throughout, sometimes producing clasts of the laminated mudstone. Mud cracks were observed near the top of this unit at 52 m and 76 m. Although entire laminae filled with abundant iron sulfides were not observed in the field, collected hand samples include very large (5 mm) iron sulfide phases in various states of *in situ* oxidative weathering. We interpret this unit as member 4 due to its pinch-and-swell couplets, convolute bedding, and abundant iron oxides.

The transition to the next unit is gradational. The first 188 m of the unit are mainly composed of green, even microlaminae and microcouplets of siltstone to claystone, with common mud cracks and mud chip breccias. This unit's massive weathering is a striking feature, and it additionally contains several 10-60 cm thick tabular siltstone beds. Several additional unique beds stand out from the siltstones and claystones in this unit. One calcareous bed weathers recessively and contains mud chips, mud cracks, and soft sediment deformation features. In the upper portions, two 3 cm thick medium-grained, well-rounded quartz sand beds with high-angle cross bedding were observed.

A change in facies up section occurs with 58 m of dark gray interbedded siltstone and claystone and even to pinch and swell couplets and microlaminae layers as well as some hummocky cross stratification in siltstones. Several 60 cm thick medium-grained sandstone beds with cross stratification occur throughout the unit. This interval contains an increasing amount of carbonate with several lenses of carbonate-rich mud chips and molar tooth hash. A 10 cm thick stromatolitic limestone bed occurs at 295 m. Mud cracks with associated mud chips are rare except in intervals near the sandstone beds. After the 58 m of wavy and pinch-and-swell layers, there is a return to green tabular siltstone beds, microlaminae, and lenticular to even siltstone to claystone couplets for another 75 m. Some intervals contain mud cracks and mud chips—textures that become more abundant near the top of the unit.

Here we interpret the entire 321 m as Appekunny member 5 with a small interval similar to Appekunny member 4 in this long complex transition. The upper portion of this has previously been identified as member 5 (Whipple et al., 1997), but due to the characteristics of the lower portion with even couplets and microlaminae and abundant mud chip breccias, we think the lower portion should be grouped with member 5 even though it is below a small interbedded interval of pinch-and-swell beds. The new description of the type-section at Apekuni Mountain highlights the complex long-gradational transition between these two members, so interbedded intervals of member 4-type facies within member 5 are not unexpected.

The top of this unit is marked by the first appearance of purple coloration in the even couplets of siltstone and claystone, with mud cracks and chips. This purple coloration appears interbedded with green-colored beds and lenses as well as frequent thin quartz sand beds for at least 148 m. This is the contact of Appekunny Formation member 5 with the overlying Grinnell Formation.

The new Mount Brown stratigraphic column and facies detailed earlier highlight the abundance of mud cracks and mud chip breccias in the lower portion of the stratigraphy previously called the Prichard transition zone, as well as a lack of stratigraphically continuous laminae of abundant iron sulfides like those common in the Prichard Formation. Therefore, we argue that these strata do not represent classic Prichard Formation or Prichard transition zone, and we instead assign them to Appekunny members 4 and 5. While still in line with the interpretations by previous authors (Whipple et al., 1997) as a transitional facies, this interpretation extends Appekunny member 4 to the west side of the park and highlights a thickening of facies to the west consistent with the larger architecture of the Belt Basin. Although facies typical of the Prichard Formation—even couplets of gray siltstone and claystone with continuous layers of iron sulfides—were observed in outcrops on the west side of Mount Brown and along McDonald Creek, we found no clear evidence that these units are preserved on the east side of Mount Brown (Fig. 4.3H). Due to through-going structures and limited continuous exposure, it is difficult to determine the relative position of these samples within the stratigraphic columns to the east. The iron mineralogy and geochemistry of these units, however, may help to evaluate these possible correlations.

4.5 Sampling and Analytical Methods

Oriented block samples were collected by hiking off-trail from the Going-to-the-Sun Road, Glacier National Park in October 2012 and August 2014 (Fig. 4.1A). Metadata including lithology, sedimentology, photographs, and global-positioning system (GPS) locations were also recorded for all samples. Samples covered all five members of the Appekunny Formation, the Grinnell Formation, and potentially the Prichard Formation (Table S4.1). Samples were cored using a nonmagnetic 25.4 mm diamond-edged drill bit, and sliced into 2-5-mm-thick specimen rounds using a saw with a nonmagnetic brass blade. Nondestructive rock magnetic experiments were performed on specimens using a 2G Enterprises SQuID magnetometer following the RAPID protocols, and the data were analyzed using the RAPID Matlab (The Mathworks, Inc.) scripts (Kirschvink et al., 2008). Our protocol included measurements of alternating field (AF) demagnetization of the natural remanent magnetization (NRM), rotational remanent magnetization (RRM) acquisition and demagnetization, anhysteretic remanent magnetization (ARM) acquisition and demagnetization, isothermal remanent magnetization

(IRM) acquisition and demagnetization, and backfield IRM acquisition. These analyses can be used to observe fundamental physical properties that can be used to distinguish different ferromagnetic minerals (e.g. Peters and Dekkers, 2003). The destructive rock magnetic technique of KappaBridge thermal susceptibility was measured on neighboring specimens for a subset of the samples using an AGICO MFK1-FA KappaBridge, with the resulting data reduced using Cureval and Matlab scripts.

The same specimens that were run through nondestructive rock magnetic experiments were then made into polished thick or thin sections to provide a flat surface for optical, magnetic, and chemical imaging. Ultrahigh-resolution scanning SQuID Microscopy (UHRSSM) was then performed on 11 of the sections with 100 μm pixels to locate ferromagnetic grains as regions for further analysis. Transmitted and reflected light microscopy was used to observe petrographic textures in all samples as well as identify additional target regions. Further petrographic observations were made using the Zeiss 1550VP field emission scanning electron microscope in the Caltech GPS Division Analytical Facility; this has a Robinson-type backscatter electron detector for imaging and a working distance of 8-9 mm. This instrument contains a paired Oxford X-Max SDD X-ray energy dispersive spectrometer (EDS) system used to determine X-ray spectra of elemental abundance at submicron sized spots on 12 thin or thick specimens. This chemical information was important for confirming detections of chalcopyrite, galena, and sphalerite in addition to iron sulfides in present in many samples.

Synchrotron-based high-energy X-ray fluorescence (XRF) imaging was performed using beam line 10-2 at the Stanford Synchrotron Radiation Lightsource to characterize elemental abundances including trace metals in 21 thick or thin sections. Applied incident X-ray energies ranged from 20,200 eV to 10,000 eV, and standards for elements of interest were run at each beam time session with the same collection parameters. Synchrotron-based X-ray absorption near-edge spectroscopy (XANES/XAS) was paired with elemental imaging using beam line 14-3 and 2-3 at the Stanford Synchrotron Radiation Lightsource. X-ray absorbance spectroscopy (XAS) was performed in fluorescence mode at specific 2-4-μm-sized spots on 13 thin or thick sections to determine the chemical form of elements (oxidation state, orbital electronics, type and number of neighbors) while preserving textural information. Differences in the shape and K-edge of these absorption spectra allow us to easily distinguish between a wide range of Fe- and S- bearing minerals (Fleet, 2005; O'Day et al., 2004). Chalcopyrite and pyrrhotite have sufficiently similar S K-edge spectra that high-energy XRF, electron microscopy, and EDS were applied to confirm the presence of these minerals. The incident X-ray energy was set to energies around the sulfur absorption edge (2472 eV) and the iron absorption edge (7112 eV) using a Si (111) double crystal monochromator. At beam line 14-3, the monochromator energy was calibrated by setting the first thiol peak of a sodium thiosulfate powder to 2472.02 eV. At beam line 2-3, the monochromator energy was calibrated by setting the inflection point of a metallic Fe foil to 7112 eV. XRF elemental maps were processed using the MicroAnalysis Toolkit (Webb, 2011) and XAS data were processed using SIXPACK (Webb, 2005).

4.6 Results

A wide array of iron-bearing minerals was observed in the samples collected from Glacier National Park, as summarized in Table 4.1. Importantly, bulk rock magnetic techniques provide a sensitive approach for finding and describing ferromagnetic minerals, but some of these techniques may not be diagnostic for a given phase. However, when coupled to petrography, phases can be confirmed and in certain cases, the mineralization sequence can be ordinated by crosscutting relationships or informed by grain shape. We discuss the results of these analyses first from the perspective of bulk techniques identifying iron minerals and then using petrographic (including chemical imaging) techniques.

The coercivity of remanence acquisition, determined using the derivative of the IRM, can be used to make ferromagnetic mineralogical determinations

(Figs. 4.4AB; Heslop et al., 2002; Peters and Dekkers, 2003; Robertson and France, 1994). Notably, most of the samples share a similar mid-coercivity peak with a few additional different high-coercivity peaks present in some of the samples. Goethite is easily identified with coercivities over 1000 mT, and the range of 140-800 mT is generally indicative of hematite. However, the coercivity ranges for hematite, magnetite, titanomagnetite, greigite, and pyrrhotite overlap between 16-140 mT, though pyrrhotite, greigite, and hematite tend to have higher coercivities. Additionally, interpretations of coercivity data can be more difficult in natural samples where more than one ferromagnetic mineral is present. Thus other techniques are valuable to provide confirmation and/or to separately identify these minerals.

The presence of RRM can be used to identify magnetic iron-sulfide phases like pyrrhotite, although the sensitivity limits are not well understood (Snowball, 1997; Thomson, 1990). Compared using B_{eff} (applied field times ratio of RRM to ARM), several samples in the west outcrops of member 4 indicated strong evidence for magnetic iron sulfides, $B_{eff} > \pm 20\ \mu T$ at 5 rps (revolutions per second) (Potter and Stephenson, 1986; Suzuki et al., 2006), while two samples of west side member 5 displayed weaker RRM signals, $B_{eff} > \pm 5\ \mu T$ at 5 rps (Fig. 4.4C). Notably, no samples on the east side showed any RRM, and thus do not contain pyrrhotite. Additionally, all of the samples that had RRM displayed coercivity peaks greater than 100 mT, above the main mid-coercivity peak, suggesting that the lower common mid-coercivity mineral observed widely in Glacier National Park samples is magnetite.

In order to confirm the presence of magnetite and other iron-bearing minerals, Kappabridge thermosusceptibility experiments were used (Figs. 4.4E-G). Magnetite was indicated by a drop in coercivity at 580°C in all of the samples measured except one from west side outcrops of member 4. However, the Verwey transition at about -150°C was not observed, suggesting either it was suppressed due to low abundance with other phases dominating the signal, or that the magnetite contains a small weight percent titanium and could include titanomagnetite (Kozłowski et al., 1996; Moskowitz et al., 1998). Many of the samples showed the transformation of a nonmagnetic iron-bearing mineral into magnetite through a peak of increased susceptibility starting between 400°C and 500°C that dropped at 580°C. This is interpreted as the decomposition of pyrite (Li and Zhang, 2005). Only one sample from the west side outcrop of member 4 displayed any sign of pyrrhotite's ferromagnetic to paramagnetic shift at its Curie temperature of 325°C (Horng and Roberts, 2006; Minyuk et al., 2013). No low-temperature peaks hinted at the presence of goethite. Hematite is difficult to identify using Kappabridge thermal susceptibility due to its low susceptibility. The pure hematite Curie temperature transition is rarely seen in samples with other minerals like chlorite or elements like S or C and the low-temperature Morin transition can be easily suppressed in submicron-size grains or with cation substitution (Bowles et al., 2010; Minyuk et al., 2011; Zhang et al., 2012). Indeed, Kappabridge experiments on samples containing hematite and carbon-, nitrogen- or sulfur-bearing phases are hard to distinguish from those of pyrite decomposition except that pyrrhotite sometimes forms during the cooling of pyrite, although cation substitutions can affect this process (Li and Zhang, 2005; Minyuk et al., 2011; Minyuk et al., 2013). Since no pyrrhotite was formed in our experiments, identification of pyrite using Kappabridge is only weak evidence for this mineral. The cooling curves are all much higher susceptibility than the initial heating curves in these thermosusceptibility experiments, often with a shifted peak toward lower temperatures of 200°C to 550°C. This suggests the decomposition of nonmagnetic minerals combining with other minerals to form titanomagnetite. This could be due to the reduction of paramagnetic hematite, the decomposition of ilmenite or other titanium bearing minerals, and/or another less well understood process (Hrouda, 2003; Zhang et al., 2012).

Using an empirical rock magnetic procedure called the Fuller test, one can use the ratio of the NRM:IRM to infer if the magnetization is detrital, chemical, or thermal in origin, especially when compared to the synthetic ARM:IRM relationships (Fuller et al., 1988; Fuller et al., 2002). In sedimentary rocks deposited in approximately Earth-strength magnetic fields, NRM:IRM ratios of 1:1000 correspond to weak detrital magnetization whereas ratios of 1:10 are typical of chemical remagnetization. This test was calibrated for magnetite, and thus can only be applied to samples where the primary ferromagnetic mineral is magnetite. When applied to the samples from the Appekunny Formation that do not show RRM (no pyrrhotite) or large amounts of hematite, most of the samples show a NRM:IRM ratio of 1:1000 with a few slightly higher, but not near 1:10. These results suggest that the magnetite in these samples is detrital in origin. Results from the ARM modification of the Lowrie-Fuller test imply that this magnetite is single domain or pseudo single domain, and is probably submicron (maximum less than 10 μm) in size (Johnson et al., 1975; Lowrie and Fuller, 1971; Xu and Dunlop, 1995).

To quantify the amount of magnetite in the samples, we used the saturation remanent magnetization measured using IRM acquisition. Magnetite has a saturation magnetization of 92 Am^2/kg (O'Reilly, 1984), and for magnetite the ratio of the saturation remanence to the saturation magnetization has been calculated for a range of grain sizes in the famous Day plot (e.g. Day et al., 1977; Dunlop, 2002). Our samples are single-domain or pseudo-single domain in size so this ratio should be between 0.5 and 0.02. By mass-normalizing a measured saturation remanence, we can divide by the saturation magnetization of magnetite times a correction factor of the ratio of saturation remanence to saturation magnetization to get approximate percentages of magnetite in our samples (e.g. Klein et al., 2014). This calculation can only be done for samples where magnetite is the only or primary ferromagnetic mineral, and due to underlying assumptions it is probably only accurate to an order of magnitude. Estimates range from tenths of a part per million (ppm) to tens of ppm of magnetite (depending on the ratio used), primarily for samples on the east side of the Glacier National Park with one from the west side.

All mineralogical identifications using light and electron microscopy were confirmed chemically/structurally using synchrotron XAS and/or EDS spectra.

All green or gray Appekunny Formation samples contained pyrite, but pyrrhotite was only observed in samples of member 4 (or Prichard Formation) on the west side of Glacier National Park (Fig. 4.5A). The presence of different sulfide phases with exotic trace metal cations such as chalcopyrite, sphalerite, galena, nickel iron monosulfide, copper sulfide, and cobalt arsenic sulfide were also observed in many samples (Fig. 4.5C). Chalcopyrite and sphalerite occured throughout the Appekunny Formation and on both sides of the park, while galena, nickel sulfides, and cobalt sulfides were only found in member 5 (east side) and member 4 (west side). Iron oxides were also identified in many of the samples throughout the Appekunny Formation and on both sides of the park, and they were primarily confirmed chemically using EDS. XAS at the Fe K-edge was used to identify the iron oxide as goethite in one sample from member 2 (Fig. 4.5B). Iron-bearing chlorite was also ubiquitous throughout the samples, identified by electron microscopy and EDS as well as synchrotron XAS at the Fe K-edge (Fig. 4.5B). Sulfate phases were identified in many samples using S XAS (Fig. 4.5A), often with more than one sulfate salt present in a given sample. Electron microscopy and EDS characterized many of these sulfates as barite, but iron sulfates were also observed—these probably reflect the recent oxidative weathering of pyrite.

Using high-energy XRF maps, we were able to quantize the abundance of iron and trace metals for two of our samples (Table 4.2). XRF counts were correlated to mass based on standards measured during the same beam time session, then corrected for X-ray attenuation for each element and the rock matrix (assuming a homogeneous quartz lithology), then summed over a measured volume, and then divided by the sample density to find weight percent. This also implicitly assumes that a representative area was chosen for chemical imaging (Fig. 4.6). For all quantized elements, the values were remarkably similar across the park, often the same order of magnitude and similar to the second significant digit. However, comparison with previously measured bulk XRF and inductively coupled plasma-mass spectrometry (ICP-MS) elemental abundances of the

Appekunny Formation (Table 4.2, González-Álvarez and Kerrich, 2010; González-Álvarez et al., 2006) suggests that while the textural XRF estimates for major elements (such as Fe) are within the expected range, the trace element estimates are often 2 to 16 times more abundant than observed in bulk. This could be due to differential sample analysis because given chemical imaging efforts were focused to a degree on reactive iron phases and thus the abundance of trace metals contained within these texturally late iron sulfide phases was overrepresented compared to background matrix.

Using these same XRF maps (Fig. 4.6), we estimated the volume percent of Fe-rich minerals such as iron sulfides and oxides. In this approach, the numbers of matrix pixels above a certain cutoff level of intensity of Fe signal were counted and divided by the total number of pixels in the XRF microprobe map to get a volume percent estimate (Table 4.2). This level was determined by cross-correlating the chemical maps with microscopy, XANES, and EDS to include all iron sulfides and oxides as identified in those regions but to exclude other minerals containing Fe such as chlorite. These calculations bear typical uncertainties associated with point count estimates, but avoid a certain degree of human error in phase identification (e.g. Johnson et al., 2014). Each pixel of the XRF maps represents the abundance over a volume of 10 μm by 10 μm by the thickness of samples, but are actually 20 x 20 μm pixels based on the chosen measurement step-size. In exporting these images from the MicroAnalysis Toolkit for point-counting processing, the pixels are redistributed at a finer scale across the map, which leads to some averaging between pixels. Therefore to be counted in the volume estimation, the Fe-rich grains or aggregates must be sufficiently large in size, consisting of the majority of a 10 x10 μm area (which has been further averaged in processing), and thus disseminate grains are not included in this estimate. In this manner, the presence of large aggregates of sulfide phases versus disseminated grains in the XRF mapped region will influence the volume percent estimation. Even with these caveats, similar volume percentages of Fe-rich minerals were attained for samples from both sides of the park and these modal abundances were the same order of magnitude as modal abundances from point-counting of other sub-biotite grade, organic-lean shales (e.g. Ferry, 1984, 2007).

From light and electron microscopy, many of the iron-bearing minerals show shapes or crosscutting textures that indicate their recrystallized and secondary nature. Much of the observed pyrite is euhedral, and often is found in large nodular aggregations from samples throughout the park (e.g. Figs. 4.7BCD). These nodules do not display evidence of differential compaction unlike early nodules in the lower Belt's Newland Formation in the Helena Embayment (Schieber, 1989; Slotznick et al., 2015) and preserved macroscale soft sediment deformation in the Appekunny Formation, implying a later diagenetic or metasomatic origin. Small aggregates of euhedral pyrite grains similar to pyrite framboids observed in modern anoxic and sulfidic sediments (Wilkin et al., 1996) were found in a few members on the east side of Glacier National Park (Fig. 4.7A), suggesting the much of the coarse euhedral pyrite could be simply recrystallized from an early diagenetic framboidal phase in these samples. These pyrite grains range in size from 1.5 to 10 μm average width/diameter with a mean size of 4.3 μm (standard deviation = 1.7, n = 168), which is similar to other measured framboids and infilled framboids in the modern sediments and in sediments throughout Earth history (Wilkin et al., 1996). In samples that contain multiple sulfide phases, various textural relationships were observed. In three samples, pyrite and pyrrhotite nodules contain small inclusions of chalcopyrite and sphalerite, often near veins or fractures within the crystal (Figs. 4.7BCF); however, in other samples, sphalerite and chalcopyrite phases coexisted with pyrite as separate crystals. While pyrrhotite and pyrite were often found in the same samples, we did not observe clear crosscutting relationships between these phases. Sometimes, the pyrrhotite occured in large aggregates with small grains of pyrite nearby, and sometimes pyrite was larger in grain size than the pyrrhotite (Fig. 4.7C). Surface weathering of iron oxides is present in many of the samples surrounding pyrite grains, and XAS showed at least one of these surrounding rims to be goethite (Fig. 4.7D). However, rims of chlorite and/or carbonate were also observed around iron sulfides on the west side of the park (Figs. 4.7EF). On the east side of the park, chlorite was present in the background fabric of the sample instead. Barite occurred in small isolated grains sometimes with lath shapes, sometimes rounded (Fig. 4.7G), and sometimes as replacement/embayed domains with unclear origins (Figs. 4.7DG). However, one sample contained barite intimately associated with the pyrite in space-filling patterns as well as small grains and rims (Fig. 4.7H).

4.7 Discussion

Despite the well-preserved nature of the fine-grained siliciclastic Belt strata in Glacier National Park, secondary overprinting of the iron-bearing minerals in the Appekunny Formation was observed in all samples from a range of bulk and texture-specific techniques. Some of these alteration processes included recent (near) surface weathering, but many point to late diagenetic and/or metasomatic events. Nearly all pyrite has defined margins that crosscut fine-grained phases and reflect either recrystallization and coarsening of prior phases or mineralization from later fluids, although pyrite in exposures on the east side of the park appears generally better preserved with several examples consistent with early diagenetic emplacement (Fig. 4.6A). Many samples contained sulfide phases enriched in As, Zn, Cu, Pb, Ni, and Co, which indicate the mobility of these metals as well as sulfur in postdepositional recrystallization events possibly involving metasomatic fluids. Sulfide phases rich in these trace metals were observed throughout the Appekunny Formation on both sides of the park, suggesting any flow of altering fluids was not restricted to a particular stratigraphic member due to differential permeability, depth within the stratigraphy, and/or proximity to local structures. Samples with multiple sulfide phases in one nodule (found both in samples with and without pyrrhotite) emphasize the recrystallization of original iron minerals to incorporate trace-metals. The impact of metasomatic fluids on the Appekunny Formation has been well noted by previous studies (González-Álvarez and Kerrich, 2010; González-Álvarez et al., 2006); however, less consideration has been given to how these processes have impacted the iron mineralogy, and the quality of interpretations of paleoenvironmental processes and chemistry of Belt Basin waters made from redox proxy data.

Pyrrhotite was found in several samples from the west side of Glacier National Park. Overall, the bulk magnetic technique of RRM appears to be a valuable indicator of the presence of magnetic iron sulfides even in samples with multiple ferromagnetic components. Pyrrhotite was confirmed using XANES and EDS in all three samples that showed a strong RRM signal. Similarly, no pyrrhotite was found in samples that showed no RRM signal. Pyrrhotite was not found texturally in the two samples with moderate RRM signal ($\pm 20 > B_{eff} > \pm 5$ μT at 5 rps), but these grains could be very small with a weaker signal due to the overwhelming presence of other ferromagnetic minerals or another magnetic mineral could be capable of producing moderate RRM. The fact that pyrrhotite was only observed in samples from the west side of Glacier National Park, both in bulk and textural measurements, highlights local variations in metamorphic conditions in samples separated by only 26 km (though palinspastic reconstruction might restore a larger distance). Although modern examples of detrital pyrrhotite and early diagenetic pyrrhotite have been found in unique environments (Horng and Roberts, 2006; Larrasoaña et al., 2007), much of the pyrrhotite in the rock record is interpreted to be due to the transformation of pyrite into pyrrhotite during metamorphism or precipitation from high temperature fluids (e.g. Craig and Vokes, 1993; Hall, 1986; Weaver et al., 2002). In the presence of organic matter or a reducing environment, pyrite may transform to pyrrhotite beginning at 200°C (Hall, 1986), with some experiments indicating that pyrrhotite can form at even lower temperatures depending on lithological constraints (Moreau et al., 2005; Raub et al., 2012). Although pyrrhotite formation is variable based on lithological constraints like organic matter (e.g. Carpenter, 1974), our new stratigraphic correlations suggest that the appearance of pyrrhotite is linked to different metamorphic conditions on the west side of the park and is not simply due to lithological differences between stratigraphic members. Although recent studies often screen for pyrrhotite (e.g. Asael et al., 2013; Planavsky et al., 2011), the presence of pyrrhotite makes interpreting iron speciation analyses tricky because it apportions iron to a highly reactive pool usually composed of oxides and carbonates; furthermore it can be difficult to mass balance iron and sulfur even when accounting for the iron in pyrrhotite as the iron and sulfur budgets associated with pyrrhotization of pyrite in open systems remain unknown (Asael et al., 2013; Craig and Vokes, 1993; Piatak et al., 2007; Shannon and White, 1991; Zhou et al., 1995). Due to the lack of quantification for pyrrhotite, it is unclear the extent to which the pyrrhotite noted in these samples has impacted the bulk iron speciation data; however, the widespread observation of pyrrhotite on the west side of Glacier National Park shows that secondary processes have played a role in changing the iron geochemistry of these strata.

The presence of pyrrhotite only on the west side of the park is consistent with increasing burial metamorphism to the west, similar to the overall trend seen across the Belt Supergroup due to thickening of the section (Duke and Lewis, 2010; Winston and Link, 1993). Indeed, pyrrhotite has been widely observed in the Prichard Formation to the west of Glacier National Park, and linked via geochemistry to the metamorphic transformation of pyrite (Luepke, 1999; Luepke and Lyons, 2001). Within Glacier National Park, the appearance of pyrrhotite could be linked to transformations at deeper burial depths in a reducing environment probably an open system, but distinct fluids could also have delivered and/or removed dissolved iron and sulfide to precipitate pyrrhotite (e.g. Hall, 1986). Supporting this suggestion is the observation that cobalt arsenic base metal sulfides from the west side of the park are closely texturally associated with the pyrrhotite. Notably the chlorite rims surrounding the pyrrhotite and pyrite aggregates on the west side of the park suggest an even later transformation (and redox change) of iron from sulfides into a mixed valence silicate phase. This highlights the increased mobility of iron between different minerals on the west side of the park explainable by either of the mechanisms detailed above, but in a second alteration event after pyrrhotite had already formed.

One of the most interesting iron mineralogical findings in this study was the discovery of nearly ubiquitous submicron-size magnetite across all of the Appekunny Formation in all members. Results from the rock magnetic Fuller test suggest that this magnetite is detrital due to its low ratio of NRM:IRM, whereas chemical precipitation would be expected to have a much stronger magnetization than was observed. The evidence for detrital magnetite is important because it represents a significant delivery process of iron into the system that is not directly linked to the redox chemistry of the depositional waters. In bulk geochemical iron speciation measurements, abundant preserved detrital magnetite would skew results toward an interpretation of ferruginous waters; however, the amounts of magnetite present in our samples are too low to dramatically impact the results of bulk geochemical extraction techniques. The observations of detrital iron fluxes provide an important view of the iron systematics in the basin, by documenting an important supply of highly reactive iron to the basin (e.g. Canfield and Berner, 1987). Furthermore, the preservation of at least some of this magnetite suggests that a large anoxic H_2S-rich zone (either in the water column or as sedimentary pore fluids), if present during deposition of the strata in Glacier National Park, was not sufficient to scavenge all this highly reactive iron to form pyrite (Canfield and Berner, 1987; Lyons and Severmann, 2006). Additionally neither the water column nor pore fluids were sufficiently rich in ferrous iron to recrystallize detrital magnetite and generate a chemical remanent magnetization (e.g. Skomurski et al., 2010).

The presence of shallow-water hematite-bearing red units in member 1 of the Appekunny Formation as well as in the overlying Grinnell Formation highlights the presence of oxygen in the atmosphere and shallow waters. All of the units in the Appekunny Formation of Glacier National Park represent relatively shallow water environments of the Belt Basin, and based on sedimentary structures from orbital water motion, long-lived stratification of the water column seems unlikely. However, the framboidal pyrite in samples from the east side of Glacier National Park (and perhaps even much of the recrystallized pyrite seen elsewhere), suggests the precipitation of early diagenetic pyrite during organic diagenesis. Thus pyrite is reasonably interpreted as an indicator of primary anoxic and sulfidic sedimentary environments in the Belt Basin, but based on the constraints noted earlier herein suggesting oxic, nonstratified conditions in shallow waters, it seems likely that these conditions were effectively limited to sediment pore waters. Detrital iron oxides likely provided an important source of highly reactive iron for pyrite formation during organic diagenesis (Canfield and Berner, 1987; Raiswell and Canfield, 1998). Based on our observations, the shallow waters and sediments of the Belt Basin preserved in Glacier National Park do not show any signs of being anoxic and sulfur-poor (i.e. ferruginous conditions) as was hypothesized for older, more distal sediments further south in the basin (Planavsky et al., 2011). The barite closely associated with pyrite in space-filling patterns (Fig. 4.7H) suggests at least some of the barite precipitated from diagenetic and/or metasomatic reactions with deep fluids and may not be representative of sulfate in the depositional waters (Griffith and Paytan, 2012; Hanor, 2000). The presence of authigenic replacement barite not associated with iron sulfides found in many of the samples (Figs. 4.7DG) could in principle record postdepositional oxidizing fluids, although these micron-scale grains may instead reflect precipitation during early organic diagenesis, associated with vacillating redox fronts of sulfate reduction with pore fluid sulfate sourced from bottom waters (Griffith and Paytan, 2012; Koski and Hein, 2004). Water column or detrital barite could be a component of our samples, but no lath-shaped euhedral barite was identified and while rounded grains were observed (Fig. 4.7G), they often occurred near barite displaying replacement or embayed textures. This suggests much of the either water column or detrital barite was recrystallized after deposition.

Ultimately, the iron mineralogy and geochemistry of the Appekunny Formation and surrounding formations suggest a redox structure of (relatively) shallow mid-Proterozoic sedimentary basins that was similar to today with detrital iron fluxes carried through oxygenated waters, wherein sedimentary environments with sufficient organic carbon loads exhausted their supply of O_2 and underwent anaerobic respiratory metabolisms that promoted sulfidic pore fluids and the production of diagenetic pyrite. Additionally, from the data generated in this study, we can link evidence for oxygenated waters directly to outcrops known to contain the early macroscale fossil *Horodyskia moniliformis*, a putative (aerobic) eukaryote. Understanding the depths in the Belt Basin to which water was oxygenated and whether anoxic and sulfidic conditions emerged from the sediments into the water column in more distal sedimentary settings (Gellatly and Lyons, 2005; Luepke and Lyons, 2001; Slotznick et al., 2015), or whether the water column instead became anoxic and ferruginous (Planavsky et al., 2011) remains a priority for future work.

Although our iron mineralogy analyses shed light onto questions about redox and geochemistry of the Belt Basin, they are not as straightforward in aiding in stratigraphic correlations across Glacier National Park. Sulfides rich in Zn, Cu, and Pb were found on both sides of the park, and they do not appear to be restricted to any single stratigraphic member. Similarly, pyrrhotite appears to be a characteristic of the west side of Glacier National Park and is not restricted to a single member. It is noteworthy that the abundance of pyrrhotite (as well as pyrite) in samples on the west side of Glacier National Park was distinct between different units. Appekunny member 4/Prichard-like lithologies from the west face of Mount Brown and McDonald Creek contained abundant pyrrhotite, as did samples in proposed member 4 on the east face of Mount Brown. Samples from member 5 in McDonald Creek and from proposed member 5 on the east face of Mount Brown contained smaller proportions or no pyrrhotite. This suggests a stratigraphic link between samples on the west side of Mount Brown and the better-studied McDonald Creek region and supports the hypothesis that the strata on the east face of Mount Brown are metamorphosed equivalents of member 4, maybe even the same member as the more Prichard-like samples on the west face and in McDonald Creek. Additionally, member 4 siltstones and claystones on the east side of the park contained abundant pyrite, which could reflect the mineralogical progenitor of the abundant pyrrhotite seen on the west side of the park in these ambiguously correlated units.

4.8 Conclusion

The Appekunny Formation of Glacier National Park is an excellently preserved shallow-water unit that, while complicated by postdepositional processes, still contains records of primary redox chemistry of the Belt Basin during mid-Proterozoic time when macroscopic life was emerging. From our iron mineralogy and chemical observations, we propose that the shallow waters in the Belt Basin were oxygenated, but with underlying suboxic H_2S-rich pore waters that promoted precipitation of pyrite. This water chemistry and these redox processes are similar to those of shallow sedimentary basins today, and they may help to explain why these rocks are notably fossiliferous (e.g. Horodyski et al., 1989), as many of the preserved biota are interpreted as (different) aerobic organisms. In the sedimentary rocks of Glacier National Park, most of the strata capture paleoenvironments that would have been habitable to diverse sets of aerobic organisms. Our interpretations of the paleoenvironment in Glacier National Park provide a geochemical constraint on paleoredox conditions that helps to support the hypotheses from many paleontologists that some of the macroscale and microscale fossils found in Glacier National Park and in the rest of the Belt Basin were early eukaryotes (e.g. Adam et al., 2014; Fedonkin and Yochelson, 2002; Horodyski, 1993; Retallack et al., 2013; Walter et al., 1976; Walter et al., 1990). It is possible that portions of the Belt Basin could have been anoxic or euxinic (e.g. Slotznick et al., 2015) in either a stratified or locally heterogeneous manner, but these paleoredox constraints are distinct in time and record deeper water environmental settings than the fossiliferous units focused on in this work. Iron mineralogy preserved in Precambrian rocks is rich and complex with the possibility of many different redox and phase transformations. By combining textural and bulk techniques, it is possible to untangle the iron phases to get a picture of key redox processes operating in the environment and the postdepositional processes that have served to complicate our interpretation of that history.

4.9 Acknowledgements

We thank Rob Thomas, Tim Lyons, Austin Chadwick, and Steven Skinner for assistance with stratigraphic measurements and sample collections under National Park Service collection permits # GLAC-2012-SCI-0195 and GLAC-2014-SCI-0008. Thanks also go to Jim Sears, Johnny MacLean, Erik Sperling, and an anonymous reviewer for helpful comments that greatly improved the manuscript. Support for this work was provided by the Agouron Institute, a Tobacco Root Geological Society scholarship, a Belt Association student research grant, a Geological Society of America student research grant, National Aeronautics and Space Administration (NASA) Exobiology program (Fischer), the David and Lucile Packard Foundation (Fischer), National Science Foundation Graduate Research Fellowship program (Slotznick), a NASA Earth and Space fellowship (S.P.S.), and a Philanthropic Educational Organization Scholar Award (Slotznick). Portions of this research were carried out at the Stanford Synchrotron Radiation Lightsource, a Directorate of SLAC National Accelerator Laboratory, and an Office of Science User Facility operated for the U.S. Department of Energy Office of Science by Stanford University.

4.10 Tables

Table 4.1: Mineral identifications from samples of the Appekunny, Grinnell, and Prichard Formations

	East side of Glacier National Park							West side of Glacier National Park		
	Mbr. 1 (red)	**Mbr. 1 (green)**	**Mbr. 2**	**Mbr. 3**	**Mbr. 4**	**Mbr. 5**	**Grinnell**	**Prichard/ Mbr. 4***	**Mbr. 4†**	**Mbr. 5**
Bulk Techniques										
Magnetite		X	X	X	X	X		X	X	X
Hematite	X				X	X	X		X	X
Goethite	X	X	X	X			X		X	X
Pyrite			X		X			X		
Pyrrhotite								X	X	X
Textural Techniques										
Goethite			X							
Iron Oxide (generic)	X	X	X		X		X	X	X	X
Pyrite		X	X	X	X	X		X	X	X
Pyrrhotite								X	X	
Chalcopyrite		X				X		X	X	X
Galena						X			X	
Sphalerite		X			X	X		X	X	X
Nickel Iron Monosulfide								X		
Cobalt Arsenic Sulfide									X	
Copper Sulfide									X	
Ferric Disulfide						X				
Chlorite	X	X	X	X	X	X		X	X	X
Barite	X	X	X	X	X				X	
Sulfate (generic)		X		X	X			X	X	

*Samples from the east face of Mt. Brown and McDonald Creek
†Samples from the west face of Mt. Brown

Table 4.2: Elemental Abundances from X-ray fluorescence microprobe for samples of Appekunny Formation

Sample*	Member	Location*	Fe (wt%)	Ti (wt%)	Mn (wt%)	Cu (ppm)	As (ppm)	Zn (ppm)	Ni (ppm)	Fe-rich mineral (vol%)†
GP12-8, Reg1	Member 4	West, McD	2.01	0.232	0.042	21.3	42.7	106	131	0.2
GP12-1, Reg4	Member 2	East	3.54	0.213	0.000056	21.7	40.1	143	237	0.3
Average Published Appekunny Formation Data§			2.59± 0.55	0.294± 0.045	0.037± 0.024	12.4± 11.0	2.57± 1.41	58.3± 18.3	22.6± 8.33	

* Reg stands for Region, East stands for east side of Glacier National Park, West stands for west side of Glacier National Park, McD stands for McDonald Creek

† Based on point counting XRF map, this includes iron sulfides and oxides that represent most of a 6 or 13 μm square pixel

§ Data from silt and claystones of González-Álvarez et al. (2006) and González-Álvarez & Kerrich (2010), Averaged with 1 population standard deviation, n= 16 for Fe, Ti, Mn, As, and Ni, n = 12 for Cu and Zn

4.11 Figures

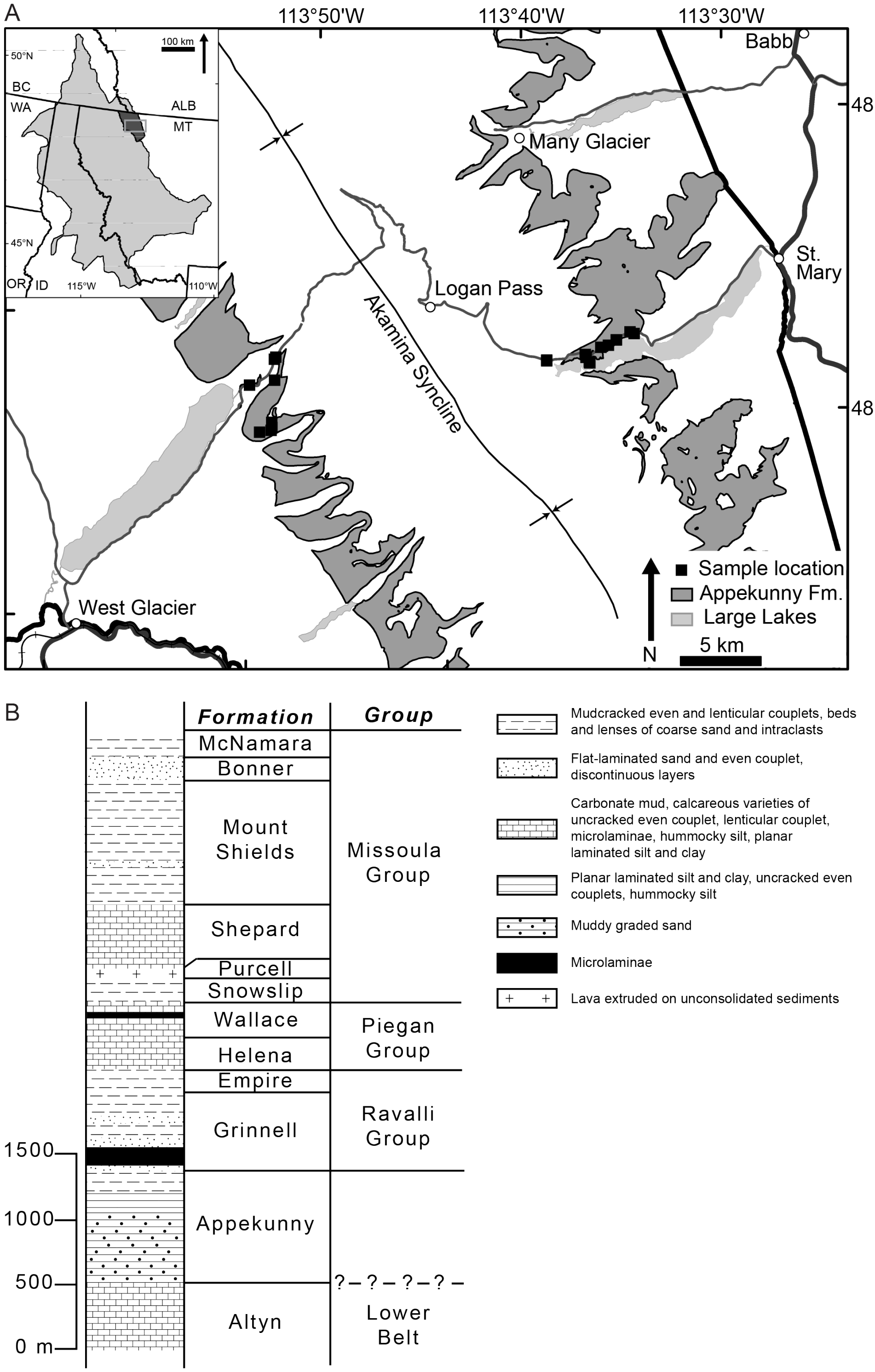

Figure 4.1: (A) Map of sample localities in Glacier National Park, as well as exposures of Appekunny Formation. Inset map shows location of these samples

within the larger Belt Supergroup outcrops. State/province abbreviations: OR—Oregon, ID—Idaho, MT—Montana, WA—Washington, BC—British Columbia, ALB—Alberta. (B) Generalized stratigraphy and stratigraphic nomenclature of the units exposed on the east side of Glacier National Park. See text for details.

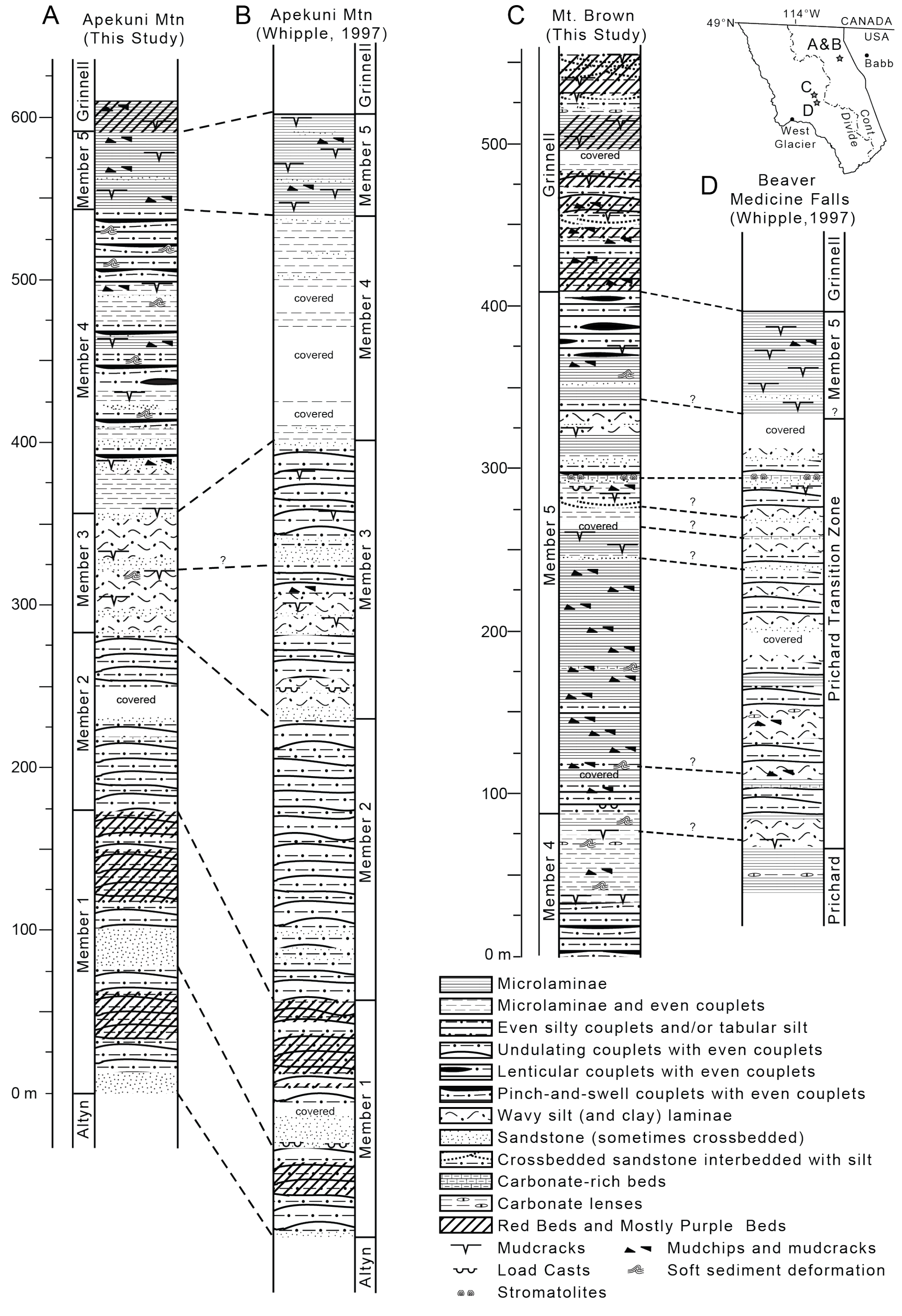

Figure 4.2: Stratigraphic columns of the Appekunny Formation. Scale is in meters and applies to all stratigraphic columns shown. Top right inset: Map showing approximate locations of the stratigraphic columns in Glacier National Park.

Note: Cont. Divide—Continental Divide. (A) New stratigraphic section of the Appekunny Formation at the type section at Apekuni Mountain, Many Glacier. (B) Original stratigraphic section detailing the Appekunny Formation's 5 informal members at the type section of Apekuni Mountain, Many Glacier from Whipple et al. (1997). (C) New stratigraphic section from the east face of Mount Brown as well as new interpretation of the units present. Sedimentology is summarized in the text. (D) Stratigraphic section from Beaver Medicine Falls, Edwards Mountain showing Prichard Formation and Prichard transition zone interpretations from Whipple et al. (1997).

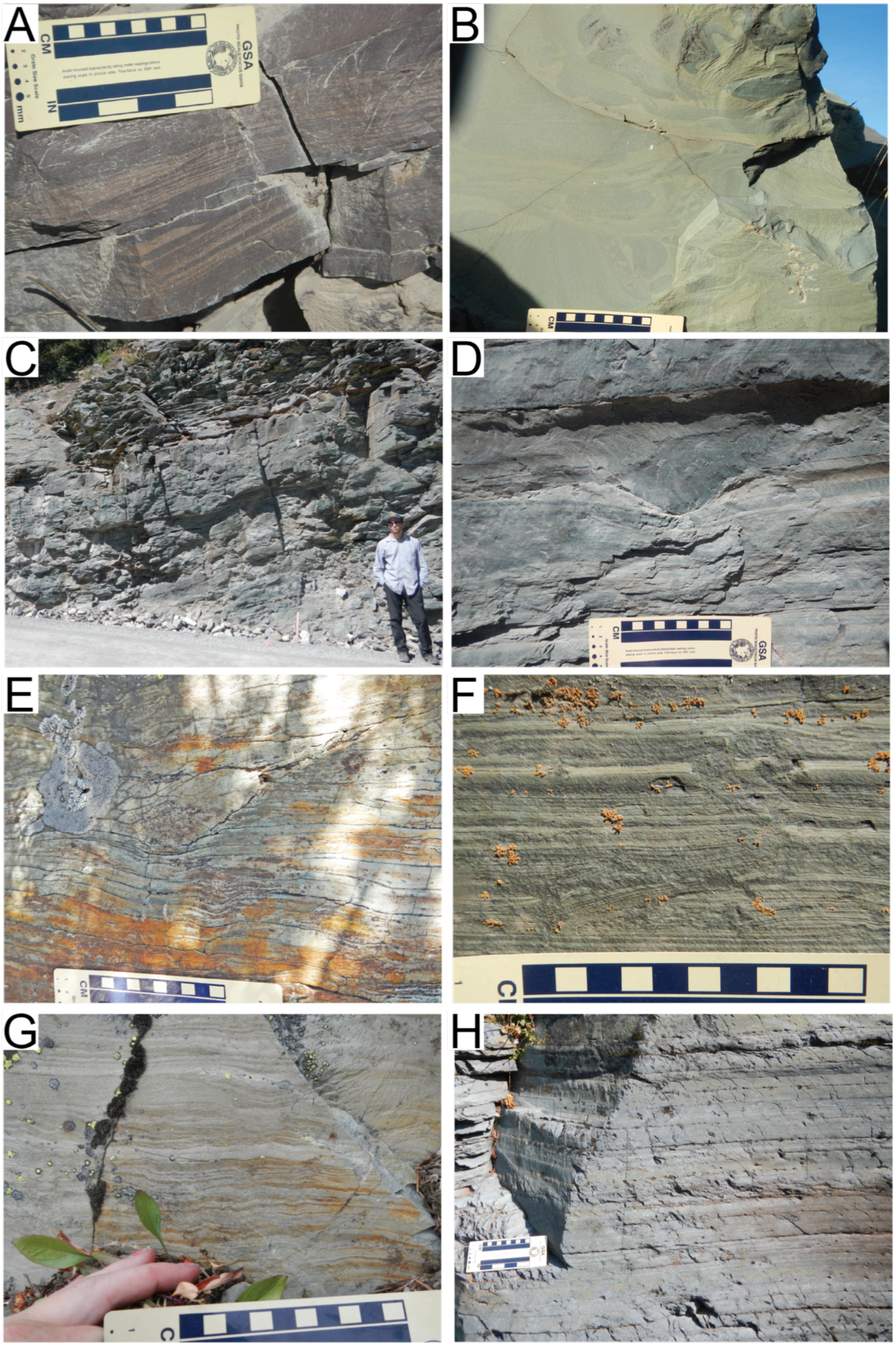

Figure 4.3: Photographs of Appekunny Formation member lithotypes and sedimentary structures along the Going-to-the-Sun Road. (A) Ripple cross-

stratification in member 1. (B) Soft-sediment deformation load structures and plumose fracturing in member 2. Person is 1.8 m for scale. (C) Large-scale hummocky cross stratification in member 3 (D) Centimeter-scale gutters in member 3. (E) Soft sediment deformation and scour in lenticular beds of interbedded siltstone and claystone in member 4 on the east side. Note red iron oxides from weathering of iron sulfides. (F) Mud cracks and mud chips in flat even laminations of alternating siltstone and claystone in member 5 on the east side. (G) Lenticular siltstone and claystone couplets as well as soft-sediment deformation on east face of Mount Brown. (H) Gray siltstone and claystone even couplets with continuous beds rich in iron sulfides on the west side of Mount Brown.

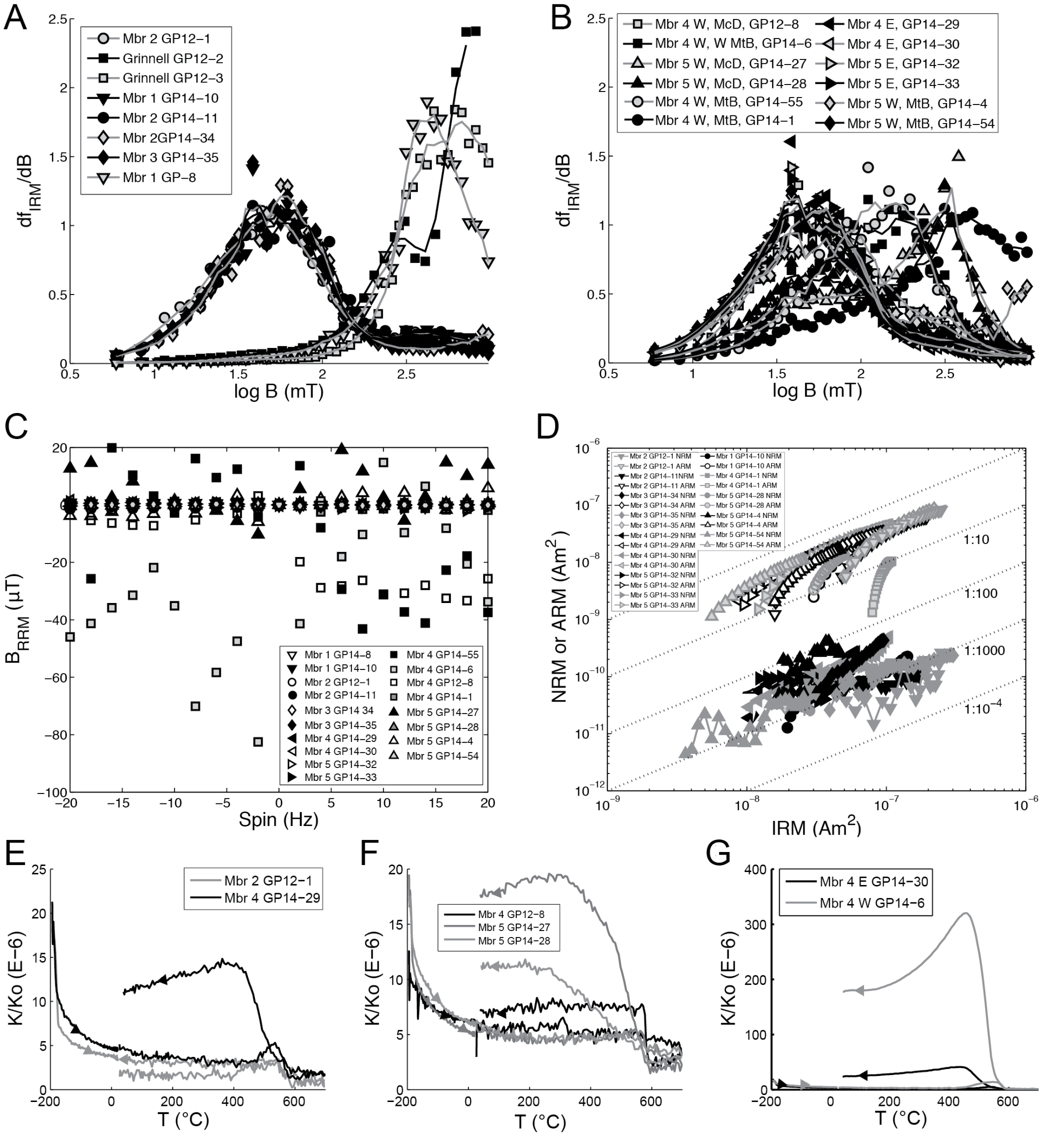

Figure 4.4: Bulk rock magnetic techniques. (A) Derivative of isothermal remanent magnetization (IRM) acquisition with respect to the applied field to determine coercivity of remanence acquisition for Grinnell Formation and Appekunny members 1-3. Abbreviations: f_{IRM}—normalized IRM, B—applied field. (B) Derivative of the IRM acquisition for members 4-5 separated by location in the park. Abbreviations: E—east side, W—west side, MtB—east face of Mount Brown, W MtB—west side of Mount Brown, McD—McDonald Creek. (C) Rotational remanent magnetization (RRM) of the Appekunny Formation samples to assess the presence or absence of magnetic iron sulfide phases. (D) Fuller test to determine origin of magnetization in samples not showing RRM or dominant hematite. (E-G) KappaBridge thermal susceptibility (abbreviated as K) to determine mineralogy, with arrows showing direction of heating, including samples from the east side of the park (E), samples from the west side of the park

(F), and some samples with strong signals (G). Sample stratigraphic member assignment is noted by number and by side of the park in part G. Data are normalized to an empty holder measurement (abbreviated as Ko).

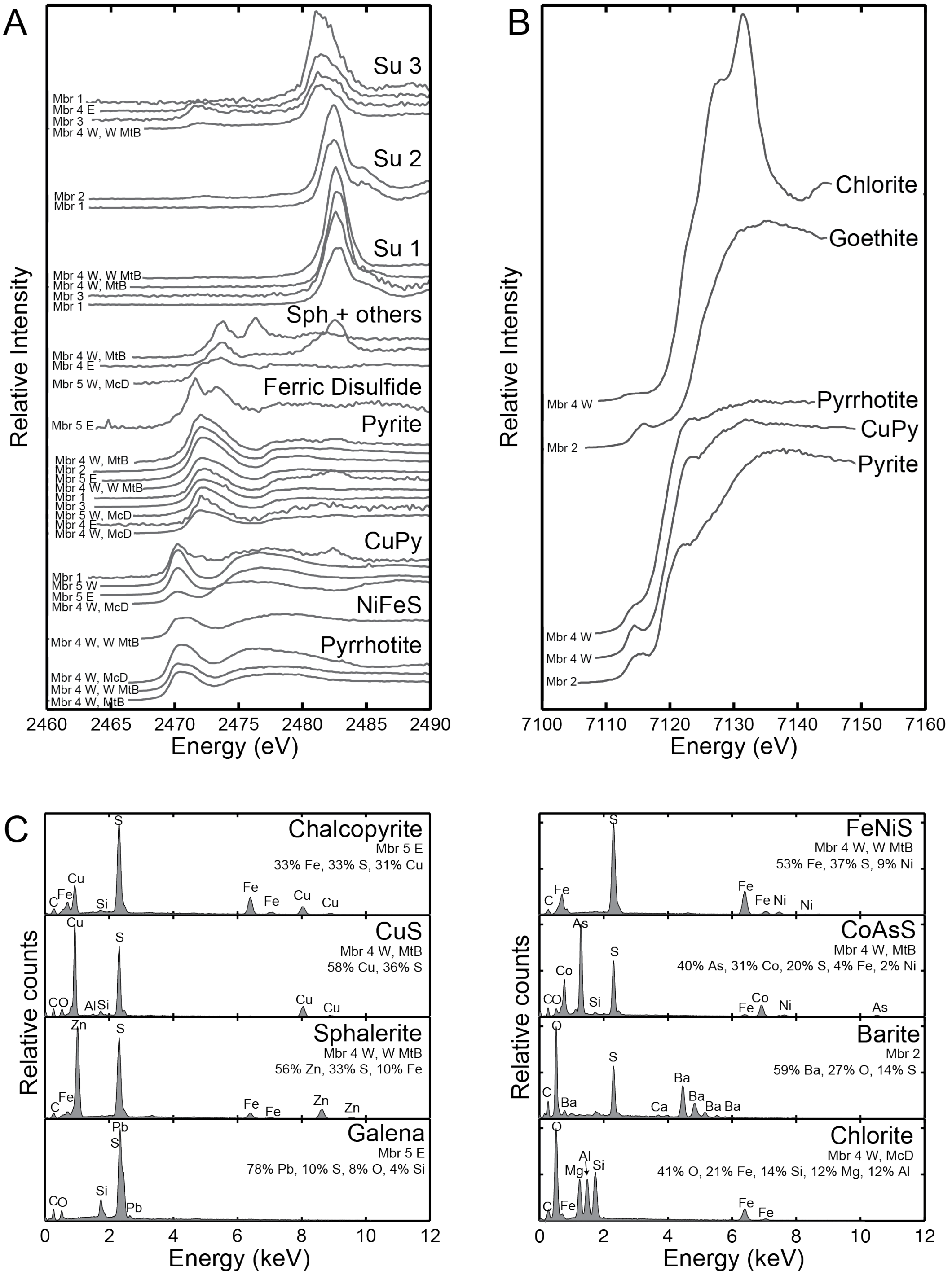

Figure 4.5: (A) End-member S X-ray absorption near-edge spectroscopy (XANES) spectra shown to exhibit mineralogical diversity found in each Appekunny member across different locations. Abbreviations for minerals: NiFeS—nickel iron monosulfide, CuPy—chalcopyrite, Sph—sphalerite, Su—sulfate. Abbreviations for location: E—east side, W—west side, MtB—east face

of Mount Brown, W MtB—west side of Mount Brown, McD—McDonald Creek. Note that three different sulfate phases are indicated by small shifts in the K-edge position. (B) End-member Fe XANES spectra for two samples, one from the member 2 and one from member 4 in McDonald Creek on the west side of Glacier National Park; abbreviation of CuPy—Chalcopyrite. (C) X-ray energy dispersive spectrometer (EDS) spectra for examples of chalcopyrite, copper sulfide, sphalerite, galena, iron nickel, sulfide, cobalt arsenic sulfide, barite and chlorite. Same abbreviations as part A; chemical composition is included in wt% of chemical species. Samples were carbon coated for analysis and carbon peaks result from this process.

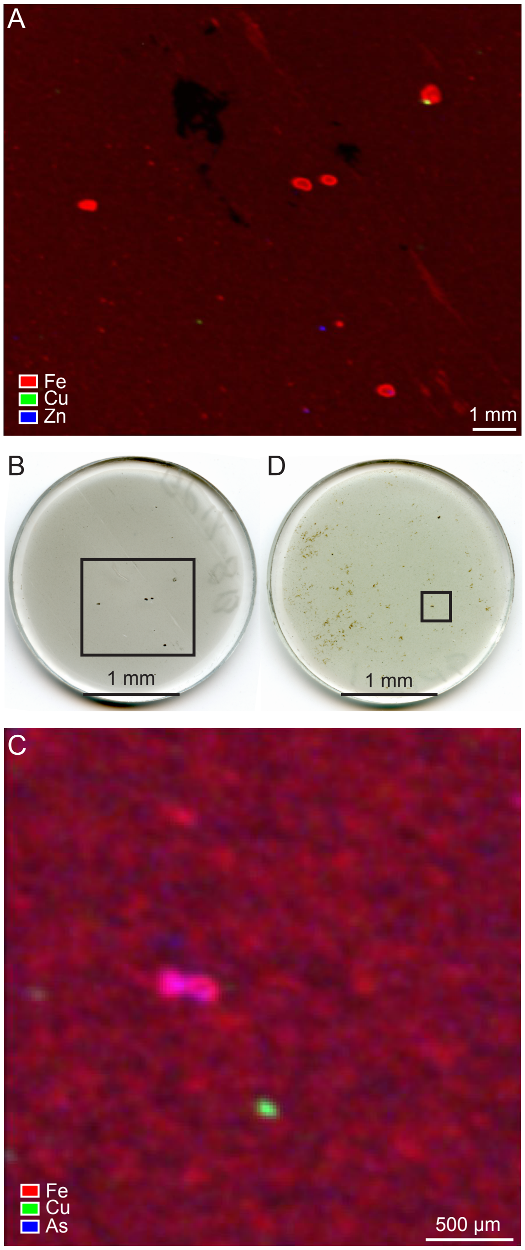

Figure 4.6: X-ray fluorescence (XRF) microprobe maps of elemental abundance used in quantification calculations as well as corresponding thin section scans. Each image has its own scale bar. (A) XRF for region 1 in GP12-8, member 4 west side on McDonald Creek. Color scales go from black at 0 to being brightly colored at maximum. Scale ranges are Fe = 0 to 4.69E-4 µg, Cu = 0 to 2.52E-5 µg, Zn = 0 to 9.20E-5 µg. (B) Scan of GP12-8 thin section showing region chosen for XRF map. (C) XRF for region 4 in GP12-1, member 2 east side. Color scales range from black at 0 to being brightly colored at maximum. Scale ranges are Fe = 0 to 4.38E-4 µg, Cu = 0 to 3.49E-6 µg, and As = 0 to 1.85E-6 µg. (D) Scan of GP12-1 thin section showing region chosen for XRF imaging.

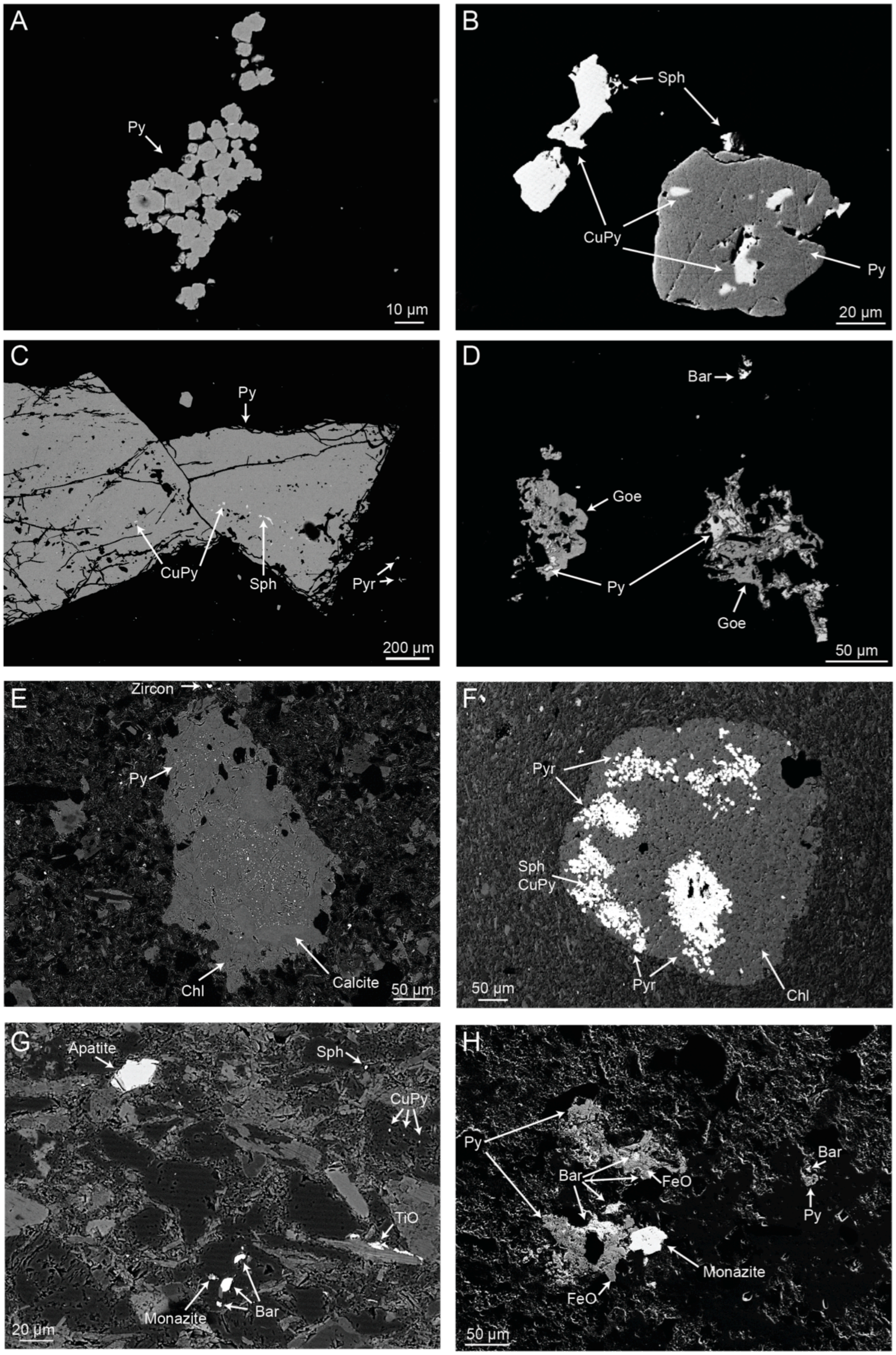

Figure 4.7: Backscatter Electron and Scanning Electron images each with own scale bar. Abbreviations for labeled minerals: Py—pyrite, CuPy—chalcopyrite,

Sph—sphalerite, Pyr—pyrrhotite, Goe—goethite, Bar—barite, Chl—chlorite, TiO—titanium oxide, FeO—iron oxide (generic). (A) Small framboidal pyrite grains in Appekunny member 3 (GP14-35). (B) Pyrite grain with inclusions of chalcopyrite and sphalerite as well as neighboring chalcopyrite grain in Appekunny member 5, east side outcropping (GP14-32). (C) Large nodular pyrite grain with small neighboring pyrrhotite grains in member 4/Prichard west side of park (GP14-6). (D) Goethite surrounding pyrite grains interpreted as replacement of euhedral recrystallized nodules in member 2 (GP12-1). (E) Small pyrite grains within carbonate nodule, rimmed by chlorite in member 5 west side of park (GP14-27). (F) Chlorite rim replacing pyrrhotite nodule in member 4/Prichard west side of park (GP12-8). (G) Individual barite grains far from sulfides or other sulfates in member 1 (GP14-10). (H) Barite rimming pyrite and iron oxides filling spaces as well as replacing grains in member 2 (GP14-11).

4.12 Supplemental Tables

Table S4.1: Detailed Sample Data For Glacier National Park Samples

Sample	GPS Location		Formation	Side of Park	Descriptive Location	Lithology
	Lat (°N)	Long (°W)				
GP14-8	48.69420	113.54347	Appekunny Member 1	East	Going-to-the-Sun Road, St. Mary Lake	Red claystone and siltstone in even microlaminae
GP14-10	48.69485	113.54699	Appekunny Member 1	East	Going-to-the-Sun Road, St. Mary Lake	Green siltstone from tabular weathering siltstone with even couplets, near ripple cross stratification
GP12-1	48.68959	113.55764	Appekunny Member 2	East	Going-to-the-Sun Road, St. Mary Lake	Massive-weathering green siltstone with concoidal fractures, near wavy laminations and soft sediment deformation
GP14-11	48.68952	113.55772	Appekunny Member 2	East	Going-to-the-Sun Road, St. Mary Lake	Massive-weathering green siltstone near faint wavy laminations and soft sediment deformation
GP14-34	48.68609	113.56375	Appekunny Member 3	East	Going-to-the-Sun Road, St. Mary Lake	Green siltstone with wavy laminations and silt-clay couplets, large m-scale hummocks
GP14-35	48.68449	113.56968	Appekunny Member 3	East	Going-to-the-Sun Road, St. Mary Lake	Green siltstone in large m-scale hummock, wavy laminations and silt-clay couplets
GP14-29	48.67574	113.57782	Appekunny Member 4	East	Sun Point, St. Mary Lake	Grayish green interbedded siltstone and claystone with shaly parting and microlaminae, oxidized bedding planes and fractures
GP14-30	48.67524	113.57734	Appekunny Member 4	East	Sun Point, St. Mary Lake	Gray siltstone and claystone in microlaminae, even couplets, and lenticular couplets with soft sediment deformation and oxidized bedding planes
GP14-32	48.67810	113.58099	Appekunny Member 5	East	Sun Point, St. Mary Lake	Green claystone and siltstone in even and wavy microlaminae with mudcracks and mudchips with a few orangish laminations, near lenses of quartz sandstone
GP14-33	48.67961	113.58194	Appekunny Member 5	East	Sun Point, St. Mary Lake	Green claystone and siltstone in even microlaminae with mudcracks, mudchips, and other soft sediment deformation features, oxidized fractures
GP12-2	48.67411	113.61337	Grinnell	East	Going-to-the-Sun Road, St. Mary Lake	Red clay-rich siltstone with euhedral rhombohedral and cubic mm-sized psuedomorphs in siltstone-claystone even couplets with mudcracks and mudchips
GP12-3	48.67374	113.61325	Grinnell	East	Going-to-the-Sun Road, St. Mary Lake	Red interbedded claystone and siltstone microlaminae with mudcracks, mudchips, and other soft sediment deformation, euhedral rhombohedral and cubic mm-sized psuedomorphs
GP12-8	48.64159	113.85725	Prichard or Appekunny Member 4	West	McDonald Creek	Dark gray siltstone and claystone in even couplets and microlaminae with continuous laminae of mm-scale oxidizing iron sulfides
GP14-6	48.64593	113.83690	Prichard or Appekunny Member 4	West	West Mt. Brown	Dark gray siltstone and claystone in even couplets and microlaminae with continuous laminae of mm-scale oxidizing iron sulfides
GP14-1	48.61807	113.83498	Appekunny Member 4	West	East Mt. Brown	Green siltstone and gray claystone in even and pinch-and-swell couplets, oxidized iron sulfides
GP14-55	48.61634	113.84432	Appekunny Member 4	West	East Mt. Brown	Greenish grey siltstone and claystone wavy laminations with mudcracks and soft sediment deformation and oxidized bedding planes and mm-sized grains, vertical mm-wide quartz veins
GP14-27	48.65734	113.83917	Appekunny Member 5	West	McDonald Creek	Green mudchip breccia in orangish green siltstone, near even and wavy microlaminae of claystone and silstone with mudcracks and mudchips
GP14-28	48.65857	113.83808	Appekunny Member 5	West	McDonald Creek	Green claystone and siltstone in even microlaminae with mudcracks, mudchips and other soft sediment deformation, oxidization along fractures
GP14-4	48.61971	113.83451	Appekunny Member 5	West	East Mt. Brown	Massive-weathering green siltstone with microlaminae, mudcracks, mudchips, and soft sediment deformation
GP14-54	48.62255	113.83518	Appekunny Member 5	West	East Mt. Brown	Green siltstone and claystone microlaminae with mudchips, mudcracks, and other soft sediment deformation, vertical cm-wide quartz veins

4.13 References

Adam, Z., Mogk, D., Skidmore, M., and Butterfield, N., Microfossils from the Greyson Formation, Lower Belt Supergroup: Support for early Mesoproterozoic biozonation, *in* Proceedings Geological Society of America Abstracts with Programs2014, Volume 46, p. 71.

Anderson, H. E., and Davis, D. W., 1995, U-Pb geochronology of the Moyie sills, Purcell Supergroup, southeastern British Columbia: implications for the Mesoproterozoic geological history of the Purcell (Belt) basin: Canadian Journal of Earth Sciences, v. 32, no. 8, p. 1180-1193.

Asael, D., Tissot, F. L., Reinhard, C. T., Rouxel, O., Dauphas, N., Lyons, T. W., Ponzevera, E., Liorzou, C., and Chéron, S., 2013, Coupled molybdenum, iron and uranium stable isotopes as oceanic paleoredox proxies during the Paleoproterozoic Shunga Event: Chemical Geology, v. 362, p. 193-210.

Bowles, J., Jackson, M., and Banerjee, S., 2010, Interpretation of low-temperature data Part II: the Hematite Morin transition: IRM Quarterly, v. 20, p. 1-10.

Canfield, D., 1998, A new model for Proterozoic ocean chemistry: Nature, v. 396, no. 6710, p. 450-453.

Canfield, D. E., and Berner, R. A., 1987, Dissolution and pyritization of magnetite in anoxie marine sediments: Geochimica et Cosmochimica Acta, v. 51, no. 3, p. 645-659.

Carpenter, R. H., 1974, Pyrrhotite isograd in southeastern Tennessee and southwestern North Carolina: Geological Society of America Bulletin, v. 85, no. 3, p. 451-456.

Cloud, P. E., 1968, Atmospheric and Hydrospheric Evolution on the Primitive Earth: Science, v. 160, no. 3829, p. 729-736.

Craig, J. R., and Vokes, F. M., 1993, The metamorphism of pyrite and pyritic ores: an overview: Mineralogical Magazine, v. 57, no. 1, p. 3-18.

Cressman, E. R., 1989, Reconnaissance stratigraphy of the Prichard Formation (Middle Proterozoic) and the early development of the Belt Basin, Washington, Idaho, and Montana: United States Geological Survey, Professional Paper, v. 1490, p. 80.

Dahlstrom, C. D., 1970, Structural geology in the eastern margin of the Canadian Rocky Mountains: Bulletin of Canadian Petroleum Geology, v. 18, no. 3, p. 332-406.

Day, R., Fuller, M., and Schmidt, V., 1977, Hysteresis properties of titanomagnetites: grain-size and compositional dependence: Physics of the Earth and Planetary Interiors, v. 13, no. 4, p. 260-267.

Dong, L., Xiao, S., Shen, B., and Zhou, C., 2008, Silicified Horodyskia and Palaeopascichnus from upper Ediacaran cherts in South China: tentative phylogenetic interpretation and implications for evolutionary stasis: Journal of the Geological Society, v. 165, no. 1, p. 367-378.

Duke, E. F., and Lewis, R. S., 2010, Near infrared spectra of white mica in the Belt Supergroup and implications for metamorphism: American Mineralogist, v. 95, no. 7, p. 908-920.

Dunlop, D. J., 2002, Theory and application of the Day plot (Mrs/Ms versus Hcr/Hc) 1. Theoretical curves and tests using titanomagnetite data: Journal of Geophysical Research: Solid Earth, v. 107, no. B3, p. EPM 4-1-EPM 4-22.

Dunlop, D. J., and Özdemir, Ö., 1997, Rock magnetism: fundamentals and frontiers, Cambridge University Press.

Elston, D., Enkin, R., Baker, J., and Kisilevsky, D., 2002, Tightening the Belt: Paleomagnetic-stratigraphic constraints on deposition, correlation, and deformation of the Middle Proterozoic (ca. 1.4 Ga) Belt-Purcell Supergroup, United States and Canada: Geological Society of America Bulletin, v. 114, no. 5, p. 619-638.

Eslinger, E. V., and Savin, S. M., 1973, Oxygen isotope geothermometry of the burial metamorphic rocks of the Precambrian Belt Supergroup, Glacier National Park, Montana: Geological Society of America Bulletin, v. 84, no. 8, p. 2549-2560.

Evans, K. V., Aleinikoff, J. N., Obradovich, J. D., and Fanning, C. M., 2000, SHRIMP U-Pb geochronology of volcanic rocks, Belt Supergroup, western Montana: evidence for rapid deposition of sedimentary strata: Canadian Journal of Earth Sciences, v. 37, no. 9, p. 1287-1300.

Fedonkin, M. A., and Yochelson, E. L., 2002, Middle Proterozoic (1.5 Ga) Horodyskia moniliformis Yochelson and Fedonkin, the oldest known tissue-grade colonial eucaryote: Smithsonian Contributions to Paleobiology, v. 94, p. 29.

Ferry, J. M., 1984, A biotite isograd in south-central Maine, USA: mineral reactions, fluid transfer, and heat transfer: Journal of Petrology, v. 25, no. 4, p. 871-893.

-, 2007, The role of volatile transport by diffusion and dispersion in driving biotite-forming reactions during regional metamorphism of the Gile Mountain Formation, Vermont: American Mineralogist, v. 92, no. 8-9, p. 1288-1302.

Fleet, M. E., 2005, XANES spectroscopy of sulfur in earth materials: The Canadian Mineralogist, v. 43, no. 6, p. 1811-1838.

Frey, M., 1987, Low temperature metamorphism, Glasgow, Blackie.

Fuller, M., Cisowski, S., Hart, M., Haston, R., Schmidtke, E., and Jarrard, R., 1988, NRM-IRM(s) Demagnetization Plots - an Aid to the Interpretation of Natural Remanent Magnetization: Geophysical Research Letters, v. 15, no. 5, p. 518-521.

Fuller, M., Kidane, T., and Ali, J., 2002, AF demagnetization characteristics of NRM, compared with anhysteretic and saturation isothermal remanence: an aid in the interpretation of NRM: Physics and Chemistry of the Earth, v. 27, no. 25-31, p. 1169-1177.

Gellatly, A. M., and Lyons, T. W., 2005, Trace sulfate in mid-Proterozoic carbonates and the sulfur isotope record of biospheric evolution: Geochimica et Cosmochimica Acta, v. 69, no. 15, p. 3813-3829.

Gilleaudeau, G. J., and Kah, L. C., 2015, Heterogeneous redox conditions and a shallow chemocline in the Mesoproterozoic ocean: evidence from carbon–sulfur–iron relationships: Precambrian Research, v. 257, p. 94-108.

González-Álvarez, I., and Kerrich, R., 2010, REE and HFSE mobility due to protracted flow of basinal brines in the Mesoproterozoic Belt-Purcell Supergroup, Laurentia: Precambrian Research, v. 177, no. 3, p. 291-307.

González-Álvarez, I., Kusiak, M. A., and Kerrich, R., 2006, A trace element and chemical Th–U total Pb dating study in the lower Belt-Purcell Supergroup, Western North America: provenance and diagenetic implications: Chemical Geology, v. 230, no. 1, p. 140-160.

Graham, G., Hitzman, M. W., and Zieg, J., 2012, Geologic Setting, Sedimentary Architecture, and Paragenesis of the Mesoproterozoic Sediment-Hosted Sheep Creek Cu-Co-Ag Deposit, Helena Embayment, Montana: Economic Geology, v. 107, no. 6, p. 1115-1141.

Grey, K., and Williams, I. R., 1990, Problematic bedding-plane markings from the Middle Proterozoic Manganese Subgroup, Bangemall Basin, Western Australia: Precambrian Research, v. 46, no. 4, p. 307-327.

Griffith, E. M., and Paytan, A., 2012, Barite in the ocean–occurrence, geochemistry and palaeoceanographic applications: Sedimentology, v. 59, no. 6, p. 1817-1835.

Hall, A. J., 1986, Pyrite-pyrrhotine redox reactions in nature: Mineralogical Magazine, v. 50, p. 223-229.

Hamilton, J., Bishop, D., Morris, H., and Owens, O., 1982, Geology of the Sullivan orebody, Kimberley, BC, Canada: Precambrian Sulphide Deposits, v. 25, p. 597-665.

Hanor, J. S., 2000, Barite–celestine geochemistry and environments of formation: Reviews in Mineralogy and Geochemistry, v. 40, no. 1, p. 193-275.

Harrison, J. E., 1972, Precambrian Belt basin of northwestern United States: Its geometry, sedimentation, and copper occurrences: Geological Society of America Bulletin, v. 83, no. 5, p. 1215-1240.

Harrison, J. E., Whipple, J. W., Lidke, D. J., Helen, Z., and Miller, R. J., 1998, Geologic map of the western part of the Cut Bank 1 degree by 2 degrees Quadrangle, northwestern Montana, scale 1:250,000.

Heslop, D., Dekkers, M., Kruiver, P., and Van Oorschot, I., 2002, Analysis of isothermal remanent magnetization acquisition curves using the expectation-maximization algorithm: Geophysical Journal International, v. 148, no. 1, p. 58-64.

Hoffman, P. F., 1988, Belt basin: a landlocked remnant oceanic basin? (Analogous to the south Caspian Sea and Black Seas). Geol. Soc. Am. Ann. Mtg. Abst. Prog. 20, A50., Geological Society of America Annual Meeting, Abstracts, Volume 20, p. A40.

Hofmann, H. J., Ediacaran enigmas, and puzzles from earlier times, *in* Proceedings Geological Association of Canada - Mineralogical Association of Canada, Joint Annual Meetings, Abstracts,, St. Johns, 2001, Volume 26, p. 64-65.

Holland, H. D., 1984, The chemical evolution of the atmosphere and oceans, Princeton University Press.

-, 2006, The oxygenation of the atmosphere and oceans: Philosophical Transactions of the Royal Society B: Biological Sciences, v. 361, no. 1470, p. 903-915.

Horng, C.-S., and Roberts, A. P., 2006, Authigenic or detrital origin of pyrrhotite in sediments?: Resolving a paleomagnetic conundrum: Earth and Planetary Science Letters, v. 241, no. 3, p. 750-762.

Horodyski, R. J., 1982, Problematic bedding-plane markings from the middle Proterozoic Appekunny argillite, Belt Supergroup, northwestern Montana: Journal of Paleontology, p. 882-889.

-, 1993, Paleontology of Proterozoic shales and mudstones: examples from the Belt Supergroup, Chuar Group and Pahrump Group, western USA: Precambrian Research, v. 61, no. 3, p. 241-278.

Horodyski, R. J., Winston, D., and Whipple, J. W., 1989, Paleontology of the middle Proterozoic belt supergroup, *in* Winston, D., Horodyski, R. J., and Whipple, J. W., eds., Middle Proterozoic Belt Supergroup, Western Montana: Great Falls, Montana to Spokane, Washington: 28th International Geological Congress, Field Trip Guidebook T334, p. 7-26.

Hrouda, F., 2003, Indices for numerical characterization of the alteration processes of magnetic minerals taking place during investigation of temperature variation of magnetic susceptibility: Studia Geophysica et Geodaetica, v. 47, no. 4, p. 847-861.

Huebschman, R. P., 1973, Correlation of fine carbonaceous bands across a Precambrian stagnant basin: Journal of Sedimentary Research, v. 43, no. 3, p. 688-699.

Johnson, H. P., Lowrie, W., and Kent, D. V., 1975, Stability of anhysteretic remanent magnetization in fine and coarse magneitte and maghemite particles: Geophysical Journal of the Royal Astronomical Society, v. 41, no. 1, p. 1-10.

Johnson, J. E., Gerpheide, A., Lamb, M. P., and Fischer, W. W., 2014, O2 constraints from Paleoproterozoic detrital pyrite and uraninite: Geological Society of America Bulletin, v. 126, no. 5-6, p. 813-830.

Kendall, B., Creaser, R. A., Gordon, G. W., and Anbar, A. D., 2009, Re–Os and Mo isotope systematics of black shales from the Middle Proterozoic Velkerri and Wollogorang formations, McArthur Basin, northern Australia: Geochimica et Cosmochimica Acta, v. 73, no. 9, p. 2534-2558.

Kirschvink, J. L., Kopp, R. E., Raub, T. D., Baumgartner, C. T., and Holt, J. W., 2008, Rapid, precise, and high-sensitivity acquisition of paleomagnetic and rock-magnetic data: Development of a low-noise automatic sample changing system for superconducting rock magnetometers: Geochemistry Geophysics Geosystems, v. 9, no. 5.

Klein, F., Bach, W., Humphris, S. E., Kahl, W.-A., Jöns, N., Moskowitz, B., and Berquó, T. S., 2014, Magnetite in seafloor serpentinite—Some like it hot: Geology, v. 42, no. 2, p. 135-138.

Knoll, A. H., Javaux, E. J., Hewitt, D., and Cohen, P., 2006, Eukaryotic organisms in Proterozoic oceans: Philosophical Transactions of the Royal Society B: Biological Sciences, v. 361, no. 1470, p. 1023-1038.

Koski, R. A., and Hein, J. R., 2004, Stratiform barite deposits in the Roberts Mountains Allochthon, Nevada: a review of potential analogs in modern sea-floor environments, US Department of the Interior, US Geological Survey Bulletin, 17 p.:

Kozłowski, A., Kakol, Z., Kim, D., Zalecki, R., and Honig, J., 1996, Heat capacity of Fe 3-α M α O 4 (M= Zn, Ti, 0⩽ α⩽ 0.04): Physical Review B, v. 54, no. 17, p. 12093.

Larrasoaña, J. C., Roberts, A. P., Musgrave, R. J., Gràcia, E., Piñero, E., Vega, M., and Martínez-Ruiz, F., 2007, Diagenetic formation of greigite and pyrrhotite in gas hydrate marine sedimentary systems: Earth and Planetary Science Letters, v. 261, no. 3, p. 350-366.

Li, H. Y., and Zhang, S. H., 2005, Detection of Mineralogical Changes in Pyrite Using Measurements of Temperature ‐ Dependence Susceptibilities: Chinese Journal of Geophysics, v. 48, no. 6, p. 1454-1461.

Lowrie, W., and Fuller, M., 1971, Alternating field demagnetization characteristics of multidomain thermoremanent magnetization in magnetite: Journal of Geophysical Research, v. 76, no. 26, p. 6339-&.

Luepke, J. J., 1999, Goechemical trends in shales of the Belt Supergroup, Northwestern US: a marine model for the evolution of the Mesoproterozoic weatern Laurentian Margin [M.S. thesis: University Missouri-Columbia, 133 p.

Luepke, J. J., and Lyons, T. W., 2001, Pre-Rodinian (Mesoproterozoic) supercontinental rifting along the western margin of Laurentia: geochemical evidence from the Belt-Purcell Supergroup: Precambrian Research, v. 111, no. 1, p. 79-90.

Lyons, T. W., Luepke, J. J., Schreiber, M. E., and Zieg, G. A., 2000, Sulfur geochemical constraints on Mesoproterozoic restricted marine deposition: lower Belt Supergroup, northwestern United States: Geochimica et Cosmochimica Acta, v. 64, no. 3, p. 427-437.

Lyons, T. W., and Severmann, S., 2006, A critical look at iron paleoredox proxies: new insights from modern euxinic marine basins: Geochimica et Cosmochimica Acta, v. 70, no. 23, p. 5698-5722.

Maxwell, D., and Hower, J., 1967, High-grade diagenesis and low-grade metamorphism of illite in Precambrian Belt Series: American Mineralogist, v. 52, no. 5-6, p. 843-857.

Minyuk, P., Subbotnikova, T., and Plyashkevich, A., 2011, Measurements of thermal magnetic susceptibility of hematite and goethite: Izvestiya, Physics of the Solid Earth, v. 47, no. 9, p. 762-774.

Minyuk, P., Tyukova, E., Subbotnikova, T., Kazansky, A. Y., and Fedotov, A., 2013, Thermal magnetic susceptibility data on natural iron sulfides of northeastern Russia: Russian Geology and Geophysics, v. 54, no. 4, p. 464-474.

Moreau, M., Ader, M., and Enkin, R., 2005, The magnetization of clay-rich rocks in sedimentary basins: low-temperature experimental formation of magnetic carriers in natural samples: Earth and Planetary Science Letters, v. 230, no. 1, p. 193-210.

Moskowitz, B. M., Jackson, M., and Kissel, C., 1998, Low-temperature magnetic behavior of titanomagnetites: Earth and Planetary Science Letters, v. 157, no. 3, p. 141-149.

Mudge, M. R., Erickson, R. L., Kleinkopf, M. D., and Zartman, R. E., 1968, Reconnaissance geology, geophysics, and geochemistry of the southeastern part of the Lewis and Clark Range, Montana: US Government Print Office.

O'Reilly, W., 1984, Rock and Mineral Magnetism, New York, Chapman and Hall.

O’Day, P. A., Rivera, N., Root, R., and Carroll, S. A., 2004, X-ray absorption spectroscopic study of Fe reference compounds for the analysis of natural sediments: American Mineralogist, v. 89, no. 4, p. 572-585.

Peters, C., and Dekkers, M., 2003, Selected room temperature magnetic parameters as a function of mineralogy, concentration and grain size: Physics and Chemistry of the Earth, v. 28, no. 16, p. 659-667.

Piatak, N. M., Seal, R. R., Sanzolone, R. F., Lamothe, P. J., Brown, Z., and Adams, M., 2007, Sequential extraction results and mineralogy of mine waste and stream sediments associated with metal mines in Vermont, Maine, and New Zealand: US Geological Survey Open-File Report, v. 1063, p. 34.

Planavsky, N. J., McGoldrick, P., Scott, C. T., Li, C., Reinhard, C. T., Kelly, A. E., Chu, X., Bekker, A., Love, G. D., and Lyons, T. W., 2011, Widespread iron-rich conditions in the mid-Proterozoic ocean: Nature, v. 477, no. 7365, p. 448-451.

Potter, D., and Stephenson, A., 1986, The detection of fine particles of magnetite using anhysteretic and rotational remanent magnetizations: Geophysical Journal International, v. 87, no. 2, p. 569-582.

Poulton, S. W., and Canfield, D. E., 2011, Ferruginous conditions: a dominant feature of the ocean through Earth's history: Elements, v. 7, no. 2, p. 107-112.

Pratt, B. R., 2001, Oceanography, bathymetry and syndepositional tectonics of a Precambrian intracratonic basin: integrating sediments, storms, earthquakes and tsunamis in the Belt Supergroup (Helena Formation, ca. 1.45 Ga), western North America: Sedimentary Geology, v. 141, p. 371-394.

Price, R., 1964, The Precambrian Purcell System in the Rocky Mountains of southern Alberta and British Columbia: Bulletin of Canadian Petroleum Geology, v. 12, no. 2, p. 399-426.

Raiswell, R., and Canfield, D. E., 1998, Sources of iron for pyrite formation in marine sediments: American Journal of Science, v. 298, no. 3, p. 219-245.

Raub, T., Johnson, S. C., and Raub, T. D., 2012, Rock magnetic detection of the pyrite-to-pyrrhotite reduction: applications to hydrocarbon maturity, mineral resources, and biogeochemistry, American Geophysical Union, Fall Meeting: San Francisco, CA, p. GP34A-08.

Retallack, G. J., Dunn, K. L., and Saxby, J., 2013, Problematic Mesoproterozoic fossil Horodyskia from Glacier National Park, Montana, USA: Precambrian Research, v. 226, p. 125-142.

Robertson, D., and France, D., 1994, Discrimination of remanence-carrying minerals in mixtures, using isothermal remanent magnetisation acquisition curves: Physics of the Earth and Planetary Interiors, v. 82, no. 3, p. 223-234.

Ross, C. P., 1959, Geology of Glacier National Park and the Flathead region, northwestern Montana: US Geological Survey Professional Paper, 2330-7102.

Ross, G. M., and Villeneuve, M., 2003, Provenance of the Mesoproterozoic (1.45 Ga) Belt basin (western North America): Another piece in the pre-Rodinia paleogeographic puzzle: Geological Society of America Bulletin, v. 115, no. 10, p. 1191-1217.

Schieber, J., 1989, Pyrite mineralization in microbial mats from the mid-Proterozoic Newland Formation, Belt Supergroup, Montana, USA: Sedimentary geology, v. 64, no. 1, p. 79-90.

Sears, J., Chamberlain, K., and Buckley, S., 1998, Structural and U-Pb geochronological evidence for 1.47 Ga rifting in the Belt basin, western Montana: Canadian Journal of Earth Sciences, v. 35, no. 4, p. 467-475.

Shannon, R. D., and White, J. R., 1991, The selectivity of a sequential extraction procedure for the determination of iron oxyhydroxides andiron sulfides in lake sediments: Biogeochemistry, v. 14, no. 3, p. 193-208.

Shen, Y., Knoll, A. H., and Walter, M. R., 2003, Evidence for low sulphate and anoxia in a mid-Proterozoic marine basin: Nature, v. 423, no. 6940, p. 632-635.

Skomurski, F. N., Kerisit, S., and Rosso, K. M., 2010, Structure, charge distribution, and electron hopping dynamics in magnetite (Fe 3 O 4)(100) surfaces from first principles: Geochimica et Cosmochimica Acta, v. 74, no. 15, p. 4234-4248.

Slack, J., Grenne, T., Bekker, A., Rouxel, O., and Lindberg, P., 2007, Suboxic deep seawater in the late Paleoproterozoic: evidence from hematitic chert and iron formation related to seafloor-hydrothermal sulfide deposits, central Arizona, USA: Earth and Planetary Science Letters, v. 255, no. 1, p. 243-256.

Slotznick, S. P., Zieg, J., Webb, S. M., Kirschvink, J. L., and Fischer, W. W., 2015, Iron Mineralogy and Redox Chemistry of the Mesoproterozoic Newland Formation in the Helena Embayment, Belt Supergroup, Montana: Northwest Geology, v. 44, p. 55-72.

Snowball, I. F., 1997, The detection of single-domain greigite (Fe3S4) using rotational remanent magnetization (RRM) and the effective gyro field (Bg): mineral magnetic and palaeomagnetic applications: Geophysical Journal International, v. 130, no. 3, p. 704-716.

Sperling, E., Rooney, A., Hays, L., Sergeev, V., Vorob'eva, N., Sergeeva, N., Selby, D., Johnston, D., and Knoll, A., 2014, Redox heterogeneity of subsurface waters in the Mesoproterozoic ocean: Geobiology, v. 12, no. 5, p. 373-386.

Sperling, E. A., Wolock, C. J., Morgan, A. S., Gill, B. C., Kunzmann, M., Halverson, G. P., Macdonald, F. A., Knoll, A. H., and Johnston, D. T., 2015, Statistical analysis of iron geochemical data suggests limited late Proterozoic oxygenation: Nature, v. 523, no. 7561, p. 451-454.

Stanley, A., and Davies-Vollum, K., 2000, A Detailed Sedimentary Analysis of the Middle Part of the Grinnell Formation, near Going-to-the-Sun Mountain, Glacier National Park, Montana, National Park Service Investigator's Annual Report 19879.

Stewart, J. H., 1972, Initial deposits in the Cordilleran geosyncline: Evidence of a late Precambrian (< 850 my) continental separation: Geological Society of America Bulletin, v. 83, no. 5, p. 1345-1360.

Stüeken, E. E., 2013, A test of the nitrogen-limitation hypothesis for retarded eukaryote radiation: nitrogen isotopes across a Mesoproterozoic basinal profile: Geochimica et Cosmochimica Acta, v. 120, p. 121-139.

Suzuki, Y., Kopp, R. E., Kogure, T., Suga, A., Takai, K., Tsuchida, S., Ozaki, N., Endo, K., Hashimoto, J., and Kato, Y., 2006, Sclerite formation in the hydrothermal-vent "scaly-foot" gastropod—possible control of iron sulfide biomineralization by the animal: Earth and Planetary Science Letters, v. 242, no. 1, p. 39-50.

Thomson, G. F., 1990, The anomalous demagnetization of pyrrhotite: Geophysical Journal International, v. 103, no. 2, p. 425-430.

Vitorello, I., and Van der Voo, R., 1977, Late Hadrynian and Helikian pole positions from the Spokane formation, Montana: Canadian Journal of Earth Sciences, v. 14, no. 1, p. 67-73.

Walcott, C. D., 1899, Pre-Cambrian fossiliferous formations: Geological Society of America Bulletin, v. 10, no. 1, p. 199-244.

Walter, M., Oehler, J. H., and Oehler, D. Z., 1976, Megascopic algae 1300 million years old from the Belt Supergroup, Montana: a reinterpretation of Walcott's Helminthoidichnites: Journal of Paleontology, v. 50, p. 872-881.

Walter, M., Rulin, D., and Horodyski, R. J., 1990, Coiled carbonaceous megafossils from the Middle Proterozoic of Jixian (Tianjin) and Montana: American Journal of Science, v. 290, p. 133-148.

Weaver, R., Roberts, A. P., and Barker, A. J., 2002, A late diagenetic (syn-folding) magnetization carried by pyrrhotite: implications for paleomagnetic studies from magnetic iron sulphide-bearing sediments: Earth and Planetary Science Letters, v. 200, no. 3, p. 371-386.

Webb, S. M., 2005, SIXPACK: A graphical user itnerface to XAS analysis using IFEFFIT: Physica Scripta, v. T115, p. 1011-1014.

-, 2011, The MicroAnalysis Toolkit: X-ray Fluorescence image processing software: AIP Conference Proceedings, v. 1365, p. 196-199.

Whipple, J., Binda, P., and Winston, D., Geologic guide to Glacier National Park, Montana and areas adjacent to Waterton, Alberta. Belt Symposium III, *in* Proceedings Geologic Guidebook to the Belt-Purcell Supergroup, Glacier

National Park and Vicinity, Montana and Adjacent Canada. Field Trip Guidebook for the Belt Symposium III. Belt Association, Pocatello, Idaho1997, p. 125-155.

Whipple, J. W., Connor, J. J., Raup, O. B., and McGimsey, R. G., Preliminary report on the stratigraphy of the Belt Supergroup, Glacier National Park and adjacent Whitefish Range, Montana, *in* Proceedings Northwest Montana and adjacent Canada. In: McBane, JD, Garrison, PB (Eds.), Guidebook, Field Conference and Symposium, Belt Association, Pocatello, Idaho, Montana Geol. Soc. 1984, p. 33-50.

Whipple, J. W., Donatich, A. J., and Williams, H. F., 1992, Geologic Map of Glacier National Park, Montana: US Geological Survey, scale 1:100000.

Wilkin, R., Barnes, H., and Brantley, S., 1996, The size distribution of framboidal pyrite in modern sediments: an indicator of redox conditions: Geochimica et Cosmochimica Acta, v. 60, no. 20, p. 3897-3912.

Willis, B., 1902, Stratigraphy and structure, Lewis and Livingston ranges, Montana: Geological Society of America Bulletin, v. 13, no. 1, p. 305-352.

Winston, D., 1986a, Belt supergroup stratigraphic correlation sections, western Montana and adjacent areas, Montana Bureau of Mines and Geology.

Winston, D., 1986b, Sedimentation and Tectonics of the Middle Proterozoic Belt Basin and Their Influence on Phanerozoic Compression and Extension in Western Montana and Northern Idaho: Part II. Northern Rocky Mountains, *in* Peterson, J. A., ed., Paleotectonics and sedimentation in the Rocky Mountain region, United States. American Association of Petroleum Geologists, Memoir 41, p. 87-118.

-, 1986c, Sedimentology of the Ravalli Group, middle Belt carbonate, and Missoula Group, Middle Proterozoic Belt Supergroup, Montana, Idaho and Washington: Belt Supergroup: A guide to Proterozoic rocks of western Montana and adjacent areas: Montana Bureau of Mines and Geology Special Publication, v. 94, p. 85-124.

-, 2007, Revised Stratigraphy and Depositional History of the Helena and Wallace Formations, Mid-Proterozoic Piegan Group, Belt Supergroup Montana and Idaho: SPECIAL PUBLICATION-SEPM, v. 86, p. 65.

Winston, D., 2016, Sheetflood sedimentology of the Middle Proterozoic Revett Formation, Belt Supergroup, Montana, USA: Geological Society of America Special Paper s, v. 522.

Winston, D., and Link, P., 1993, Middle Proterozoic rocks of Montana, Idaho and eastern Washington: the Belt Supergroup: Precambrian: Conterminous US: The Geology of North America, v. 2, p. 487-517.

Xu, S., and Dunlop, D. J., 1995, Toward a better understanding of the Lowrie‐Fuller test: Journal of Geophysical Research: Solid Earth (1978‐2012), v. 100, no. B11, p. 22533-22542.

Zhang, C., Paterson, G. A., and Liu, Q., 2012, A new mechanism for the magnetic enhancement of hematite during heating: the role of clay minerals: Studia Geophysica et Geodaetica, v. 56, no. 3, p. 845-860.

Zhou, T., Phillips, G. N., Dong, G., and Myers, R. E., 1995, Pyrrhotite in the Witwatersrand gold fields, South Africa: Economic Geology, v. 90, no. 8, p. 2361-2369.

Chapter 5

Iron Mineralogy, Secondary Overprints, and Paleoredox Conditions During Deposition of the Mid-Proterozoic Belt Supergroup

Coauthors:

Samuel M. Webb, Joseph L. Kirschvink, and Woodward W. Fischer

5.1 Abstract

Observing iron chemistry in sedimentary rocks is one of the primary methods for understanding ancient redox environments; however, major questions still revolve around Proterozoic redox chemistry after the rise of oxygen. We utilize a hybrid approach coupling microscale textural techniques of light microscopy, electron microscopy, magnetic microscopy, and (synchrotron) x-ray spectroscopy with bulk rock magnetic techniques to untangle complex iron mineralogy in a case study of the ~1.4 Ga lower Belt group, Belt Supergroup, Montana and Idaho. Samples were collected across a range of metamorphic, metasomatic, and diagenetic regimes to understand post-depositional iron transformation. A pyrrhotite-siderite isograd was identified marking metamorphic iron-bearing mineral reactions beginning in the sub-greenschist facies samples. Even in the best-preserved parts of the Belt Basin, secondary overprints were common including recrystallization of iron sulfide phases, base metal sulfides, and nano-phase pyrrhotite. Despite these overprints, some record of redox chemistry was preserved in the early diagenetic framboidal pyrite and detrital iron oxides including (sub)micron-sized magnetite. Although only a small percentage of the samples (<10 ppm), this magnetite represents an important supply of highly-reactive iron to the basin for the formation of pyrite. Based on our analyses, we interpret the Belt Basin as having shallow oxic waters overlying sediments with anoxic and sulfidic pore fluids, potentially with suboxic or euxinic deep waters, consistent with the redox results from some earlier studies and evidence for eukaryotes.

5.2 Introduction

Understanding the early Earth's atmospheric and oceanic chemistry has important implications for understanding the evolution of life. Specifically, paleoredox during the Proterozoic is vital to understanding the emergence of eukaryotes and multicellular life since both depend on oxygen for biosynthesis and for metabolic processes (Embley and Martin, 2006; Summons et al., 2006). Almost all eukaryotes today contain mitochondria, which are also believed to be in the last common eukaryotic ancestor (Embley and Martin, 2006), and the mitochondrial aerobic respiration pathway requires oxic environments with approximately 0.01 present atmospheric oxygen levels before organisms are forced to utilize other metabolisms such as fermentation or die (Berkner and Mashall, 1964; Fischer, 2016).

Observations of iron chemistry and mineralogy in sedimentary rocks have been utilized for decades to understand ancient environmental redox shifts, primarily due to iron's redox sensitivity as it cycles between +II and +III valence states (e.g. Cloud, 1968; Holland, 1984). One popular method of measuring iron and iron redox in rock samples is iron speciation, a bulk sequential chemical extraction technique measuring the proportions of different reactive iron species, which are mapped to redox conditions based on empirical calibrations from modern sediment samples (Poulton and Canfield, 2005, 2011). Iron speciation gives surprising results that have dramatically altered views on Proterozoic geochemistry, revealing a complex picture of predominately anoxic iron-rich (i.e. ferruginous) conditions with additional oxic and anoxic H2S-rich (i.e. euxinic) environments varying in time, geography, and water depth (e.g. Gilleaudeau and Kah, 2015; Kendall et al., 2009; Planavsky et al., 2011; Shen et al., 2003; Sperling et al., 2014). However, it is poorly understood how post-depositional processes such as diagenesis, metamorphism and metasomatism could affect these proxies in the sedimentary rock record (e.g. Clarkson et al., 2014; Reinhard et al., 2013). We chose an alternative approach that allows us to analyze the redox state of iron within samples while also preserving textural data to understand how and when the iron-bearing minerals formed. In order to test the application of novel techniques to understand the iron mineralogy, post-depositional alteration, and paleoredox, we chose a location with well-known metamorphic gradients, the classic mid-Proterozoic basin of the Belt Supergroup.

5.3 Geology of the Belt Supergroup

The Belt Supergroup, dated between 1470 Ma and 1401 Ma (Anderson and Davis, 1995; Evans et al., 2000; Sears et al., 1998), is an extensive, well-preserved, mid-Proterozoic sedimentary succession, currently exposed across parts of Montana, Idaho, Washington, Alberta, and British Columbia (Fig. 5.1). Over 18 km thick stratigraphically in some regions (Winston and Link, 1993), the Belt Supergroup contains a mixture of siliciclastic and carbonate rocks (Fig. 5.2), deposited in a large intercontinental lake (e.g. Grotzinger, 1981; Winston, 1986) or a (restricted) marine setting (e.g. Cressman, 1989; Luepke and Lyons, 2001; Lyons et al., 2000). Paleontologically, the strata preserve an abundance of stromatolites and diverse micro- and macrofossils, some of which are interpreted to be eukaryotes (e.g. Horodyski et al., 1989; Knoll et al., 2006). Due to increased thickness to the west (burial metamorphism) and intrusions in the west of syndepositional sills and Cretaceous batholiths, metamorphic conditions range from sub-biotite facies in Glacier National Park and the Helena Embayment to garnet facies by Lake Pend Orielle to staurolite facies near batholiths in Idaho (Duke and Lewis, 2010) (Fig. 5.1).

We focus on the green, grey, and black shales, siltstones, and sandstones of the lower Belt group (Fig. 5.2, Fig. S5.1), which have been previously studied to understand redox conditions of mid-Proterozoic time. Based on sulfate levels, sulfur isotopes, nitrogen isotopes, and organic-carbon richness as well as basin-wide laminations reminiscent of the Black Sea, many previous studies on the Prichard, Newland, and Greyson Formations suggested a stratified euxinic basin with oxic surface waters (Gellatly and Lyons, 2005; Huebschman, 1973; Luepke and Lyons, 2001; Lyons et al., 2000; Stüeken, 2013). Additional support for euxinic bottom water conditions comes syndepositional to early diagenetic sulfide-hosted base metal deposits in the lower Belt group, notably the Pb-Zn-Ag Sullivan Deposit in British Columbia and the Cu-Co-Ag Black Butte Deposit in the Helena Embayment (Graham et al., 2012; Hamilton et al., 1982; Present et al., in review). However, contrary to these proxies, iron speciation results from the Newland Formation suggested predominantly ferruginous water column conditions with episodic euxinic events (Planavsky et al., 2011). Our study sheds light on this geochemical result, highlights important caveats in interpreting iron speciation results, and deconvolves complex iron mineralogy to make paleoredox interpretations.

5.4 Coupled Textural and Bulk Methods

When investigating rocks that have undergone diagenesis and metamorphism, it is necessary to observe samples at a microscale to connect chemistry and mineralogy with petrographic textures within the rocks and to ordinate mineralization using cross-cutting relationships. First, samples were made into thin or thick sections and studied using transmitted and reflected optical microscopy. Further petrographic observations were made in the Caltech GPS Division Analytical Facility using the Zeiss 1550VP Field Emission scanning electron microscope with a Robinson-type backscatter electron detector for imaging. This instrument contains a paired Oxford X-Max SDD X-ray Energy Dispersive Spectrometer (EDS) system used to determine X-ray spectra of elemental abundance and HKL Electron Back Scatter Diffraction (EBSD) system used to determine structural information. Quantitative chemical information for formula derivation was determined using a JXA-8200 Electron Probe Micro-Analyzer (EPMA).

In addition to these more conventional textural analyses, we used Caltech's ultrahigh resolution scanning SQuID microscope (UHRSSM) to create 2D images of the magnetic field (sensitivity of 0.1 nT) at a resolution of 40 to 130 μm after giving samples a saturation magnetization in order to identify ferromagnetic minerals texturally. We also performed synchrotron-based X-ray spectroscopy at the Stanford Synchrotron Radiation Lightsource. High energy X-ray fluorescence (XRF) imaging was performed on thin and thick sections using energies from 20,200 eV to 10,000 eV at beam line 10-2 to characterize elemental abundances including trace metals over large regions in 30-35 μm pixels. Standards for quantification were run at each beam time session with the same collection parameters. Synchrotron-based X-ray absorption near-edge spectroscopy (XANES/XAS) was paired with XRF and elemental imaging using beam lines 14-3 and 2-3 at energies centering around the sulfur absorption edge (2472 eV) and the iron absorption edge (7112 eV) respectively. XANES was performed in fluorescence mode at specific 2-4 μm-sized spots to determine the chemical form of elements (oxidation state, orbital electronics, type and number of neighbors). Differences in the shape and K-edge of these absorption spectra can distinguish between a wide range of Fe- and S- bearing minerals (Fleet, 2005; O'Day et al., 2004). Additionally, XRF maps were collected at multiple excitation energies over the XANES spectrum, and images differentiating between phases, coordination environment and redox state were created by fitting the endmember spectra of different minerals from the sample to the XRF maps (e.g. Mayhew et al., 2011). XRF elemental maps were processed using the MicroAnalysis Toolkit (Webb, 2011) and XAS data was processed using SIXPACK (Webb, 2005).

On the same sample used for textural analyses and/or on a neighboring specimen, non-destructive bulk rock magnetic experiments were performed to observe fundamental magnetic properties that can distinguish between different magnetic minerals (e.g. Peters and Dekkers, 2003). Rock magnetic experiments were performed on all samples at the Caltech Paleomagnetics Laboratory using a 2G Enterprises SQuID magnetometer following the RAPID protocols, and analyzed using the RAPID Matlab scripts (Kirschvink et al., 2008). Our protocol includes measurements of alternating field (AF) demagnetization of the natural remanent magnetization (NRM), rotational remanent magnetization (RRM) acquisition and demagnetization, anhysteretic remanent magnetization (ARM) acquisition and demagnetization, isothermal remanent magnetization (IRM) acquisition and demagnetization, and backfield IRM acquisition. At the Institute for Rock Magnetism at the University of Minnesota, hysteresis loops and backfield acquisition measurements were also measured on all specimens at room temperature using a Princeton Measurements Vibrating Sample Magnetometer in order to characterize mineralogy, grain size, and magnetite abundance. Using the Quantum Designs Magnetic Property Measurement System (MPMS) at the Institute for Rock Magnetism, samples were cooled to 10 K under a variety of applied fields to confirm the presence of ferromagnetic minerals using unique low temperature transitions.

A total of 63 samples were analyzed using these coupled textural and bulk methods from all units of the lower Belt Supergroup (except the carbonate Altyn Formation) and the overlying red and green siliciclastic units of the lower Ravalli Group, spanning a range of metamorphic grades and paleo-water depths; additional description and GPS information can be found in Table S5.1, Slotznick et al. (2015), and Slotznick et al. (2016). Mineralogical results are summarized in Figure 5.1 with additional minerals listed in Table S5.2 and detailed data in Figures S5.2-S5.5.

5.5 Metamorphic Transformations and Diagenetic Overprints

By looking at correlated strata across a metamorphic gradient, we were able to demarcate a new iron-mineral isograd as well note other changes to iron-bearing minerals that occurred through progressive diagenesis/metamorphism. Recognized in both Glacier National Park (Slotznick et al., 2016) and in the Helena Embayment, pyrrhotite and siderite appear only in rocks in the western halves of these sub-basins, which we interpret as secondary overprints created by increased burial metamorphism (Fig. 5.1). Mineralogical variations based on outcropping of distinct stratigraphic units was controlled for by sampling stratigraphically correlated members of the Appekunny Formation across Glacier

National Park (Slotznick et al., 2016) and focusing on the lower Newland Formation across the Helena Embayment. Pyrrhotite can form from the metamorphic transformation of pyrite and addition of iron from neighboring iron-bearing minerals or from externally supplied iron-rich fluids; this reaction can begin at 200°C in the presence of organic matter or a reducing environment, with some experiments indicating transformation at even lower temperatures (Craig and Vokes, 1993; Hall, 1986; Moreau et al., 2005; Raub et al., 2012). Although pyrrhotite can be detrital or diagenetic in origin (Horng and Roberts, 2006; Larrasoaña et al., 2007), there is abundant pyrite, but no pyrrhotite in the Appekunny Formation on the east side of Glacier National Park and in the lower Belt units near White Sulphur Springs and the Black Butte Deposit, supporting our interpretation of a metamorphic isograd. Similarly, siderite as identified magnetically using RRM (Fig. S5.2) and its low temperature transition on the MPMS (Fig. S5.3), is only found in samples in the western halves of Glacier National Park and the Helena Embayment, while Fe-rich dolomite was identified chemically using EDS and EPMA across these sub-basins (Tables S5.2, S5.3). We believe that small domains of siderite formed as iron was repartitioned in these Fe-rich carbonates or was added from iron silicates, iron sulfides, or iron-rich fluids during burial metamorphism (e.g. French, 1973; Kholodov and Butuzova, 2008; Piché and Jébrak, 2006).

The pyrrhotite-siderite isograd occurs well below the biotite zone highlighting that these iron mineral reactions are occurring in rocks of very low metamorphic grade, often in rocks not considered “metamorphosed”. Both of these metamorphic reactions can utilize iron from within the pyrite, highly reactive iron, and silicate iron pools in a closed system or from external sources in an open system. Recent iron speciation studies often screen for pyrrhotite using hydrochloric acid extractions for acid-volatile sulfides (e.g. Asael et al., 2013; Li et al., 2015; Planavsky et al., 2011) and most methodologies have a separate carbonate extraction step, but if there is no petrography or investigation of iron source for these secondary minerals (e.g. Partin et al., 2015), interpretation of iron speciation studies can be difficult.

Pyrrhotite and siderite continue to be found through the biotite zone/greenschist facies rocks further west in the Belt Basin. Additional minerals suggest further transformations within the iron system, specifically the presence of an iron calcium aluminosilicate (epidote probably or pumpellyite) and an iron titanium oxide with trace Mn (ilmenite or titanomagnetite) (Table S5.2, Fig. 5.3C). Epidote and pumpellyite are common silicate metamorphic minerals of lower greenschist and prehnite-pumpellyite facies. Prior studies on regional metamorphic gradients do not discuss the presence of pumpellyite and classify the region as greenschist facies (Duke and Lewis, 2010 and references therein); epidote has been previously identified within the garnet zone (Cressman, 1989). Pumpellyite and epidote are proposed to form from reactions involving calcium aluminosilicates, muscovite, chlorite, carbonate, and/or Fe-rich external fluids (Bishop, 1972; Muffler and White, 1969). A reaction pathway utilizing carbonate is supported by the disappearance of the (large) Fe-rich dolomite grains, identified texturally in samples from Glacier National Park and the Helena Embayment. Biotite, ubiquitous through the Prichard Fm. (Table S5.2, S5.3) (Cressman, 1989), is also believed to form through the reaction of muscovite, chlorite, carbonates, iron oxides, iron sulfides, and/or fluids (Ferry, 1983, 1984, 2007). The iron titanium oxide with trace amounts of Mn likely formed from recrystallization of titanium oxides with other iron-bearing minerals or iron-rich fluids (Ferry, 1988); titanium oxides, identified using EDS, are common throughout the Glacier National Park and Helena Embayment regions, but become rarer to the west (Table S5.2). These metamorphic reactions highlight the mobility of iron in the greenschist facies; iron moves between the highly-reactive and silicate iron pools and possible external fluids can transport iron in an open system.

Quantitative analysis of our textural XRF maps highlights that there are similar amounts of iron and base metals across the Belt Basin with slight variations based on lithology and region, suggesting either similar initial provenance and redox chemistries or a wide-spread homogenization in post-depositional metamorphic events (Table S5.4). Although greater variance and higher trace metal abundances are seen in our data than prior work, previous bulk XRF and ICP-MS studies also suggested pervasive diagenetic basinal brines across the sub-biotite zone (González-Álvarez and Kerrich, 2010; González-Álvarez et al., 2006). Striking differences are only observed in Fe-Cu-As-Pb abundance within the massive sulfide zones of the Black Butte Deposit. Textural high-energy XRF maps (Figs. S5.6-S5.9) paired with S XANES and EDS-SEM images highlight that the plentiful base-metals identified throughout the lower Belt are usually mineralized as sulfides (Table S5.2). Even in the best preserved parts of the Belt Supergroup, the east side of Glacier National Park and the Helena Embayment far from the ore-containing sulfide zones, there are Cu, Pb, Zn, and Ag sulfides, highlighting the mobility of these metals as well as sulfur in secondary diagenetic recrystallization events probably involving diagenetic/metasomatic fluids in an open system (e.g. González-Álvarez and Kerrich, 2010; González-Álvarez et al., 2006). Sometimes base-metal sulfides occur as separate grains (Figs. S5.10, S5.15), but often there are multiple sulfide phases within the same nodule (Figs. 5.4, S5.12-S5.14), emphasizing that recrystallization of original iron minerals occurred to incorporate trace metals. MPMS experiments also identified nano-phase pyrrhotite, i.e. pyrrhotite below the micron-size-threshold for ferromagnetism, in most specimens that did not contain ferromagnetic pyrrhotite throughout the lower Belt (Figs. 5.5A, S5.3). This fine-grained pyrrhotite can form at temperatures of 85-95°C (Aubourg and Pozzi, 2010). Although the amount of nano-phase pyrrhotite cannot be quantified using our methods, its presence suggests that the pyrite-pyrrhotite metamorphic transformation had begun even east of the pyrrhotite-siderite gradient described above, probably in small domains within pyrite. The movement of iron from pyrite to any other phase or out of the system entirely will affect iron speciation proxies and make interpretations for paleoredox difficult.

Chlorite and calcite rims seen around trace-metal-bearing pyrrhotite and pyrite nodules in samples on the west side of Glacier National Park (Figs. 5.3D, 5.4) highlight an additional redox-transforming reaction moving iron from sulfides to silicates; therefore, more than one recrystallization event affected these slightly higher-grade rocks, which are still sub-biotite zone. Based on our textural analyses, we found that recrystallization is present across the entire Belt Basin, and most of the pyrite occurs in large euhedral grains cross-cutting fine-grained matrix minerals (e.g. Figs. S5.12, S5.17). However, there is a notable increase in grain size to the west, observable in both the matrix minerals and in the iron sulfides and oxides (compare Figs. 5.3ABEF, S5.10-S5.12 to Figs. 5.3D, 5.4, S5.13-S5.15 to Figs. 5.3AC, S5.16-S5.18). Coercivity spectra of the ferromagnetic minerals spanning the extent of the lower Belt Supergroup also highlight the recrystallization of magnetite into other minerals (Fig. S5.2); although conservatively, some of this change could be due to an increase in the proportion of other magnetic minerals. Previous work has suggested the formation of magnetite in the biotite zone based on petrography and trace element work of the Ravalli Group (Nadoll et al., 2012), and our sample from the Burke Formation also contains large multi-domain magnetite identified magnetically (Fig. 5.5B) and large euhedral (secondary) iron oxides up to 270 um identified petrographically. The coercivity spectrum of our Burke formation sample suggests two size populations of magnetite (Fig. S5.2) and the Fuller Test for nature of magnetization, which has only been calibrated for predominantly magnetite-bearing samples, suggests some of this magnetite is detrital due to the weak NRM:IRM ratio of 1:1000 (Fig. 5.5C) (Fuller et al., 1988; Fuller et al., 2002). For magnetite in the most westward sample of the Prichard Formation, the Fuller test suggests the magnetization carried is a chemical remanent magnetization (NRM:IRM ratio of 1:10) from recrystallization and/or precipitation of new magnetite (Fig. 5.5C). In these greenschist facies rocks, recrystallization events and metamorphic transformations have overprinted the primary record of iron-oxides and iron-sulfides as well as iron-silicates and carbonates in multiple events that may be impossible to separate. Studying the iron mineralogy of the lower Belt Supergroup both texturally and magnetically reveals the involvement of iron-bearing minerals in metamorphic and diagenetic alterations in an open system, which need to be peeled away to discover the primary mineralogy and paleoredox; a task that is simplified by focusing on the least-altered regions of the Belt Basin.

5.6 Primary Mineralogy and Paleoredox

One of the more surprising results of our mineralogical studies was the ubiquitous presence of magnetite in all samples from the lower Belt (other than the red Appekunny Member 1). We double checked initial findings from coercivity spectra (Fig. S5.2; Slotznick et al., 2016; Slotznick et al., 2015) using hysteresis loops and MPMS to confirm magnetite's presence in both well-preserved rocks as well as in samples from the sulfide zones of the Black Butte Deposit and western greenschist facies (Figs. 5.5A, S5.3, S5.4). In many samples from the east side of Glacier National Park and White Sulphur Springs regions, magnetite is the only ferromagnetic mineral. The Day Plot of these samples suggests that the grain size for much of magnetite is between 0.1 to 20 μm (pseudo-single domain) (Fig. 5.5B) (Day et al., 1977; Dunlop, 2002). The Fuller Test suggests the magnetite in the White Sulphur Springs and Glacier National Park regions is by and large detrital in origin, due to the NRM:IRM ratios of 1:1000 (Fig. 5.5C). We therefore interpret the magnetite as a highly-reactive iron residue remaining after scavenging by early diagenetic sulfides.

Magnetite abundance, calculated by comparing the saturation magnetization with that of magnetite (Klein et al., 2014), in all lower Belt samples is approximately 1-8 ppm with 1.2 wt% magnetite in the Burke Formation sample

(Table S5.5). We were unable to image the magnetite using the SEM due to its low-abundance. Notably, our magnetite abundance calculations are much lower than those determined by chemical extraction. Even once correcting by the stoichiometry of magnetite, our results are one order of magnitude lower than the 0.06 to 0.17 wt% extracted iron from magnetite from disseminated pyritic drill core shales of the Black Butte Deposit and another order of magnitude below 0.10 to 0.51 wt% iron from magnetite in the disseminated pyritic and sulfide zone drill core shales of the Soap Gulch Prospect (Lyons et al., 2000; Planavsky et al., 2011). Two explanations exist for this disparity: 1) The high ratio of paramagnetic minerals such as chlorite and illite to magnetite within the samples made hysteresis corrections and precise determination of saturation magnetization difficult (Fig. S5.4), which could also explain why calculated magnetite percentages show such a tight range, or 2) iron sequential extraction by ammonium oxalate (after sodium acetate and dithionite extractions) dissolved other minerals such as iron carbonates in addition to magnetite within the sample (e.g. Algoe et al., 2012; Raiswell et al., 2011; Reinhard et al., 2009).

Understanding this difference is important due to the relative amount of iron attributed to magnetite using iron speciation; in the Newland Formation samples, the iron from the ammonium oxalate extraction accounts 2 to 10% of the total iron in the Black Butte Deposit and 6 to 21% of the total iron in Soap Gulch samples. The high percentage of iron from the ammonium oxalate extraction, especially for Soap Gulch samples, is an important contributor to the iron speciation data implying ferruginous paleoredox for the Newland Formation. The Soap Gulch prospect is to the west of the pyrrhotite-siderite isograd, and both siderite and pyrrhotite, targeted for extraction in the sodium acetate extraction for carbonates (Poulton and Canfield, 2005; Reuschel et al., 2012), may not completely dissolve and then are sequentially extracted with magnetite (Burton et al., 2006; Raiswell et al., 2011; Reinhard et al., 2009). While all samples from both cores were tested to have < 0.1 wt% pyrrhotite (Planavsky et al., 2011), we are discussing percentages at the limits of chemical extraction so this amount could be important. Therefore the ferruginous iron speciation result in the Soap Gulch samples may come from issues with the sequential extraction technique and unrecognized metamorphic overprints moving iron from the pyrite or silicate pool toward the highly-reactive pool.

The main contributor for a ferruginous paleoredox interpretation from iron speciation of the Black Butte Deposit shales and an important factor for the Soap Gulch Prospect shales is the presence of iron carbonates. The Black Butte Deposit samples had a high percentage of iron extracted in the sodium acetate step (the carbonate pool) accounting for between 2 to 4% and 12 to 25% of the total iron in respectively pyrite-rich and pyrite-poor samples of the Black Butte Deposit and 2 to 16% of the total iron in Soap Gulch samples (Planavsky et al., 2011). Our study did find Fe-bearing dolomite within the Newland Formation and the Appekunny Formation in addition to the magnetic siderite in western samples (Tables S5.2, S5.3), but textural imaging of these carbonates suggests they are cements or secondary diagenetic transformations with clear zonation (Figs. 5.3D-F). Therefore, we interpret the Fe-bearing carbonates in the best preserved lower Belt samples as indicative of anoxic pore-water processes, not water column redox conditions.

Pyrite is present in almost all of the sampled lower Belt rocks, although it is often recrystallized as described above (Table S5.2). However, in the best-preserved rocks of the Appekunny and Newland Formations, there are examples of small aggregates of euhedral pyrite grains similar to the pyrite framboids observed in modern anoxic and sulfidic waters and sediments (Figs. 5.3ABF, S5.19E) (Wilkin and Barnes, 1997; Wilkin et al., 1996). Based on hydrodynamic calculations of suspension and settling, their large size suggests the pyrite formed in sedimentary pore fluids and comparison to modern examples suggests the sediments underlay oxic or suboxic waters (Wilkin et al., 1996). Other macro- and microscopic textures within drill-core of the Newland Formation such as differential compaction, pyritic debris flow clasts, and detrital pyrite tube structures emphasize the early timing of pyrite formation (Fig. S5.19) (Graham et al., 2012; Present et al., in review). Pyrite and these early diagenetic textures become more prevalent in the slightly deeper waters of the Newland Formation compared to the shallow Appekunny Formation suggesting an increased flux of organic matter and potentially more reducing water column conditions aiding in preservation (e.g. Lyons et al., 2000).

Directly overlying the lower Belt strata, the Grinnell Formation and the Spokane Formation are large deposits of shallow-water hematitic siltstone and shale, and Appekunny Member 1 also contains red strata. This oxidized iron highlights the oxic nature of shallow water environments in the Belt Basin. Detrital magnetite also served as an important flux of highly reactive iron to the basin; its preservation suggests water column and pore-fluid chemistry was not rich enough in either H_2S to scavenge all of the highly reactive iron to form pyrite or ferrous iron to recrystallize the detrital magnetite to chemically precipitate authigenic magnetite (Canfield and Berner, 1987; Lyons and Severmann, 2006; Skomurski et al., 2010). Early diagenetic pyrite framboids and Fe-dolomite diagenetic cements in the lower Belt samples highlight the presence of anoxic and sulfidic pore fluid conditions, potentially extending into deep portions of the water column.

5.7 Concluding Remarks

Major first-order questions exist about the paleoredox conditions during the Proterozoic. In the present study, we use a new approach utilizing iron systematics and iron's redox sensitivity to understand paleoenvironmental conditions. Our detailed microscale textural and bulk magnetic analyses on the case-example of the mid-Proterozoic Belt Supergroup found several overprinting alterations of iron-bearing minerals. In higher-grade strata, metamorphic transformations formed pyrrhotite, siderite, and iron-silicates in the sub-biotite zone and even in the best preserved rocks, diagenetic transformations occurred to form base-metal sulfides and nano-phase pyrrhotite. Both types of reactions probably occurred in a fluid-rich open system. Some primary minerals were preserved in the form of shallow hematite-rich red beds, ubiquitous fine-grained detrital magnetite, Fe-dolomite cements, and early diagenetic framboidal pyrite. Microscale textural observations were critical for untangling these signals to form a complete understanding of the Belt Basin. Our study concludes that deposition of the lower Belt strata occurred in oxic waters, potentially with suboxic to euxinic deep waters in permanent or episodic stratification, consistent with the results from some geochemical studies (Gellatly and Lyons, 2005; Huebschman, 1973; Luepke and Lyons, 2001; Lyons et al., 2000; Stüeken, 2013). Detrital fluxes of magnetite provided an input of highly reactive iron to the both the shallow and deep waters for the early diagenetic precipitation of pyrite in anoxic and sulfidic pore waters. Overall, this suggests a mid-Proterozoic basin chemistry inhabitable by eukaryotes that is very similar to water bodies today, in contrast to recent geochemical studies using the iron-speciation proxy which suggest predominantly ferruginous water column conditions.

Are ferruginous conditions compatible with our knowledge of microbial metabolic diversity and eukaryotic evolution by mid-Proterozoic time? Although ferrous iron will dominate ocean redox in the absence of life (Walker and Brimblecombe, 1985), upon the rise of atmospheric oxygen ~2.3 Ga, riverine input of detrital iron oxides and sulfate will substantially increase as seen in the Belt Supergroup (this study; Gellatly and Lyons, 2005; Present et al., in review). Although dissimilatory iron reduction could reduce iron oxides to maintain anoxic conditions, when sulfate is present in addition to iron (oxyhydr)oxides, fermentation and sulfate reduction metabolisms are preferred (Hansel et al., 2015; Lentini et al., 2012). All large anoxic basins in the modern are also sulfidic, e.g. the Black Sea and Cariaco Basin, due to sulfate reduction outpacing iron delivery (Berner, 1984; Lyons and Severmann, 2006), whereas the best studied modern ferruginous basins are lakes with incredibly low sulfate concentrations comparable to Archean values even in overlying oxic waters (Crowe et al., 2014; Halevy, 2013; Koeksoy et al., 2015). Although minimal sulfate delivery to the deep ocean has been suggested for mid-Proterozoic time (Poulton and Canfield, 2011), the presence of detrital iron minerals and water-column sulfate in deep waters such as within the Belt Basin raises questions about whether ferruginous conditions could have persisted in the ocean much beyond the Great Oxidation Event.

5.8 Acknowledgements

We thank Don Winston, Jerry Zieg, Mike Jackson, Courtney Roach, John Grotzinger, Tim Lyons, Austin Chadwick, and members of the 2013 Agouron Field Course, especially Ted Present and Kirsten Siebach, for assistance during sample collection and analysis. Samples from Glacier National Park were collected under NPS Collection Permits # GLAC-2012-SCI-0195 and GLAC-2014-SCI-0008. Support for this work was provided by the Agouron Institute, Tobacco Root Geological Society Scholarship, Belt Association Student Research Grant, Geological Society of America Student Research Grant, NASA Exobiology (W.W.F.), the David and Lucile Packard Foundation (W.W.F.), NSF Graduate Research Fellowship program (S.P.S.), NASA Earth and Space Fellowship (S.P.S.), and a PEO Scholar Award (S.P.S.). Portions of this research were carried out at the Stanford Synchrotron Radiation Lightsource, a Directorate of SLAC National Accelerator Laboratory and an Office of Science User Facility operated for the U.S. Department of Energy Office of Science by Stanford University. Part of this work was performed as a US Visiting Student Fellow at the Institute for Rock Magnetism at the University of Minnesota, a US National Multi-user Facility supported through the Instrumentation and Facilities program of the National Science Foundation, Earth Sciences Division, and by funding from the University of Minnesota.

5.9 Figures

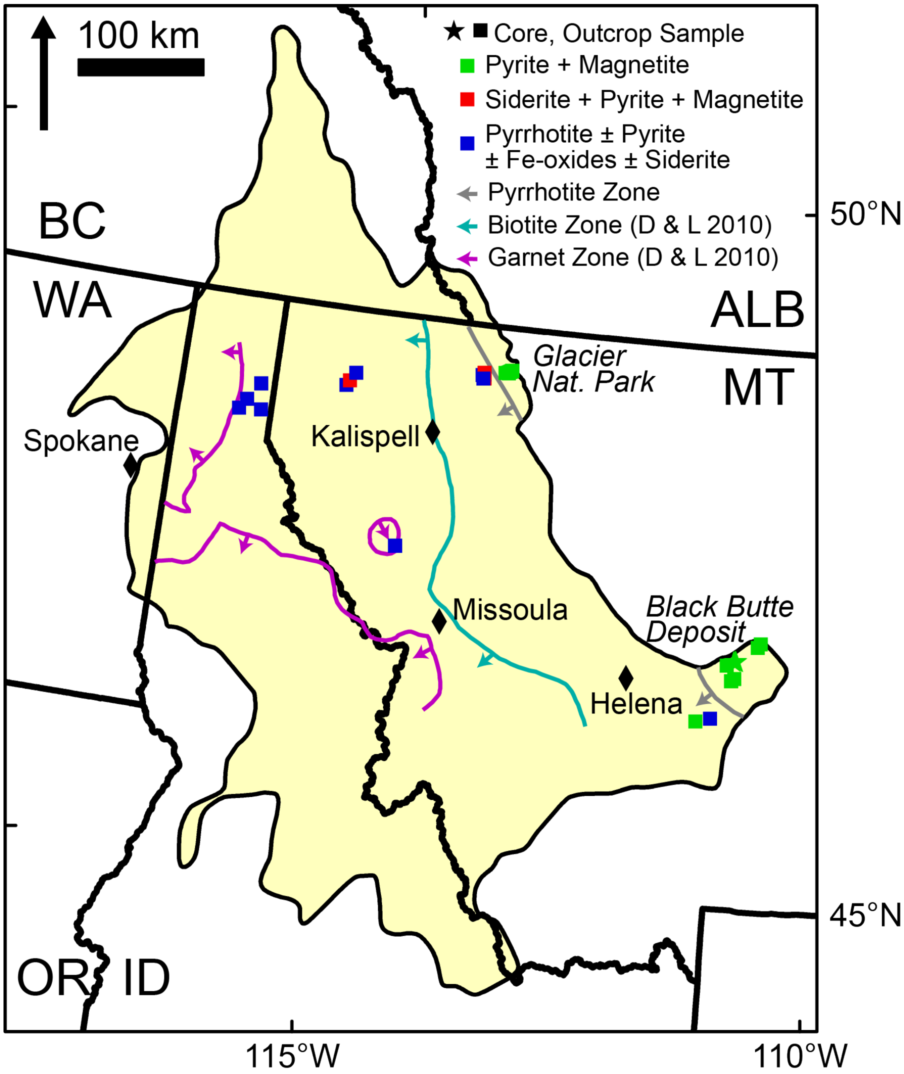

Figure 5.1: Map of the extent of the Belt Supergroup with samples from the lower Belt and Burke Formation color-coded by iron mineralogy with overlain metamorphic zone contours (this study; Duke and Lewis, 2010).

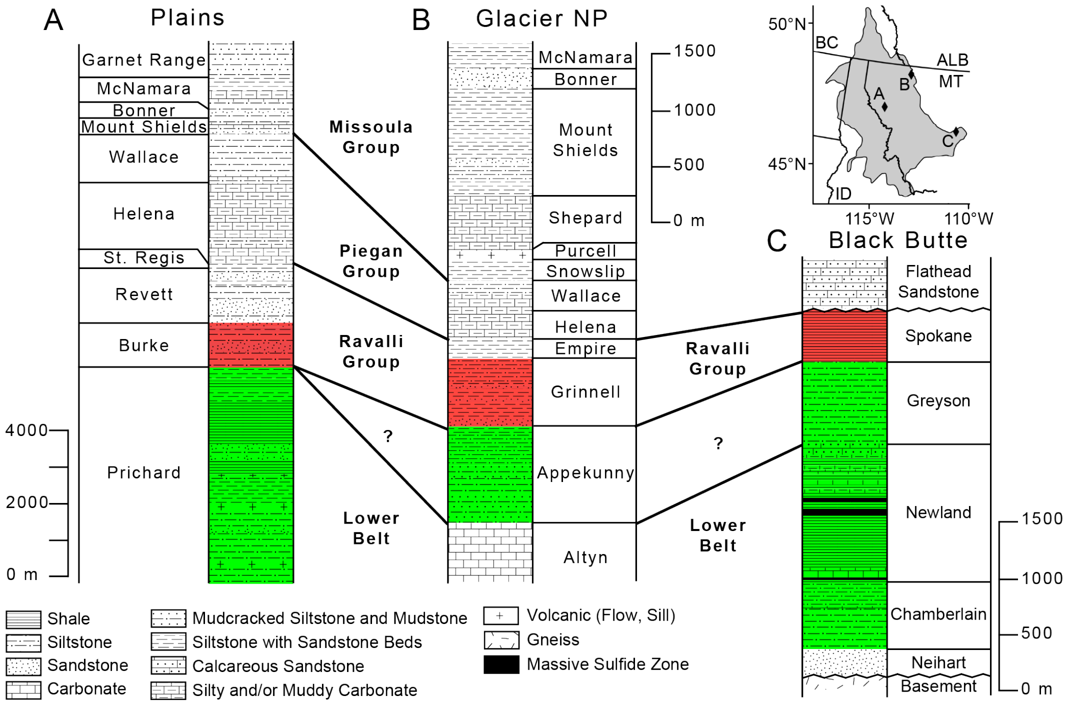

Figure 5.2: Stratigraphic nomenclature, relationships, and thickness across the Belt Basin. The lower Belt formations that are the focus of this study are shaded in green, and a few samples come from the overlying Ravalli Group formations shaded in red; these do not represent true rock color (see Fig. S5.1, S5.19). A) Stratigraphy at Plains representing nomenclature for western Montana and Idaho, B) Stratigraphy on the east side of Glacier National Park, C) Stratigraphy near the Black Butte Deposit, White Sulphur Springs representing nomenclature for the entire Helena Embayment. Note A is a different scale than B and C. Stratigraphic data from (Cressman, 1989; Harrison, 1972; Slotznick et al., 2016; Winston, 2007; Winston and Link, 1993; Zieg et al., 2013).

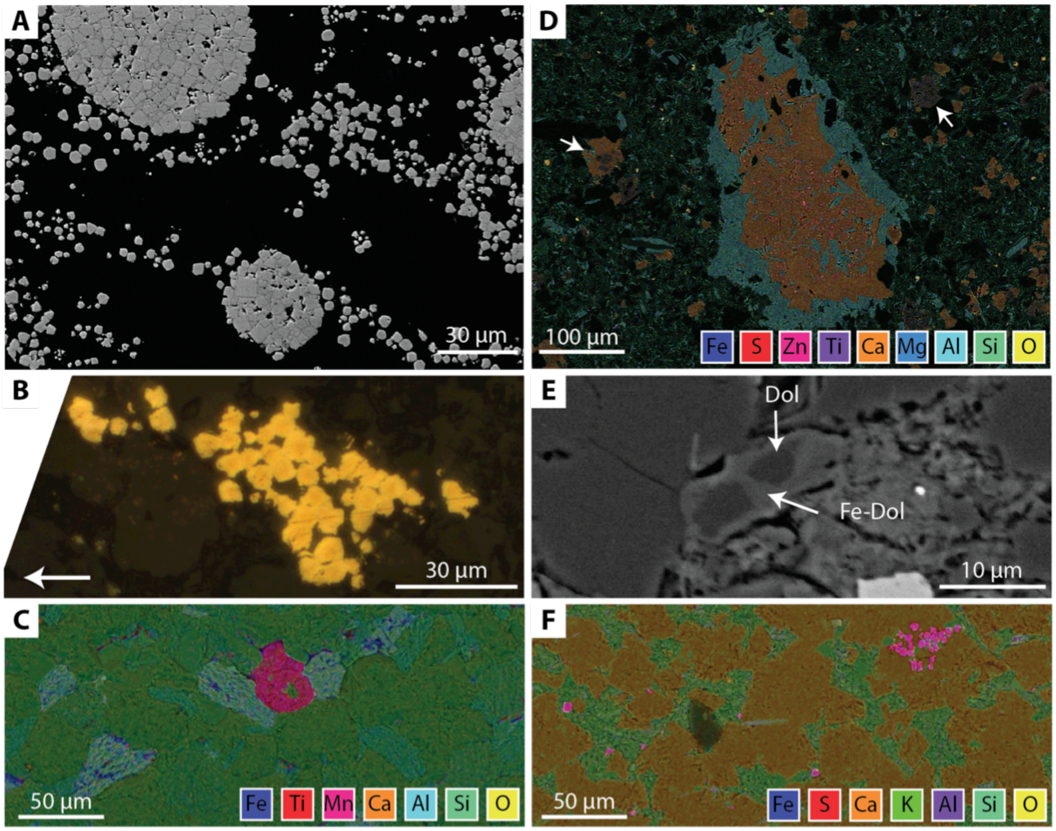

Figure 5.3: Textural examples from lower Belt samples using backscatter electron imaging, reflected light microscopy, or energy dispersive X-ray spectroscopy (EDS) overlain on backscatter images, each with own scale bar (and chemical color-code key) and all field-oriented unless otherwise stated. A) Recrystallized framboidal iron sulfides in Newland Formation, sulfide-zone Black Butte Deposit drill core sample (T095-389), B) Pyrite disaggregated framboids from Appekunny Formation, Member 3, east side of Glacier National Park (GP14-35) with arrow pointing in field up-direction, C) FeTiMnO grain and surrounding coarse-grained matrix from Prichard Formation, Transition Member, Libby (BS13-37), D) Small pyrite grains within calcite nodule rimmed by chlorite with Fe-dolomite or zoned calcite and Fe-dolomite grains pointed out with arrows in Appekunny Formation, Member 5, west side of Glacier National Park (GP14-27), E) Dolomite (Dol) rimmed by Fe-bearing dolomite (Fe-Dol) in Appekunny Formation, Member 3, east side of Glacier National Park (GP14-35), F) Fe-bearing dolomite cements in Newland Formation, far from sulfide zones in the Black Butte Deposit drill core (T112-334).

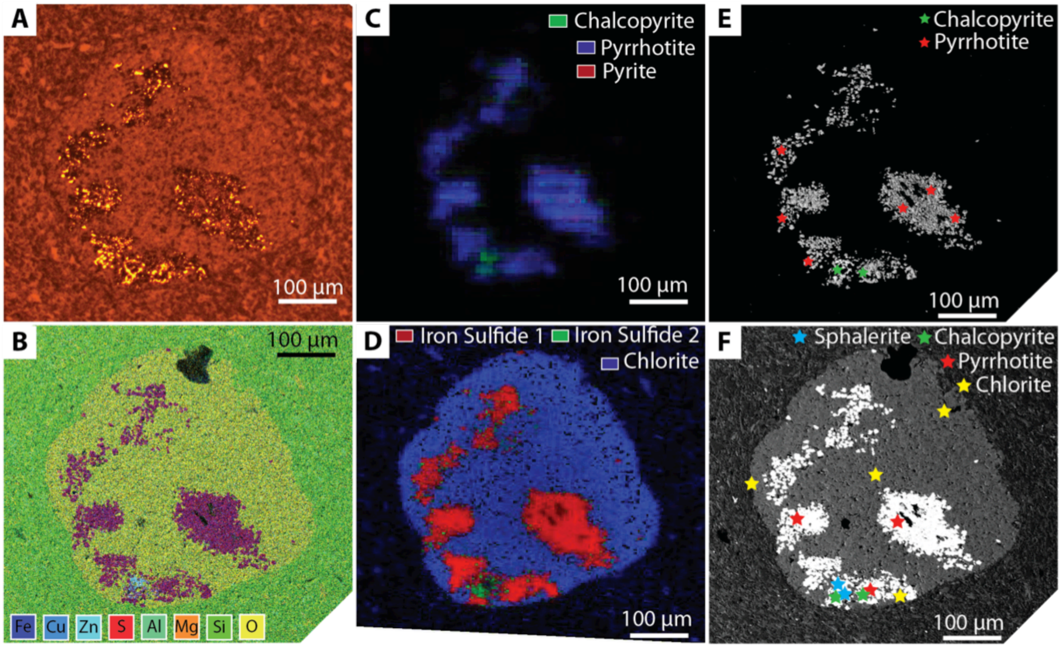

Figure 5.4: Detailed textural analysis of sample GP12-8, Appekunny Formation Member 4 or Prichard Formation, west side of Glacier National Park revealing a pyrrhotite nodule recrystallized with chalcopyrite and sphalerite inclusions and secondary chlorite replacing the original nodule. A) Reflected light microscopy, B) Energy dispersive X-ray spectroscopy (EDS), C) Synchrotron-based X-ray absorption near-edge spectroscopy (XANES) at sulfur energies, D) XANES at iron energies, E) Electron backscatter diffraction (EBSD) point mineral identifications on backscatter electron image, F) Electron probe micro-analyzer (EPMA) point mineral identifications (see Table S5.3 for details) on backscatter electron image. For XANES endmember fitted spectra, EBSD diffraction patterns, and ultrahigh resolution scanning SQuID microscope (UHRSSM) imagery see Figure S5.13.

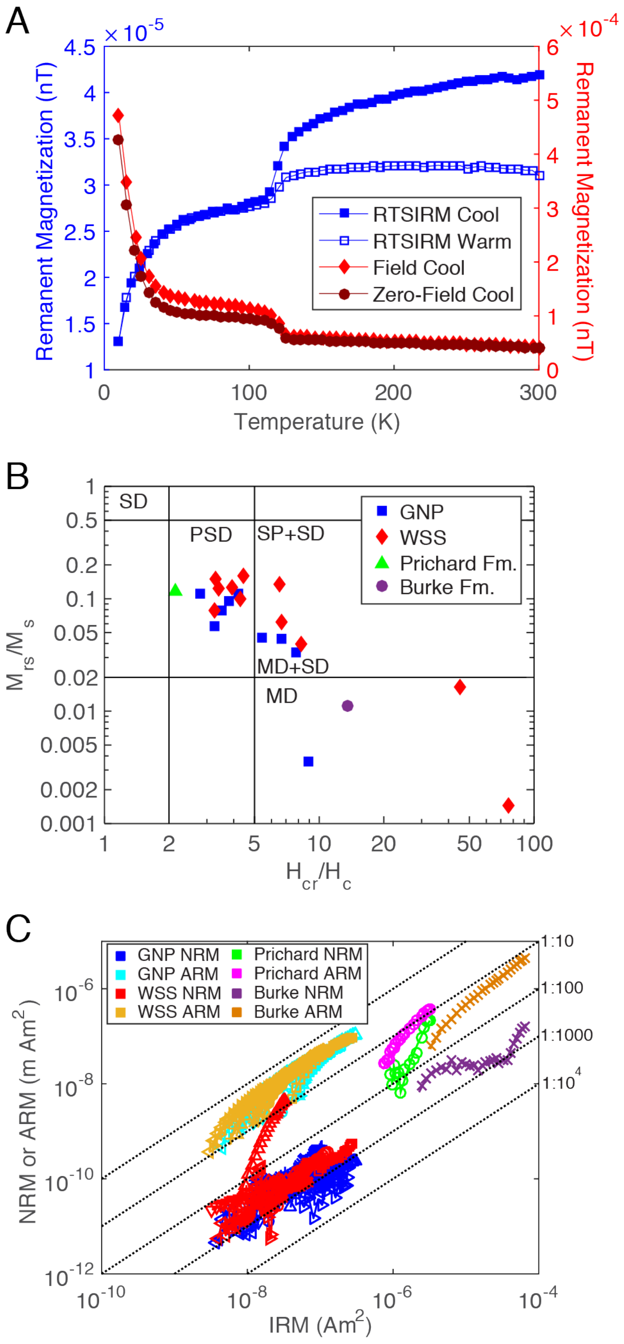

Figure 5.5: Rock magnetic measurements on samples where magnetite is the predominant ferromagnetic mineral. A) Example MPMS measurement of room temperature saturation magnetization (RTSIRM) cooling and warming, cooling in a field, and cooling in zero field on a sample from the Appekunny Formation, Member 2, Glacier National Park (GP12-1) identifying magnetite by the Verwey transition at 120 K and suggesting nanophase pyrrhotite based on the transition at

35K (Aubourg and Pozzi, 2010). More examples in Figure S5.3. B) Day Plot showing predominantly pseudo-single-domain (PSD) grain size with some multi-domain (MD) grains and possible mixtures of single-domain (SD) and MD grains. (Day et al., 1977; Dunlop, 2002) Abbreviations: SP = superparamagnetic, M_{rs} = remanent saturation magnetization, Ms = saturation magnetization, Hc = coercivity, Hcr = coercivity of remanent magnetization, GNP = Glacier National Park, WSS = White Sulphur Springs. C) Fuller Test for nature of magnetization (on all samples from part B minus one MD WSS samples and plus one GNP sample) highlights that most of the magnetite is detrital in the GNP and WSS regions based on a NRM:IRM ratio of 1:1000. The Prichard sample from Sagle Point is chemically remagnetized and the Burke sample ratio suggests a detrital remanent magnetization. (Fuller et al., 1988; Fuller et al., 2002). Abbreviations: NRM = natural remanent magnetization, IRM = isothermal remanent magnetization, ARM = anhysteretic remanent magnetization.

5.10 Supplemental Tables

Table S5.1: Detailed Sample Data for Belt Supergroup Samples*

Sample	Drill Core	Depth	GPS Location		Location†	Formation	Stratigraphic Details	Lithology
			Lat (°N)	Long (°W)				
BS13-2	--	--	46.88778	110.68635	WSS	Chamberlain	Lower (below carbonates)	Grey shale, near carbonate concretions, lenses of sand to pebble-sized siliciclastics, and rare mud cracks
BS13-1	--	--	46.91387	110.65591	WSS	Chamberlain	Upper (carbonate-rich)	Massive black dolomitic shale, interbedded with lenses of molar tooth and carbonate clasts
T029-61.08	SC11-029	61.07-61.09	46.78189	110.91287	WSS	Newland	Lower Newland right above USZ	Early diagenetic barite laths with differential compaction of laminated black and grey dolomitic shale with intergrown subparallel iron sulfide blebs
T029-76	SC11-029	76.36-76.37	46.78189	110.91287	WSS	Newland	Lower Newland in USZ	Multiple generations of iron sulfides with early unfilled circular tube network of iron sulfides <1mm in diameter and broken tubes in larger massive sulfide zone
T095-63	SC11-095	63.42-63.50	46.77910	110.92575	WSS	Newland	Upper Newland far from USZ	Early diagenetic fine-grained iron sulfide laminae showing differential compaction in laminated black and grey dolomitic shale
T095-140.08	SC11-095	140.045-140.115	46.77910	110.92575	WSS	Newland	Upper Newland SZ	Early diagenetic wrinkly iron sulfide laminations within dolomitic shale
T095-388.26	SC11-095	388.24-388.305	46.77910	110.92575	WSS	Newland	Lower Newland SZ	Early diagenetic wrinkly iron sulfide laminations including broken tubes and recrystallized framboids showing differential compaction of laminated dolomitic shale in larger massive sulfide zone
T095-388.70	SC11-095	388.70-388.73	46.77910	110.92575	WSS	Newland	Lower Newland SZ	Dolomitic shale breccia/debris flow clasts in predominantly iron sulfide matrix including early diagenetic iron sulfide broken tubes and framboids
T095-390	SC11-095	390.165-390.20	46.77910	110.92575	WSS	Newland	Lower Newland SZ	Early diagenetic fine-grained iron sulfides and recrystallized framboid laminae in dolomitic shale with broken iron sulfide tubes in massive sulfide zone
T095-400	SC11-095	400.795-400.87	46.77910	110.92575	WSS	Newland	Lower Newland right above USZ	Debris flow clasts of early diagenetic whole (<1mm) and broken iron sulfide tubes in dolomitic shale
T095-408	SC11-095	408.89-409.00	46.77910	110.92575	WSS	Newland	Lower Newland in the USZ	Multiple generations of cross-cutting sulfides (up to 1 mm blebs) including <1mm tube structures in heavily recrystallized dolomite and shale within larger massive sulfide zone
T095-410	SC11-095	410.08 - 410.11	46.77910	110.92575	WSS	Newland	Lower Newland in the USZ	Multiple generations of sulfides including 1-4mm tube structures infilled by heavily recrystallized dolomite and shale within larger massive sulfide zone
T100-407	SC12-100	407.75-407.8	46.78085	110.90605	WSS	Newland	Lower Newland right above LSZ	Secondary dolomite alteration with large (>1cm) crystals with cross-cutting secondary sulfides in laminated dolomitic shale with fine-grained iron sulfides
T101-392	SC12-101	392.125-392.15	46.78143	110.90588	WSS	Newland	Lower Newland in LSZ	Multiple generations of cross-cutting sulfides (up to 2 mm blebs) and large dolomite crystals (>1cm) in heavily recrystallized dolomite and shale within larger massive sulfide zone

Table S5.1 (Continued)

Sample	Drill Core	Depth	GPS Location		Location†	Formation	Stratigraphic Details	Lithology
			Lat (°N)	Long (°W)				
T112-345	SC12-112	345.13-345.15	46.78098	110.89963	WSS	Newland	Lower Newland in VVF Shear Zone	Black and grey laminated shale with disseminated iron sulfides
BS13-3	--	--	46.74519	110.99410	WSS	Newland	Upper Newland, Unit 5†	Orange and white sandy siltstone with even microlaminae, near ripple cross-stratification
BS13-9	--	--	46.65250	110.90630	WSS	Greyson	Upper	Grey siltstone and claystone in microlaminae and couplets with hummocky beds, gutters, and shaly parting
BS13-6	--	--	46.63475	110.93685	WSS	Spokane		Red evenly laminated interbedded siltstone and claystone with secondary (subparallel) green and orange coloration and mud cracks
BS13-8	--	--	46.63497	110.93651	WSS	Spokane		Red evenly laminated siltstone and claystone with minor orange subparallel coloration, near green mudchips
BS13-10	--	--	46.35829	111.12573	Townsend	Newland	Lower	Black dolomitic shale with faint laminations and microlenses of carbonate, near cross stratification and oolites
BS13-13	--	--	46.32876	111.27402	Townsend	Greyson	Lower	Dark grey siltstone and light grey sandstone interbedded with hummocky beds and shaly parting
PP13-6	--	--	47.36050	114.56292	Perma	Prichard	Unit F, 1.6m from sill	Grey claystone with faint laminations and weathered iron minerals and planar bedding
PP13-11	--	--	47.3603#	114.5624#	Perma	Prichard	Unit F, 25m from sill	Grey siltstone and claystone in even microlaminae with large secondary iron sulfide aggregates (>1mm), planar bedding
PP13-13	--	--	47.35963	114.56079	Perma	Prichard	Unit F, 171m from sill	Grey siltstone with faint laminations with coarse secondary mineralization (biotite?) sometimes rimming medium-sized iron sulfides (<0.5 mm), planar bedding
BS13-39	--	--	48.54377	115.20847	Libby	Prichard	Upper Member	Light grey very fine-grained sandstone with wavy lamination, thin oxidized laminae, and large (>1mm) partly oxidized iron sulfides
BS13-37	--	--	48.48608	115.26403	Libby	Prichard	Transition Member	Dark grey siltstone with faint lamination and oxidized medium (<1mm) iron sulfides
BS13-34	--	--	48.44957	115.29385	Libby	Burke		Green siltstone and claystone in even couplets with large biotite (1mm) and euhedral magnetite crystals
BS13-16	--	--	48.19321	116.15716	Lightning Ck	Prichard	Unit F	Mottled purple and green siltstone with wavy laminations and weathered out iron minerals
BS13-23	--	--	48.37509	116.19399	Lightning Ck	Prichard	Unit C	Grey fine grained sandstone with planar bedding
BS13-31	--	--	48.25364	116.31812	Hope	Prichard	Unit C	Grey very fine-grained sandstone with medium weathering iron sulfides (<.5mm), planar bedding
BS13-29	--	--	48.18188	116.39135	Sagle Pt	Prichard	Unit F	Black siltstone with very large (>2mm) secondary iron sulfide aggregates and localized alteration

*See Table A1 in Slotznick et al. (2016) for details on the 20 samples from Glacier National Park and Table 1 in Slotznick et al. (2015) for details on 11 additional samples from Black Butte drill cores

†Abbreviations: WSS= White Sulphur Springs, Ck= Creek, Pt = Point

§Zieg et al. (2015) for stratigraphic nomenclature

#Not taken in field, from Google Earth and other PP13 GPS points

Table S5.2: Mineralogy of Samples from the Belt Supergroup

Location*	Formation	Details*	Bulk Rock Magnetic Techniques†§#						
			Mag	Hem	Goe	Pyr	NP	Sid	Alloy
GNP-East	Appekunny	Mbr 1 (R)		X	X		--		
		Mbr 1 (G)	X		X		X		
		Mbr 2	X		X		X		
		Mbr 3	X		X		X		
		Mbr 4	X	X	X		X		
		Mbr 5	X				X		
	Grinnell			X	X		--		
GNP-West	Prichard	or Mbr 4	X			X			
	Appekunny	Mbr 4	X	X	X	X			
		Mbr 5	X		X			X	
White Sulphur Springs	Chamberlain		X				X		
	Newland	Outcrop	X	X	X		--		
		Diss. Core	X		X		X		
		SZ Core	X						X
	Greyson		X		X		X		
	Spokane		X	X			--		
Townsend	Newland		X	X	X	X		X	
	Greyson		X	X	X		--		
Perma	Prichard	Unit F, 171m	X					X	
		Unit F, 25m	X			X		--	
		Unit F, 1.6m	X	X		?	--	?	
Libby	Prichard		X		X	X		--	
		Transition Mbr	X	X	X		X	X	
	Burke		X			?	--	?	
Lightning Creek	Prichard	Unit C	X		X	X		X	
		Unit F	X	X		X		--	
Hope	Prichard	Unit C	X			X		--	
Sagle Pt	Prichard	Unit F	X		X	X		X	

*Abbreviations: GNP = Glacier National Park, Pt = Point, Mbr = Member, (R) = Red in color, (G) = Green in color, Diss. = Disseminated Iron Sulfides, SZ = Massive Sulfide Zone (not necessarily of economic interest)

†Abbreviations for Minerals: Mag = Magnetite, Hem = Hematite, Goe = Goethite, Pyr = Pyrrhotite, NP = nanophase pyrrhotite, Sid = siderite

§ X indicates presence of mineral, -- indicates sample was not analyzed on Magnetic Property Measurement System (MPMS) to determine if siderite or nanophase pyrrhotite were present, ? indicates within moderate Rotational Remanent Magnetization (RRM) but no additional analyses to distinguish between pyrrhotite and siderite

#Bulk Magnetic techniques for mineral identification included Coercivity spectra (Figure S5.2), RRM (Figure S5.2), MPMS (Figure S5.3), and Hysteresis loops (Figure S5.4)

Table S5.2 (Continued)

Location*	Formation	Details*	Textural Techniques†§#											
			Py	Pyr	CuPy	Gal	Sph	NiFeS	CoAsS	CuS	AgS	FerS	Bar	Su-S
GNP-East	Appekunny	Mbr 1 (R)											X	
		Mbr 1 (G)	X		X		X						X	X
		Mbr 2	X										X	
		Mbr 3	X										X	X
		Mbr 4	X				X						X	X
		Mbr 5	X		X	X	X							
	Grinnell													X
GNP-West	Prichard	or Mbr 4	X	X	X		X	X						X
	Appekunny	Mbr 4	X	X	X	X	X		X	X			X	X
		Mbr 5	X		X		X							
White Sulphur Springs	Chamberlain		X		X	X							X	
	Newland	Outcrop	X		X							X		X
		Diss. Core	X		X					X	X			X
		SZ Core	X		X	X	X					X	X	X
	Greyson		X				X							X
	Spokane													X
Townsend	Newland		X				X							X
	Greyson		X				X							X
Perma	Prichard	Unit F, 171m	X											X
		Unit F, 25m	X	X	X				X					X
		Unit F, 1.6m	X						X					X
Libby	Prichard		X		X	X	X						X	X
		Transition Mbr	X		X		X			X				X
	Burke		?	?			X							X
Lightning Creek	Prichard	Unit C		?	?		X							X
		Unit F												
Hope	Prichard	Unit C	X		X					X				X
Sagle Pt	Prichard	Unit F	X			X								X

*Abbreviations: GNP = Glacier National Park, Pt = Point, Mbr = Member, (R) = Red in color, (G) = Green in color, Diss. = Disseminated Iron Sulfides, SZ = Massive Sulfide Zone (not necessarily of economic interest)

†Abbreviations for Minerals: Py = Pyrite, Pyr = Pyrrhotite, CuPy = Chalcopyrite, Gal = Galena, Sph = Sphalerite, NiFeS = Nickel Iron Sulfide, CoAsS = Cobaly Arsenic Sulfide, CuS = Copper Sulfide, AgS = Silver Sulfide, FerS = Ferric Disulfide, Bar = Barite, Su-S = Sulfate and/or Elemental Sulfur

§ X indicates presence of mineral. Note that blank does not mean mineral is not present. ? indicates uncertainty in identification, either due to lack of structural information or lack of chemical information to provide confirmation.

#Textural techniques include X-ray absorption near-edge spectroscopy (XANES, Figure S5.5), X-ray Energy Dispersive Spectroscopy (EDS), Electron Back Scatter Diffraction (EBSD), and the Electron Probe Micro-Analyzer (EPMA, Table S3)

Table S5.2 (Continued)

Location*	Formation	Details*	Textural Techniques†§#							
			FeCrO	**FeO**	**Fe(Mn)TiO**	**TiO**	**Fe-Dol**	**Chl**	**Ill-Bio**	**FeCaAlSiO**
GNP-East	Appekunny	Mbr 1 (R)		X	X			X		
		Mbr 1 (G)		X		X		X	X	
		Mbr 2		X		X			X	
		Mbr 3				X	X	X	X	
		Mbr 4		X		X		X	X	
		Mbr 5				X				
	Grinnell			X	X	X				
GNP-West	Prichard	or Mbr 4		X		X		X	X	
	Appekunny	Mbr 4		X		X		X		
		Mbr 5				X	X	X	X	
White Sulphur Springs	Chamberlain		X			X		X		
	Newland	Outcrop								
		Diss. Core				X	X	X	X	
		SZ Core				X	X	X	X	
	Greyson									
	Spokane									
Townsend	Newland			X		X	X	X	X	
	Greyson									
Perma	Prichard	Unit F, 171m								
		Unit F, 25m			X	X				
		Unit F, 1.6m			X			X	X	
Libby	Prichard			X	X			X	X	X
		Transition Mbr			X			X	X	
	Burke			X		X		X	X	X
Lightning Creek	Prichard	Unit C		X	X			X	X	X
		Unit F								
Hope	Prichard	Unit C			X	X		X	X	
Sagle Pt	Prichard	Unit F				X		X		

*Abbreviations: GNP = Glacier National Park, Pt = Point, Mbr = Member, (R) = Red in color, (G) = Green in color, Diss. = Disseminated Iron Sulfides, SZ = Massive Sulfide Zone (not necessarily of economic interest)

†Abbreviations for Minerals: FeCrO = Iron Chromium Oxide, FeO = Iron Oxide, Fe(Mn)TiO = Iron Titanium Oxide with a few wt% of Manganese present in all Prichard examples, Fe-Dol = Iron-rich Dolomite, Chl = Chlorite, Ill-Bio = Illite or Biotite, FeCaAlSiO = Iron Calcium Aluminosilicate

§ X indicates presence of mineral. Note that blank does not mean mineral is not present.

#Textural techniques include X-ray absorption near-edge spectroscopy (XANES, Figure S5.5), X-ray Energy Dispersive Spectroscopy (EDS), Electron Back Scatter Diffraction (EBSD), and the Electron Probe Micro-Analyzer (EPMA, Table S3)

Table S5.3: Composition of Minerals from Select Samples of the Lower Belt Supergroup

A. SULFIDES, OXIDES, SULFATES

Sample Location* Formation† Mineral§	GP12-1 GNP-East App, Mbr 2 Pyrite	GP12-1 GNP-East App, Mbr 2 Goethite	GP12-1 GNP-East App, Mbr 2 Fe-Sulfate	GP12-8 GNP-West App 4/Prich Pyrrhotite	GP12-8 GNP-West App 4/Prich Chalcopyrite	GP12-8 GNP-West App 4/Prich Sphalerite	Detection Limits (wt%)#
Fe	1.011	1.065	1.671	0.896	0.501	0.098	0.052
Cu	--	--	--	--	0.479	0.002	0.061
Zn	--	--	--	--	0.002	0.900	0.081
As	--	--	--	--	--	--	0.052
Ti	--	--	--	--	--	--	0.012
S	2.000	--	1.091	1.000	1.000	1.000	0.013
O	--	2.000	4.000	--	--	0.292	0.098
Elemental Sum (wt%)	98.822	93.065	94.206	99.244	97.668	104.005	
Number of grains	2	2	2	4	1	2	
Number of spots	4	6	3	9	2	3	

B. CARBONATES

Sample Location* Formation† Mineral**	GP12-1 GNP-East App, Mbr 2 Calcite	GP14-35 GNP-East App, Mbr 3 Calcite	GP14-27 GNP-West App, Mbr 5 Calcite	GP14-35 GNP-East App, Mbr 3 Fe-Dolomite	GP14-27 GNP-West App, Mbr 5 Fe-Dolomite	T095-53 WSS Newld, Diss Fe-Dolomite	BS13-10A10 Townsend Lower Newld Dolomite	Detection Limits (wt%)#
Ca	0.978	0.976	0.974	1.028	1.184	1.019	1.031	0.010
Mg	0.013	0.016	0.011	0.871	0.550	0.829	0.937	0.014
Fe	0.009	0.008	0.015	0.101	0.265	0.152	0.033	0.033
Oxide Sum (wt%)	98.406	102.191	100.000	95.552	100.000	87.341	96.047	
Number of grains	2	2	3	2	4	5	6	
Number of spots	4	4	7	5	10	7	8	

Table S5.3 (Continued)

C. SILICATES

Sample	**GP12-1**	**GP12-8**	**GP12-8**	**GP14-27**	
Location*	**GNP-East**	**GNP-West**	**GNP-West**	**GNP-West**	
Formation†	**App, Mbr 2**	**App 4/Prich**	**App 4/Prich**	**App, Mbr 5**	**Detection Limits (wt%)#**
Mineral††	**Illite**	**Illite**	**Chlorite**	**Chlorite**	
Fe	0.256	0.176	1.824	2.245	0.036
Mg	0.332	0.290	2.792	2.321	0.014
Ca	0.009	0.001	0.004	0.012	0.010
Al	2.114	2.343	2.396	2.528	0.019
Ti	0.017	0.047	0.006	0.003	0.026
Na	0.008	0.015	0.010	0.007	0.021
K	0.911	0.891	0.012	0.004	0.010
Si	3.368	3.236	2.882	2.809	0.018
Oxide Sum (wt%)	95.296	95.036	85.270	85.158	
Number of grains	5	2	2	3	
Number of spots	10	3	6	10	

*Abbrevations: GNP-East = east side of Glacier National Park, GNP-West = west side of Glacier National Park, WSS = White Sulphur Springs

†Abbreviations: App = Appekunny Formation, Mbr = Member also just designated by number, Prich = Prichard Formation, Newld = Newland Formation, Diss =Disseminated sulfide drill core

§Formula for Sulfides, Oxides, and Sulfates normalized to either oxygen or sulfur in formula

#Detection Limits averaged for all spectra based on elemental or oxide weight%, -- should be interpreted as no signal above detection limit

** Calcite: cations per oxygen atom (less CO_2); (Fe-)Dolomite: cations per 2 oxygen atoms (less CO_2)

††Illite: cations per 11 oxygen atoms (less H_2O); Chlorite: cations per 14 oxygen atoms (less H_2O)

Table S5.4: Elemental abundances from X-ray fluorescence microprobe for Belt Supergroup samples*

Sample†	Location†	Formation†	Fe (wt%)	Ti (wt%)	Mn (wt%)	Cu (ppm)	Zn (ppm)	As (ppm)§	Pb (ppm)§	Ni (ppm)
GP14-10, Reg1	GNP-East	App, Mbr 1 (G)	4.68	0.192	--	40.9	282	38.7	255	559
GP12-1, Reg4	GNP-East	App, Mbr 2	3.54	0.213	0.000056	21.7	143	40.1	--	237
GP14-35, Reg1	GNP-East	App, Mbr 3	4.99	0.190	--	27.1	229	36.9	242	565
GP14-30, Reg1	GNP-East	App, Mbr 4	3.06	0.183	--	28.61	165	29.9	196	324
GP14-33, Reg2	GNP-East	App, Mbr 5	10.4	0.474	0.273	47.4	362	92.3	543	986
GP12-8, Reg1	GNP-West	Prich/App, Mbr 4	2.01	0.232	0.042	21.3	106	42.7	--	131
GP14-55, Reg1#	GNP-West	App, Mbr 4	10.3	0.147	0.235	161	570	752	5432	1513
GP14-28, Reg1	GNP-West	App, Mbr 5	8.74	0.339	--	48.8	343	46.1	303	1011
GP14-54, Reg1#	GNP-West	App, Mbr 5	5.44	0.150	--	33.4	360	49	353	748
Average Published Appekunny Formation Data**			2.59±0.55	0.294±0.045	0.037±0.024	12.4±11.0	58.3±18.3	2.57±1.41	8.03±4.53	22.6±8.33
GP14-8, Reg1	GNP-East	App, Mbr 1 (R)	8.74	0.474	0.224	46.4	340	96.6	569	813
GP12-2, Reg1	GNP-East	Grinnell	3.82	0.258	0.126	65.7	1310	101	593	363
BS13-6, Reg1	WSS	Spokane	3.56	0.269	0.217	59.9	249	9795	57699	390
Average Published Grinnell Formation Data††			3.26±0.925	0.316±0.030	0.068±0.113	4.52±4.29	58.8±20.6	4.90±2.53	12.3±4.22	20.4±4.86
T095_38#	WSS	Newld, Diss. Core	3.41	0.049	0.365	41.1	423	155	1006	417
T095_53#	WSS	Newld, Diss. Core	6.42	0.143	0.120	118	282	154	1114	875
T112_334#	WSS	Newld, Diss. Core	4.70	0.048	0.372	47.5	71.4	115	828	691
T112_384#	WSS	Newld, Diss. Core	4.33	0.109	0.071	40.9	232	108	697	540
T029_56	WSS	Newld, SZ Core	7.00	0.176	0.118	1153	318	924	5153	767
T095_140.36	WSS	Newld, SZ Core	18.2	0.483	0.386	101	229	1227	6921	1940
T101_389	WSS	Newld, SZ Core	8.89	0.189	0.155	3409	496	362	1646	987
Average Published Newland Formation Data§§			2.23±0.415	--	--	--	110±105	--	--	--
BS13-2, Reg1#	WSS	Chamberlain	12.3	0.231	0.247	139	300	84	560	1412
BS13-13, Reg1#	Townsend	Greyson	6.38	0.209	0.132	85.9	341	124	802	65
PP13-13, Reg2#	Perma	Prich, Unit F, 171m	4.21	0.104	0.0978	44.2	380	49.4	357	575
PP13-11, Reg1#	Perma	Prich, Unit F, 25m	9.52	0.175	0.227	149	529	132	853	1300
PP13-6, Reg1#	Perma	Prich, Unit F, 1.6m	3.95	0.086	0.088	37.3	228	65.1	471	496
BS13-37, Reg1#	Libby	Prich, Trans Mbr	6.14	0.113	0.150	142	489	67.0	484	892
BS13-31, Reg1#	Hope	Prich, Unit C	10.3	0.341	0.219	302	756	379	6481	1638
BS13-29, Reg1#	Sagle Pt	Prich, Unit F	1.78	0.051	0.032	35.0	99.8	94.2	1545	270

*For detailed explanation of methodology to produce this data see Slotznick et al. (2016). X-ray fluorescence maps used for calculations are in Figures S5.6-S5.9.

†Reg = scanned region on thin or thick section, GNP-East = East side of Glacier National Park, GNP-West = West side of Glacier National Park, WSS =White Sulphur Springs, Ck = Creek, Pt = Point, App = Appekunny Formation, Mbr = Member, Newld = Newland Formation, Prich = Prichard Formation,

§As and Pb energy windows overlap in XRF so most samples are a mixture of these two minerals, each calculation assumes the channel is solely for As or Pb. -- when Pb standard not run for calculations

Thick section (3-8.5 mm) instead of thin section (20-30 µm); since homogeneous correction is made assuming same material across entire depth this could lead to larger error in calculation

** Data from silt and claystones of González-Álvarez et al. (2006) and González-Álvarez and Kerrich (2010) averaged with 1 population standard deviation, n= 16 for Fe, Ti, Mn, As, and Ni, n = 12 for Cu and Zn

†† Data from silt and claystones of González-Álvarez et al. (2006) and González-Álvarez and Kerrich (2010) averaged with 1 population standard deviation, n= 10 for Fe, Ti, Mn, As, Pb, and Ni, n = 6 for Cu and Zn

§§ Data from SC93 drill core samples of Planavsky et al. (2011) averaged with 1 population standard deviation, n=7. Note Zn was measured as a proxy for alteration and one can see from our data that it is not an important mineral signaling secondary mineralization

Table S5.5: Hysteresis magnetic parameters for dominantly magnetite-bearing Belt Supergroup Samples with calculated magnetite content

Sample	Location*	Formation, Details*	Ms (Am/kg)	Mr (Am/kg)	Hc (mT)	Hcr (mT)	Magnetite (ppm)
GP14-10	GNP-East	Appekunny, Mbr 1	0.000225014	2.13434E-05	10.3396	39.571	2.4458
GP12-1	GNP-East	Appekunny, Mbr 2	0.000470666	5.21753E-05	12.4585	52.9032	5.1159
GP14-11	GNP-East	Appekunny, Mbr 2	0.00018216	2.01237E-05	12.8275	36.0801	1.9800
GP14-34	GNP-East	Appekunny, Mbr 3	0.000476883	2.13196E-05	7.72136	42.1604	5.1835
GP14-35	GNP-East	Appekunny, Mbr 3	0.000720169	0.000031621	5.74438	38.8214	7.8279
GP14-29	GNP-East	Appekunny, Mbr 4	0.000337311	1.17617E-06	5.03967	45.2754	3.6664
GP14-30	GNP-East	Appekunny, Mbr 4	0.000337506	2.61416E-05	11.3329	40.2592	3.6685
GP14-32	GNP-East	Appekunny, Mbr 5	0.000184434	1.04356E-05	11.741	38.6041	2.0047
GP14-33	GNP-East	Appekunny, Mbr 5	0.00038637	1.28502E-05	5.65243	44.5852	4.1997
GP14-54	GNP-West	Appekunny, Mbr 5	0.000191623	-1.17473E-07	2.57526	55.7777	2.0829
BS13-1	WSS	Chamberlain	0.000120955	1.20091E-05	8.54055	37.0†	1.3147
BS13-2	WSS	Chamberlain	0.000381684	1.51018E-05	4.83784	40.1†	4.1487
T112_334	WSS	Newland, Diss. Core	0.000145519	9.00742E-06	6.9962	47.2†	1.5817
T112_345	WSS	Newland, Diss. Core	0.000263676	3.32256E-05	11.9087	47.3916	2.8660
T112_384	WSS	Newland, Diss. Core	0.000174942	2.51843E-07	0.465604	36.0557	1.9015
T095_53	WSS	Newland, Diss. Core	0.000414195	5.12036E-05	12.2904	42.3†	4.5021
T095_63	WSS	Newland, Diss. Core	0.000263349	4.17803E-05	10.2505	46.0†	2.8625
T029_61.08	WSS	Newland, USZ Core	0.000088051	1.18154E-05	6.93643	45.8162	0.9571
T029_61.21	WSS	Newland, USZ Core	0.000108826	1.62341E-05	13.2581	44.2799	1.1829
T100_407	WSS	Newland, LSZ Core	0.000420261	6.85198E-06	1.37417	63.1387	4.5681
BS13-9	WSS	Greyson	0.00028543	2.21245E-05	11.9577	39.2776	3.1025
BS13-29	Sagle Pt	Prichard, Unit F	0.00038247	4.47785E-05	22.0431	47.4701	4.1573
BS13-34	Libby	Burke	1.14258	0.0125691	1.9211	26.3241	1.2419%[§]

Note: Ms is saturation magnetization, Mr is remanent saturation magnetization, Hc is coercivity, and Hcr is coercivity of remanent magnetization (using backfield method). Magnetite content is calculated following Klein et al. (2014) by dividing the Ms by Ms value for pure magnetite (92 Am/kg).

*Abbreviations: GNP = Glacier National park, WSS = White Sulphur Springs, Pt = Point, Mbr = Member, Diss. = Disseminated Iron Sulfides, USZ = Upper Sulfide Zone, LSZ =Lower Sulfide Zone

†Measured on 2G SQuID Magnetometer on neighboring slice instead of on VSM like all other measurements.

[§] Note: This is in weight percent as opposed to ppm like the rest of the data.

5.11 Supplemental Figures

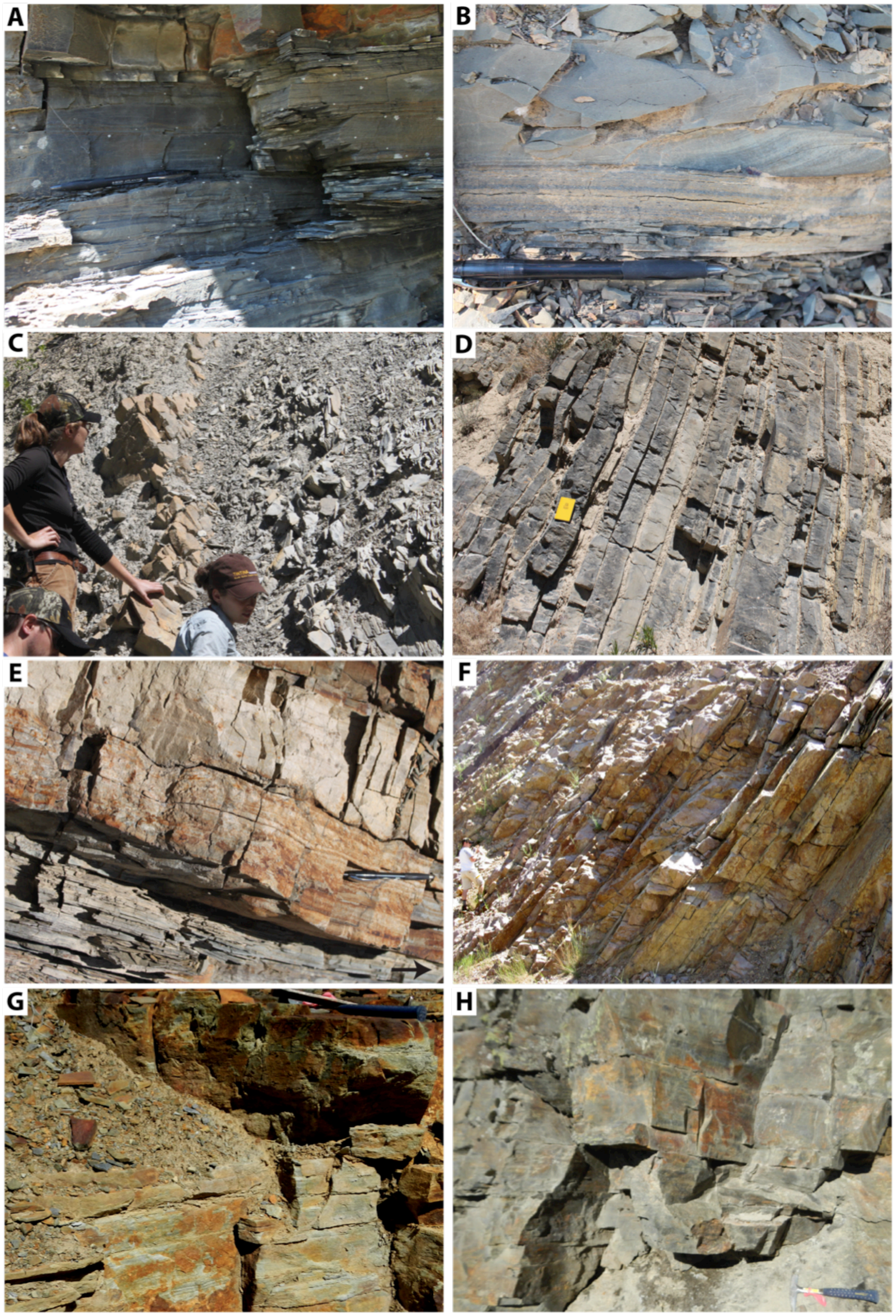

Figure S5.1: Photographs of the lower Belt Supergroup outcrops in the Helena Embayment and western Montana and Idaho. See Slotznick et al. (2016) for images of lithologies from Glacier National Park. A) Grey, finely laminated shale and siltstone with decimeter-scale hummocky cross-stratification and early carbonate concretions causing differential compaction in the Lower Chamberlain Formation, White Sulphur Springs. Pen is 15 cm for scale. B) Finely laminated grey shale and siltstone displaying ripple-cross stratification in the Upper Newland Formation, Unit 5, White Sulphur Springs. Pen is 15 cm for scale. C) Interbedded black dolomitic shale displaying shaly parting and blocky carbonate-rich sandstone in Lower Newland Formation, Townsend. People for scale. D) Interbedded dark grey carbonate and shale beds showing meter-scale hummocky cross-stratification in the Upper Newland Formation, Unit 3, Townsend. Rite-in-the-Rain notebook is 19 cm tall for scale. E) Interbedded finely laminated dark grey siltstone-claystone and light grey sandstone showing decimeter-scale hummocky cross stratification and shaly parting in the Lower Greyson Formation, Townsend. Note the individual red iron oxides from the surface weathering of iron sulfides. Beds are steeply dipping in this location, with field up-direction noted by arrow. Pen is 15 cm for scale. F) Thick planer bedded grey siltstone and claystone with reddish-orange surface-weathering varnish of the Prichard Formation, Unit F, Perma. Person in lower left for scale. G) Even to wavy couplets of light grey very fine-grained sandstone and dark grey siltstone and claystone showing blocky planar bedding and reddish-orange surface-weathering varnish in the Prichard Formation, Upper Member, Libby. Hammer (under chisel) is 33 cm for scale. H) Even couplets of grey very fine-grained sandstone and silt-claystone in blocky planar beds of the Prichard Formation, Unit C, Hope. Hammer is 33 cm for scale.

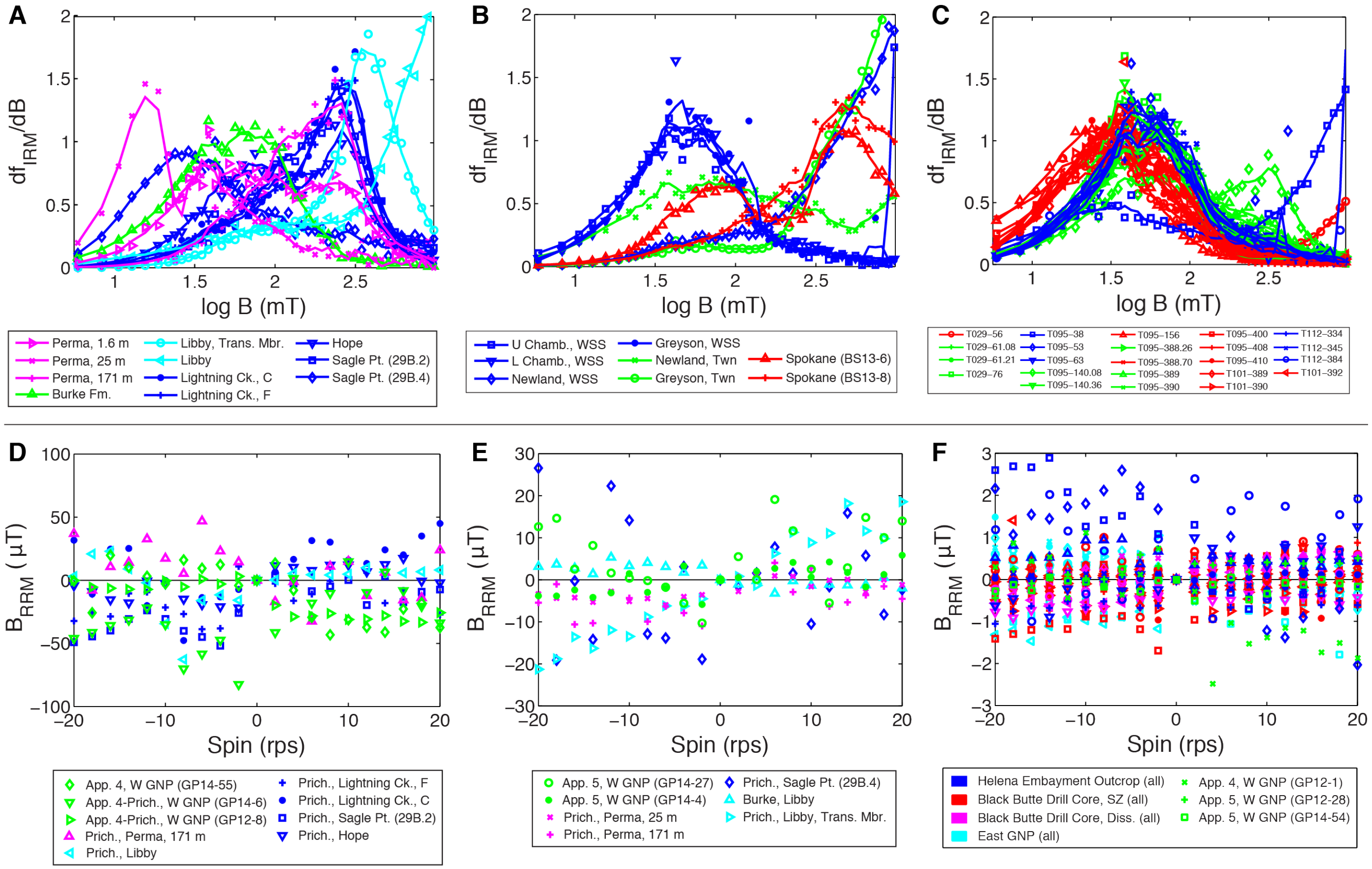

Figure S5.2: A-C) Coercivity of remanence spectra created from the derivative of the isothermal remanent magnetization (IRM) to the applied field (B) to determine ferromagnetic mineralogy (Heslop et al., 2002; Robertson and France, 1994). The samples from the

Prichard Formation (part A), Burke Formation (part A), and Helena Embayment Outcrop Samples (part B) are color-coded by location. The Black Butte drill core samples (part C) are color-coded by disseminated pyrite core in blue, sulfide zone core in red or green if the coercivity is changed by the unknown low-coercivity (alloy?) phase. All sulfide zone drill-core samples were shown to contain the unknown low-coercivity phase in hysteresis diagrams. For data from Glacier National Park, see Slotznick et al. (2016) and eight of the spectra in part C were previously published in Slotznick et al. (2015). D-F) Presence of rotational remanent magnetization (RRM) here shown as deviation from zero by B_{RRM} to identify magnetic iron sulfides and siderite (Snowball, 1997; Thomson, 1990). D) Samples with a strong RRM ($B_{RRM} > \pm 20$ μT at 5 rps) contain pyrrhotite (Potter and Stephenson, 1986; Suzuki et al., 2006). E) Samples with a moderate RRM may contain pyrrhotite or siderite. F) Samples with no RRM ($B_{RRM} < \pm 3$ μT at 5 rps) do not contain pyrrhotite. Samples are color-coded by region, although part F uses a different color-code. Legend abbreviations used: Fm. —Formation, Trans. Mbr. —Transition Member, Ck. —Creek, Pt.—Point, C—Prichard Formation, Unit C, F—Prichard Formation Unit F, Chamb.—Chamberlain, Twn—Townsend, U—Upper, L—lower, WSS—White Sulfur Springs, App. —Appekunny Formation (and following number is Member), Prich.—Prichard Formation, W GNP—west side of Glacier National Park. If two samples have the same location and formation description, sample number is also shown.

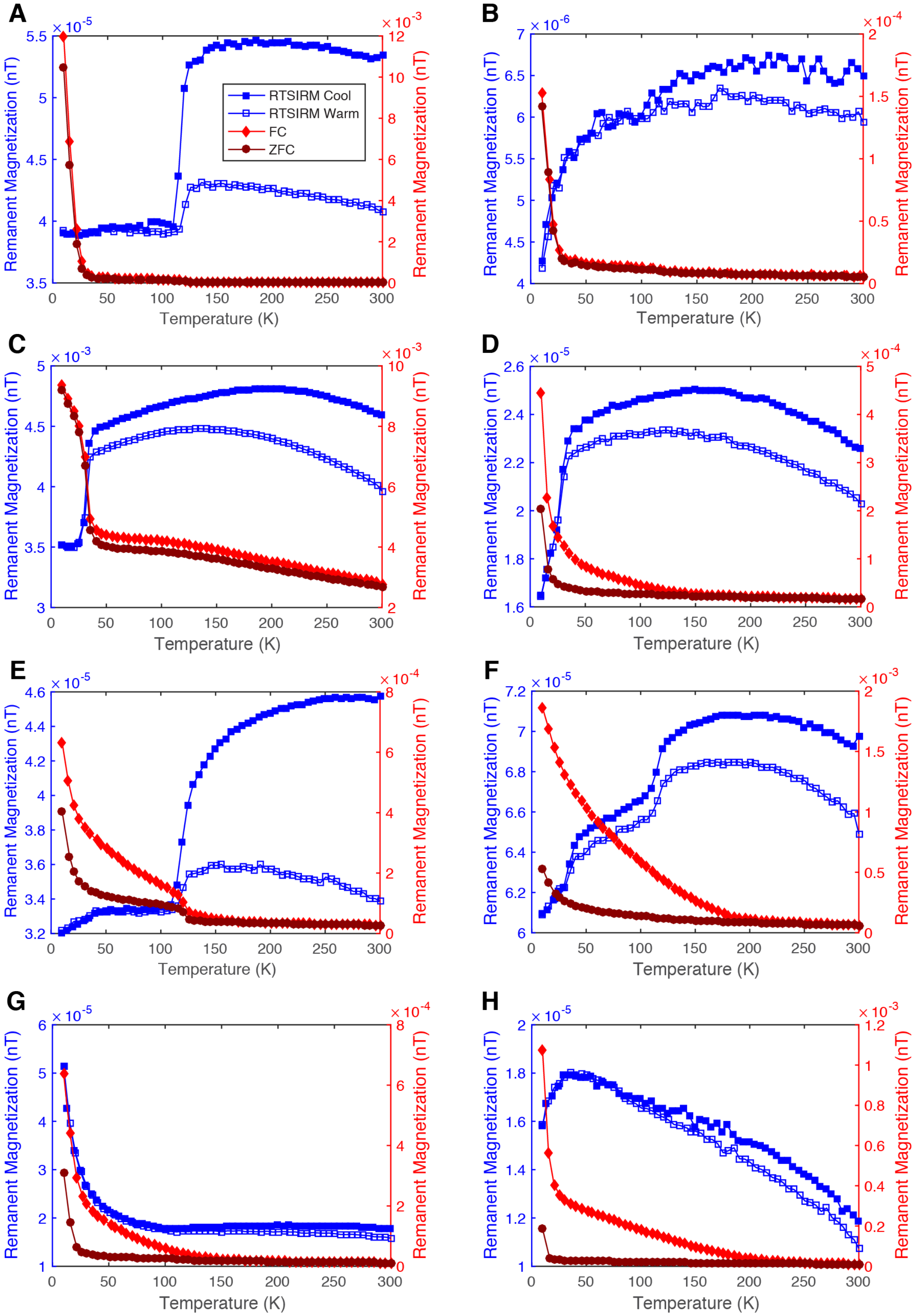

Figure S5.3: Additional example MPMS measurements of room temperature saturation magnetization (RTSIRM) cooling and warming, cooling in a field (FC), and cooling in zero field (ZFC) for 8 out of the 21 lower Belt samples measured, spanning a variety of mineralogies and mineral mixtures. Key for all plots is in part A, and RTSIRM are scaled to left Y-axis while FC and ZFC are scaled to the right. A) Magnetite from the Verwey transition at 120K (Verwey, 1939) as well as a low-temperature ordering/blocking phase are present in T095-156, Newland Fm. (Fm.), Massive Sulfide Zone drill core, White Sulphur Springs. B) Nano-phase pyrrhotite dominates the magnetic signal with a sudden reversible transition in RTSIRM at 35K and nearly indistinguishable FC and ZFC below this transition (Aubourg and Pozzi, 2010) in sample T112-334, Newland Fm., disseminated sulfide drill core, White Sulphur Springs. A very small Verwey transition i.e. a small amount of magnetite is present as well. C) Pyrrhotite showing classic Besnus transition at 32K (Besnus and Meyer, 1964; Rochette et al., 1990) is identified in GP12-8, Appekunny Fm., Member 4 or Prichard, west side of Glacier National Park. D) Pyrrhotite mixed with goethite, identified by its exponential rise starting at 150K in FC >ZFC (e.g. Liu et al., 2006), and siderite, identified by transitions at its Néel temperature of 37K with FC>ZFC (Hilscher et al., 2005; Housen et al., 1996), were found in BS13-23, Prichard Fm., Unit C, Lightning Creek. E) Magnetite is present as well as goethite and nano-phase pyrrhotite in BS13-9, Greyson Fm., White Sulphur Springs. F) A complex but identifiable mixture of magnetite, goethite, pyrrhotite and potentially siderite are present in BS13-10, Newland Fm., Townsend. G) Goethite and siderite are present with superparamagnetic minerals (maybe nano-phase magnetite with rise in RTSIRM at ~100K) and a very small amount of magnetite in GP14-27A, Appekunny Fm., Member 5, west side of Glacier National Park. H) Mixture of goethite, siderite, nanophase pyrrhotite, and very small amount of magnetite are identified in sample BS13-37, Prichard Fm., transition member, Libby.

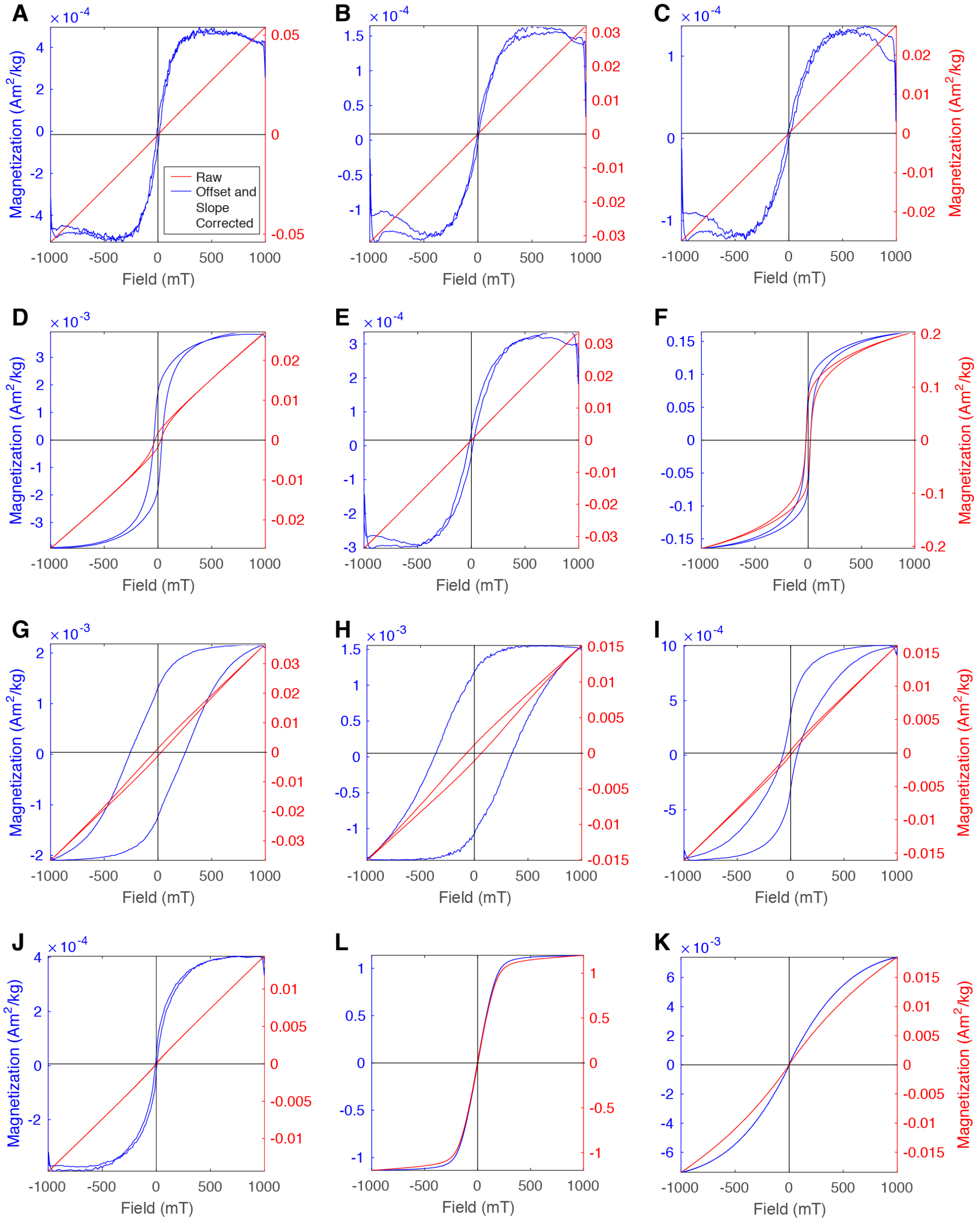

Figure S5.4: Example hysteresis loops displaying the range of magnetic mineralogies identified by shape, coercivity, and field of saturation in the 63 samples measured (e.g. Roberts et al., 2006; Tauxe et al., 1996). The raw data highlights the large proportion of paramagnetic minerals in the samples. A) Pseudo-single-domain (PSD) magnetite in GP12-1 Appekunny Formation (Fm.), Member 2, east side of Glacier National Park. B) PSD magnetite in T112-334, Newland Fm., disseminated sulfide drill core, White Sulphur Springs. C) PSD magnetite in BS13-37, Prichard Fm., Transition Member, Libby. D) Pyrrhotite in GP12-8, Appekunny Fm., Member 4 or Prichard, west side of Glacier National Park. E) Pyrrhotite and magnetite mixture in GP14-6, Appekunny Fm., Member 4 or Prichard, west side of Glacier National Park. F) Pyrrhotite with multi-domain (MD) magnetite in PP13-11, Prichard Fm., Unit F, 25m from sill, Perma. G) Hematite in GP14-8, Appekunny Fm., Member 1 Red, east side of Glacier National Park. H) Hematite and goethite in GP12-2A, Grinnell Fm., east side of Glacier National Park. I) Hematite and magnetite mixture in BS13-6, Spokane Fm., White Sulphur Springs. J) PSD magnetite and SD magnetite mixture, BS13-10, lower Newland Fm., Townsend. K) MD magnetite in BS13-34, Burke Fm., Libby. L) Unknown magnetic mineral, perhaps an alloy, with low coercivity but high saturation field in T095-156, Newland Fm., sulfide zone drill core, White Sulphur Springs.

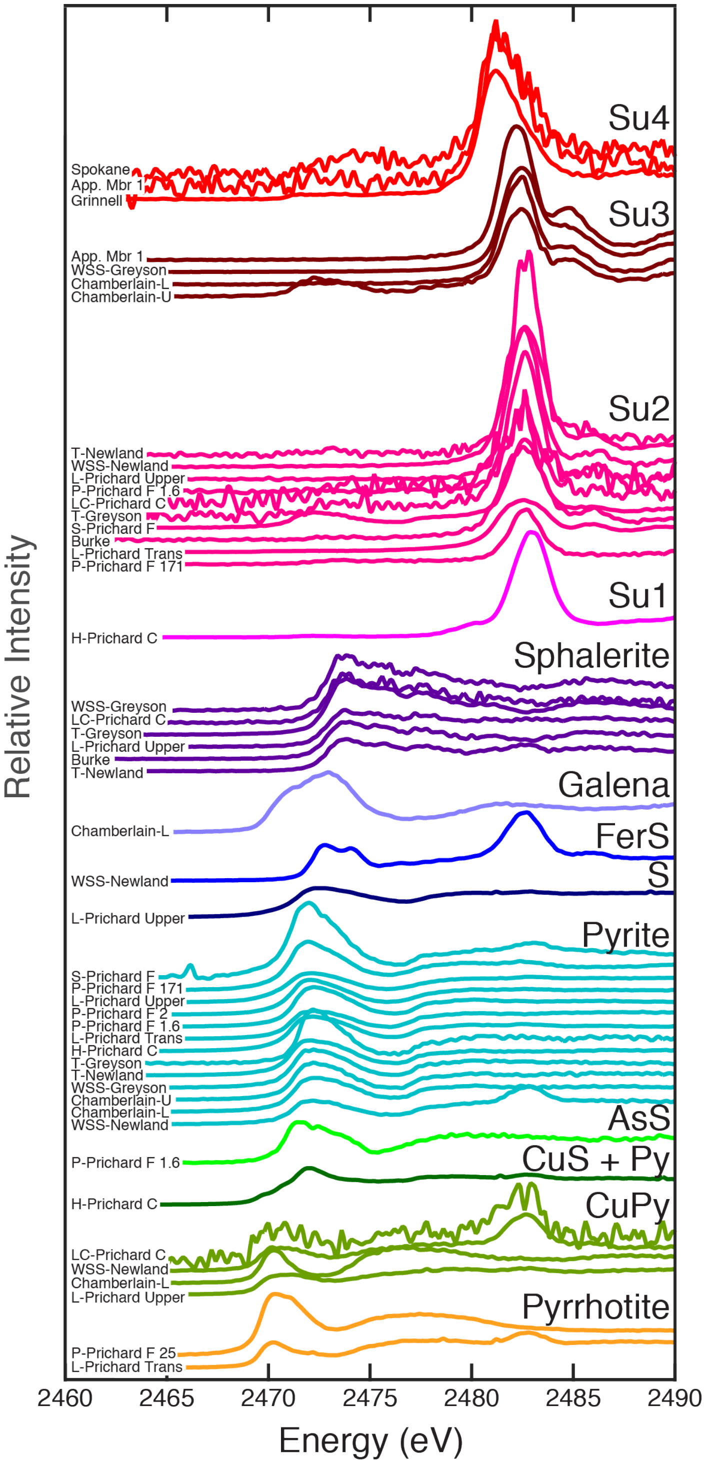

Figure S5.5: End-member X-ray absorption near-edge spectra (XANES) for samples of the Prichard Formation, Burke Formation, outcrop samples from the

Helena Embayment, and red-beds in Glacier National Park grouped based on mineralogy. Note that there are 4 different types of sulfates found in the specimens based on slightly different spectra. Mineralogy abbreviations: CuPy–chalcopyrite, CuS + Py—copper disulfide (either chalcocite or chalcopyrite) mixed with pyrite, AsS—arsenic disulfide, S—elemental sulfur, FerS—ferric disulfide, Su1—sulfate 1, Su2—sulfate 2, Su3—sulfate 3, Su4—sulfate 4. Location and sample abbreviations: App.—Appekunny Formation, Mbr—Member, WSS—White Sulphur Springs, L—Lower Chamberlain Formation, U—Upper Chamberlain Formation, T—Townsend, L—Libby, P—Perma, LC—Lightning Creek, H—Hope, C—Prichard Unit C, F—Prichard Unit F, 1.6—1.6 m from sill, 25—25 m from sill, 171—171 m from sill, S—Sagle Point, Trans—Prichard Formation Transition Member. For additional XANES endmember spectra from the rest of the Belt Basin that informed mineralogy in Table S5.2, see Slotznick et al. (2015) and Slotznick et al. (2016).

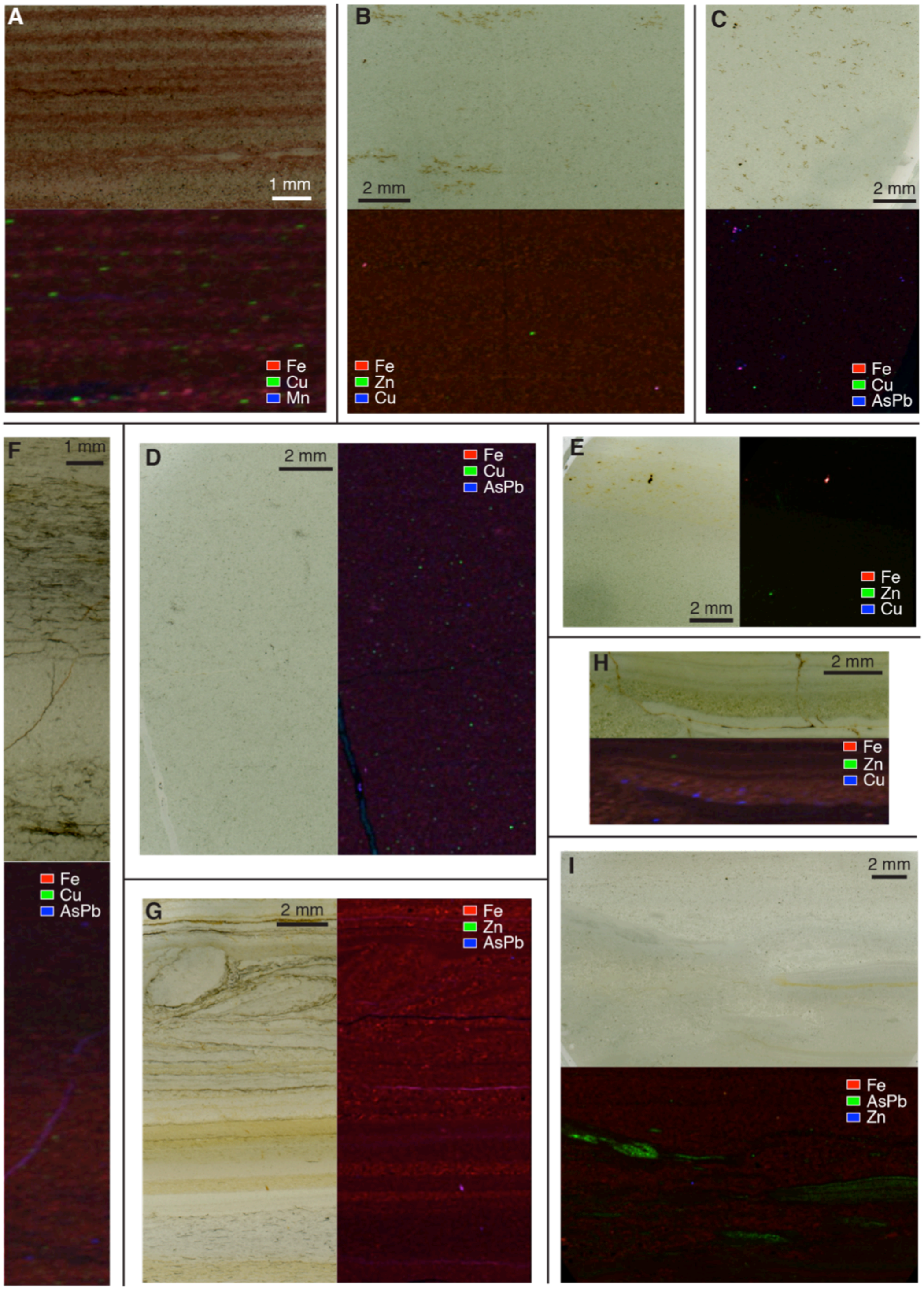

Figure S5.6: High-energy X-ray fluorescence (XRF) maps displaying elemental abundances paired with scans of the corresponding thin section region in the

Appekunny Formation on the east side of Glacier National Park. Separate scale bar and element key for each image pair (black to brightly colored at maximum). A) GP14-8, Member 1, Red. B) GP14-10, Member 1, Green. C) GP14-11, Member 2. D) GP14-35, Member 3. E) GP14-34, Member 4. F) GP14-29, Member 4. G) GP14-30, Member 4. H) GP14-33, Member 5. I) GP14-32, Member 5. A, B, D, G, H were used for elemental abundance quantification in Table S5.4. See Slotznick et al. (2016) for XRF map of GP12-1, Member 2 and sample details.

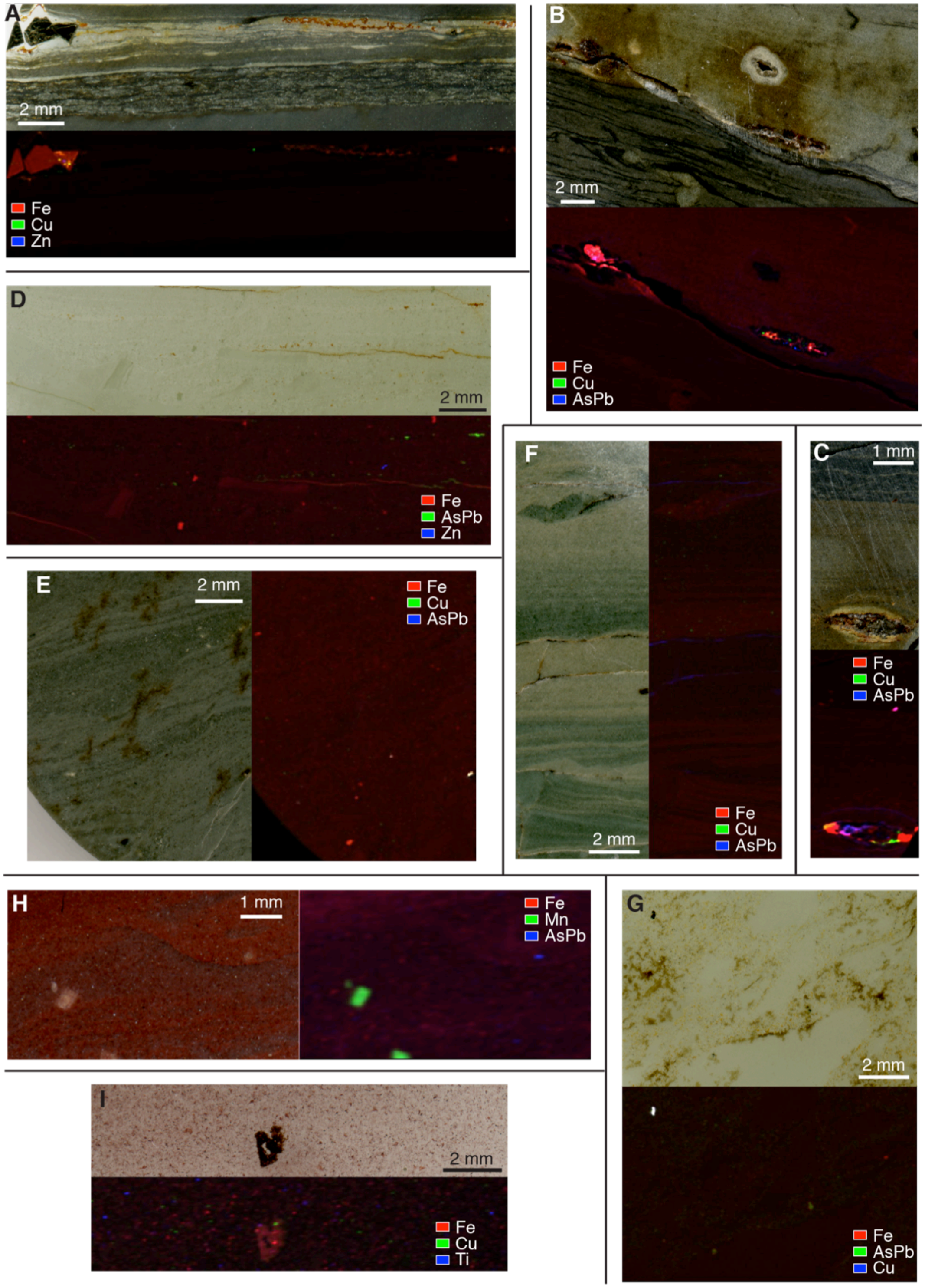

Figure S5.7: High-energy X-ray fluorescence (XRF) maps displaying elemental abundances paired with scans of the corresponding thick or thin section region in the Appekunny Formation on the west side of Glacier National Park and the Grinnell Formation on the east side of Glacier National Park. Separate scale bar and element key for each image pair (black to brightly colored at maximum). A) GP14-6, Prichard or Member 4, West Mt. Brown. B) GP14-55, Member 4, East Mt. Brown. C) GP14-1, Member 4, East Mt. Brown. D) GP14-28, Member 5, McDonald Creek. E) GP14-4, Member 5, East Mt. Brown. F) GP14-54, Member 5, East Mt. Brown. G) GP14-27, Member 5, McDonald Creek. H) GP12-3, Grinnell Formation. I) GP12-2, Grinnell Formation. B, D, F, I were used for elemental abundance quantification in Table S5.4. See Slotznick et al. (2016) for XRF map of GP12-8, Prichard or Appekunny Member 4 and sample details.

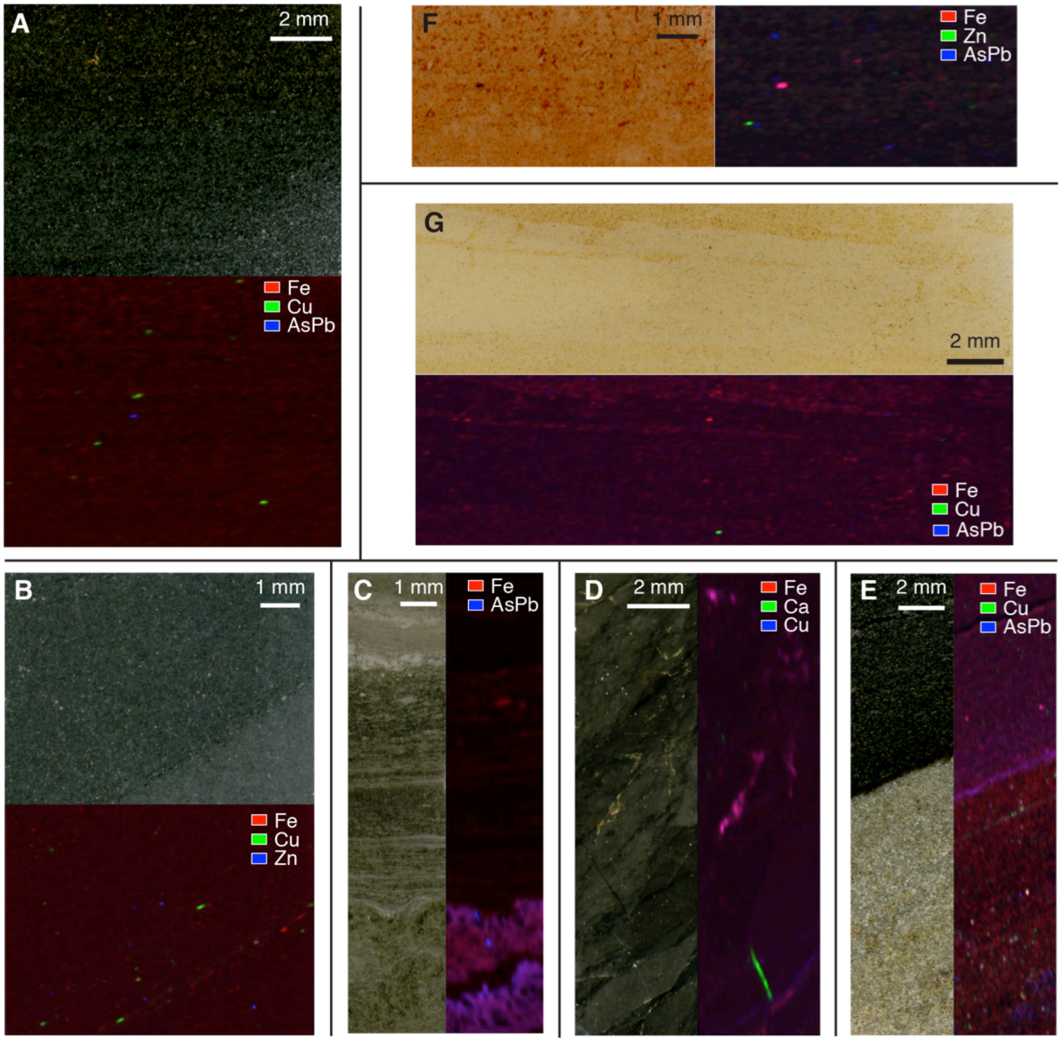

Figure S5.8: High-energy X-ray fluorescence (XRF) maps displaying elemental abundances paired with scans of the corresponding thin or thick section region in the samples from the Helena Embayment. Separate scale bar and element key for each image pair (black to brightly colored at maximum). Images for Black Butte drill core samples are brightened to highlight subtle sedimentary features. A) BS13-2, Chamberlain Formation, White Sulphur Springs. B) T095-53, Newland Formation, Disseminated Pyrite Core, White Sulphur Springs. C) T095-140.36, Newland Formation, Sulfide Zone Core, White Sulphur Springs. D) T112-384, Newland Formation, Disseminated Pyrite Core, White Sulphur Springs. E) BS13-13, Greyson Formation, Townsend. F) BS13-8, Spokane Formation, White Sulphur Springs. G) BS13-6, Spokane Formation, White Sulphur Springs. All except F were used for elemental abundance quantification in Table S5.4.

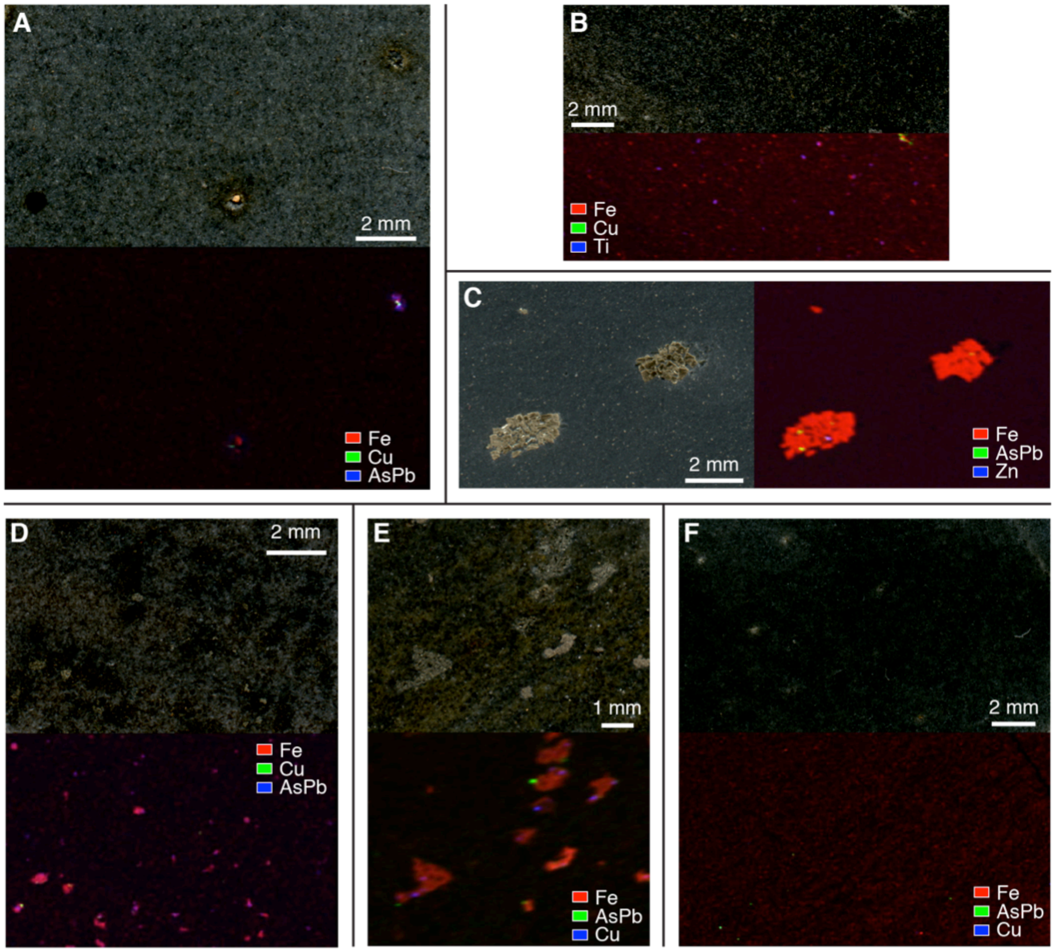

Figure S5.9: High-energy X-ray fluorescence (XRF) maps displaying elemental abundances paired with scans of the corresponding thick section region in the Prichard Formation. Separate scale bar and element key for each image pair (black to brightly colored at maximum). A) BS13-37, Transition Member, Libby. B) BS13-31, Unit C Hope. C) BS13-29, Unit F, Sagle Point. D) PP13-13, Unit F, 171 m away from sill, Perma. E) PP13-11, Unit F, 25 m away from sill, Perma. F) PP13-6, Unit F, 1.6 m away from sill, Perma. All were used for elemental abundance quantification in Table S5.4.

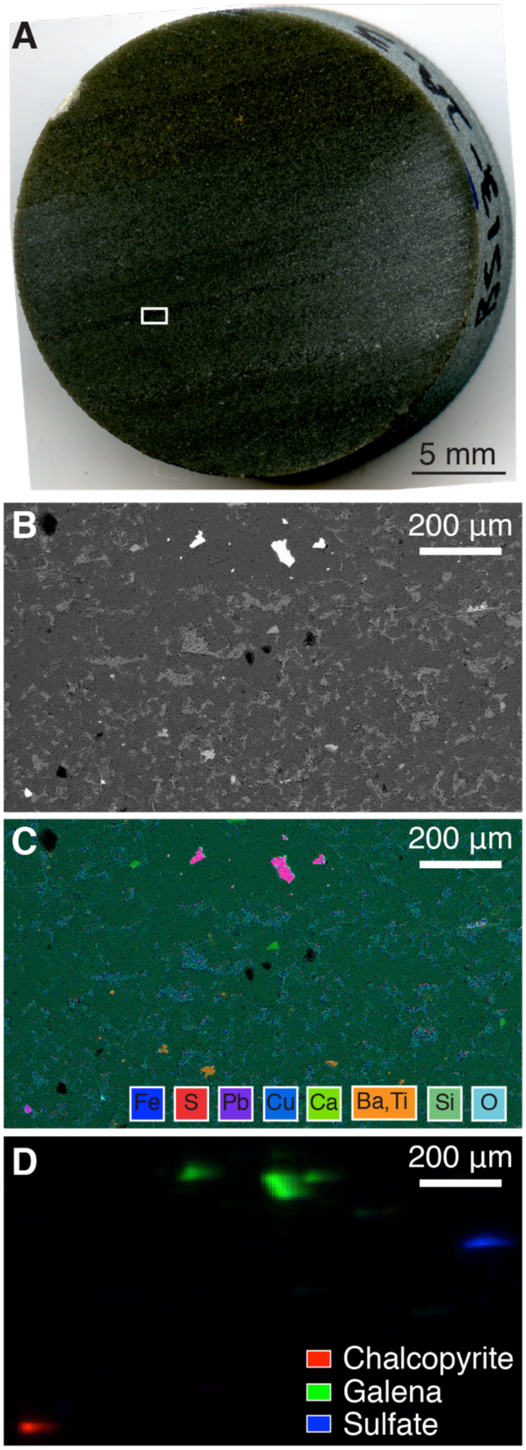

Figure S5.10: Detailed textural analysis of sample BS13-2, Lower Chamberlain Formation, White Sulphur Springs reveals euhedral base-metal sulfide grains where the galena grains potentially formed from a larger recrystallized sulfide grain based on texture. Additionally, a recrystallized or secondary barite grain is found. A) Image of thick section with box showing region displayed in parts B-D. B) Backscatter electron image. C) Energy dispersive X-ray spectroscopy (EDS) map. E) Multiple energy X-ray fluorescence (XRF) map at sulfur energies fitted with end-member X-ray absorption near-edge spectra (XANES) shown in Figure S5.5.

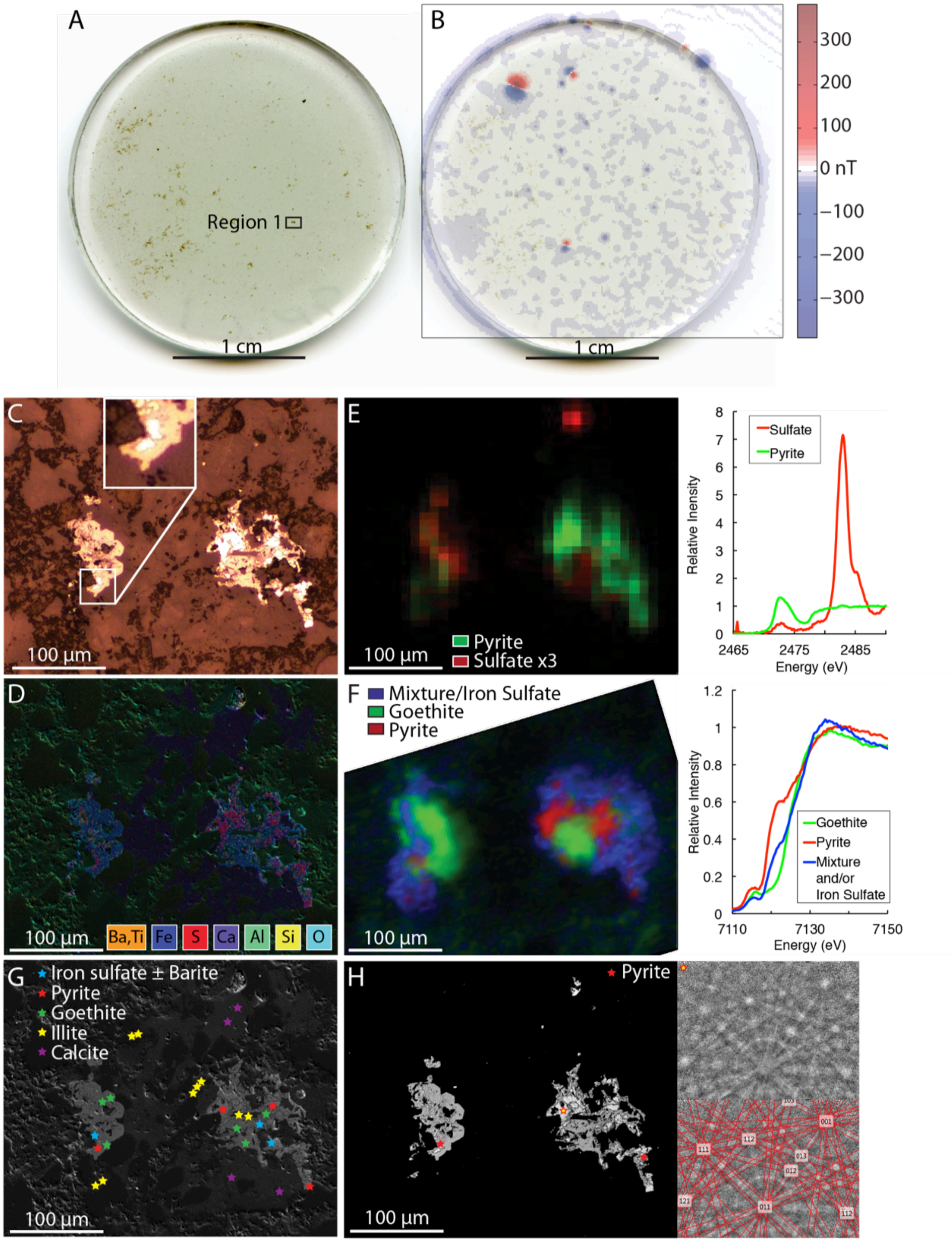

Figure S5.11: Detailed textural analysis of sample GP12-1, Appekunny Formation, Member 2, east side of Glacier National Park reveals scattered background magnetic dipoles and pyrite surrounded by goethite, interpreted to be surface weathering replacement of euhedral recrystallized sulfide nodules. Iron sulfates and barite also occur in the goethite rim and barite occurs as separate grains, interpreted to be authigenic replacements (not detrital or water column) from post-depositional oxidizing fluids or more likely, diagenesis in pore fluids. A) Image of thin section. B) Ultrahigh resolution scanning SQuID microscope (UHRSSM) image. C) Reflected light microscopy with inset highlighting goethite rim around pyrite. D) Energy dispersive X-ray spectroscopy (EDS) map. E) Multiple energy X-ray fluorescence (XRF) map at sulfur energies fitted with displayed end-member X-ray absorption near-edge spectra (XANES). F) Multiple energy XRF map at iron energies fitted to displayed end-member XANES. G) Electron probe micro-analyzer (EPMA) point mineral identifications on backscatter electron image (see Table S5.3 for detailed formulas). H) Electron backscatter diffraction (EBSD) point mineral identifications on backscatter electron image with diffraction pattern and standard match of select point shown.

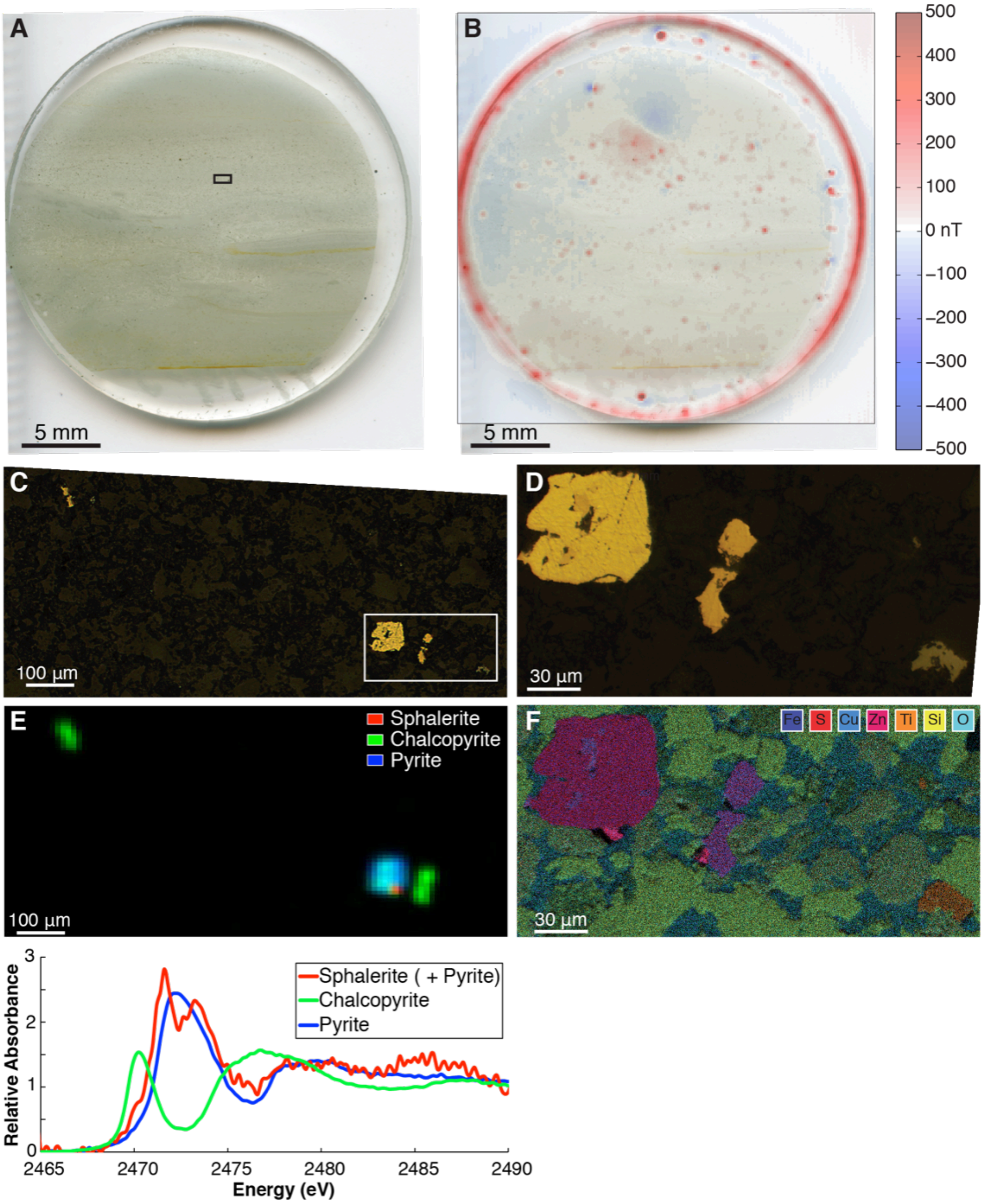

Figure S5.12: Detailed textural analysis of sample GP14-32, Appekunny Formation Member 5, east side of Glacier National Park reveals scattered background magnetic dipoles and euhedral sulfide nodules composed of multiple phases—pyrite, chalcopyrite, and sphalerite. A) Image of thin section with box showing region displayed in parts C and E. B) Ultrahigh resolution scanning SQuID microscope (UHRSSM) image. C) Reflected light microscopy with box showing region in parts D and F. D) Reflected light microscopy. E) Multiple energy X-ray fluorescence (XRF) map at sulfur energies fitted with displayed end-member X-ray absorption near-edge spectra (XANES). F) Energy dispersive X-ray spectroscopy (EDS) map.

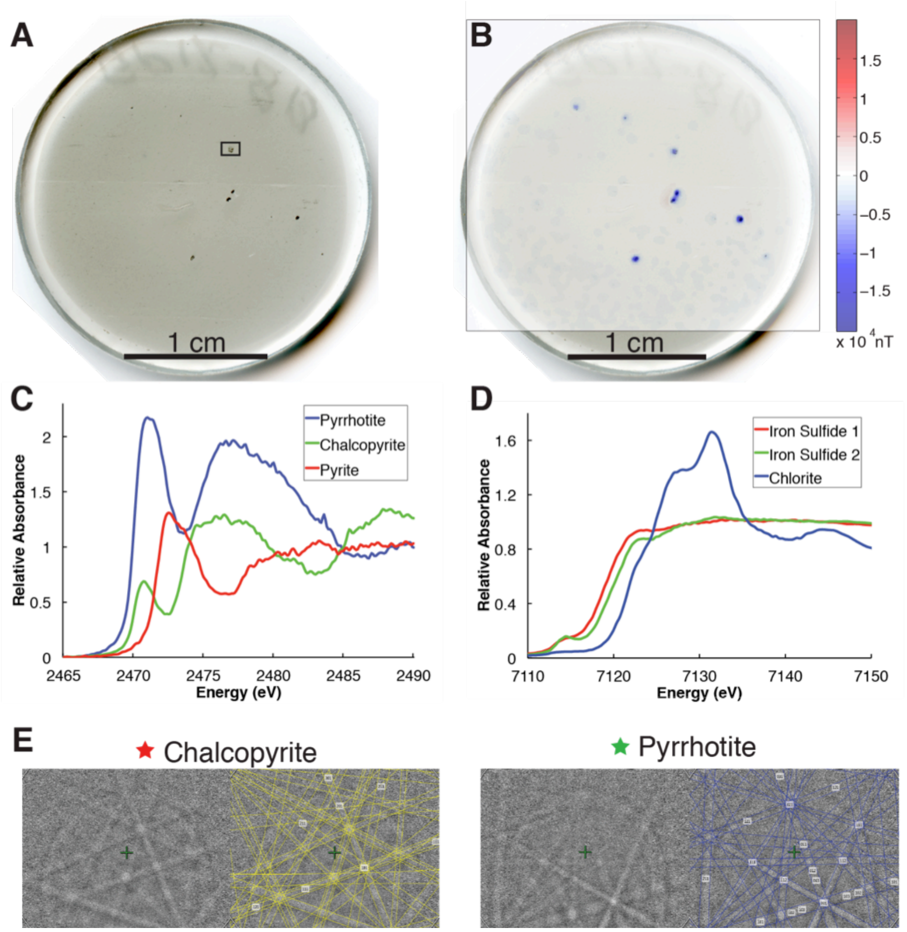

Figure S5.13: Additional textural analyses of sample GP12-8, Appekunny Formation Member 4 or Prichard Formation, west side of Glacier National Park highlight that the pyrrhotite nodules are magnetic. A) Image of thin section with box showing region displayed in Figure 5.4. B) Ultrahigh resolution scanning SQuID microscope (UHRSSM) image. C) End-member X-ray absorption near-edge spectra (XANES) at sulfur energies to which Figure 5.4C was fit. E) End-member XANES at iron energies to which Figure 5.4D was fit. E) Example electron backscatter diffraction (EBSD) patterns and standard match from the ones used to identify points shown in Figure 5.4E.

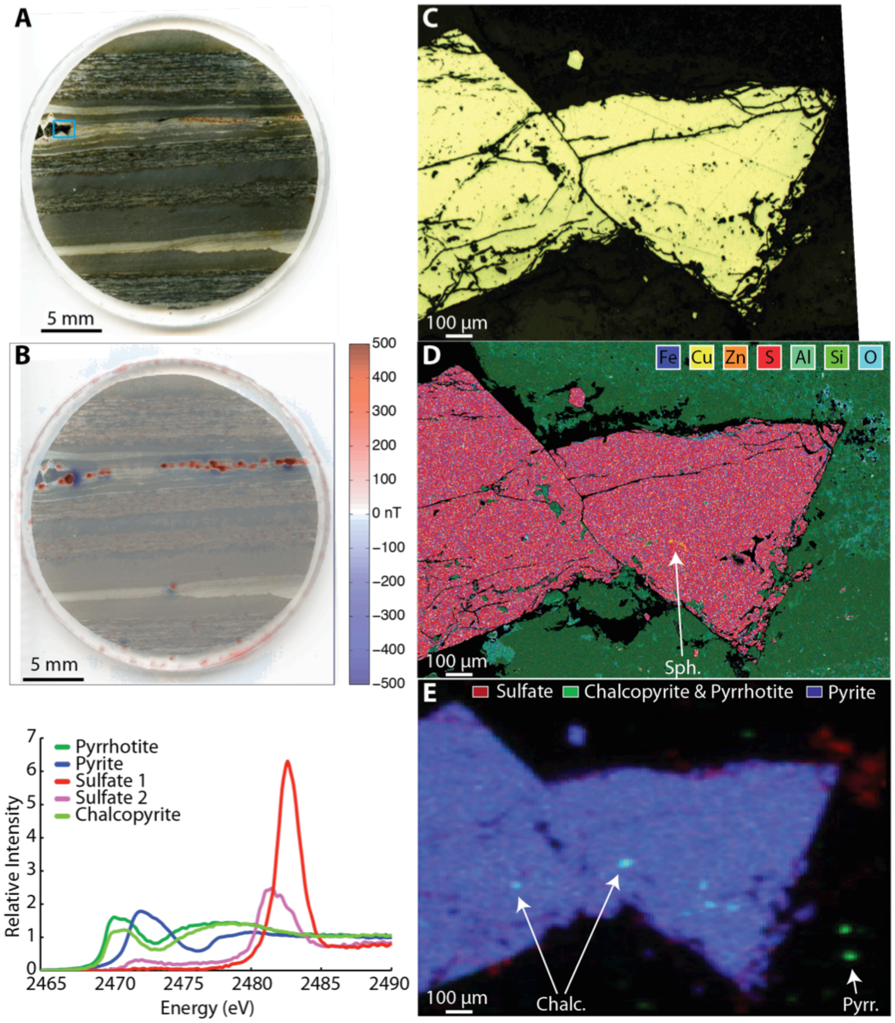

Figure S5.14: Detailed textural analysis of sample GP14-6, Appekunny Formation Member 4 or Prichard Formation, west side of Glacier National Park displays strong magnetic dipoles concentrated to certain laminae surrounding large secondary euhedral pyrite nodules which contain small domains of chalcopyrite and sphalerite. Pyrrhotite is located in small neighboring grains. A) Image of thin section with box showing region displayed in parts C-E. B) Ultrahigh resolution scanning SQuID microscope (UHRSSM) image. C) Reflected light microscopy. D) Energy dispersive X-ray spectroscopy (EDS) map. E) Multiple energy X-ray fluorescence (XRF) map at sulfur energies fitted with displayed end-member X-ray absorption near-edge spectra (XANES). Due to limitations in the mapping software, chalcopyrite and pyrrhotite are fit together even through the pyrrhotite spectra was used for analysis. Additional end-member XANES spectra are included for chalcopyrite and a second sulfate mineral to show their presence in the sample.

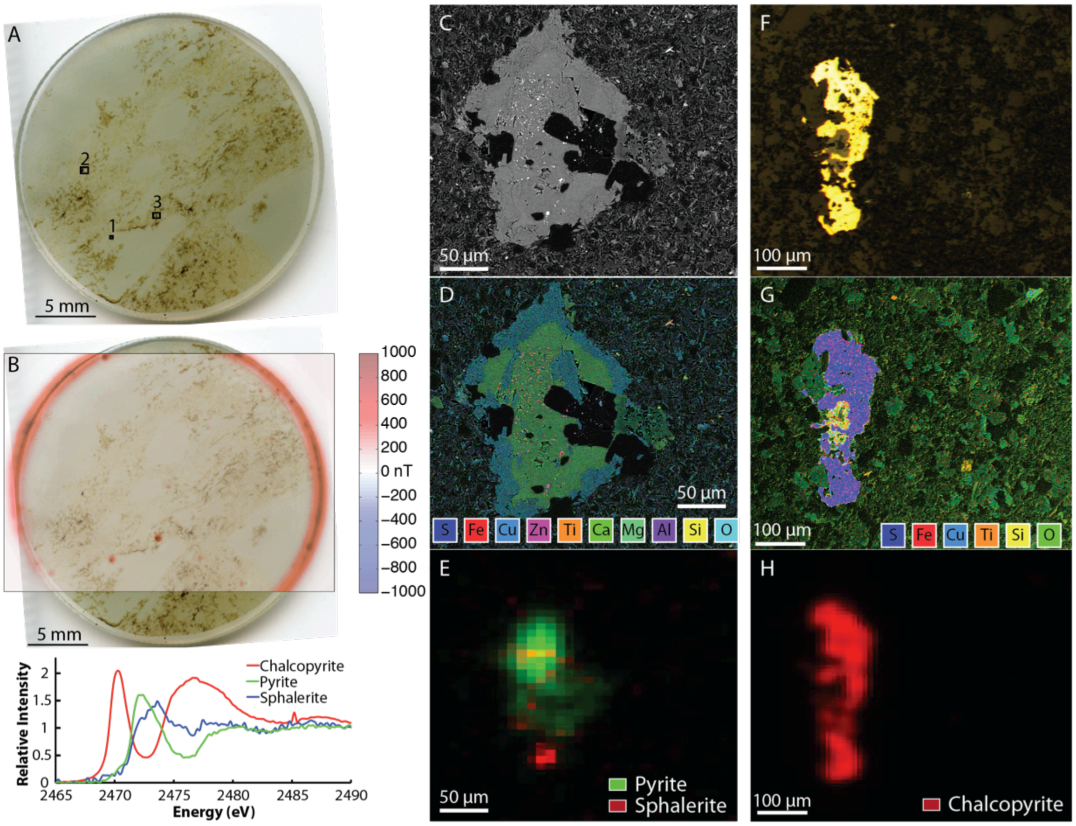

Figure S5.15: Detailed textural analysis of sample of GP14-27, Appekunny Formation Member 5, west side of Glacier National Park displays strong magnetic dipoles near recrystallized pyrite nodules suggesting the goethite detected in magnetic measurements is localized and from surface weathering. Sulfide minerals include chalcopyrite, sphalerite, and pyrite; chalcopyrite occurs in large distinct nodules while the sphalerite and pyrite are recrystallized remanents of a former nodule within a calcite and chlorite rim with neighboring Fe-rich dolomite. A) Image of thin section with boxes showing numbered regions displayed in parts C-E and parts F-H and in Figure 5.3D. B) Ultrahigh resolution scanning SQuID microscope (UHRSSM) image. C) Backscatter electron image of Region 1. D) Energy dispersive X-ray spectroscopy (EDS) map of Region 1. E) Multiple energy XRF map at sulfur energies of Region 1. F) Backscatter electron image of Region 2. G) EDS map of Region 2. H) Multiple energy X-ray fluorescence (XRF) map at sulfur energies of Region 2. E and H fitted with the same end-member X-ray absorption near-edge spectra (XANES) shown in Figure S5.5.

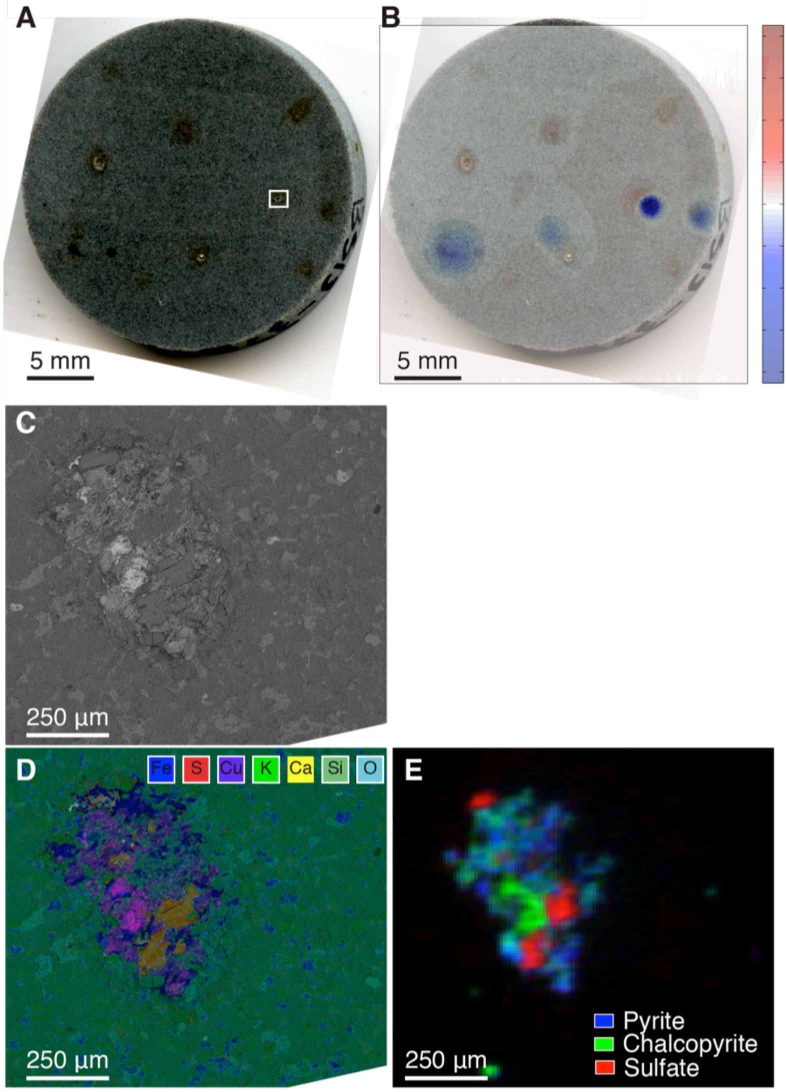

Figure S5.16: Detailed textural analysis of sample of BS13-37, Prichard Formation, Transition Member, Libby displays weathered pits from iron sulfides with mixed nodules of pyrite, chalcopyrite, and calcium sulfate remaining. Background magnetic dipoles are concentrated in near the pits and could be predominantly surface-weathering goethite identified using magnetic techniques. A) Image of thick section with boxes showing numbered regions displayed in parts C-E. B) Ultrahigh resolution scanning SQuID microscope (UHRSSM) image. C) Backscatter electron image. D) Energy dispersive X-ray spectroscopy (EDS) map. E) Multiple energy XRF map at sulfur energies fitted with the end-member X-ray absorption near-edge spectra (XANES) shown in Figure S5.5.

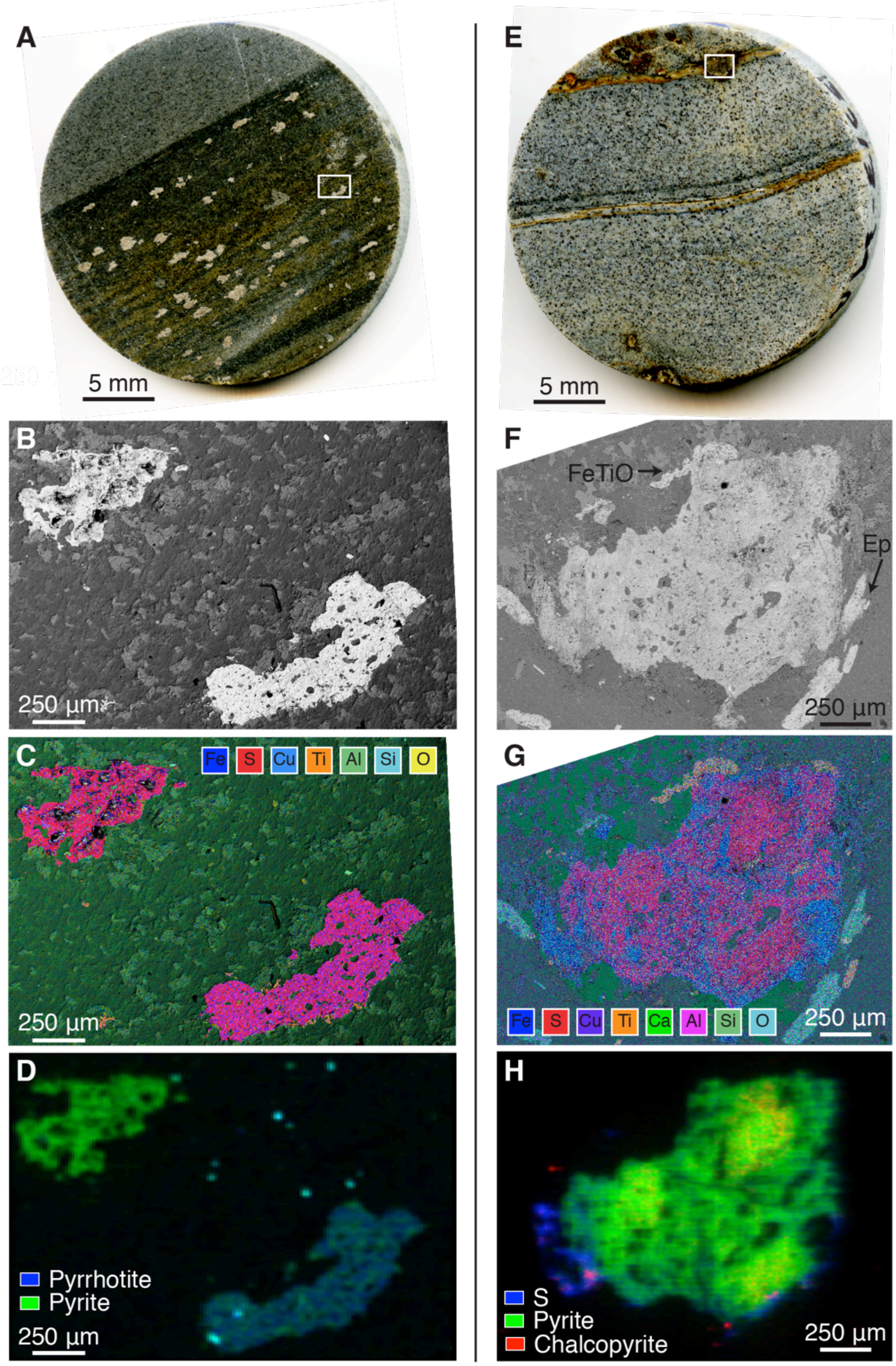

Figure S5.17: Detailed textural analysis of samples PP13-11 and BS13-39. Analyses of PP13-1, Prichard Formation, Unit F, 25m from sill, Perma reveal large secondary pyrite and pyrrhotite nodules that contain small domains of chalcopyrite. A) Image of thick section with box showing region displayed in parts B-D. B) Backscatter electron image. C) Energy dispersive X-ray spectroscopy (EDS) map. D) Multiple energy X-ray fluorescence (XRF) map at sulfur energies fitted with end-member X-ray absorption near-edge spectra (XANES) shown in Figure S5.5. Analyses of BS13-39, Prichard Formation, Upper Member, Libby reveal a large secondary pyrite nodule with small domains of chalcopyrite rimmed by elemental sulfur and iron titanium oxides. Discrete grains of chalcopyrite are also present along with euhedral grains of iron titanium oxides and epidote. E) Image of thick section with box showing region displayed in parts F-G with example epidote (Ep) and the iron titantium oxide (FeTiO) grains identified with arrows. F) Backscatter electron image. G) EDS map. H) Multiple energy XRF map at sulfur energies fitted with end-member XANES shown in Figure S5.5.

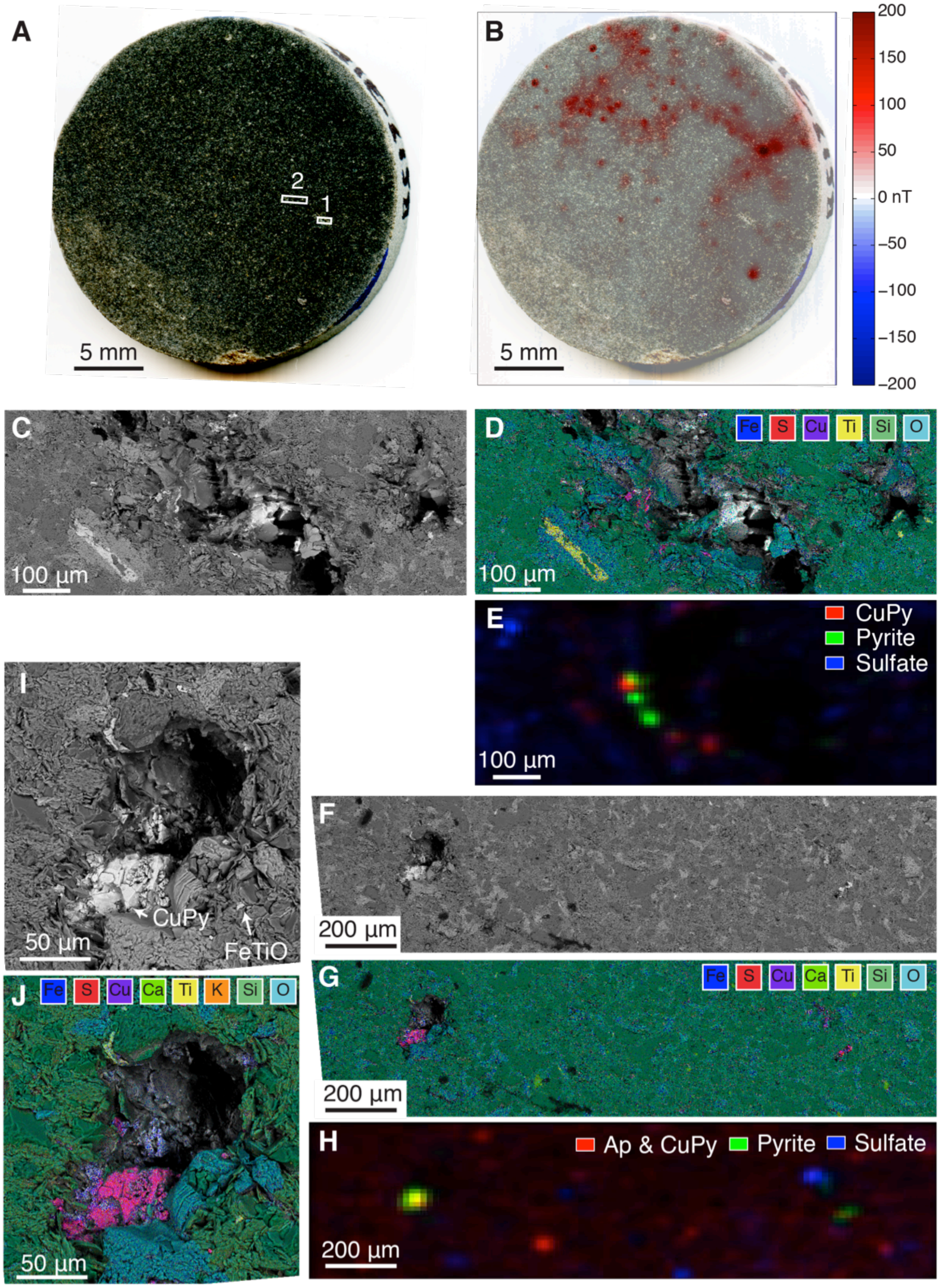

Figure S5.18: Detailed textural analysis of sample of BS13-31, Prichard Formation, Unit F, Hope displays weathered pits from iron sulfides with mixed nodules of pyrite, chalcocite, and chalcopyrite remaining. Iron titanium oxide

(FeTiO) occurs within this sample in small and large secondary euhedral grains; background magnetic dipoles appear concentrated in certain regions, but not specifically on weathered sulfide pits. A) Image of thick section with boxes showing numbered regions displayed in parts C-E and parts F-H. B) Ultrahigh resolution scanning SQuID microscope (UHRSSM) image. C) Backscatter electron image of Region 1. D) Energy dispersive X-ray spectroscopy (EDS) map of Region 1. E) Multiple energy XRF map at sulfur energies of Region 1. F) Backscatter electron image of Region 2. Based on EDS, the chalcopyrite (CuPy) may actually be chalcocite in this region. G) EDS map of Region 2. H) Multiple energy X-ray fluorescence (XRF) map at sulfur energies of Region 2. E and H fitted with the same end-member X-ray absorption near-edge spectra (XANES) shown in Figure S5.5; subtle differences in copper sulfides are based on EDS data. Note that apatite (Ap) is included with chalcopyrite (CuPy) on the XRF maps due to limitations of the fitting program. I) Zoomed backscatter electron image of sulfide nodule in Region 2 with chalcopyrite and FeTiO pointed out with arrows. J) Zoomed EDS of sulfide nodule in Region 2.

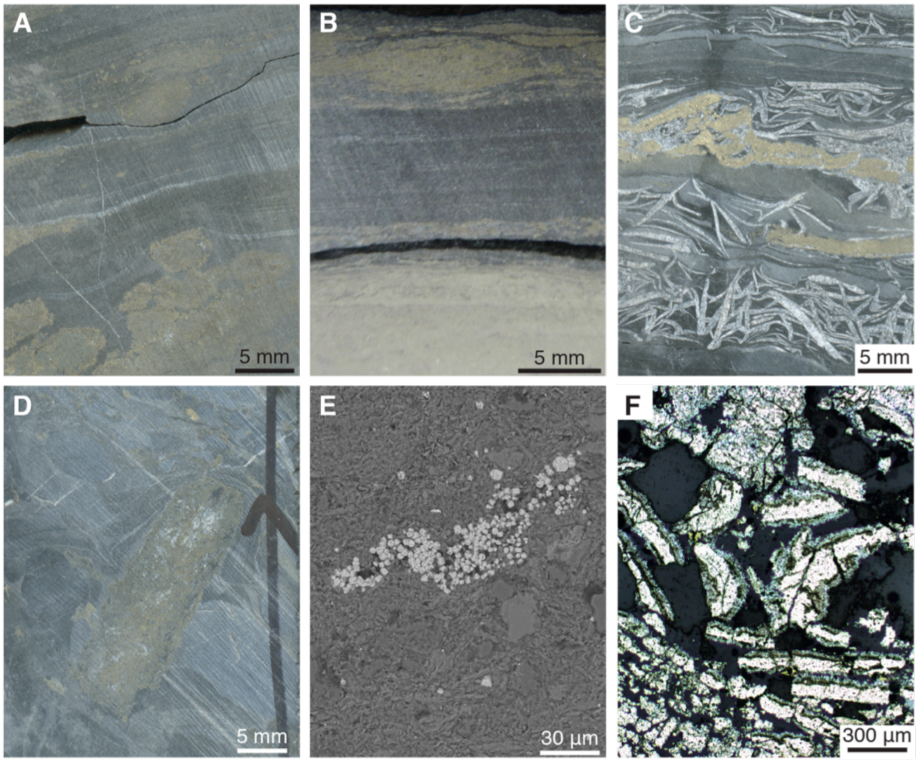

Figure S5.19. Macroscopic and microscopic textures in Newland Formation samples from the Black Butte Deposit drill core highlighting early diagenetic formation of pyrite and sulfates. A) SC11-095, 140.39 displays differential compaction of dolomitic shale layers around early pyrite nodules. B) SC11-09, 388.26 also shows differential compaction of dolomitic shale around early pyrite nodules and laminae. C) SC11-61.27 displays differential compaction of dolomitic shale laminae around early diagenetic barite laths with secondary intergrown sub-parallel iron sulfides. D) SC11-095, 400.83 displays a debris flow clast made of pyrite. E) The backscatter electron image of T095-53 (SC11-095, 53.52 m) shows it contains fine-grained recrystallized pyrite framboids. F) The reflected light image of T029-76 (SC11-029, 76.34 m) displays broken detrital early iron sulfide tubes.

5.12 References

Algoe, C., Stoops, G., Vandenberghe, R., and Van Ranst, E., 2012, Selective dissolution of Fe–Ti oxides—Extractable iron as a criterion for andic properties revisited: Catena, v. 92, p. 49-54.

Anderson, H. E., and Davis, D. W., 1995, U-Pb geochronology of the Moyie sills, Purcell Supergroup, southeastern British Columbia: implications for the Mesoproterozoic geological history of the Purcell (Belt) basin: Canadian Journal of Earth Sciences, v. 32, no. 8, p. 1180-1193.

Asael, D., Tissot, F. L., Reinhard, C. T., Rouxel, O., Dauphas, N., Lyons, T. W., Ponzevera, E., Liorzou, C., and Chéron, S., 2013, Coupled molybdenum, iron and uranium stable isotopes as oceanic paleoredox proxies during the Paleoproterozoic Shunga Event: Chemical Geology, v. 362, p. 193-210.

Aubourg, C., and Pozzi, J.-P., 2010, Toward a new< 250 C pyrrhotite–magnetite geothermometer for claystones: Earth and Planetary Science Letters, v. 294, no. 1, p. 47-57.

Berkner, L., and Mashall, L., 1964, The History of Growth of Oxygen in the Earth's Atmosphere, *in* Brancazio, P., and Cameron, A., eds., The Origin and Evolution of Atmospheres and Oceans: New York, John WIley & Sons, Inc.

Berner, R. A., 1984, Sedimentary pyrite formation: an update: Geochimica et Cosmochimica Acta, v. 48, no. 4, p. 605-615.

Besnus, M., and Meyer, A., Nouvelles données expérimentales sur le magnétisme de la pyrrhotine naturelle, *in* Proceedings Proc. Int. Conf. Mag., Nottingham1964, Volume 20, p. 507-511.

Bishop, D., 1972, Progressive metamorphism from prehnite-pumpellyite to greenschist facies in the Dansey Pass area, Otago, New Zealand: Geological Society of America Bulletin, v. 83, no. 11, p. 3177-3198.

Burton, E. D., Bush, R. T., and Sullivan, L. A., 2006, Sedimentary iron geochemistry in acidic waterways associated with coastal lowland acid sulfate soils: Geochimica et Cosmochimica Acta, v. 70, no. 22, p. 5455-5468.

Canfield, D. E., and Berner, R. A., 1987, Dissolution and pyritization of magnetite in anoxie marine sediments: Geochimica et Cosmochimica Acta, v. 51, no. 3, p. 645-659.

Clarkson, M., Poulton, S., Guilbaud, R., and Wood, R., 2014, Assessing the utility of Fe/Al and Fe-speciation to record water column redox conditions in carbonate-rich sediments: Chemical Geology, v. 382, p. 111-122.

Cloud, P. E., 1968, Atmospheric and Hydrospheric Evolution on the Primitive Earth: Science, v. 160, no. 3829, p. 729-736.

Craig, J. R., and Vokes, F. M., 1993, The metamorphism of pyrite and pyritic ores: an overview: Mineralogical Magazine, v. 57, no. 1, p. 3-18.

Cressman, E. R., 1989, Reconnaissance stratigraphy of the Prichard Formation (Middle Proterozoic) and the early development of the Belt Basin, Washington, Idaho, and Montana: United States Geological Survey, Professional Paper, v. 1490, p. 80.

Crowe, S. A., Paris, G., Katsev, S., Jones, C., Kim, S.-T., Zerkle, A. L., Nomosatryo, S., Fowle, D. A., Adkins, J. F., and Sessions, A. L., 2014, Sulfate was a trace constituent of Archean seawater: Science, v. 346, no. 6210, p. 735-739.

Day, R., Fuller, M., and Schmidt, V., 1977, Hysteresis properties of titanomagnetites: grain-size and compositional dependence: Physics of the Earth and Planetary Interiors, v. 13, no. 4, p. 260-267.

Duke, E. F., and Lewis, R. S., 2010, Near infrared spectra of white mica in the Belt Supergroup and implications for metamorphism: American Mineralogist, v. 95, no. 7, p. 908-920.

Dunlop, D. J., 2002, Theory and application of the Day plot (Mrs/Ms versus Hcr/Hc) 1. Theoretical curves and tests using titanomagnetite data: Journal of Geophysical Research: Solid Earth, v. 107, no. B3, p. EPM 4-1-EPM 4-22.

Embley, T. M., and Martin, W., 2006, Eukaryotic evolution, changes and challenges: Nature, v. 440, no. 7084, p. 623-630.

Evans, K. V., Aleinikoff, J. N., Obradovich, J. D., and Fanning, C. M., 2000, SHRIMP U-Pb geochronology of volcanic rocks, Belt Supergroup, western Montana: evidence for rapid deposition of sedimentary strata: Canadian Journal of Earth Sciences, v. 37, no. 9, p. 1287-1300.

Ferry, J. M., 1983, Regional metamorphism of the Vassalboro Formation, south-central Maine, USA: a case study of the role of fluid in metamorphic petrogenesis: Journal of the Geological Society, v. 140, no. 4, p. 551-576.

-, 1984, A biotite isograd in south-central Maine, USA: mineral reactions, fluid transfer, and heat transfer: Journal of Petrology, v. 25, no. 4, p. 871-893.

-, 1988, Infiltration-driven metamorphism in northern New England, USA: Journal of Petrology, v. 29, no. 6, p. 1121-1159.

-, 2007, The role of volatile transport by diffusion and dispersion in driving biotite-forming reactions during regional metamorphism of the Gile Mountain Formation, Vermont: American Mineralogist, v. 92, no. 8-9, p. 1288-1302.

Fischer, W. W., 2016, Breathing room for early animals: Proceedings of the National Academy of Sciences, v. 113, no. 7, p. 1686-1688.

Fleet, M. E., 2005, XANES spectroscopy of sulfur in earth materials: The Canadian Mineralogist, v. 43, no. 6, p. 1811-1838.

French, B. M., 1973, Mineral assemblages in diagenetic and low-grade metamorphic iron-formation: Economic Geology, v. 68, no. 7, p. 1063-1074.

Fuller, M., Cisowski, S., Hart, M., Haston, R., Schmidtke, E., and Jarrard, R., 1988, NRM-IRM(s) Demagnetization Plots - an Aid to the Interpretation of Natural Remanent Magnetization: Geophysical Research Letters, v. 15, no. 5, p. 518-521.

Fuller, M., Kidane, T., and Ali, J., 2002, AF demagnetization characteristics of NRM, compared with anhysteretic and saturation isothermal remanence: an aid in the interpretation of NRM: Physics and Chemistry of the Earth, v. 27, no. 25-31, p. 1169-1177.

Gellatly, A. M., and Lyons, T. W., 2005, Trace sulfate in mid-Proterozoic carbonates and the sulfur isotope record of biospheric evolution: Geochimica et Cosmochimica Acta, v. 69, no. 15, p. 3813-3829.

Gilleaudeau, G. J., and Kah, L. C., 2015, Heterogeneous redox conditions and a shallow chemocline in the Mesoproterozoic ocean: evidence from carbon–sulfur–iron relationships: Precambrian Research, v. 257, p. 94-108.

González-Álvarez, I., and Kerrich, R., 2010, REE and HFSE mobility due to protracted flow of basinal brines in the Mesoproterozoic Belt-Purcell Supergroup, Laurentia: Precambrian Research, v. 177, no. 3, p. 291-307.

González-Álvarez, I., Kusiak, M. A., and Kerrich, R., 2006, A trace element and chemical Th–U total Pb dating study in the lower Belt-Purcell Supergroup, Western North America: provenance and diagenetic implications: Chemical Geology, v. 230, no. 1, p. 140-160.

Graham, G., Hitzman, M. W., and Zieg, J., 2012, Geologic Setting, Sedimentary Architecture, and Paragenesis of the Mesoproterozoic Sediment-Hosted Sheep Creek Cu-Co-Ag Deposit, Helena Embayment, Montana: Economic Geology, v. 107, no. 6, p. 1115-1141.

Grotzinger, J. P., 1981, The stratigraphy and sedimentation of the Wallace Formation northwest Montana and northern Idaho [M.S. Thesis: University of Montana, 153 p.

Halevy, I., 2013, Production, preservation, and biological processing of mass-independent sulfur isotope fractionation in the Archean surface environment: Proceedings of the National Academy of Sciences, v. 110, no. 44, p. 17644-17649.

Hall, A. J., 1986, Pyrite-pyrrhotine redox reactions in nature: Mineralogical Magazine, v. 50, p. 223-229.

Hamilton, J., Bishop, D., Morris, H., and Owens, O., 1982, Geology of the Sullivan orebody, Kimberley, BC, Canada: Precambrian Sulphide Deposits, v. 25, p. 597-665.

Hansel, C. M., Lentini, C. J., Tang, Y., Johnston, D. T., Wankel, S. D., and Jardine, P. M., 2015, Dominance of sulfur-fueled iron oxide reduction in low-sulfate freshwater sediments: The ISME Journal, v. 9, no. 11, p. 2400-2412.

Harrison, J. E., 1972, Precambrian Belt basin of northwestern United States: Its geometry, sedimentation, and copper occurrences: Geological Society of America Bulletin, v. 83, no. 5, p. 1215-1240.

Heslop, D., Dekkers, M., Kruiver, P., and Van Oorschot, I., 2002, Analysis of isothermal remanent magnetization acquisition curves using the expectation-maximization algorithm: Geophysical Journal International, v. 148, no. 1, p. 58-64.

Hilscher, G., Peter, R., Zemann, J., and Ntaflos, T., 2005, Low-temperature magnetic investigation of ankerite: European journal of mineralogy, v. 17, no. 1, p. 103-105.

Holland, H. D., 1984, The chemical evolution of the atmosphere and oceans, Princeton University Press.

Horng, C.-S., and Roberts, A. P., 2006, Authigenic or detrital origin of pyrrhotite in sediments?: Resolving a paleomagnetic conundrum: Earth and Planetary Science Letters, v. 241, no. 3, p. 750-762.

Horodyski, R. J., Winston, D., and Whipple, J. W., 1989, Paleontology of the middle Proterozoic belt supergroup, *in* Winston, D., Horodyski, R. J., and Whipple, J. W., eds., Middle Proterozoic Belt Supergroup, Western Montana: Great Falls, Montana to Spokane, Washington: 28th International Geological Congress, Field Trip Guidebook T334, p. 7-26.

Housen, B. A., Banerjee, S., and Moskowitz, B., 1996, Low‐temperature magnetic properties of siderite and magnetite in marine sediments: Geophysical Research Letters, v. 23, no. 20, p. 2843-2846.

Huebschman, R. P., 1973, Correlation of fine carbonaceous bands across a Precambrian stagnant basin: Journal of Sedimentary Research, v. 43, no. 3, p. 688-699.

Kendall, B., Creaser, R. A., Gordon, G. W., and Anbar, A. D., 2009, Re–Os and Mo isotope systematics of black shales from the Middle Proterozoic Velkerri and Wollogorang formations, McArthur Basin, northern Australia: Geochimica et Cosmochimica Acta, v. 73, no. 9, p. 2534-2558.

Kholodov, V., and Butuzova, G. Y., 2008, Siderite formation and evolution of sedimentary iron ore deposition in the Earth's history: Geology of Ore Deposits, v. 50, no. 4, p. 299-319.

Kirschvink, J. L., Kopp, R. E., Raub, T. D., Baumgartner, C. T., and Holt, J. W., 2008, Rapid, precise, and high-sensitivity acquisition of paleomagnetic and rock-magnetic data: Development of a low-noise automatic sample changing system for superconducting rock magnetometers: Geochemistry Geophysics Geosystems, v. 9, no. 5.

Klein, F., Bach, W., Humphris, S. E., Kahl, W.-A., Jöns, N., Moskowitz, B., and Berquó, T. S., 2014, Magnetite in seafloor serpentinite—Some like it hot: Geology, v. 42, no. 2, p. 135-138.

Knoll, A. H., Javaux, E. J., Hewitt, D., and Cohen, P., 2006, Eukaryotic organisms in Proterozoic oceans: Philosophical Transactions of the Royal Society B: Biological Sciences, v. 361, no. 1470, p. 1023-1038.

Koeksoy, E., Halama, M., Konhauser, K. O., and Kappler, A., 2015, Using modern ferruginous habitats to interpret Precambrian banded iron formation deposition: International Journal of Astrobiology, p. 1-13.

Larrasoaña, J. C., Roberts, A. P., Musgrave, R. J., Gràcia, E., Piñero, E., Vega, M., and Martínez-Ruiz, F., 2007, Diagenetic formation of greigite and pyrrhotite in gas hydrate marine sedimentary systems: Earth and Planetary Science Letters, v. 261, no. 3, p. 350-366.

Lentini, C. J., Wankel, S. D., and Hansel, C., 2012, Enriched iron (III)-reducing bacterial communities are shaped by carbon substrate and iron oxide mineralogy: Frontiers in Microbiology, v. 3, p. 404.

Li, C., Planavsky, N. J., Love, G. D., Reinhard, C. T., Hardisty, D., Feng, L., Bates, S. M., Huang, J., Zhang, Q., and Chu, X., 2015, Marine redox conditions in the middle Proterozoic ocean and isotopic constraints on authigenic carbonate formation: Insights from the Chuanlinggou Formation, Yanshan Basin, North China: Geochimica et Cosmochimica Acta, v. 150, p. 90-105.

Liu, Q., Yu, Y., Torrent, J., Roberts, A. P., Pan, Y., and Zhu, R., 2006, Characteristic low‐temperature magnetic properties of aluminous goethite [α‐(Fe, Al) OOH] explained: Journal of Geophysical Research: Solid Earth, v. 111, no. B12.

Luepke, J. J., and Lyons, T. W., 2001, Pre-Rodinian (Mesoproterozoic) supercontinental rifting along the western margin of Laurentia: geochemical evidence from the Belt-Purcell Supergroup: Precambrian Research, v. 111, no. 1, p. 79-90.

Lyons, T. W., Luepke, J. J., Schreiber, M. E., and Zieg, G. A., 2000, Sulfur geochemical constraints on Mesoproterozoic restricted marine deposition: lower Belt Supergroup, northwestern United States: Geochimica et Cosmochimica Acta, v. 64, no. 3, p. 427-437.

Lyons, T. W., and Severmann, S., 2006, A critical look at iron paleoredox proxies: new insights from modern euxinic marine basins: Geochimica et Cosmochimica Acta, v. 70, no. 23, p. 5698-5722.

Mayhew, L., Webb, S., and Templeton, A., 2011, Microscale imaging and identification of Fe speciation and distribution during fluid–mineral reactions under highly reducing conditions: Environmental science & technology, v. 45, no. 10, p. 4468-4474.

Moreau, M., Ader, M., and Enkin, R., 2005, The magnetization of clay-rich rocks in sedimentary basins: low-temperature experimental formation of magnetic carriers in natural samples: Earth and Planetary Science Letters, v. 230, no. 1, p. 193-210.

Muffler, L. P., and White, D. E., 1969, Active metamorphism of upper Cenozoic sediments in the Salton Sea geothermal field and the Salton Trough, southeastern California: Geological Society of America Bulletin, v. 80, no. 2, p. 157-182.

Nadoll, P., Mauk, J. L., Hayes, T. S., Koenig, A. E., and Box, S. E., 2012, Geochemistry of magnetite from hydrothermal ore deposits and host rocks of the Mesoproterozoic Belt Supergroup, United States: Economic Geology, v. 107, no. 6, p. 1275-1292.

O'Day, P. A., Rivera, N., Root, R., and Carroll, S. A., 2004, X-ray absorption spectroscopic study of Fe reference compounds for the analysis of natural sediments: American Mineralogist, v. 89, no. 4, p. 572-585.

Partin, C., Bekker, A., Planavsky, N., and Lyons, T., 2015, Euxinic conditions recorded in the ca. 1.93 Ga Bravo Lake Formation, Nunavut (Canada): Implications for oceanic redox evolution: Chemical Geology, v. 417, p. 148-162.

Peters, C., and Dekkers, M., 2003, Selected room temperature magnetic parameters as a function of mineralogy, concentration and grain size: Physics and Chemistry of the Earth, v. 28, no. 16, p. 659-667.

Piché, M., and Jébrak, M., 2006, Determination of alteration facies using the normative mineral alteration index: Selbaie Cu-Zn deposit, northern Abitibi greenstone belt, Canada: Canadian Journal of Earth Sciences, v. 43, no. 12, p. 1877-1885.

Planavsky, N. J., McGoldrick, P., Scott, C. T., Li, C., Reinhard, C. T., Kelly, A. E., Chu, X., Bekker, A., Love, G. D., and Lyons, T. W., 2011, Widespread iron-rich conditions in the mid-Proterozoic ocean: Nature, v. 477, no. 7365, p. 448-451.

Potter, D., and Stephenson, A., 1986, The detection of fine particles of magnetite using anhysteretic and rotational remanent magnetizations: Geophysical Journal International, v. 87, no. 2, p. 569-582.

Poulton, S. W., and Canfield, D. E., 2005, Development of a sequential extraction procedure for iron: implications for iron partitioning in continentally derived particulates: Chemical Geology, v. 214, no. 3, p. 209-221.

-, 2011, Ferruginous conditions: a dominant feature of the ocean through Earth's history: Elements, v. 7, no. 2, p. 107-112.

Present, T. M., Bergmann, K. D., Meyers, C. E., Slotznick, S. P., Creveling, J. R., Zieg, G. A., Fischer, W. W., Knoll, A. H., and Grotzinger, J. P., in review, Pyrite-walled tube structures in a Mesoproterozoic SEDEX massive sulfide deposit: Geological Society of America Bulletin.

Raiswell, R., Reinhard, C. T., Derkowski, A., Owens, J., Bottrell, S. H., Anbar, A. D., and Lyons, T. W., 2011, Formation of syngenetic and early diagenetic iron minerals in the late Archean Mt. McRae Shale, Hamersley Basin, Australia: New insights on the patterns, controls and paleoenvironmental implications of authigenic mineral formation: Geochimica et Cosmochimica Acta, v. 75, no. 4, p. 1072-1087.

Raub, T., Johnson, S. C., and Raub, T. D., 2012, Rock magnetic detection of the pyrite-to-pyrrhotite reduction: applications to hydrocarbon maturity, mineral resources, and biogeochemistry, American Geophysical Union, Fall Meeting: San Francisco, CA, p. GP34A-08.

Reinhard, C. T., Lyons, T. W., Rouxel, O., Asael, D., Dauphas, N., and Kump, L. R., 2013, 7.10.4 Iron Speciaiton and Isotope Perspectives on Palaeoproterozoic Water Column Chemistry, *in* Melezhik, V., Prave, A.R., Hanski, E.J., Fallick, A.E., Lepland, A., Kump, L.R., Strauss, H., ed., Reading the Archive of Earth's Oxygenation, Volume 3: Berlin Heidelberg, Springer, p. 1483-1492.

Reinhard, C. T., Raiswell, R., Scott, C., Anbar, A. D., and Lyons, T. W., 2009, A late Archean sulfidic sea stimulated by early oxidative weathering of the continents: Science, v. 326, no. 5953, p. 713-716.

Reuschel, M., Melezhik, V., and Strauss, H., 2012, Sulfur isotopic trends and iron speciation from the c. 2.0 Ga Pilgujärvi Sedimentary Formation, NW Russia: Precambrian Research, v. 196, p. 193-203.

Roberts, A. P., Liu, Q., Rowan, C. J., Chang, L., Carvallo, C., Torrent, J., and Horng, C. S., 2006, Characterization of hematite (α - Fe2O3), goethite (α - FeOOH), greigite (Fe3S4), and pyrrhotite (Fe7S8) using first - order reversal curve diagrams: Journal of Geophysical Research: Solid Earth, v. 111, no. B12.

Robertson, D., and France, D., 1994, Discrimination of remanence-carrying minerals in mixtures, using isothermal remanent magnetisation acquisition curves: Physics of the Earth and Planetary Interiors, v. 82, no. 3, p. 223-234.

Rochette, P., Fillion, G., Mattéi, J.-L., and Dekkers, M. J., 1990, Magnetic transition at 30–34 Kelvin in pyrrhotite: insight into a widespread occurrence of this mineral in rocks: Earth and Planetary Science Letters, v. 98, no. 3, p. 319-328.

Sears, J., Chamberlain, K., and Buckley, S., 1998, Structural and U-Pb geochronological evidence for 1.47 Ga rifting in the Belt basin, western Montana: Canadian Journal of Earth Sciences, v. 35, no. 4, p. 467-475.

Shen, Y., Knoll, A. H., and Walter, M. R., 2003, Evidence for low sulphate and anoxia in a mid-Proterozoic marine basin: Nature, v. 423, no. 6940, p. 632-635.

Skomurski, F. N., Kerisit, S., and Rosso, K. M., 2010, Structure, charge distribution, and electron hopping dynamics in magnetite (Fe 3 O 4)(100) surfaces from first principles: Geochimica et Cosmochimica Acta, v. 74, no. 15, p. 4234-4248.

Slotznick, S. P., Winston, D., Webb, S. M., Kirschvink, J. L., and Fischer, W. W., 2016, Iron mineralogy and redox conditions during deposition of the Mid-Proterozoic Appekunny Formation, Belt Supergroup, Glacier National Park: Geological Society of America Special Papers, v. 522.

Slotznick, S. P., Zieg, J., Webb, S. M., Kirschvink, J. L., and Fischer, W. W., 2015, Iron Mineralogy and Redox Chemistry of the Mesoproterozoic Newland Formation in the Helena Embayment, Belt Supergroup, Montana: Northwest Geology, v. 44, p. 55-72.

Snowball, I. F., 1997, The detection of single-domain greigite (Fe3S4) using rotational remanent magnetization (RRM) and the effective gyro field (Bg): mineral magnetic and palaeomagnetic applications: Geophysical Journal International, v. 130, no. 3, p. 704-716.

Sperling, E., Rooney, A., Hays, L., Sergeev, V., Vorob'eva, N., Sergeeva, N., Selby, D., Johnston, D., and Knoll, A., 2014, Redox heterogeneity of subsurface waters in the Mesoproterozoic ocean: Geobiology, v. 12, no. 5, p. 373-386.

Stüeken, E. E., 2013, A test of the nitrogen-limitation hypothesis for retarded eukaryote radiation: nitrogen isotopes across a Mesoproterozoic basinal profile: Geochimica et Cosmochimica Acta, v. 120, p. 121-139.

Summons, R. E., Bradley, A. S., Jahnke, L. L., and Waldbauer, J. R., 2006, Steroids, triterpenoids and molecular oxygen: Philosophical Transactions of the Royal Society B: Biological Sciences, v. 361, no. 1470, p. 951-968.

Suzuki, Y., Kopp, R. E., Kogure, T., Suga, A., Takai, K., Tsuchida, S., Ozaki, N., Endo, K., Hashimoto, J., and Kato, Y., 2006, Sclerite formation in the hydrothermal-vent “scaly-foot” gastropod—possible control of iron sulfide biomineralization by the animal: Earth and Planetary Science Letters, v. 242, no. 1, p. 39-50.

Tauxe, L., Mullender, T., and Pick, T., 1996, Potbellies, wasp-waists, and superparamagnetism in magnetic hysteresis: Journal of geophysical research, v. 101, p. 571-583.

Thomson, G. F., 1990, The anomalous demagnetization of pyrrhotite: Geophysical Journal International, v. 103, no. 2, p. 425-430.

Verwey, E., 1939, Electronic conduction of magnetite (Fe3O4) and its transition point at low temperatures: Nature, v. 144, no. 3642, p. 327-328.

Walker, J. C., and Brimblecombe, P., 1985, Iron and sulfur in the pre-biologic ocean: Precambrian Research, v. 28, no. 3-4, p. 205-222.

Webb, S. M., 2005, SIXPACK: A graphical user itnerface to XAS analysis using IFEFFIT: Physica Scripta, v. T115, p. 1011-1014.

-, 2011, The MicroAnalysis Toolkit: X-ray Fluorescence image processing software: AIP Conference Proceedings, v. 1365, p. 196-199.

Wilkin, R., and Barnes, H., 1997, Formation processes of framboidal pyrite: Geochimica et Cosmochimica Acta, v. 61, no. 2, p. 323-339.

Wilkin, R., Barnes, H., and Brantley, S., 1996, The size distribution of framboidal pyrite in modern sediments: an indicator of redox conditions: Geochimica et Cosmochimica Acta, v. 60, no. 20, p. 3897-3912.

Winston, D., 1986, Sedimentation and Tectonics of the Middle Proterozoic Belt Basin and Their Influence on Phanerozoic Compression and Extension in Western Montana and Northern Idaho: Part II. Northern Rocky Mountains, *in* Peterson, J. A., ed., Paleotectonics and sedimentation in the Rocky Mountain region, United States. American Association of Petroleum Geologists, Memoir 41, p. 87-118.

-, 2007, Revised Stratigraphy and Depositional History of the Helena and Wallace Formations, Mid-Proterozoic Piegan Group, Belt Supergroup Montana and Idaho: Special Publication-SEPM, v. 86, p. 65.

Winston, D., and Link, P., 1993, Middle Proterozoic rocks of Montana, Idaho and eastern Washington: the Belt Supergroup: Precambrian: Conterminous US: The Geology of North America, v. 2, p. 487-517.

Zieg, G., Scartozzi, V., Chutas, N., Albers, D., Gostomski, K., and Jones, J., 2013, Black Butte copper deposits, lower Belt Supergroup, Montana: Northwest Geology, v. 42, p. 131-147.

Chapter 6

How Metamorphism Affects Iron Mineralogy and the Iron Speciation Redox Proxy: a Data-Driven Theoretical Study

Coauthors:

John M. Eiler and Woodward W. Fischer

6.1 Abstract

As the most abundant transition metal in the Earth's crust, iron controls the planetary redox budget. Observations of iron minerals in the sedimentary record have been used to understand surface atmospheric and aqueous redox environments over the evolution of our planet; today, the most popular method is iron speciation, a geochemical sequential extraction proxy calibrated to modern sediments. We tested the limits of this proxy to understand the mobility of iron in sediments post-deposition by utilizing data from two classic well-understood localities where Silurian-Devonian shales, sandstones, and carbonates deposited in oxic conditions have been regionally metamorphosed from lower-greenschist facies to granulite facies: Waits River and Gile Mountain Formations, Vermont and the Waterville and Sangerville-Vassalboro Formations, Maine. Plotting iron speciation ratios determined for samples from these localities revealed apparent paleoredox conditions of the depositional water column spanning the entire range from oxic to ferruginous (anoxic) to euxinic (anoxic and sulfidic.) The presence of diagenetic iron carbonates in the samples severely affected the proxy even at low grade, creating ferruginous conditions in all lithologies especially in carbonate rocks. Increasing metamorphic grades transformed iron in carbonates into iron in silicate minerals, which when combined with a slight increase in pyrrhotite, resulted in reconstructed conditions being driven more oxic and more euxinic. Metamorphic reactions involving iron were offset between carbonate and siliciclastics and could be abrupt between metamorphic facies or more gradual in nature. Comparison with previously published metamorphic transformations highlighted the many ways in which the iron speciation proxy can be affected with increasing grade; notably, our work highlights the importance of trace iron in phases which otherwise might not be included when studying the iron systematics of a region. Iron is incredibly mobile and reactive during diagenesis and metamorphism, and subsequent processes can easily overprint primary redox information. Detailed geologic field observations and petrographic

work to understand alteration and metamorphism are important tools needed for understanding paleoenvironmental conditions on Earth.

6.2 Introduction

Iron is by far the most abundant transition metal in the crusts of rocky planets, planetary bodies, and asteroids (Lodders and Fegley, 1997), and it buffers (bio)geochemical processes and redox state on a planetary scale. As a redox-sensitive element that cycles between +II and +III valence states, the abundance of different Fe phases within rocks can provide a window into the redox balance and oxygen levels/fugacity of the formation environment—whether it be deep in the mantle or on the surface within a sedimentary basin. Therefore, iron has played a central role in studies of Earth's development over the past 4.5 billion years into a life-sustaining, oxygen-rich planet.

Early observations of changing iron abundance and mineralogy in sedimentary rocks documented the rise of atmospheric oxygen based on the transition from ferrous to ferric iron-bearing detrital minerals and paleosols leached of soluble Fe^{+2} versus accumulation of insoluble Fe^{+3} (Cloud, 1968; Holland, 1984; Roscoe, 1969). Key evolutionary innovations have been linked to the rise of atmospheric oxygen (e.g. Johnson et al., 2013; Kopp et al., 2005; Williamson et al., 2011), and it is clear that this global environmental change dramatically altered evolutionary pathways for early life (Sleep and Bird, 2008). On the microscale, changes in redox state of the Earth's atmosphere and oceans changed the proportions of the metals used in enzymes for early life (Anbar, 2008; Williams and Frausto Da Silva, 2003; Zerkle et al., 2005). Therefore, the question of redox state of the atmospheres and oceans during the Precambrian has become a research priority in recent years in order to help understand the environmental controls on the pacing of evolution.

A variety of geochemical techniques have been applied to understand paleoredox based on diverse transition metal abundances and isotopologues; one of the most popular proxies is iron speciation. Iron speciation is a bulk sequential chemical extraction technique to quantify the proportions of different iron phases, which are interpreted using empirical calibrations of modern sedimentary environments to determine paleoredox state of the depositional environment: oxic, anoxic/ferruginous (< 5 micromolar O_2), or euxinic (anoxic and sulfide bearing) (Poulton and Canfield, 2005; Raiswell and Canfield, 2012). Iron speciation data on a multitude of Precambrian successions suggest ferruginous, euxinic, and oxic waters varying between different basins, different water depths, and temporally with dominant ferruginous conditions (e.g. Poulton and Canfield, 2011; Sperling et al., 2015) distinctly different and far more complex than the canonical view (ferruginous before 2.3 Ga, then oxic surface waters with deep ocean euxinia) (Canfield, 1998; Cloud, 1968). Additionally, other paleoenvironmental proxies (such as Mo isotopes) have used the redox interpretations from iron speciation as a basic assumption to develop their methodology and build their interpretation models (e.g. Arnold et al., 2004; Kendall et al., 2009). However, since iron speciation is calibrated for sediment, it is poorly understood how metamorphism, metasomatism, and diagenesis could alter results and paleoenvironmental interpretations, an important caveat since all Precambrian rocks have undergone post-depositional alteration. Our approach analyzed case examples of sedimentary strata, which have undergone a range of well-understood metamorphic transformations, in “iron speciation space” to understand the effects of metamorphism on iron mineralogy and the iron speciation proxy.

6.3 Background

6.3.1 Development of the Iron Speciation Proxy

The iron speciation paleoredox proxy developed from work by Bob Berner and his students and colleagues at Yale to understand controls on the formation of pyrite in modern environments (Raiswell and Canfield, 2012). Iron is classified broadly into three hierarchical pools: pyrite iron (Fe_{py}), highly reactive (toward sulfide) iron (Fe_{HR}), and total iron (Fe_T). The ratio of Fe_{HR}/Fe_T is used to determine whether the depositional water column is oxic or anoxic, and then within those that are anoxic, the ratio of Fe_{py}/Fe_{HR} is used to determine euxinic versus ferruginous water conditions (Fig. 6.1). As the proxy has evolved and been refined, different chemical extraction techniques have been used to resolve the various pools of iron (Table 6.1) adding a layer of complexity when applying or interpreting the proxy, which was originally operationally-defined based on the extraction steps.

The development of Fe_{py}/Fe_{HR} as an indicator for euxinic conditions is based on the Degree of Pyritization (DOP) ratio defined by Berner (1970). DOP and Fe_{py}/Fe_{HR} are both statistics measuring how much of the reactive iron in a sample has been transformed to pyrite iron. The distinction between these proxies is that DOP defines Fe_{HR} as pyrite iron plus iron extracted using boiling HCl while today, alternative extraction methods for Fe_{HR} have become widely utilized (e.g. Leventhal and Taylor, 1990; Poulton and Canfield, 2005; Raiswell et al., 1994). DOP was calibrated as euxinic if greater than 0.75 and oxic if less than 0.45 based on a survey of Cretaceous, Jurassic, and Devonian shales whose paleoenvironment was determined based on bioturbation and faunal assemblages (Raiswell et al., 1988). A later survey of modern siliciclastic sediments suggested that a DOP < 0.4 indicated oxic environments, but many euxinic environments had DOP < 0.75, interpreted as being due to additional transformation of iron oxides into pyrite during diagenesis in euxinic systems (Raiswell and Canfield, 1998). As studies moved toward using Fe_{HR} extractions when HR is extracted using dithionite instead of just boiling HCl, calculations were performed for Fe_{py}/Fe_{HR} to show that Fe_{py}/Fe_{HR} is on average 0.87 for euxinic deep Black Sea samples, 0.65 for Black Sea shelf sediments, and 0.61 for dysoxic marine samples (data from Anderson and Raiswell, 2004; Raiswell and Canfield, 1998). From this data, an upper limit of $Fe_{py}/Fe_{HR}=0.8$ was chosen for ferruginous conditions (Poulton and Canfield, 2011; Raiswell and Canfield, 2012). No further calibrations on large surveys of sediment or rocks have been done with the standard detailed sequential extraction technique for Fe_{HR} (Poulton and Canfield, 2005). However, a study on Cretaceous marine shale from Ocean Anoxic Event 3 independently defined euxinia based on lack of bioturbation and presence of sulfurized organic matter and trace elements (Cd, V, Mo, Zn) as a test of the proxy; ratios of Fe_{py}/Fe_{HR} corroborated the upper limit of 0.8 and suggested a lower limit of euxinia at $Fe_{py}/Fe_{HR} = 0.7$ (März et al., 2008). These limits have become the standard (Fig. 6.1), and have been widely applied to differentiate euxinic and ferruginous conditions of Precambrian-age rocks (Fig. 6.2) (Poulton and Canfield, 2011; Raiswell and Canfield, 2012).

Although the anoxia proxy was developed independently, today most studies pair the Fe_{HR}/Fe_T anoxia proxy with the Fe_{py}/Fe_{HR} euxinia proxy discussed above (first done by Shen et al., 2002). The primary focus of the Raiswell and Canfield (1998) modern siliciclastic sediment survey was to understand the abundances of highly-reactive iron (extracted using dithionite). They discovered a range of $0.06<Fe_{HR}/Fe_T<0.38$ bound oxic and dysoxic sediments. Samples from modern euxinic and anoxic basins contained Fe_{HR}/Fe_T ratios primarily above 0.38, but included values down to 0.18. Phanerozoic shales deposited in normal oxic marine conditions, based on faunal assemblages and DOP values, had a Fe_{HR}/Fe_T average of 0.14 significantly lower than the modern sediment average of 0.26 (Poulton and Raiswell, 2002). Additionally, a detailed test of Fe_{HR}/Fe_T on the Jurassic Kimmeridge Clay highlighted that Fe_{HR}/Fe_T ratios tracked well with oxygen limitation and anoxia as determined by faunal assemblages and bioturbation (Raiswell et al., 2001). Based on these compilations, the paleo-proxy was defined as having a lower Fe_{HR}/Fe_T limit of 0.22 chosen for anoxic sediments and an upper limit of oxic conditions at 0.38 (Fig. 6.1) (Poulton and Canfield, 2011). Notably, the Fe_{HR}/Fe_T limits have not been updated for the new sequential extraction techniques, although a test on modern carbonate samples from a range of oxic and anoxic environments using the new sequential extraction technique suggested that the Fe_{HR}/Fe_T limits were similar (Clarkson et al., 2014). Re–evaluation of the low Phanerozoic shale average compared to the modern sediment average raises the question as to whether samples are in an open system (previous assumption) or a closed system, where highly reactive iron was transformed into iron minerals targeted in newer extraction methods or was moved into clays and the unreactive silicate pool (Raiswell and Canfield, 2012).

6.3.2 Sequential Extraction Pools

Bulk geochemical extraction techniques help provide quantitative results, and have allowed the development of this paleoredox proxy. However, questions always exist as to whether the targeted phases are being extracted or not; this is exemplified through the development of the highly reactive iron extraction techniques over the past 30 years within the iron speciation proxy. Today most studies follow the sequential extraction technique developed by Poulton and Canfield (2005) with slight modifications depending on the samples, mineralogy, and personal preference. This technique keeps Fe_{py} the same and divides the Fe_T and Fe_{HR} pools as such:

$$Fe_{HR} = Fe_{carb} + Fe_{ox1} + Fe_{ox2} + Fe_{mag} + Fe_{py}$$

$$Fe_T = Fe_U + Fe_{PRS} + Fe_{HR}$$

where Fe_{carb} is the iron carbonate pool, Fe_{ox1} and Fe_{ox2} combined are the ferric iron oxide pool, Fe_{mag} is the magnetite pool, Fe_U is the unreactive pool, and Fe_{PRS} is the poorly reactive sheet silicates (see Table 6.1 for additional details). The addition of these extra extraction steps was to target magnetite and iron-rich carbonates, which might precipitate in the water-column or in diagenesis from original reactive iron in Precambrian rocks and be of importance for paleoenvironmental interpretations (Poulton and Canfield, 2005; Raiswell and Canfield, 2012).

Even with these new targeted phases, there are still several iron-bearing (and sulfur-bearing) minerals present in ancient rocks that can be extracted during the iron speciation steps, but are not explicitly defined (e.g. Tables 6.1, 6.2). Notably, pyrrhotite is entirely or partially dissolved during the Fe_{carb} extraction (Poulton and Canfield, 2005; Reuschel et al., 2012), potentially with more extracted in the Fe_{mag} extraction (Burton et al., 2006), and can also be extracted in the Fe_{py} pool (Partin et al., 2015; Praharaj and Fortin, 2004; Schumann et al., 2012); therefore additional extraction steps and calculations are often included when pyrrhotite is present. Pyrrhotite, if tested for separately, is usually grouped within the Fe_{py} pool in a new sulfurized iron pool (Fe_S) with the assumption that it formed from pyrite and/or represents original euxinic conditions on its own (e.g. Asael et al., 2013; März et al., 2008; Reuschel et al., 2012). An additional complexity with chemical extraction techniques is that some work has suggested the abundance of minerals or mixture of minerals within samples can affect extraction recovery (Hsieh et al., 2002; Praharaj and Fortin, 2004; Reuschel et al., 2012). Recent concern about the Poulton and Canfield (2005) method for iron speciation involves samples with high proportions of siderite and ankerite; in these samples, siderite is not fully extracted in the Fe_{carb} step and can continue to be extracted during the Fe_{mag} and Fe_{PRS} steps, which in the latter case will affect the iron speciation paleoredox proxy (Raiswell et al., 2011; Reinhard et al., 2009).

6.3.3 Previous Adjustments and Models for Metamorphism

As the iron speciation proxy has been developed, it has been applied to more diagenetically altered and metamorphosed samples, sometimes with detailed discussion, additional extractions, or petrography to understand how the iron moved during diagenesis/metamorphism and to attempt to recreate the original iron pools. Testing for pyrrhotite is one such adjustment, although calculation of "original" iron can be difficult since pyrrhotite has variable stoichiometry and in AVS and CRS extractions for sulfides, the sulfur is measured not the iron. Studies sometimes attempt to calculate pyrrhotite stoichiometrically (e.g. Asael et al., 2013; Cabral et al., 2013) while other times it is simply grouped with pyrite using stoichiometric equations that will under-estimate the amount of iron (e.g. Li et al., 2015; Partin et al., 2015). The question of authigenic syndepositional or diagenetic pore-water phases has begun to be addressed by Raiswell et al. (2011) who provided additional extraction tools with which to calculate poorly reactive silicates such as mica and chlorite and to more precisely measure iron carbonate phases. Although this method allows more precise determination of Fe_{carb}, iron from the authigenic sheet silicate pool is interpreted using other geochemical proxies as simple delivery of hydrothermal Fe into an open system with no additional calculations or adjustments to Fe_{HR}/Fe_T. Studies on paired limestone and dolomite samples from early Triassic carbonates show an increase in Fe_{HR}/Fe_T ratios and Fe_{carb} in the dolomites due to deep burial dolomitization, and modern samples with low total iron (<0.5 wt%) also show enrichments in Fe_{HR}/Fe_T above the 0.38 oxic limit, interpreted to be from diagenetic dolomitization or pyrite formation (Clarkson et al., 2014).

The effect on iron speciation of iron movement between the silicate, highly reactive, and pyrite pools has been addressed through simple models. Transformation of carbonates and oxides to silicate phases will lower Fe_{HR}/Fe_T values and increase Fe_{py}/Fe_{HR} values as will the authigenic formation of iron silicates, making paleoredox appear more oxic and more euxinic (Reinhard et al., 2013). The formation of pyrrhotite from pyrite by loss of sulfur from the system without any iron transformations will lower Fe_{HR}/Fe_T and Fe_{py}/Fe_{HR} ratios in ferruginous systems making basins appear more ferruginous and/or more oxic; if iron sulfides are the main highly-reactive mineral, possible in some euxinic environments, less of a shift in Fe_{py}/Fe_{HR} toward ferruginous conditions would be seen (Reinhard et al., 2013). In this study, we expanded upon this previous work by considering additional iron reactions, using data from metamorphosed rocks as test-cases, and increasing the span of studied metamorphic conditions.

6.4 Approach

6.4.1 Locality Selection

We combed the literature for publications with detailed mineral assemblages of sedimentary rocks, preferably fine-grained siliciclastics, across a metamorphic gradient. Due to the low-abundance of iron in shales (<7 wt%, e.g. Li and Schoonmaker, 2003), accessory minerals needed to be carefully tabulated as well, excluding normative XRF analyses. Many iron-bearing carbonates and silicates such as chlorite and biotite have variable stoichiometries, and therefore, mineral chemical composition also needed to be analyzed for each mineral in each rock sample. Several hundred metamorphic petrology papers were evaluated, but less than 30 publications fit the criteria established above. Two geologic locations stood out as particularly well-studied, the metamorphosed Silurian-Devonian sedimentary rocks of Vermont and Maine, so we focused on them. It is important to note that the sedimentary protoliths of these rocks were deposited as interbedded sandstones, shales, and carbonates in Paleozoic coastal marine settings; this type of setting is interpreted to be oxic even in benthic sediments based on other localities which contain abundant aerobic animal fossils (brachiopods, corals, echinoderms, etc.) (Watkins, 1996).

6.4.1.1 Waits River and Gile Mountain Formations, Vermont

The Waits River and Gile Mountain Formations of Vermont are a classic case of the Barrovian metamorphic series spanning from the chlorite to the kyanite zone. The Waits River Formation is composed predominately of tan siliceous limestone interbedded with calcareous black sulfidic shales, while the overlying Gile Mountain Formation contains grey sandstones and shales with some interbedded black shales and rare carbonate beds (Fisher and Karabinos, 1980; Hatch, 1988; Lyons, 1955; Woodland, 1977). The proportion of carbonate beds in the Waits River Formation increases to the east (Hatch, 1988). Layers in both formations are on the centimeter to decimeter scale (Fisher and Karabinos, 1980). The sequence is dated to Silurian and early Devonian based on Devonian plant fossils in the Gile Mountain Formation and a felsic dike through volcanics within the Waits River Formation having a zircon age of 423 ± 4 Ma (Hueber et al., 1990). Although fairly unfossiliferous, a poorly preserved echinoderm was found in the Waits River Formation (Hueber et al., 1990). The Waits River and Gile Mountain Formations were folded, intruded by granitic plutons, and then regionally metamorphosed during the Devonian Acadian orogeny (Osberg et al., 1989; Thompson and Norton, 1968; Thompson et al., 1968). Hornblendes dated using Ar-Ar in and near structural domes are between 350 and 397 Ma confirming the age of this metamorphism (Spear and Harrison, 1989). Based on the minerals in the pelitic schists, preserved rocks were metamorphosed following the Barrovian series from the chlorite zone through the biotite, garnet, staurolite and kyanite zones (Doll et al., 1961; Ferry, 1994). Within the metamorphosed carbonate rocks of the Waits River Formation, isograds and zones were mapped based on the presence of ankerite, oligoclase, biotite, amphibole, and diopside (Ferry, 1992). Temperature conditions ranged from 400-450°C in the chlorite zone with similar temperatures for the ankerite-albite zone up to 525-575°C in the diopside and kyanite zones (Ferry, 1988b, 1992, 1994; Léger and Ferry, 1993). Pressure estimates vary from 3.5 to 7.8 kbar (Ferry, 1988b, 1992; Léger and Ferry, 1993). Although we will refer to this dataset as the Silurian-Devonian Waits River and Gile Mountain Formations, two samples in this data set are from the neighboring Albee-Dead River Formation, composed of thinly bedded greenish-grey shale with less common sandstone, which is roughly constrained to between Ordovician and Cambrian in age (Moench et al., 1995). These are biotite zone samples with similar metamorphic histories and P-T conditions as the Gile Mountain Formation nearby (Ferry, 1988b). Numerous studies have been performed on the metamorphism of the region with a focus on fluid infiltration (e.g. Ferry, 1988b; Léger and Ferry, 1993).

A total of 116 samples were utilized in our study from the Waits River, Gile Mountain, and Albee-Dead River Formations—82 metacarbonates, 12 psammites (metamorphosed quartz-rich siliclastics/sandstones), and 20 pelites (metamorphosed fine-grained aluminous siliclastics/claystones)—with mineral assemblages and mineral chemistry from Ferry (1988b), (1992), (1994), (2007), Léger and Ferry (1991), (1993), Penniston-Dorland and Ferry (2006), (2008). Metamorphic grade between carbonate and pelitic isograds was correlated based on temperature estimates; note that the biotite zone in carbonates is approximately the same as the garnet zone (not the biotite zone) in pelites and they have been grouped to prevent confusion.

6.4.1.2 Waterville and Sangerville-Vassalboro Formations, Maine

The Waterville and Sangerville-Vassalboro Formations of Maine record a classic example of the metamorphic gradient following the Buchan series from the chlorite to the sillimanite zone. The Waterville Formation is composed of thinly bedded greenish grey shale, sulfidic black shale, and shaly sandstone with a shaly carbonate member while the overlying Sangerville-Vassalboro Formation is composed of interbedded gray shaly sandstones and carbonates with minor sulfidic black shales (Ferry, 1981, 1983b; Osberg, 1988; Osberg, 1968). Compositional layering occurs on the centimeter to decimeter scale (Ferry, 1981, 1983b). The sequence is dated from Silurian to Devonian based on graptolites within the Waterville and Sangerville-Vassalboro Formations (Osberg, 1968; Pankiwskyj et al., 1976) and subsequent granite intrusions dated at 378±1 to 381±1 Ma (Tucker et al., 2001). The intrusions occurred after structural deformation of the Waterville-Sangerville-Vassalboro Formations, and then the entire package was subjected to regional metamorphism during the Devonian Acadian orogeny, overprinting any contact aureoles (Osberg, 1988; Tucker et al., 2001). Dating on monazite neoblasts in the Waterville Formation suggested that mineral reactions producing andalusite occurred at 364.3 ±3.5 Ma (Wing et al., 2003). Metamorphic isograds following the Buchan Facies Series have been mapped in the pelitic schists spanning the biotite, garnet, staurolite-andalusite, and sillimanite zones (Osberg, 1968). Isograds in the metacarbonate rocks were also noted from appearances of biotite-chlorite, amphibole-anorthite, zoisite, microcline-amphibole, diopside, and scapolite in increasingly higher grade rocks; these isograds are mapped directly on top of the pelitic isograds so direct comparison is possible (Ferry, 1976b). Numerous studies have highlighted the open system nature of regional metamorphic reactions with fluid infiltration of the rock package (e.g. Ferry, 1988a; Penniston-Dorland and Ferry, 2006). Pressure conditions during metamorphism are estimated at 3.5 kbar with temperature ranging from 380°C at the biotite isograd to 550°C in the sillimanite zone (Ferry, 1976a; Ferry, 1980).

A total of 52 samples were utilized in our study from the Waterville and Sangerville-Vassalboro Formations—35 metacarbonates, 9 psammites, and 8 pelites—with mineral assemblages and mineral chemistry from Ferry (1976b), Ferry (1984), Ferry (1988a), Ferry (1994), and Penniston-Dorland and Ferry (2006). Lithology was poorly denoted within some papers due to analysis of impure carbonates (Ferry, 1976b; Ferry, 1988a), so classification of samples as pelite versus sandstone versus carbonate was made based on the modal volume ratio of micas or carbonates to quartz (< 25% cut off for pelite or carbonate) and/or the elemental ratio of $Al_2O_3/CaO/SiO_2$ as per Bickle et al. (1997). Metamorphic grade between carbonate and pelitic isograds was correlated and combined based on the isograd map of the locality from Ferry (1976b) and Ferry (1994) with pelitic schist terminology preferred if there were approximately equivalent metamorphic facies.

6.4.2 Model

For the two targeted localities above, we used the data on iron-bearing minerals to approximate the samples' iron speciation Fe_{HR}/Fe_T and Fe_{py}/Fe_{HR} ratios, assuming phases were completely and correctly extracted as designed by the standard sequential technique (e.g. Table 6.2). These results were paired with information about the sample lithology and metamorphic zone to understand how progressive metamorphism affects the results of iron speciation. In order to take the published literature data detailed above and use it to find Fe_{HR}/Fe_T and Fe_{py}/Fe_{HR} ratios, several processing steps were required.

Mineral assemblages are presented in the literature as modal volume percentages or moles per liter rock based on point counting minerals in thin section (usually 2,000 points). For the former, volume percent was converted to molar amount per liter rock using molar volume data from Robie et al. (1967) and Holland and Powell (1998). Hexagonal pyrrhotite's molar volume was used, and molar volumes of micas, garnet, allanite, tourmaline, and amphiboles were found by averaging endmembers. In some trace minerals (less than 0.05 vol%), the exact abundance of a mineral was not quantified, and simply absence or presence was noted in the published mineral assemblage. If presence was marked, we calculated molar amount per liter rock based on the maximum abundance (0.05 vol%) as well as for the minimal abundance (0 vol%). In various samples, chalcopyrite, pyrite, pyrrhotite, ankerite, calcite, ilmenite, paragonite, muscovite, biotite, chlorite, clinozoisite, allanite, amphibole, staurolite, and tourmaline were listed as trace minerals. Overall, this treatment of trace minerals did not affect the results significantly; however, the change was noticeable in Fe_{py}/Fe_{HR} due to the low abundance of sulfides in many samples (Figs. S6.1-S6.4). All further calculations and discussion in the main text will include the trace minerals and can be treated as a maximum ratio. The amount of iron in the reference 1 liter of rock was calculated by multiplying the moles of a mineral by the iron content within the mineral based on its formula. The mineral formula was calculated based on the published average electron microprobe analyses for each mineral within a given sample/thin section. In some cases, the mineral composition was not precisely published for a given sample. In that case, the average from other samples within the publication at the same metamorphic grade and/or same lithology was used. If this was not possible, the average for the mineral within the publication was used. When no mineral composition data was reported, standard formulas were used and are listed in Table 6.2.

Each mineral was then partitioned into an iron pool following the current standard extraction techniques (Poulton and Canfield, 2005) (Table 6.1): pyrite, carbonate, ferric oxide, magnetite, poorly reactive sheet silicates, or unreactive silicates. The assignments used for all minerals within the model are noted in Table 6.2. Pyrrhotite's assignment was complicated; as discussed above, if studies did not test for pyrrhotite then it would be extracted in Fe_{carb}, but today many studies have started to include a separate extraction test in which case pyrrhotite is grouped with Fe_{py}. In order to have our model comparable to both modern and older iron speciation studies, we have done two sets of calculations with pyrrhotite in either the Fe_{carb} and Fe_{py} pool. After the iron per pool was summed, non-dimensional ratios of Fe_{py}/Fe_{HR} and Fe_{HR}/Fe_T could be calculated and are presented in Figures 6.3-6.8.

6.5 Case Example Results and Discussion

A wide range of Fe_{py}/Fe_{HR} and Fe_{HR}/Fe_T ratios were found from the data of the Waits River, Gile Mountain, Waterville, and Sangerville-Vassalboro Formations, which would indicate oxic, ferruginous, and euxinic water conditions using the iron speciation proxy (Figs. 6.3, 6.6). We know these samples were deposited in oxic conditions, and there are several factors which could contribute to the high ratios of Fe_{py}/Fe_{HR} and Fe_{HR}/Fe_T. Through more detailed plots to look at trends by lithology and metamorphic zone (Figs. 6.4, 6.5, 6.7, 6.8) as well as the mineral data itself (Figs. 6.9, 6.10), we untangled some of the causes changing Fe_{py}/Fe_{HR} and Fe_{HR}/Fe_T, and discuss the importance of these in actual iron speciation experiments. On a cautionary note, although data were selected carefully to make certain trace minerals were counted, one driver for increased Fe_{py}/Fe_{HR} and Fe_{HR}/Fe_T is simply that iron from certain phases (e.g. oxides or unreactive minerals) was underrepresented by the point counting technique due to small grain size or domains within larger minerals.

6.5.1 Pyrrhotite Pool Placement

One of the largest differences in the ratio results was determined by which pool pyrrhotite was assigned, whether Fe_{carb} or Fe_{py} (Figs. 6.3, 6.6). The Fe_{HR}/Fe_T ratios were not affected since pyrite and carbonate are both highly reactive species and therefore included in Fe_{HR}. However, Fe_{py}/Fe_{HR} was significantly increased due to the additional pyrrhotite fraction in Fe_{py} (Figs. 6.5, 6.8). In the metasedimentary rocks studied here, pyrrhotite in general is more common than other iron sulfides (pyrite or chalcopyrite) across all zones. This addition of pyrrhotite to the Fe_{py} pool was enough to push Fe_{py}/Fe_{HR} ratios above the 0.8 certainty boundary of euxinic redox conditions in some of the carbonates and a sandstone from the Vermont and Maine localities.

Therefore, if pyrrhotite is included in Fe_{carb} as in older studies or through misdiagnosis of the mineral assemblage, the samples will appear much more ferruginous than paleoredox conditions, assuming that the iron in the pyrrhotite comes from the metamorphic transformation of water-column pyrite or primary precipitation. In fact, prior metamorphic analyses on pelites from the Waterville Formation suggested a direct transformation of iron in pyrrhotite into pyrite due to a progressive loss of sulfur (Ferry, 1981). On the other hand, pyrrhotite can form from the decomposition of iron oxides and iron silicates even at low-metamorphic grade (<200°C) with addition of H_2S fluids or co-decomposition of pyrite (Gillett, 2003; Hall, 1986; Nesbitt and Kelly, 1980; Tracy and Robinson, 1988). In these circumstances, placing pyrrhotite in the Fe_{py} pool is erroneous and will drive rocks toward the euxinic zone giving poor paleoenvironmental interpretations. Careful petrographic study of the pyrrhotite could help determine which scenario is the case through pseudomorphs, rims, or partially reacted phases (e.g. Zhou et al., 1995). Isotope study could help determine the importance of S-rich fluids (e.g. Gillett, 2003), although determining “background” or “normal” could be difficult in ancient, relatively metamorphosed samples. Mineral assemblages could give clues as well, but often clear-cut metamorphic grades cannot be or are not sampled. The simplest solution is to avoid analysis of samples containing pyrrhotite.

6.5.2 Lithological Controls and Diagenesis

Another striking variable which appears to be an important control on iron speciation ratios is the lithology of the samples. To a certain degree, different lithologies should represent different paleoenvironments, e.g. sandstones are nearer to shore with more detrital inputs and shallower waters than shales and carbonates (Walker and James, 1992). However, fine-scale interbedding is noticed within all of the formations studied here, and within the Waterville and Gile Mountain Formations, it is clearly detailed that these thin interbeds of carbonates, pelites, and psammites were sampled (e.g. Ferry, 1994). Additionally, we understand that all results should show oxic water column conditions based on the global biological constraints of aerobic benthic animals, and therefore high Fe_{HR}/Fe_{T} or Fe_{py}/Fe_{HR} values implying ferruginous or euxinic conditions should be investigated.

Lithological differences were most noticeable in Fe_{HR}/Fe_{T}, where pelites had much lower values and a lower range than psammites and carbonates of the same formation regardless of metamorphic zone (Figs. 6.4a, 6.7a). Even if samples only were examined at the lowest metamorphic grades (chlorite, ankerite, biotite) to separate that confounding factor, pelites had low Fe_{HR}/Fe_{T} ratios compared to the carbonates and psammites at the same metamorphic grade (Figs. 6.4bcd, 6.7bcd.) Additionally, at low-metamorphic grades, Fe_{py}/Fe_{HR} was generally higher in pelites than in psammites and carbonates (Figs. 6.5bcd, 6.8bcd), especially when pyrrhotite was included in the Fe_{py} pool (Figs. 6.5fgh, 6.8fgh).

By looking at the mineralogy/detailed calculations, it became clear that the primary reason for the differences between lithologies was the abundance of iron in carbonates either as minor components in calcite or as ankerite (Figs. 6.9d, 6.10d). Almost all of the psammites studied here included some carbonate minerals while the pelites had much lower amounts of carbonate. Although previous geochemical work suggested that carbonate samples behave in the Fe_{HR}/Fe_{T} proxy similarly to siliciclastic samples (Clarkson et al., 2014), this work was performed on modern carbonates with minimal diagenetic overprints. Iron can be incorporated into carbonates in primary precipitates; however, in modern oxygenated waters, soluble iron contents are very low, so most iron is incorporated in carbonates through early or secondary diagenetic cements formed in anoxic pore fluids (Barnaby and Rimstidt, 1989; French, 1973; Warren, 2000). As shown here, these diagenetic overprints could dominate the Fe_{HR}/Fe_{T} signals in Paleozoic carbonate rocks enough to create erroneous paleoredox interpretations for the water column. Notably, this signal was not simply due to the presence of ankerite in samples, which has been suggested as a screening method for diagenetic alteration before doing iron speciation (Clarkson et al., 2014). Trace amount of iron in calcite constituted over 50% of the Fe_{carb} pool in almost all of the low-grade carbonates and even samples with low abundances of ankerite had high Fe_{HR}/Fe_{T} above the boundaries of the anoxic zone. In contrast, more of the iron in the Fe_{carb} pool of low-grade psammites usually came from ankerite, and its presence in siliciclastics could be a better signal for diagenetic alteration. Overall, samples with proportionately large Fe_{carb} pools should be investigated petrographically to determine whether the carbonates are primary or not. Calibration of the Fe_{HR}/Fe_{T} ratios on modern samples (and without the new sequential extraction system) ignores this important pool of diagenetic transformations, which will affect the proxy.

The observation that low-grade pelites had higher Fe_{py}/Fe_{HR} ratios than psammites or carbonates was also expected from common early diagenetic reactions. Although pyrite can form within the water column (Raiswell and Berner, 1985; Wilkin and Barnes, 1997), it also forms in sediments underlying oxic and sub-oxic waters through scavenging of highly-reactive iron in pore waters that are anoxic and sulfide-rich (Berner, 1970; Canfield and Berner, 1987; Wilkin et al., 1996). Due to their high organic content and slow depositional rate, deep-water shales are more likely to form pyrite than sandstones or carbonates (e.g. Berner, 1984; Curtis, 1978). Although low-grade pelites had higher Fe_{py}/Fe_{HR} ratios than other lithologies, generally these higher ratios were not large enough to fall within the boundaries for euxinic conditions, suggesting the proxy is less sensitive to diagenetic alteration. Notably, the pelite data used in this study had approximately 1 vol% sulfides with one sample in the Waterville Formation containing 3.2 vol% sulfides. Within the Waits River, Waterville, and Sangerville-Vassalboro Formations, there are distinct sulfidic black shale layers containing over 10 vol. % sulfides (Waterville Formation, Ferry, 1981) that are closer to the expected facies for a euxinic water column-system.

6.5.3 Increasing Grade and Metamorphic Reactions

The detailed breakdown of the Fe_{HR}/Fe_T and Fe_{py}/Fe_{HR} ratios by metamorphic zone highlighted trends that occur with increasing metamorphic grade (Figs. 6.4, 6.5, 6.7, 6.8). Observations of trends were clearer in the Waits River and Gile Mountain Formation due to the larger number of data points, but the Waterville and Sangerville-Vassalboro samples were also considered in untangling these numerical shifts and their causes. Fe_{HR}/Fe_T in general decreased with increasing grade, although slight differences were seen between the siliciclastic and carbonate samples (Figs. 6.4bcd, 6.7bcd). While a more monotonic decrease was seen in siliciclastics starting from the chlorite zone, the decrease in carbonates occurred only after the garnet zone. The kyanite zone carbonates of the Waits River with the highest P-T conditions in either locality (Ferry, 1994; Penniston-Dorland and Ferry, 2006) showed a sudden return to previous values.

Fe_{py}/Fe_{HR} was more complicated, but it appears metamorphic effects are separated by lithology. In pelitic samples, the Fe_{py} pool was differently affected based on the inclusion or exclusion of pyrrhotite. When pyrrhotite was excluded from the Fe_{py} pool, a slight increase in Fe_{py}/Fe_{HR} occurred with metamorphic grade whereas when pyrrhotite was included in the Fe_{py} pool, a decrease was observed. (Note: the Waterville Formation staurolite zone sample is probably an outlier due to lithological differences; it contains the 3.2 vol% pyrrhotite discussed earlier.) In carbonate samples, trends were difficult to resolve when pyrrhotite was excluded from the Fe_{py} pool due to distinct variable directional shifts in the Vermont and Maine localities. We chose not to make further observations due to concerns of over-interpreting a single point's importance or small magnitude complex trends. However, when pyrrhotite was included in the Fe_{py} pool, values for Fe_{py}/Fe_{HR} for carbonates increased with increasing metamorphic grade with some samples falling within the limits for euxinic redox conditions at high grades. Notably, the highest-grade samples from the kyanite and scapolite zones showed a decrease in Fe_{py}/Fe_{HR} similar to the rebound seen in Fe_{HR}/Fe_T in this metamorphic zone. Psammite samples were the least numerous in these studies; no clear trend appeared in either of the localities, although the three high Fe_{py}/Fe_{HR} ratios within the euxinic boundaries occurred in samples from above the biotite isograd.

It was clear that these ratio changes of Fe_{HR}/Fe_T and Fe_{py}/Fe_{HR} were due to movement of iron between different pools during progressive metamorphism; however, for each ratio, we needed to determine which of the two pools was changing in size (or whether both were changing). Total iron did not vary systematically with metamorphic grade, although it did by lithology (Figs. 6.9a, 6.10a), suggesting that these metamorphic systems were closed with respect to iron although open with respect to fluids carrying C-O-H-S and other elements (e.g. Ferry, 1981, 1983b, 1988b). Therefore, the individual pools were normalized by total iron for comparison purposes. Additionally, changes in Fe_{carb}, Fe_{mag}, Fe_{py}, Fe_{PRS}, and Fe_U could occur due to changes in abundances of minerals or due to changes in mineral composition with loss or addition of iron; we did not distinguish between these options, although in general it appears that abundance plays a larger role since Fe compositions of minerals did not vary greatly across metamorphic zones (at least within the publications). The one possible exception is ankerite, which on average may loose iron with increasing metamorphic grade (e.g. Waits River Formation, Ferry (1992) and Waterville Formation, Ferry (1994)), but this trend did not reproduce well in all studies.

For Fe_{HR}/Fe_T, the main driver appeared to be variation in the Fe_{carb} pool, specifically of the iron carbonates, not pyrrhotite. In carbonate samples, a decrease in Fe_{carb} began within the garnet zone for a significant drop afterwards with an upswing at the kyanite zone while in pelites and psammites, a sharp decrease occurred after the biotite zone and continued slowly with increasing metamorphic grade (Figs. 6.9d, 6.10d). There was an inverse correlation with these decreases and increases in the Fe_U pool suggesting that the metamorphic formation of silicates containing iron such as garnet, amphibole, etc. utilized iron from iron carbonates (Figs. 6.9b, 6.10b). Although Fe_{PRS} was at times a significant part of the total iron pool, the poorly reactive sheet silicates did not appear to drive Fe_{HR} or Fe_T to any substantial degree and the data from the two localities differ greatly. In the Waterville and Sangerville-Vassalboro Formations, significant formation of sheet silicates was seen in carbonate samples in the biotite and garnet zone with subsequent destruction; with a lack of samples in sub-biotite zones, siliciclastic rocks simply showed progressive decrease of Fe_{PRS} after the biotite zone (Figs. 6.10ef). In the Waits River and Gile Mountain Formations, no significant trends in sheet silicates were seen within pelites and psammites whereas the carbonate samples showed a significant increase in Fe_{PRS} in the garnet zone, which is correlative to the biotite zone in carbonates and thus not unexpected (Figs. 6.9ef). Although a decrease in Fe_{PRS} was seen within the diopside zone, there was a return to high values in the kyanite zone so distinctions in lithological sampling could be biasing the diopside results. Metamorphically, this suggests that several reactions exist forming and destroying micas and chlorite across metamorphic grades or that multiple minerals are involved in reactions adding complexity; within carbonates, iron may come from iron carbonates for the formation of biotite and transfer upon destruction to help form unreactive silicates (or pyrrhotite) while siliciclastic rocks may have more internal cycling of iron within the Fe_{PRS} pool. It is interesting that some of the iron transitions are fairly abrupt whereas others, such as the slow decrease in biotite with metamorphic grade, occur progressively across increasing metamorphic regimes.

Fe_{mag} only contained ilmenite in this study and overall is a relatively small amount of the Fe_T pool especially in carbonates. Therefore, changes in ilmenite did not significantly affect the Fe_{HR}/Fe_T ratios, but did show interesting trends with metamorphic implications. In carbonate samples, ilmenite showed significant increases at the garnet zone whereas in pelites, ilmenite decreased across increasing metamorphic grades (Figs. 6.9c, 6.10c). Psammites appeared to be a mixture of these changes with a slight decrease until the kyanite zone where Fe_{mag}/Fe_T ratios return to their former values. From the literature, it is unclear whether the iron in ilmenite is actually “highly reactive” toward sulfides; it is included in Fe_{mag} due to sequential extraction methodology studies. Within carbonates, ilmenite varied similarly to unreactive silicate phases, while in pelites, it appeared to be transformed slowly through metamorphism.

Deconvolving causes of the $Fe_{py/}Fe_{HR}$ trends was more difficult due to less clear variations, low abundance of iron sulfides, and the large changes in Fe_{HR} detailed above. In the pelites, chalcopyrite and pyrite did not change in fraction very much across metamorphic zones; slight increases in Fe_{py}/Fe_{HR} when pyrrhotite was in the Fe_{carb} pool appeared to be related to decreases in the rest of the Fe_{HR} pools. Pyrrhotite did significantly decrease in pelites after the biotite zone, which drove the decreases in Fe_{py}/Fe_{HR} when pyrrhotite was in the Fe_{py} pool. For carbonates, pyrrhotite might increase slightly with metamorphic grade (on average), which combined with the decrease of the Fe_{HR} pool increased the $Fe_{py/}Fe_{HR}$ ratio. Based on detailed analysis of the raw data, pyrrhotite formation might also be dependent on lithological differences or local fluid flow conditions as certain sites had higher pyrrhotite abundances than other sites at the same metamorphic grade. Although this is a factor to consider in all the mineralogical changes discussed above, the low amount of sulfides highlighted this variability in pyrrhotite abundance.

The trends and shifts described above correspond to metamorphic reactions known to occur with increasing pressure and temperature. Prior work on the Waits River, Gile Mountain, Waterville, and Sangerville-Vassalboro Formations has proposed various metamorphic reactions based on analysis of mineral assemblages and thermodynamic calculations, which correspond well to the changes seen above (Table 6.3). However, prior studies usually did not focus on the iron mineralogy, sometimes excluding iron or accessory minerals entirely from calculations, so some transformations were not accounted for but are well known from other sites (Table 6.3). We display these metamorphic reactions by metamorphic grade as well as others, which may not have occurred in the Paleozoic sediments of the eastern US, in iron speciation space to elucidate the potential effects of iron mobility during metamorphism on the iron speciation redox proxy (Fig. 6.11). Notably, some of the phases affecting the iron speciation ratios in the data-driven model above (including important factors like calcite) do not contain Fe in their general formulas/endmember stoichiometries (Table 6.2) expanding the number of metamorphic reactions that could affect iron systematics significantly.

6.6 Conclusions

Iron speciation is a widely used proxy for understanding paleoredox of ancient oceans and lakes; however, it is empirically calibrated on modern sediments and errors could occur through improper boundaries for interpreted redox conditions, mixing of iron between pools in sequential extraction, or due to diagenetic and metamorphic transformations. Utilizing data from the metamorphic petrology literature of sedimentary strata deposited in Paleozoic oxic marine conditions, we assessed how variations in metamorphic grade, lithology, and iron speciation pool placement (through different extraction techniques) affect the iron speciation proxy.

Pyrrhotite and iron in carbonates stood out as important minerals affecting the proxy for our data set. Grouping pyrrhotite in the Fe_{carb} pool (as in older studies or those that do not screen for pyrrhotite) provided significantly lower estimates of Fe_{py}/Fe_{HR} than when it was grouped with the sulfides in Fe_{py}. The correct pool will vary based on the locality, lithology, and metamorphic reactions. Although study of low-grade pelites suggested the pyrrhotite in our samples formed from pyrite and should be grouped in the Fe_{py} pool (Ferry 1981), pyrrhotite did appear to be added to the carbonate rocks during progressive metamorphism with minimal decrease in pyrite suggesting iron movement from other pools. Iron carbonates were prevalent across all three types of lithologies and significantly increased the Fe_{HR}/Fe_{T} ratios suggesting ferruginous depositional conditions. In fact, these carbonates probably formed in anoxic pore fluids in early or late diagenetic processes and do not reflect water column chemistry. With increasing metamorphic grade, the iron within this carbonate transferred to the silicate pool (Fe_{PRS} + Fe_U) and significantly decreased the $Fe_{HR}/Fe_{T,}$ which could be an erroneous oxic result if an anoxic water column did exist during deposition. Proportionately less carbonate was seen within the pelitic samples and even through increasing metamorphic grade, this lithology preserved the oxic paleoredox information better than psammites and carbonate samples. Overall, the iron speciation proxy is heavily affected by early diagenetic minerals and secondary diagenetic/metamorphic reactions especially in carbonate lithologies.

Plotting iron data from sedimentary rocks within iron speciation space also provided a new perspective to analyze the mobility of iron during progressive metamorphism. Iron moved from iron carbonates to form poorly reactive sheet silicates and unreactive silicate minerals in the biotite, garnet, and amphibole zones. Biotite formation within carbonates occurred in the pelitic schist garnet zone, and by delaying this metamorphic reaction, the formation of unreactive silicates started mainly in the amphibole zone. In carbonates, ilmenite formed at the same time as these unreactive silicates whereas in pelites and psammites, ilmenite acted as a reactive oxide phase that was slowly consumed. In pelites, pyrrhotite was also destroyed through progressive desulfurization reactions with increasing grade, but in carbonates a slight increase in abundance occurred, suggesting the iron for its formation could come from the iron carbonate pool. Many of these reactions have been previously hypothesized by study of metamorphic mineral assemblages, and our work provides corroboration while highlighting the mobile nature of iron in diagenesis and metamorphism. A unit of rock may encounter several redox environments over the course of its history, and untangling these environments to understand paleoredox and sustainability for life requires the application of multiple techniques, specifically textural analyses.

6.7 Acknowledgements

Support for this work was provided by the NSF Graduate Research Fellowship program (S.P.S.) and NASA Earth and Space Fellowship (S.P.S.).

6.8 Tables

Table 6.1: Sequential extraction methods and targeted minerals

Pool	Short Name*	Details	Extractable Fe from Minerals †	Source§
Fe_{carb}	Acetate	(1) 1M Na Acetate, pH 4.5, 24 hours room temperature or 48 hours 50°C	Carbonate iron, siderite, ankerite (pyrrhotite)	1
Fe_{ox1}	Hydroxylamine	(2) 1M Hydroxylamine-HCl, 48h	Ferrihydrite, lepidocrocite	1
Fe_{ox2}	Dithionite	(3) Na dithionite solution (50 g l-1), pH 4.8, 2 hours	Goethite, akaganéite, hematite (ferrihydrite, lepidocrocite)	1
Fe_{mag}	Oxalate	(4) 0.2 M ammonium oxalate/0.17 M oxalic acid, pH 3.2, 6 hours	Magnetite (titanomagnetite, ilmenite, goethite, ferrihydrite, lepidocrocite, siderite, pyrrhotite)	1,2,3,4
Fe_{PRS}	Boiling HCl	(5) 12 M HCl, 1 minute boiling	Poorly reactive sheet silicates like nontronite, biotite, chlorite, glauconite (all of the above)	1, 5
Fe_{py}	CRS	Chromium reduction with 1 M $CrCl_2$ solution, 2 hours boiling + Zn, Ag distillation	Pyrite (pyrrhotite, S, Ni-Zn-Cu-As-Cd-Pb sulfides)	1,6,7
Fe_U	--	Total iron (from XRF, ashing and boiling in 6 M HCl, etc.) minus above sum	Silicates	1
--	AVS	Several options using HCl of different strengths, temperatures, times ± chlorides	Monosulfides like amorphous FeS, mackinawite, greigite, pyrrhotite	8,9

* Abbreviations: CRS = chromium-reducible sulfide, AVS = acid-volatile sulfide

† Minerals in parenthesis are those that can be extracted in this step, but should already have been extracted using the sequential extraction technique or are not the targeted minerals.

§ References: 1) Poulton and Canfield (2005), 2) Dold (2003), 3) Algoe et al. (2012), 4) Burton et al. (2006), 5) Raiswell et al. (1994), 6) Canfield et al. (1986), 7) Schumann et al. (2012), 8) Cornwell and Morse (1987), 9) Praharaj and Fortin (2004)

Table 6.2: Minerals identified within the Waits River, Gile Mountain, Waterville, and Sangerville-Vassalboro Formations

Name	General Formula	Assumed Formula	Assigned Iron Pool
Fe-bearing minerals			
Muscovite	$KAl_2(AlSi_3O_{10})(OH)_2$	--	Fe_{PRS}
Paragonite	$NaAl_2(AlSi_3O_{10})(OH)_2$	--	Fe_{PRS}
Biotite	$K(Mg,Fe)_3(AlSi_3O_{10})(F,OH)_2$	--	Fe_{PRS}
Chlorite	$(Al,Fe, Mg,Mn,Ti)_{5\text{-}6}(Al,Fe,Si)_4(O,OH)_{18}$	--	Fe_{PRS}
Calcite	$CaCO_3$	--	Fe_{carb}
Ankerite	$Ca(Fe,Mg,Mn)(CO_3)_2$	$CaFe_{0.5}Mg_{0.5}(CO_3)_2$*	Fe_{carb}
Ilmenite	$FeTiO_3$	$FeTiO_3$†	Fe_{mag}
Pyrrhotite	$Fe_{(1-x)}S$ (x = 0 to 0.2)	$Fe_{0.95}S$ or $Fe_{0.907}S$)§	Fe_{carb} or Fe_{py}
Pyrite	FeS_2	FeS_2	Fe_{py}
Chalcopyrite	$CuFeS_2$	$CuFeS_2$	Fe_{py}
Epidote	$Ca_2Al_2Fe(Si_2O_7)(SiO_4)O(OH)$	--	Fe_U
Allanite	$(Ce,Ca,Y,La,etc.)_2(Al,Fe)_3(SiO_4)_3(OH)$	$CeCaFe_{1.5}Al_{1.5}(SiO_4)_3(OH)$	Fe_U
Clinozoisite-Zoisite	$Ca_2Al_3(Si_2O_7)(SiO_4)O(OH)$	--	Fe_U
Garnet	$(Ca,Mg,etc.)_3(Fe,Al,Ti,etc.)_2(SiO_4)_3$	--	Fe_U
Staurolite	$Fe_2Al_9Si_4O_{23}(OH)$	$Fe_2Al_9Si_4O_{23}(OH)$ #	Fe_U
Diopside	$CaMgSi_2O_6$	--	Fe_U
Amphibole	$(Na,K,Ca,Pb,[])(Li,Na,Mg,Fe,Mn,Ca)_2$ $(Li,Na,Mg,Fe,Mn,Zn,etc.)_5(Si,Al,Ti)_8O_{22}$ $(OH,F,Cl,O)_2$**	--	Fe_U
Tourmaline	$(Ca,Na,K,[])(Al,Fe,Li,Mg,Mn)_3\,(Al,Cr,Fe,V)_6$ $Si_6O_{18}(BO_3)_3(O,OH)_3(F,O,OH)$ **	$NaFeMg_2Al_6(Si_6O_{18})(BO_3)_3$ $(OH)_3(OH)$	Fe_U
Non-Fe bearing minerals			
Quartz	SiO_2	--	--
Plagioclase	$NaAlSi_3O_8$ – $CaAl_2Si_2O_8$	--	--
Titanite	$CaTi(SiO_4)O$	--	--
Rutile	TiO_2	--	--
Graphite	C	--	--
Alkali feldspar	$KAlSi_3O_8$	--	--
Kyanite	$Al_2(SiO_4)O$	--	--
Apatite	$Ca_5(PO_4)_3(F,Cl,OH)$	--	--
Zircon	$Zr(SiO_4)$	--	--
Monazite	$(Ce,La,Nd,Th,Sm,Gd)PO_4$	--	--
Scapolite	$Na_4Al_3Si_9O_{24}Cl$ – $Ca_4Al_6Si_6O_{24}CO_3$	--	--

* Assumed formula only used for trace amounts in Léger and Ferry (1991).

† Assumed formula is used in all studies except Gile Mountain and Waits River Formation data from Ferry (1994) and Ferry (2007).

§ $Fe_{0.95}S$ was used as the assumed formula for the Waits River and Gile Mountain Formation samples. $Fe_{0.907}S$ was used as the assumed formula for the Waterville and Sangerville-Vassalboro Formation samples since this is the average pyrrhotite composition from 18 samples in the Waterville Formation (Ferry, 1981).

\# Assumed formula only used for trace amounts in Ferry (1994).

** [] stands for no element in this structural position.

Table 6.3: Example metamorphic reactions that transfer iron between pools*

Eq.	Equation†	Lithology	Locality or Model-System§	Zone	Ref.[#]
1	2 py + CH4-->2 po + 2H_2S + C	Graphitic pelite	Waterville	<chlorite	1
2	2.689 ms + 4.648 pl + 1.99 qz + 1.567 dol + 0.029 po + 0.03 rt + 3.139 CH4 --> bt + 6.269 pl + 1.6 afs + 6.273 C + 0.029 H_2S + 7.937 H_2O	Graphitic pelite	Waterville	biotite	1
3	ms + 3 qz + 8 ank+4 H_2O --> 8 cal + chl + bt + 8 CO_2	Calcareous pelite	Waterville & Sangerville-Vassalboro	biotite	2
4	5 ms + 8 cal + 3 chl+7 qz --> 5 bt + 8 pl + 12 H_2O+8 CO_2	Calcareous pelite	Waterville & Sangerville-Vassalboro	biotite	2
5	2.77 ms + 0.26 ilm +11.04 ank +1.86 qz+ 4.02 H_2O + 0.08 HCl --> chl + 2.83 bt+11.87 cal+ 10.21 CO_2 + 0.08 NaCl	Carbonate	Sangerville-Vassalboro	biotite	3
6	0.98 ms + 2.23 ank + 0.65 qz + 0.09 ilm + 0.03 HCl+ 0.01 H_2O --> 1.09 bt + 1.89 cal + 0.48 pl + 0.03 NaCl+ 2.57 CO_2	Carbonate	Sangerville-Vassalboro	biotite	3
7	ms +1.28 cal +0.84 HCl -->0.12 bt + 0.02 spn + 0.36 qz + 1.22 pl + 0.79 KCl+ 0.05 NaCl+ 1.30 H_2O + 1.28 CO_2	Carbonate	Sangerville-Vassalboro	biotite	3
8	ilm + 2 cal + qz--> spn + ank	Carbonate	Sangerville-Vassalboro	biotite	4
9	afs + 3po + 4H_2O --> bt + 3 H_2S	Graphitic pelite	Waterville	garnet	1
10	0.560 ms + 0.174 chl +1.080 cal + 0.006 ilm + 0.953 HCl --> 0.190 bt + 0.173 grt + 0.394 pl + 0.941 qz + 1.080 CO_2+1.541 H_2O + 0.621 NaCl + 0.332 KCl	Carbonate	Waterville	garnet	5
11	5 ank + 8 qz + H_2O--> amp + cal + 7 CO_2	Carbonate	Waterville	garnet	6
12	chl + 2.94 cal + 5.73 qz + 0.05 ilm + 0.19 pl --> 1.02 amp + 0.86 pl + 2.94 CO_2 + 2.98 H_2O	Carbonate	Sangerville-Vassalboro	amphibole	3
13	0.07 amp + 0.59 cal + 1.31 pl +0.01 HCl + 0.59 H_2O --> zois + 0.002 spn + 0.10 qz + 0.01 NaCl + 0.59 CO_2 + 0.16 H_2	Carbonate	Sangerville-Vassalboro	zoisite	3
14	2 py + H_2O + C --> 2 po + 2 H_2S + CO_2	Graphitic pelite	Waterville	sillimanite	1
15	1.378 ms + 0.049 chl + 0.33 qz + 0.485 ank + 2.641 sd + 0.340 rt --> 1.492 bt + 0.454 pl + 0.254 ilm +3.162 CO_2 + 0.082 H_2	Pelite	Gile Mountain	biotite	7

Table 6.3 (continued)

Eq.	Equation†	Lithology	Locality or Model-System§	Zone	Ref.[#]
16	0.005 ms + 0.052 ank+0.056 pl + 0.002 rt + 0.068 CO_2 --> 0.172 cal + 0.25 qz + 0.005 H_2O	Carbonate	Gile Mountain	biotite	7
17	1.021 ms+0.034 chl + 1.497 ank + 0.024 rt + 1.573 HCl-->0.465 bt + 0.225 pl + 0.324 grt + 1.579 qz + 2.994 CO_2 + 1.479 H_2O +1.139 NaCl + 0.434KCl	Psammite	Gile Mountain	garnet	5
18	0.007 bt + 0.119 chl + 0.065 ank + 0.078 pl + 0.279 qz → 0.003 ms + 0.252 grt+ 0.002 ilm + 0.129 CO_2 + 0.481 H_2O	Pelite	Waits River	garnet	5
19	ilm + py --> 2 po + rt + 0.5 O_2	Graphitic pelite	FTS-GCOHS	<chlorite	8
20	4 py + 3 CO_2 + CH_4 + H_2O --> 4 sd + 8 H_2S	Graphitic pelite	NCKFMASH-S	chlorite	9
21	chl + 4 hem --> cld + 4 mag + 2 qz +H_2O	Fe-rich pelite	FASH	chlorite	10
22	3 chl --> 3 alm + 2 mag +12 H_2O (+ QFM)	Fe-rich pelite	FASH	garnet	10
23	mag + 3 py + 2 C --> 6 po + 2 CO_2	Carbonate	Orr Fm., UT	<chlorite	11
24	3 sid + 0.5 O_2 --> mag + 3 CO_2	Iron formation	Biwabik Fm., MN & Naugeene Fm., MI	chlorite	12,13
25	5.31 ank + 8.75 pg + 4.8 po +3.57 pl + 16.83 qz + 1.97 O_2 --> grt + 16.44 pl + 1.53 chl + 2.4 S_2 + 1.9 H_2O + 10.62 CO_2	Pelite	Horsethief Creek Grp., British Columbia	garnet	14
26	bt + 3 py + 1.5 CH_4 --> afs + 6 po + 4 H_2O + 1.5 C	Graphitic pelite	Partridge and Paxton Fm., MA	sillimanite	15
27	ilm + H_2S --> rt + po + H_2O	Graphitic pelite	Partridge and Paxton Fm., MA	sillimanite	15
28	bt + 3 H_2S --> afs + 3 po + 4 H_2O	Graphitic pelite	Partridge and Paxton Fm., MA	sillimanite	15
29	2 ank + 3 qz --> di + opx + cal + 3 CO_2	Iron formation	Wabush Fm., Newfoundland	kyanite	16
30	14 ank + 16 qz + H_2O --> tr + amp + 14 cal +14 CO_2	Iron formation	Wabush Fm., Newfoundland	kyanite	16

* The numerous reactions moving iron between poorly reactive silicate and unreactive silicate pools are not included in this sampling.

† Abbreviations for minerals following Whitney and Evans (2010)

§ Abbreviations: N = Na_2O, C = CaO, K = K_2O, F = FeO, M = MgO, T = TiO_2, S = SiO_2, A = Al_2O_3, H = H_2O, -GCOHS = graphite saturated C-O-H-S fluids, -S = H_2S, Fm. = Formation, Grp. = Group, UT= Utah, MN = Minnesota, MI =Michigan, MA = Massachusetts

References: 1) Ferry (1981), 2) Ferry (1976b), 3) Ferry (1983a), 4) Ferry (1983b), 5) Ferry (1994), 6) Ferry (1979), 7) Ferry (1988b), 8) Connolly and Cesare (1993), 9) Tomkins (2010), 10) Bucher and Frey (2002), 11) Gillett (2003), 12) Jones (1972), 13) French (1973),14) Haase (1982), 15) Tracy and Robinson (1988), 16) Klein (1966)

6.9 Figures

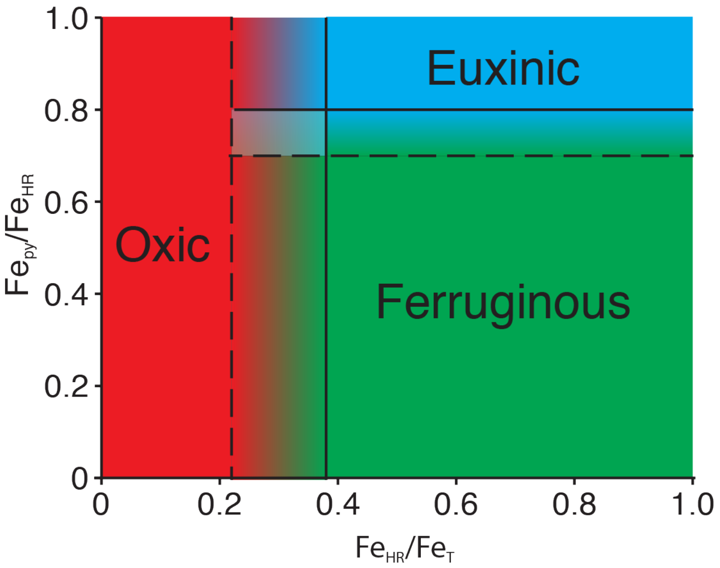

Figure 6.1: Iron Speciation cross-plot with ratio of pyrite iron to highly reactive iron (Fe_{py}/Fe_{HR}) plotted against highly reactive iron to total iron (Fe_{HR}/Fe_{T}) with paleowater column redox conditions bounded by limits from empirical calibrations discussed in text.

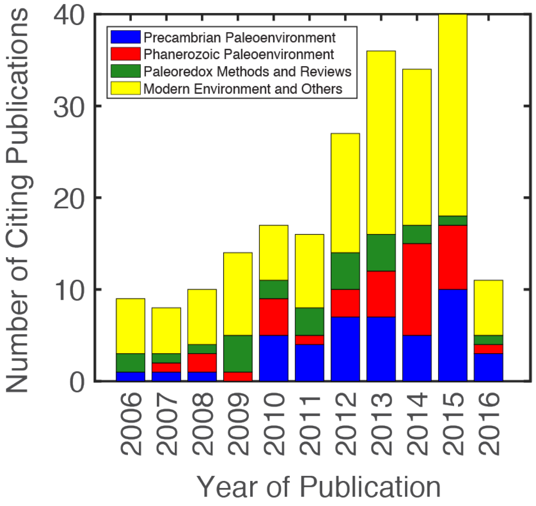

Figure 6.2: Stacked bar graph showing widespread use and growing popularity of iron speciation technique as a paleoenvironmental redox proxy based on number of publications each year citing the sequential extraction methods paper (Poulton and Canfield, 2005). Total number of citations is 222; data from Web of Science citation report accessed April 25, 2016.

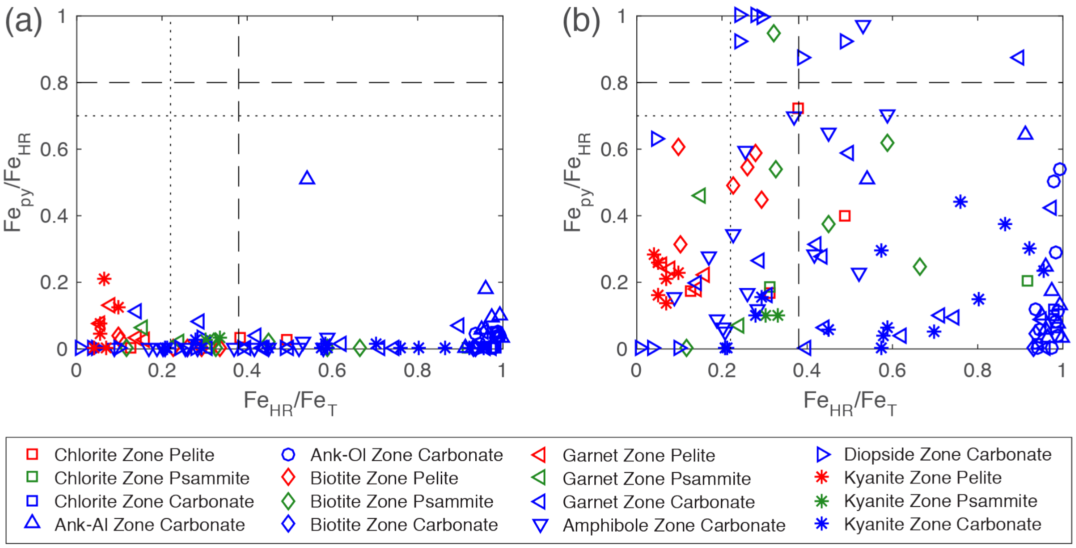

Figure 6.3: Waits River and Gile Mountain Formation data plotted in iron speciation space. Legend is the same for both plots with different symbols representing the 8 different metamorphic zones color-coded by lithology. Ank-Al stands for Ankerite-Albite and Ank-Ol stands for Ankerite-Oligoclase. (a) Pyrrhotite in the iron carbonate (Fe$_{carb}$) pool. (b) Pyrrhotite in the pyrite pool (Fe$_{py}$). Fe$_{py}$/Fe$_{HR}$ is the ratio of pyrite to highly reactive iron and Fe$_{HR}$/Fe$_{T}$ is the ratio of highly reactive to total iron. Figures 6.4 and 6.5 show expanded plots for more detail.

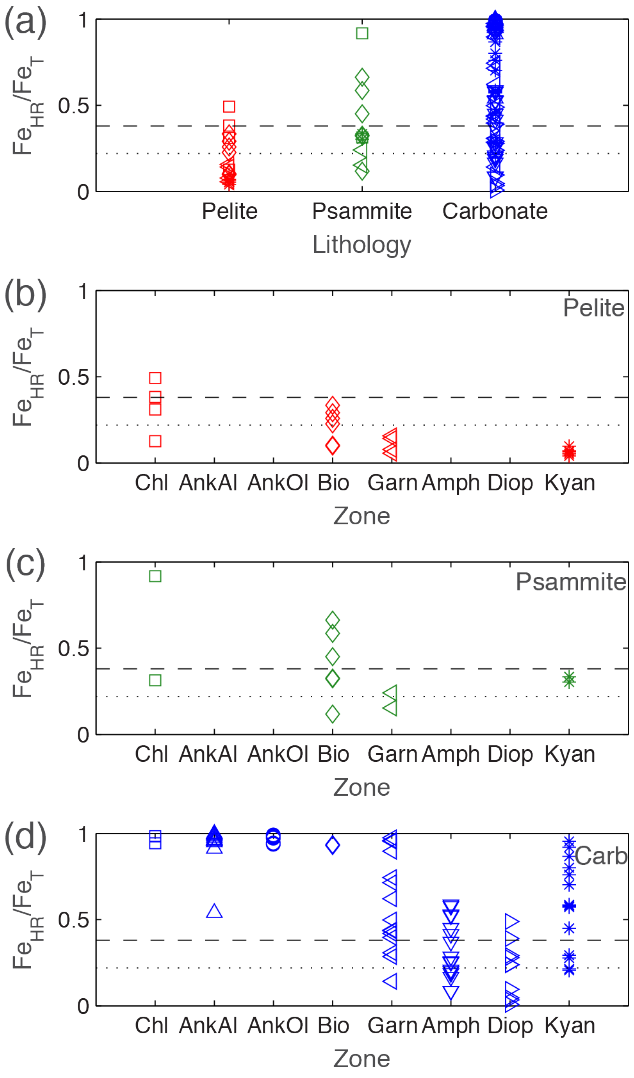

Figure 6.4: Highly reactive iron to total iron (Fe_{HR}/Fe_T) ratios in detail separated by lithology and zone for Waits River and Gile Mountain Formations. Same symbols as Figure 6.3; here labeled on the plots with symbols for metamorphic zone color-coded by lithology. Abbreviations are: Chl = Chlorite, Ank-Al = Ankerite–Albite, Ank-Ol = Ankerite-Oligoclase, Bio = Biotite, Amph = Amphibole, Diop = Diopside, Kyan = Kyanite, Carb = Carbonate.

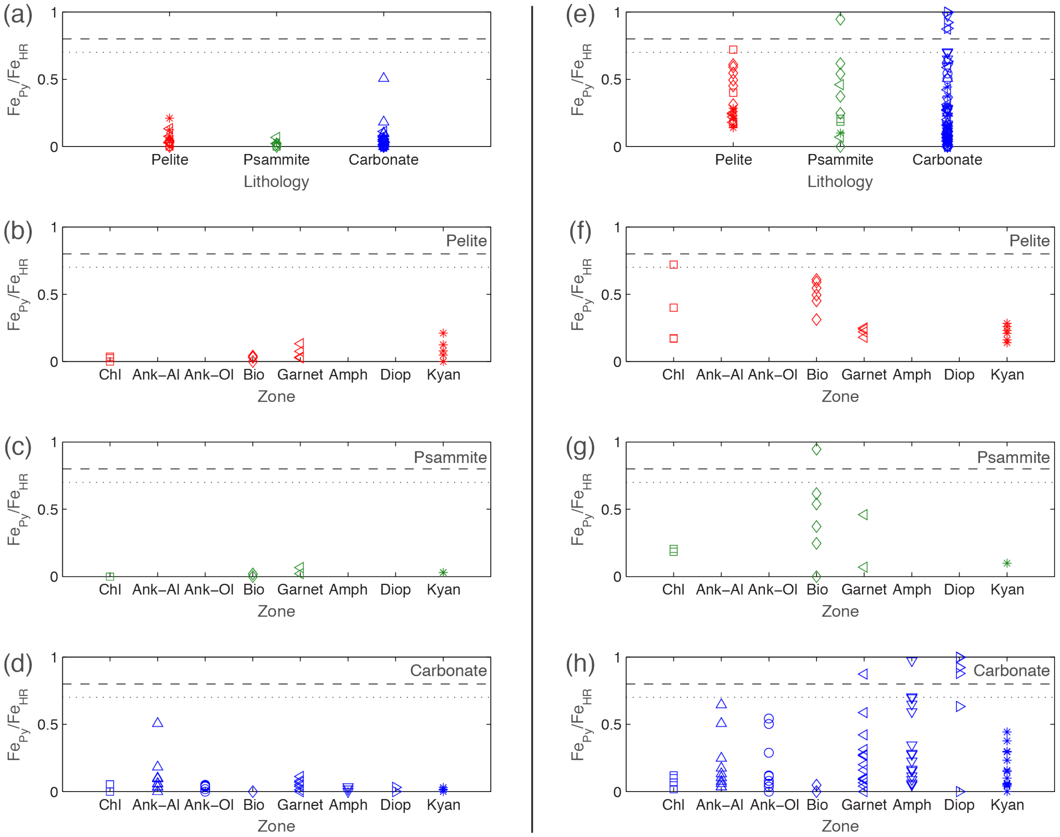

Figure 6.5: Pyrite to highly reactive iron (Fe_{py}/Fe_{HR}) ratios in detail separated by lithology and zone for Waits River and Gile Mountain Formations. (a-d) Pyrrhotite in the iron carbonate (Fe_{carb}) pool. (e-h) Pyrrhotite in the Fe_{py} pool. Same symbols as Figure 6.3; here labeled on the plots with symbols for metamorphic zone color-coded by lithology. Abbreviations for zones are: Chl = Chlorite, Ank-Al = Ankerite–Albite, Ank-Ol = Ankerite-Oligoclase, Bio = Biotite, Amph = Amphibole, Diop = Diopside, Kyan = Kyanite.

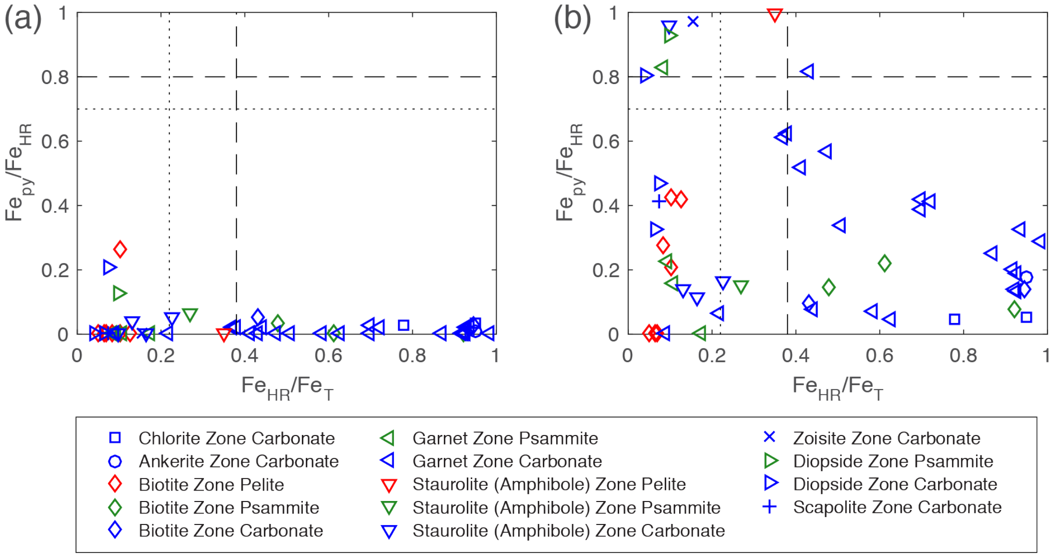

Figure 6.6: Waterville and Sangerville-Vassalboro Formation data plotted in iron speciation space. Legend is the same for both plots with different symbols representing the 8 different metamorphic zones color-coded by lithology. Staurolite (Amphibole) stands for the pelitic schist and carbonate facies respectively. (a) Pyrrhotite in the Fe_{carb} pool. (b) Pyrrhotite in the pyrite pool (Fe_{py}). Figures 6.7 and 6.8 show expanded plots for more detail.

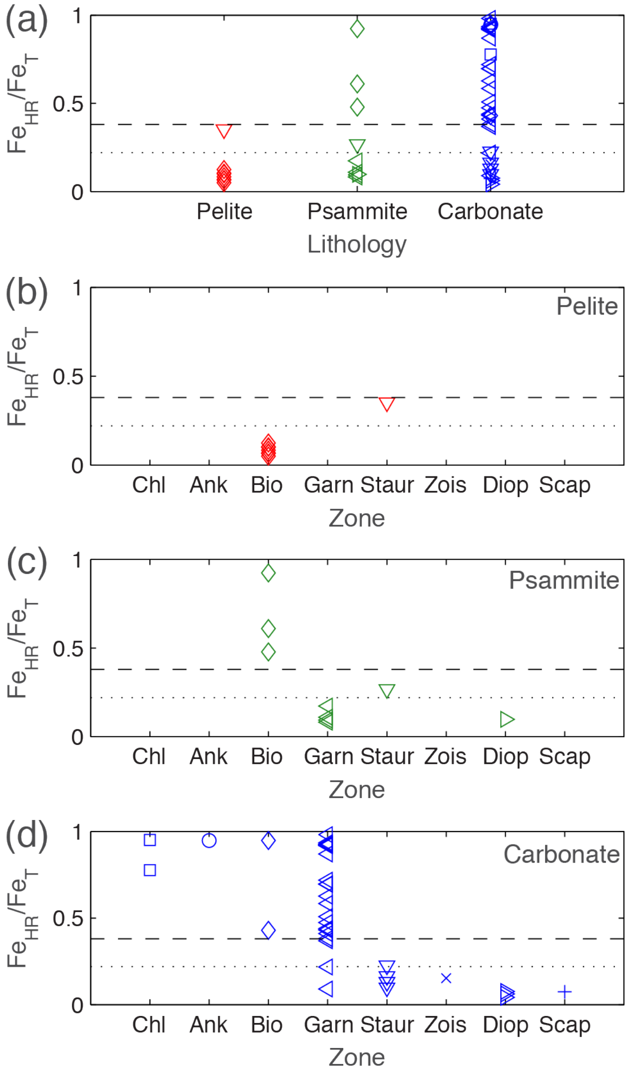

Figure 6.7: Highly reactive iron to total iron (Fe_{HR}/Fe_T) ratios in detail separated by lithology and zone for the Waterville and Sangerville-Vassalboro Formations. Same symbols as Figure 6.6; here labeled on the plots with symbols for metamorphic zone color-coded by lithology. Abbreviations for zones are: Chl = Chlorite, Ank = Ankerite, Bio = Biotite, Garn = Garnet, Staur = Staurolite (Amphibole), Zois = Zoisite, Diop = Diopside, Scap = Scapolite.

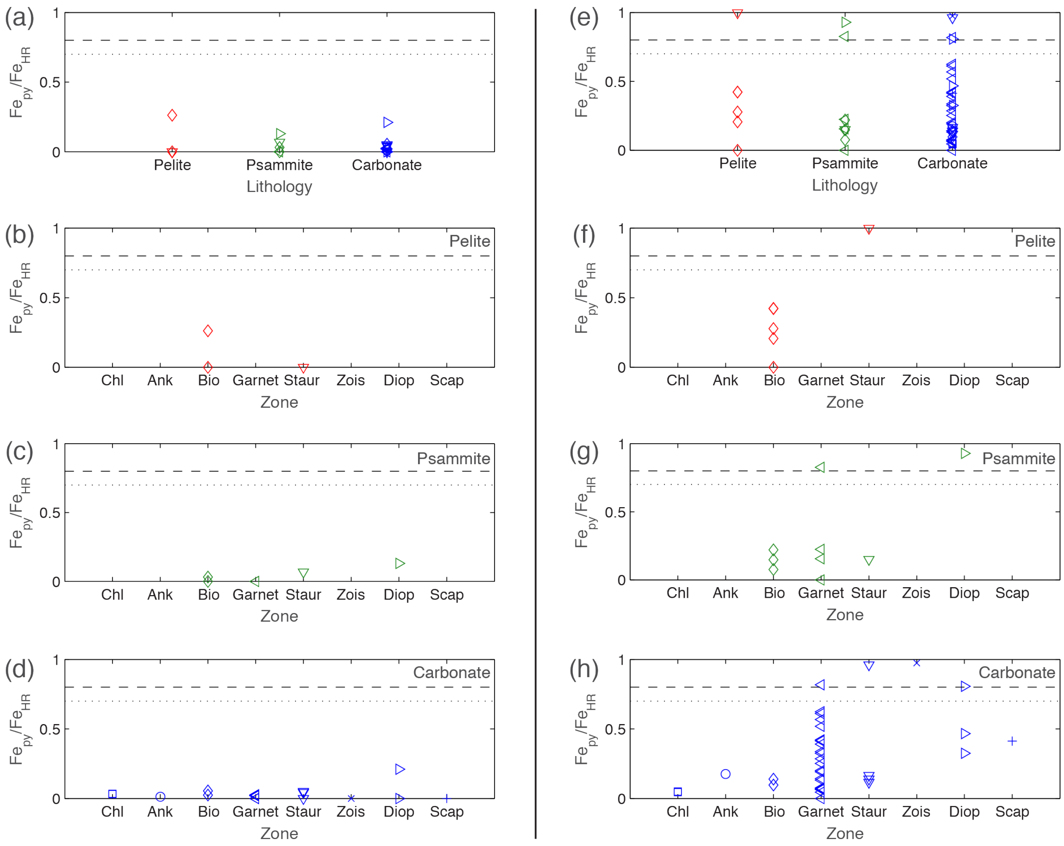

Figure 6.8: Pyrite to highly reactive iron (Fe_{py}/Fe_{HR}) ratios in detail separated by lithology and zone for the Waterville and Sangerville-Vassalboro Formations. (a-d) Pyrrhotite in the iron carbonate pool (Fe_{carb}). (e-h) Pyrrhotite in the pyrite pool (Fe_{py}). Same symbols as Figure 6.6; here labeled on the plots with symbols for metamorphic zone color-coded by lithology. Abbreviations for zones are: Chl = Chlorite, Ank = Ankerite, Bio = Biotite, Staur = Staurolite (Amphibole), Zois = Zoisite, Diop = Diopside, Scap = Scapolite.

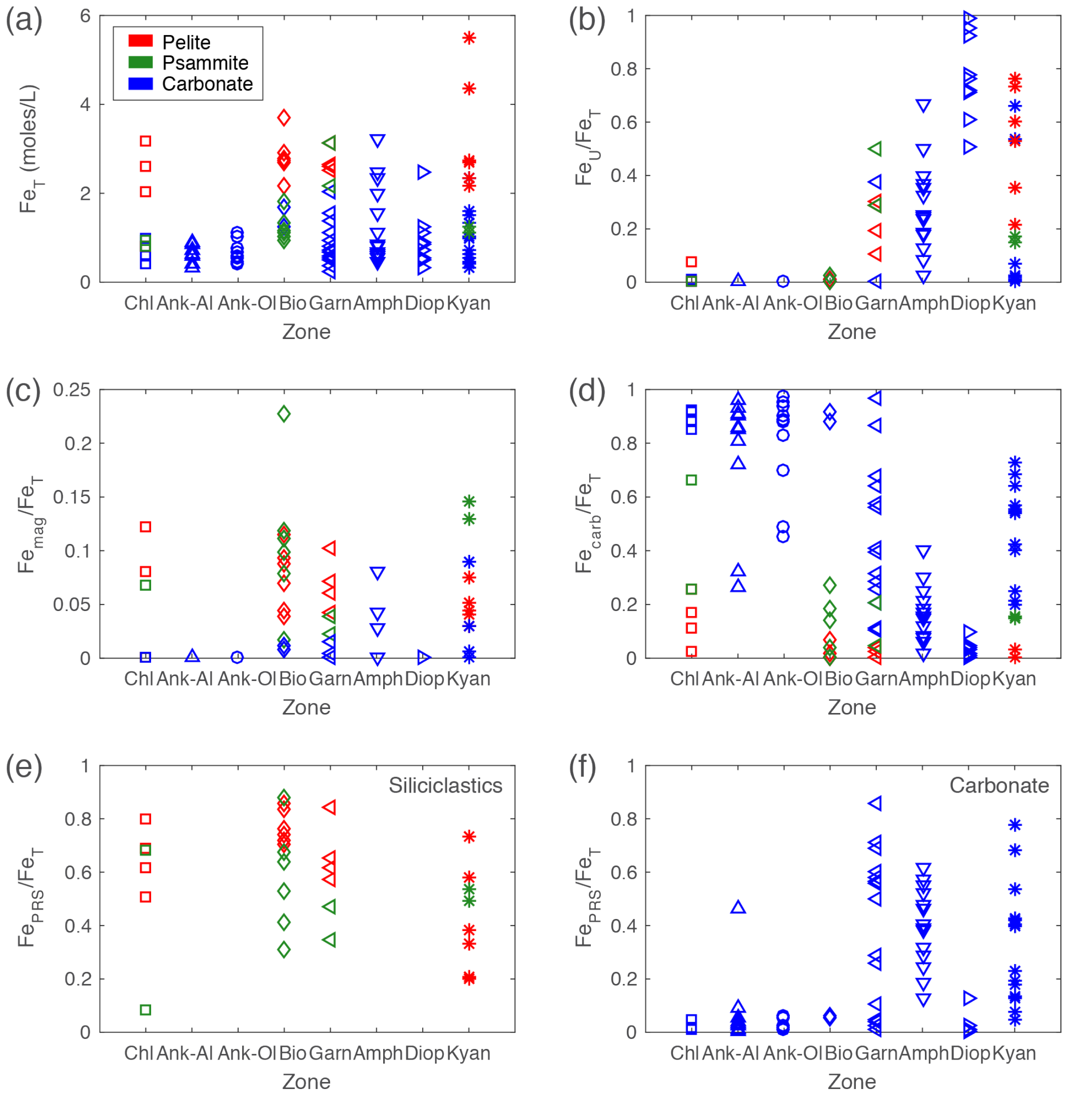

Figure 6.9: Different iron pools separated by metamorphic grade in samples from Waits River and Gile Mountain Formations. (a) Total iron (Fe_T). (b) Ratio of unreactive silicate iron to total iron (Fe_U/Fe_T). (c) Ratio of magnetite iron pool (entirely ilmenite here) to total iron (Fe_{mag}/Fe_T). Note this is at a different scale than (b-f). (d) Ratio of carbonate iron to total iron (Fe_{carb}/Fe_T). (e) Ratio of poorly reactive sheet silicates to total iron (Fe_{PRS}/Fe_T) for pelites and psammites. (f) Ratio of poorly reactive sheet silicates to total iron (Fe_{PRS}/Fe_T) for carbonate. Same symbols as Figure 6.3; lithology color codes in legend in (a) with symbols for metamorphic zone labeled on plots. Abbreviations for zones are: Chl = Chlorite, Ank-Al = Ankerite–Albite, Ank-Ol = Ankerite-Oligoclase, Bio = Biotite, Garn = Garnet, Amph = Amphibole, Diop = Diopside, Kyan = Kyanite. All data here is assuming pyrrhotite is in the pyrite pool (Fe_{py}).

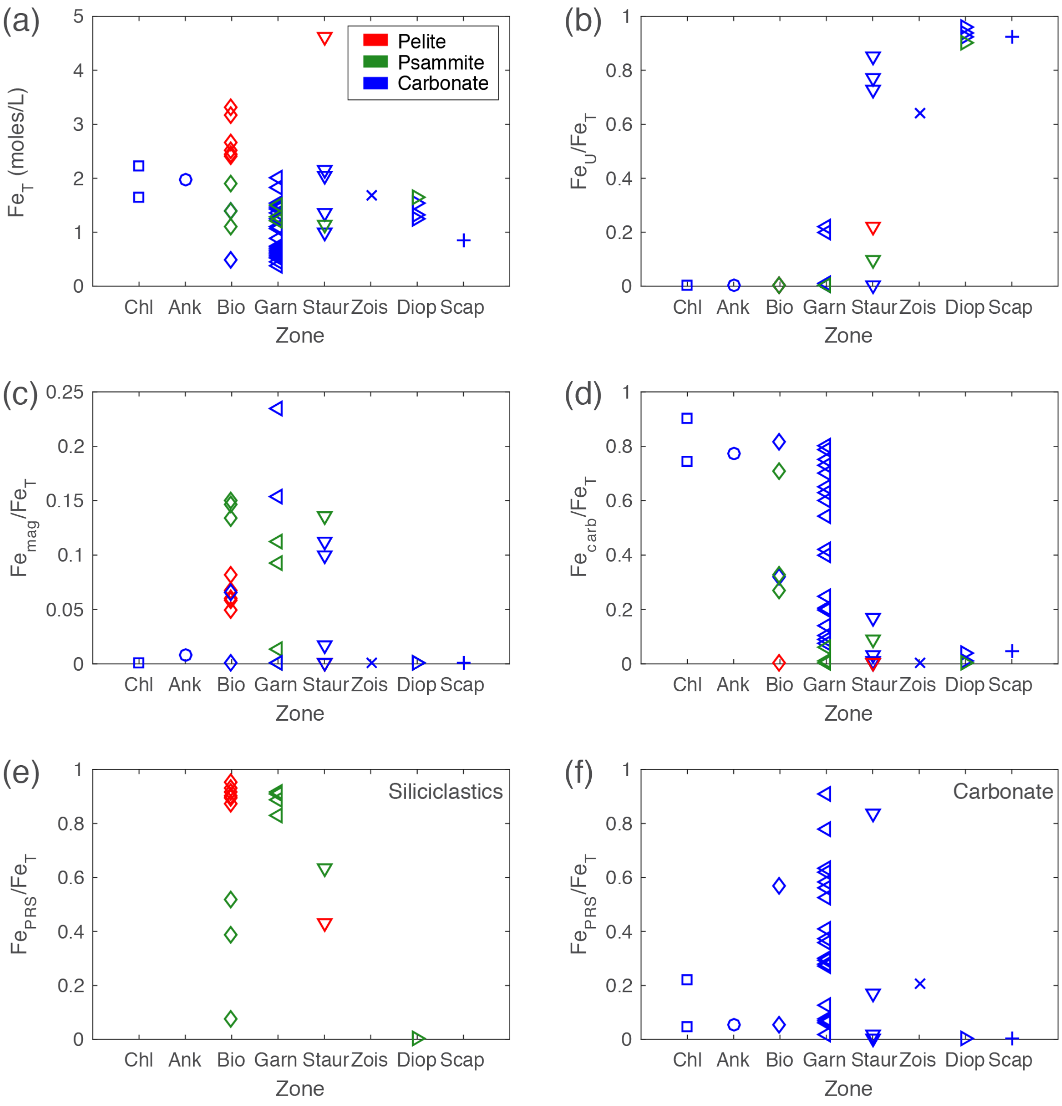

Figure 6.10: Different iron pools separated by metamorphic grade in samples from Waterville and Sangerville-Vassalboro Formations. (a) Total iron (Fe_T). (b) Ratio of unreactive silicate iron to total iron (Fe_U/Fe_T). (c) Ratio of magnetite iron pool (entirely ilmenite here) to total iron (Fe_{mag}/Fe_T). Note this is at a different scale than (b-f). (d) Ratio of carbonate iron to total iron (Fe_{carb}/Fe_T). (e) Ratio of poorly reactive sheet silicates to total iron (Fe_{PRS}/Fe_T) for pelites and psammites. (f) Ratio of poorly reactive sheet silicates to total iron (Fe_{PRS}/Fe_T) for carbonate. Same symbols as Figure 6.6; lithology color codes in legend in (a) with symbols for metamorphic zone labeled on plots. Abbreviations for zones are: Chl = Chlorite, Ank = Ankerite, Bio = Biotite, Garn = Garnet, Staur = Staurolite (Amphibole), Zois = Zoisite, Diop = Diopside, Scap = Scapolite. All data here is assuming pyrrhotite is in the pyrite pool (Fe_{py}).

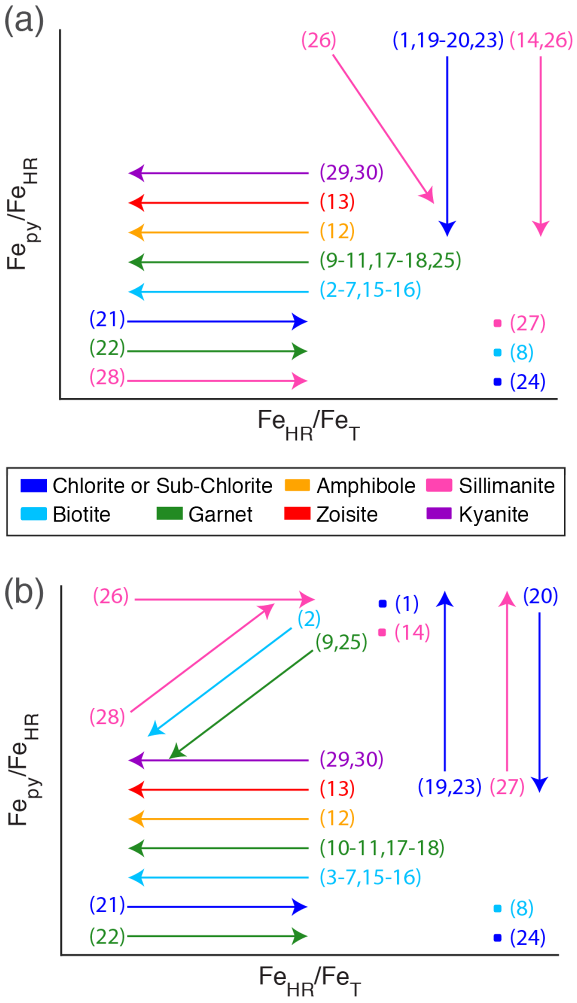

Figure 6.11: Example metamorphic reactions that transform iron between pools plotted in iron speciation place. Each vector shows the direction ratios will move as a given reaction progresses and are not quantitative. Vectors are color-coded by metamorphic zone when the reaction first occurs (cooler colors are lower metamorphic grade) with the same key for both plots. Numbers correspond to equations in Table 6.3 where more details on the reactions can be found. (a) Pyrrhotite in the Fe$_{carb}$ pool. (b) Pyrrhotite in the pyrite pool (Fe$_{py}$).

6.10 Supplemental Figures

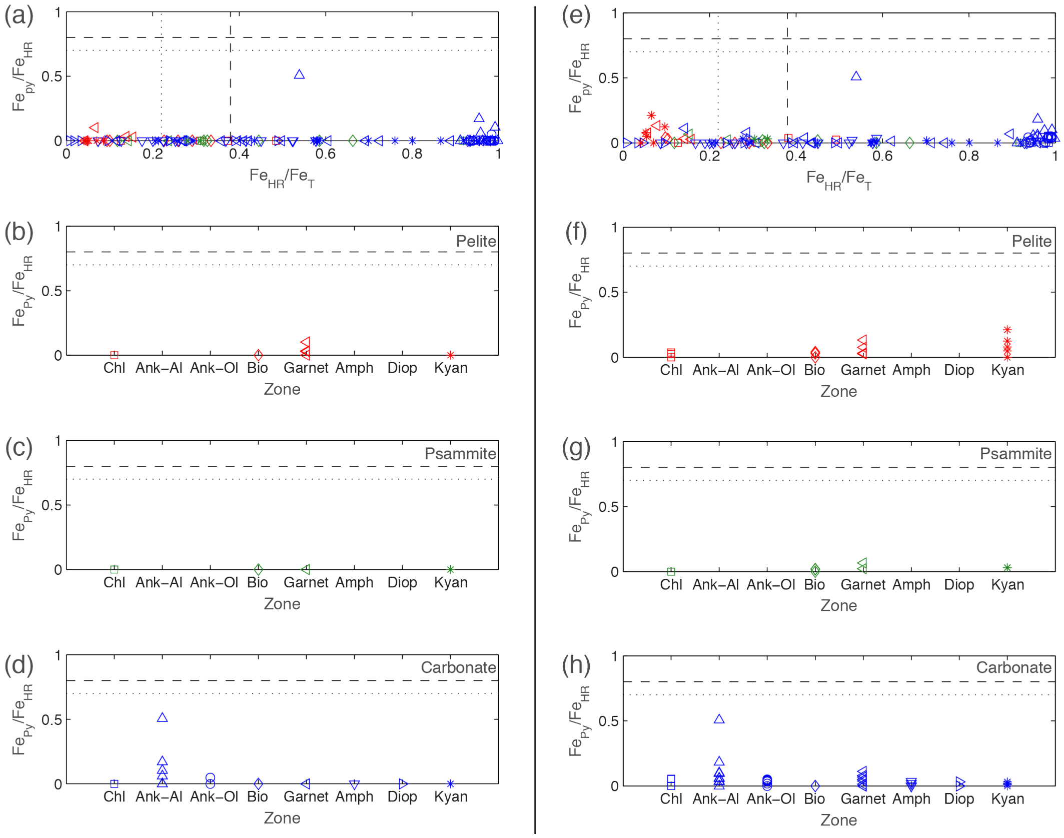

Figure S6.1: Waits River and Gile Mountain Formation data plotted in iron speciation space assuming pyrrhotite in the iron carbonate (Fe_{carb}) pool with details of Fe_{py}/Fe_{HR} ratios separated by lithology and zone. Same symbols as Figure 6.3; here labeled on the plots with different symbols representing the 8 different metamorphic zones color-coded by lithology. (a) Without trace minerals included. (b) With trace minerals included. Abbreviations for zones are: Chl = Chlorite, Ank-Al = Ankerite–Albite, Ank-Ol = Ankerite-Oligoclase, Bio = Biotite, Amph = Amphibole, Diop = Diopside, Kyan = Kyanite.

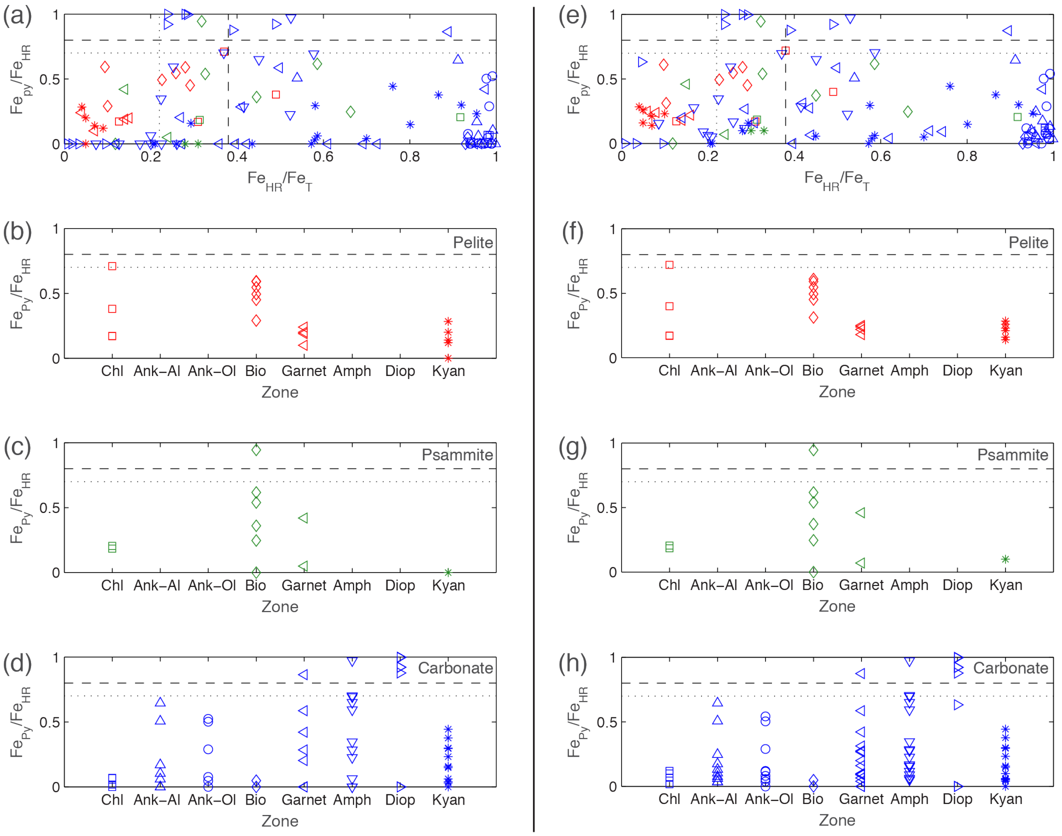

Figure S6.2: Waits River and Gile Mountain Formation data plotted in iron speciation space assuming pyrrhotite in the pyrite (Fe_{py}) pool with details of Fe_{py}/Fe_{HR} ratios separated by lithology and zone. Same symbols as Figure 6.3; here labeled on the plots with different symbols representing the 8 different metamorphic zones color-coded by lithology. (a) Without trace minerals included. (b) With trace minerals included. Abbreviations for zones are: Chl = Chlorite, Ank-Al = Ankerite–Albite, Ank-Ol = Ankerite-Oligoclase, Bio = Biotite, Amph = Amphibole, Diop = Diopside, Kyan = Kyanite.

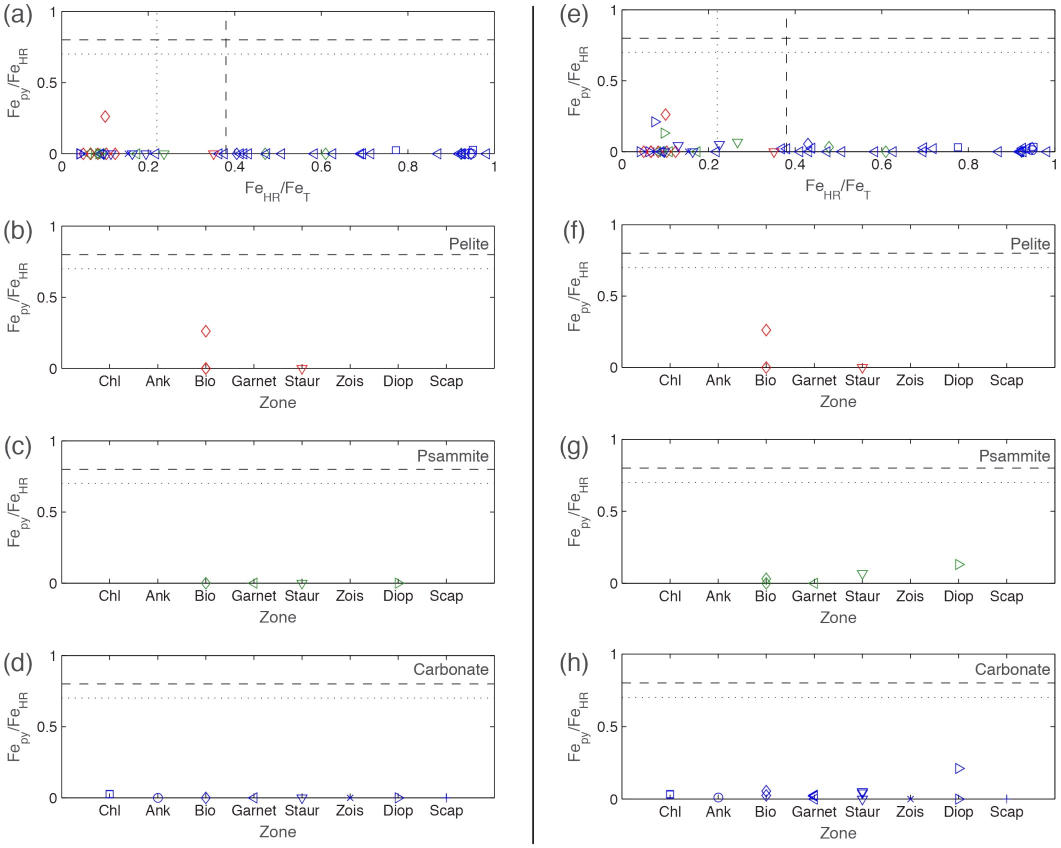

Figure S6.3: Waterville and Sangerville-Vassalboro Formation data plotted in iron speciation space assuming pyrrhotite in the iron carbonate (Fe_{carb}) pool with details of Fe_{py}/Fe_{HR} ratios separated by lithology and zone. Same symbols as Figure 6.6; here labeled on the plots with different symbols representing the 8 different metamorphic zones color-coded by lithology. (a) Without trace minerals included. (b) With trace minerals included. Abbreviations for zones are: Chl = Chlorite, Ank = Ankerite, Bio = Biotite, Staur = Staurolite (Amphibole), Zois = Zoisite, Diop = Diopside, Scap = Scapolite.

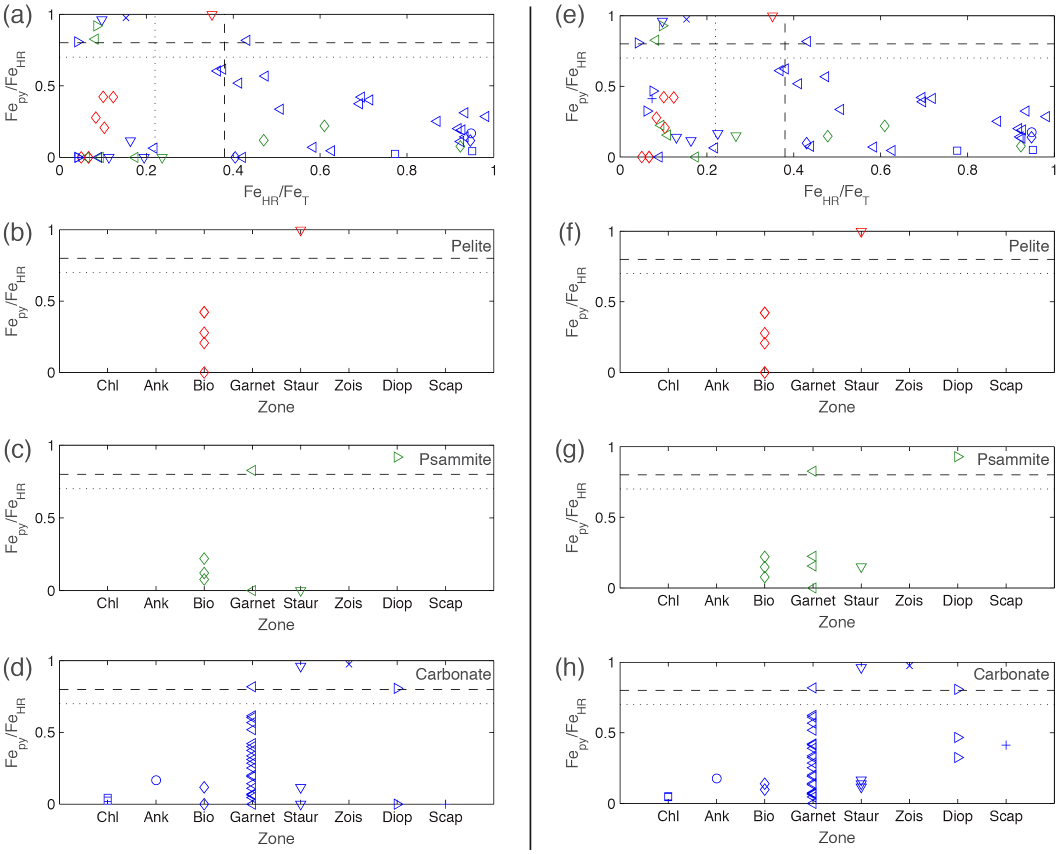

Figure S6.4: Waterville and Sangerville-Vassalboro Formation data plotted in iron speciation space assuming pyrrhotite in the pyrite (Fe_{py}) pool with details of Fe_{py}/Fe_{HR} ratios separated by lithology and zone. Same symbols as Figure 6.6; here labeled on the plots with different symbols representing the 8 different metamorphic zones color-coded by lithology. (a) Without trace minerals included. (b) With trace minerals included. Abbreviations for zones are: Chl = Chlorite, Ank = Ankerite, Bio = Biotite, Staur = Staurolite (Amphibole), Zois = Zoisite, Diop = Diopside, Scap = Scapolite.

6.11 References

Algoe, C., Stoops, G., Vandenberghe, R., and Van Ranst, E., 2012, Selective dissolution of Fe–Ti oxides—Extractable iron as a criterion for andic properties revisited: Catena, v. 92, p. 49-54.

Anbar, A. D., 2008, Elements and evolution: Science, v. 322, no. 5907, p. 1481-1483.

Anderson, T. F., and Raiswell, R., 2004, Sources and mechanisms for the enrichment of highly reactive iron in euxinic Black Sea sediments: American Journal of Science, v. 304, no. 3, p. 203-233.

Arnold, G. L., Anbar, A., Barling, J., and Lyons, T., 2004, Molybdenum isotope evidence for widespread anoxia in mid-Proterozoic oceans: Science, v. 304, no. 5667, p. 87-90.

Asael, D., Tissot, F. L., Reinhard, C. T., Rouxel, O., Dauphas, N., Lyons, T. W., Ponzevera, E., Liorzou, C., and Chéron, S., 2013, Coupled molybdenum, iron and uranium stable isotopes as oceanic paleoredox proxies during the Paleoproterozoic Shunga Event: Chemical Geology, v. 362, p. 193-210.

Barnaby, R. J., and Rimstidt, J. D., 1989, Redox conditions of calcite cementation interpreted from Mn and Fe contents of authigenic calcites: Geological Society of America Bulletin, v. 101, no. 6, p. 795-804.

Berner, R. A., 1970, Sedimentary pyrite formation: American journal of science, v. 268, no. 1, p. 1-23.

-, 1984, Sedimentary pyrite formation: an update: Geochimica et Cosmochimica Acta, v. 48, no. 4, p. 605-615.

Bickle, M., Chapman, H., Ferry, J., Rumble, D., and Fallick, A., 1997, Fluid Flow and Diffusion in the Waterville Limestone, South—Central Maine: Constraints from Strontium, Oxygen and Carbon Isotope Profiles: Journal of Petrology, v. 38, no. 11, p. 1489-1512.

Bucher, K., and Frey, M., 2002, Petrogenesis of metamorphic rocks, Berlin, Springer, Springer, Berlin, 341 p.:

Burton, E. D., Bush, R. T., and Sullivan, L. A., 2006, Sedimentary iron geochemistry in acidic waterways associated with coastal lowland acid sulfate soils: Geochimica et Cosmochimica Acta, v. 70, no. 22, p. 5455-5468.

Cabral, A., Creaser, R., Nägler, T., Lehmann, B., Voegelin, A., Belyatsky, B., Pašava, J., Gomes, A. S., Galbiatti, H., and Böttcher, M., 2013, Trace-element and multi-isotope geochemistry of Late-Archean black shales in the Carajás iron-ore district, Brazil: Chemical Geology, v. 362, p. 91-104.

Canfield, D., 1998, A new model for Proterozoic ocean chemistry: Nature, v. 396, no. 6710, p. 450-453.

Canfield, D. E., and Berner, R. A., 1987, Dissolution and pyritization of magnetite in anoxie marine sediments: Geochimica et Cosmochimica Acta, v. 51, no. 3, p. 645-659.

Canfield, D. E., Raiswell, R., Westrich, J. T., Reaves, C. M., and Berner, R. A., 1986, The use of chromium reduction in the analysis of reduced inorganic sulfur in sediments and shales: Chemical geology, v. 54, no. 1, p. 149-155.

Clarkson, M., Poulton, S., Guilbaud, R., and Wood, R., 2014, Assessing the utility of Fe/Al and Fe-speciation to record water column redox conditions in carbonate-rich sediments: Chemical Geology, v. 382, p. 111-122.

Cloud, P. E., 1968, Atmospheric and Hydrospheric Evolution on the Primitive Earth: Science, v. 160, no. 3829, p. 729-736.

Connolly, J., and Cesare, B., 1993, C ‐ O ‐ H ‐ S fluid composition and oxygen fugacity in graphitic metapelites: Journal of metamorphic geology, v. 11, no. 3, p. 379-388.

Cornwell, J. C., and Morse, J. W., 1987, The characterization of iron sulfide minerals in anoxic marine sediments: Marine Chemistry, v. 22, no. 2, p. 193-206.

Curtis, C., 1978, Possible links between sandstone diagenesis and depth-related geochemical reactions occurring in enclosing mudstones: Journal of the Geological Society, v. 135, no. 1, p. 107-117.

Dold, B., 2003, Speciation of the most soluble phases in a sequential extraction procedure adapted for geochemical studies of copper sulfide mine waste: Journal of Geochemical Exploration, v. 80, no. 1, p. 55-68.

Doll, C. G., Cady, W. M., Thompson Jr, J. B., and Billings, M. P., 1961, Centennial geologic map of Vermont: Vermont Geol: Survey, scale, v. 1, no. 250,000.

Ferry, J., 1976a, P, T, fCO2 and fH2O during metamorphism of calcareous sediments in the Waterville-Vassalboro area, south-central Maine: Contributions to Mineralogy and Petrology, v. 57, no. 2, p. 119-143.

Ferry, J. M., 1976b, Metamorphism of calcareous sediments in the Waterville-Vassalboro area, South-central Maine; mineral reactions and graphical analysis: American Journal of Science, v. 276, no. 7, p. 841-882.

Ferry, J. M., 1979, A map of chemical potential differences within an outcrop: American Mineralogist, v. 64, no. 9-10, p. 966-985.

Ferry, J. M., 1980, A comparative study of geothermometers arld geobarometers in pelitic schists from south-central Maine: American Mineralogist, v. 65, p. 720-732.

Ferry, J. M., 1981, Petrology of graphitic sulfide-rich schists from south-central Maine: an example of desulfidation during prograde regional metamorphism: American Mineralogist, v. 66, p. 908-930.

-, 1983a, Mineral reactions and element migration during metamorphism of calcareous sediments from the Vassalboro Formation, south-central Maine: American Mineralogist, v. 68, no. 3-4, p. 334-354.

-, 1983b, Regional metamorphism of the Vassalboro Formation, south-central Maine, USA: a case study of the role of fluid in metamorphic petrogenesis: Journal of the Geological Society, v. 140, no. 4, p. 551-576.

-, 1984, A biotite isograd in south-central Maine, USA: mineral reactions, fluid transfer, and heat transfer: Journal of Petrology, v. 25, no. 4, p. 871-893.

-, 1988a, Contrasting mechanisms of fluid flow through adjacent stratigraphic units during regional metamorphism, south-central Maine, USA: Contributions to Mineralogy and Petrology, v. 98, no. 1, p. 1-12.

-, 1988b, Infiltration-driven metamorphism in northern New England, USA: Journal of Petrology, v. 29, no. 6, p. 1121-1159.

-, 1992, Regional metamorphism of the Waits River Formation, eastern Vermont: delineation of a new type of giant metamorphic hydrothermal system: Journal of Petrology, v. 33, no. 1, p. 45-94.

-, 1994, Overview of the petrologic record of fluid flow during regional metamorphism in northern New England: American Journal of Science, v. 294, no. 8, p. 905-988.

-, 2007, The role of volatile transport by diffusion and dispersion in driving biotite-forming reactions during regional metamorphism of the Gile Mountain Formation, Vermont: American Mineralogist, v. 92, no. 8-9, p. 1288-1302.

Fisher, G. W., and Karabinos, P., 1980, Stratigraphic sequence of the Gile Mountain and Waits River Formations near Royalton, Vermont: Geological Society of America Bulletin, v. 91, no. 5, p. 282-286.

French, B. M., 1973, Mineral assemblages in diagenetic and low-grade metamorphic iron-formation: Economic Geology, v. 68, no. 7, p. 1063-1074.

Gillett, S. L., 2003, Paleomagnetism of the Notch Peak contact metamorphic aureole, revisited: pyrrhotite from magnetite+ pyrite under submetamorphic conditions: Journal of Geophysical Research: Solid Earth, v. 108, no. B9.

Haase, C. S., 1982, Metamorphic petrology of the Negaunee Iron Formation, Marquette District, northern Michigan; mineralogy, metamorphic reactions, and phase equilibria: Economic Geology, v. 77, no. 1, p. 60-81.

Hall, A. J., 1986, Pyrite-pyrrhotine redox reactions in nature: Mineralogical Magazine, v. 50, p. 223-229.

Hatch, N. L., Jr., 1988, Some revisions to the stratigraphy and structure of the Connecticut Valley trough, eastern Vermont: American Journal of Science, v. 288, no. 10, p. 1041-1059.

Holland, H. D., 1984, The chemical evolution of the atmosphere and oceans, Princeton University Press.

Holland, T., and Powell, R., 1998, An internally consistent thermodynamic data set for phases of petrological interest: Journal of Metamorphic Geology, v. 16, no. 3, p. 309-343.

Hsieh, Y.-P., Chung, S.-W., Tsau, Y.-J., and Sue, C.-T., 2002, Analysis of sulfides in the presence of ferric minerals by diffusion methods: Chemical Geology, v. 182, no. 2, p. 195-201.

Hueber, F. M., Bothner, W. A., Hatch, N. L., Finney, S. C., and Aleinikoff, J. N., 1990, Devonian plants from southern Quebec and northern New Hampshire and the age of the Connecticut Valley trough: American Journal of Science, v. 290, no. 4, p. 360-395.

Johnson, J. E., Webb, S. M., Thomas, K., Ono, S., Kirschvink, J. L., and Fischer, W. W., 2013, Manganese-oxidizing photosynthesis before the rise of cyanobacteria: Proceedings of the National Academy of Sciences, v. 110, no. 28, p. 11238-11243.

Jones, J., 1972, An almandine garnet isograd in the Rogers Pass area, British Columbia: the nature of the reaction and an estimation of the physical conditions during its formation: Contributions to Mineralogy and Petrology, v. 37, no. 4, p. 291-306.

Kendall, B., Creaser, R. A., Gordon, G. W., and Anbar, A. D., 2009, Re–Os and Mo isotope systematics of black shales from the Middle Proterozoic Velkerri and Wollogorang formations, McArthur Basin, northern Australia: Geochimica et Cosmochimica Acta, v. 73, no. 9, p. 2534-2558.

Klein, C., 1966, Mineralogy and petrology of the metamorphosed Wabush Iron Formation, southwestern Labrador: Journal of Petrology, v. 7, no. 2, p. 246-305.

Kopp, R. E., Kirschvink, J. L., Hilburn, I. A., and Nash, C. Z., 2005, The Paleoproterozoic snowball Earth: a climate disaster triggered by the evolution of oxygenic photosynthesis: Proceedings of the National Academy of Sciences of the United States of America, v. 102, no. 32, p. 11131-11136.

Léger, A., and Ferry, J., 1993, Fluid infiltration and regional metamorphism of the Waits River Formation, North ‐ east Vermont, USA: Journal of Metamorphic Geology, v. 11, no. 1, p. 3-29.

Léger, A., and Ferry, J. M., 1991, Highly aluminous hornblende from low-pressure metacarbonates and a preliminary thermodynamic model for the Al content of calcific amphibole: American Mineralogist, v. 76, p. 1002-1017.

Leventhal, J., and Taylor, C., 1990, Comparison of methods to determine degree of pyritization: Geochimica et Cosmochimica Acta, v. 54, no. 9, p. 2621-2625.

Li, C., Planavsky, N. J., Love, G. D., Reinhard, C. T., Hardisty, D., Feng, L., Bates, S. M., Huang, J., Zhang, Q., and Chu, X., 2015, Marine redox conditions in the middle Proterozoic ocean and isotopic constraints on authigenic carbonate formation: Insights from the Chuanlinggou Formation, Yanshan Basin, North China: Geochimica et Cosmochimica Acta, v. 150, p. 90-105.

Li, Y., and Schoonmaker, J., 2003, Chemical Composition and Mineralogy of Marine Sediments, *in* Mackenzie, F. T., ed., Sediments, Diagenesis, and Sedimentary Rocks: Treatise on Geochemistry, Volume 7, p. 1-35.

Lodders, K., and Fegley, B., 1997, An oxygen isotope model for the composition of Mars: Icarus, v. 126, no. 2, p. 373-394.

Lyons, J. B., 1955, Geology of the Hanover quadrangle, New Hampshire-Vermont: Geological Society of America Bulletin, v. 66, no. 1, p. 105-146.

März, C., Poulton, S., Beckmann, B., Küster, K., Wagner, T., and Kasten, S., 2008, Redox sensitivity of P cycling during marine black shale formation:

dynamics of sulfidic and anoxic, non-sulfidic bottom waters: Geochimica et Cosmochimica Acta, v. 72, no. 15, p. 3703-3717.

Moench, R. H., Boone, G., Bothner, W., Boudette, E., Hatch Jr, N., Hussey III, A., and Marvinney, R., 1995, Geologic Map of the Sherbrooke-Lewiston Area, Maine, New Hampshire, and Vermont, United States, and Quebec, Canada: US Geological Survey.

Nesbitt, B., and Kelly, W., 1980, Metamorphic zonation of sulfides, oxides, and graphite in and around the orebodies at Ducktown, Tennessee: Economic Geology, v. 75, no. 7, p. 1010-1021.

Osberg, P., 1988, Geologic relations within the shale-wacke sequence in south-central Maine: Studies in Maine geology, v. 1, p. 51-73.

Osberg, P. H., 1968, Stratigraphy, structural geology, and metamorphism of the Waterville-Vassalboro area, Maine, Maine Geological Survey.

Osberg, P. H., Tull, J. F., Robinson, P., Hon, R., and Butler, J. R., 1989, The Acadian orogen: The Appalachian–Ouachita orogen in the United States, The geology of North America: Geological Society of America, Boulder, v. 2, p. 179-232.

Pankiwskyj, K. A., Ludman, A., Griffin, J. R., and Berry, W., 1976, Stratigraphic relationships on the southeast limb of the Merrimack synclinorium in central and west-central Maine: Geological Society of America Memoirs, v. 146, p. 263-280.

Partin, C., Bekker, A., Planavsky, N., and Lyons, T., 2015, Euxinic conditions recorded in the ca. 1.93 Ga Bravo Lake Formation, Nunavut (Canada): Implications for oceanic redox evolution: Chemical Geology, v. 417, p. 148-162.

Penniston-Dorland, S. C., and Ferry, J. M., 2006, Development of spatial variations in reaction progress during regional metamorphism of micaceous carbonate rocks, northern New England: American Journal of Science, v. 306, no. 7, p. 475-524.

-, 2008, Element mobility and scale of mass transport in the formation of quartz veins during regional metamorphism of the Waits River Formation, east-central Vermont: American Mineralogist, v. 93, no. 1, p. 7-21.

Poulton, S., and Raiswell, R., 2002, The low-temperature geochemical cycle of iron: from continental fluxes to marine sediment deposition: American Journal of Science, v. 302, no. 9, p. 774-805.

Poulton, S. W., and Canfield, D. E., 2005, Development of a sequential extraction procedure for iron: implications for iron partitioning in continentally derived particulates: Chemical Geology, v. 214, no. 3, p. 209-221.

-, 2011, Ferruginous conditions: a dominant feature of the ocean through Earth's history: Elements, v. 7, no. 2, p. 107-112.

Praharaj, T., and Fortin, D., 2004, Determination of acid volatile sulfides and chromium reducible sulfides in Cu-Zn and Au mine tailings: Water, air, and soil pollution, v. 155, no. 1-4, p. 35-50.

Raiswell, R., and Berner, R. A., 1985, Pyrite formation in euxinic and semi-euxinic sediments: American Journal of Science, v. 285, no. 8, p. 710-724.

Raiswell, R., Buckley, F., Berner, R. A., and Anderson, T., 1988, Degree of pyritization of iron as a paleoenvironmental indicator of bottom-water oxygenation: Journal of Sedimentary Research, v. 58, no. 5.

Raiswell, R., Canfield, D., and Berner, R., 1994, A comparison of iron extraction methods for the determination of degree of pyritisation and the recognition of iron-limited pyrite formation: Chemical Geology, v. 111, no. 1, p. 101-110.

Raiswell, R., and Canfield, D. E., 1998, Sources of iron for pyrite formation in marine sediments: American Journal of Science, v. 298, no. 3, p. 219-245.

-, 2012, The iron biogeochemical cycle past and present: Geochemical Perspectives, v. 1, no. 1, p. 1-2.

Raiswell, R., Newton, R., and Wignall, P., 2001, An indicator of water-column anoxia: resolution of biofacies variations in the Kimmeridge Clay (Upper Jurassic, UK): Journal of Sedimentary Research, v. 71, no. 2, p. 286-294.

Raiswell, R., Reinhard, C. T., Derkowski, A., Owens, J., Bottrell, S. H., Anbar, A. D., and Lyons, T. W., 2011, Formation of syngenetic and early diagenetic iron minerals in the late Archean Mt. McRae Shale, Hamersley Basin, Australia: New insights on the patterns, controls and paleoenvironmental implications of authigenic mineral formation: Geochimica et Cosmochimica Acta, v. 75, no. 4, p. 1072-1087.

Reinhard, C. T., Lyons, T. W., Rouxel, O., Asael, D., Dauphas, N., and Kump, L. R., 2013, 7.10.4 Iron Speciaiton and Isotope Perspectives on Palaeoproterozoic Water Column Chemistry, *in* Melezhik, V., Prave, A.R., Hanski, E.J., Fallick, A.E., Lepland, A., Kump, L.R., Strauss, H., ed., Reading the Archive of Earth's Oxygenation, Volume 3: Berlin Heidelberg, Springer, p. 1483-1492.

Reinhard, C. T., Raiswell, R., Scott, C., Anbar, A. D., and Lyons, T. W., 2009, A late Archean sulfidic sea stimulated by early oxidative weathering of the continents: Science, v. 326, no. 5953, p. 713-716.

Reuschel, M., Melezhik, V., and Strauss, H., 2012, Sulfur isotopic trends and iron speciation from the c. 2.0 Ga Pilgujärvi Sedimentary Formation, NW Russia: Precambrian Research, v. 196, p. 193-203.

Robie, R. A., Bethke, P. M., and Beardsley, K. M., 1967, Selected X-ray crystallographic data, molar volumes, and densities of minerals and related substances: US Government Printing Office.

Roscoe, S., 1969, Huronian rocks and uraniferous conglomerates in the Canadian Shield: Geological Survey of Canada.

Schumann, R., Stewart, W., Miller, S., Kawashima, N., Li, J., and Smart, R., 2012, Acid–base accounting assessment of mine wastes using the chromium reducible sulfur method: Science of the Total Environment, v. 424, p. 289-296.

Shen, Y., Canfield, D. E., and Knoll, A. H., 2002, Middle Proterozoic ocean chemistry: evidence from the McArthur Basin, northern Australia: American Journal of Science, v. 302, no. 2, p. 81-109.

Sleep, N. H., and Bird, D. K., 2008, Evolutionary ecology during the rise of dioxygen in the Earth's atmosphere: Philosophical Transactions of the Royal Society of London B: Biological Sciences, v. 363, no. 1504, p. 2651-2664.

Spear, F. S., and Harrison, T. M., 1989, Geochronologic studies in central New England I: Evidence for pre-Acadian metamorphism in eastern Vermont: Geology, v. 17, no. 2, p. 181-184.

Sperling, E. A., Wolock, C. J., Morgan, A. S., Gill, B. C., Kunzmann, M., Halverson, G. P., Macdonald, F. A., Knoll, A. H., and Johnston, D. T., 2015, Statistical analysis of iron geochemical data suggests limited late Proterozoic oxygenation: Nature, v. 523, no. 7561, p. 451-454.

Thompson, J., and Norton, S. A., 1968, Paleozoic regional metamorphism in New England and adjacent areas, *in* E-an Zen, W. S. W., J.B. Hadley,, and and J.B. Thompson, J., eds., Studies of Appalachian Geology: Northern and Maritime: New York, Wiley, p. 319-327.

Thompson, J. B., Jr., Robinson, P., Clifford, T. N., and Trask Jr, N. J., 1968, Nappes and gneiss domes in west-central New England, *in* E-an Zen, W. S. W., and J.B. Hadley, a. J. B. T., Jr., eds., Studies of Appalachian Geology: Northern and Maritime: New York, Wiley, p. 203-218.

Tomkins, A. G., 2010, Windows of metamorphic sulfur liberation in the crust: implications for gold deposit genesis: Geochimica et Cosmochimica Acta, v. 74, no. 11, p. 3246-3259.

Tracy, R. J., and Robinson, P., 1988, Silicate-sulfide-oxide-fluid reactions in granulite-grade pelitic rocks, central Massachusetts: American Journal of Science, v. 288, p. 45-74.

Tucker, R., Osberg, P., and Berry, H., 2001, The geology of a part of Acadia and the nature of the Acadian orogeny across central and eastern Maine: American Journal of Science, v. 301, no. 3, p. 205-260.

Walker, R., and James, N., 1992, Facies models: Response to sea level change, St. John's, Newfoundland, Geological Association of Canada, John's, Newfoundland, Geological Association of Canada.

Warren, J., 2000, Dolomite: occurrence, evolution and economically important associations: Earth-Science Reviews, v. 52, no. 1, p. 1-81.

Watkins, R., 1996, Skeletal composition of Silurian benthic marine faunas: Palaios, p. 550-558.

Whitney, D. L., and Evans, B. W., 2010, Abbreviations for names of rock-forming minerals: American mineralogist, v. 95, no. 1, p. 185.

Wilkin, R., and Barnes, H., 1997, Formation processes of framboidal pyrite: Geochimica et Cosmochimica Acta, v. 61, no. 2, p. 323-339.

Wilkin, R., Barnes, H., and Brantley, S., 1996, The size distribution of framboidal pyrite in modern sediments: an indicator of redox conditions: Geochimica et Cosmochimica Acta, v. 60, no. 20, p. 3897-3912.

Williams, R. P. J., and Frausto Da Silva, J. J. R., 2003, Evolution was chemically constrained: Journal of Theoretical Biology, v. 220, no. 3, p. 323-343.

Williamson, A., Conlan, B., Hillier, W., and Wydrzynski, T., 2011, The evolution of Photosystem II: insights into the past and future: Photosynthesis research, v. 107, no. 1, p. 71-86.

Wing, B. A., Ferry, J. M., and Harrison, T. M., 2003, Prograde destruction and formation of monazite and allanite during contact and regional metamorphism of pelites: petrology and geochronology: Contributions to Mineralogy and Petrology, v. 145, no. 2, p. 228-250.

Woodland, B. G., 1977, Structural analysis of the Silurian-Devonian rocks of the Royalton area, Vermont: Geological Society of America Bulletin, v. 88, no. 8, p. 1111-1123.

Zerkle, A. L., House, C. H., and Brantley, S. L., 2005, Biogeochemical signatures through time as inferred from whole microbial genomes: American Journal of Science, v. 305, no. 6-8, p. 467-502.

Zhou, T., Phillips, G. N., Dong, G., and Myers, R. E., 1995, Pyrrhotite in the Witwatersrand gold fields, South Africa: Economic Geology, v. 90, no. 8, p. 2361-2369.